PROCESS DISTORTIONS IN COMPOSITE MANUFACTURING

- From an Experimental Characterization to a Prediction Approach - for the Global Scale

DISSERTATION

zur Erlangung des akademischen Grades
Doktoringenieur
(Dr.-Ing.)

von Dipl.-Ing. Erik Kappel geb. am 02. April 1983 in Rostock

genehmigt durch die Fakultät für Maschinenbau der Otto-von-Guericke-Universität Magdeburg

Gutachter

Prof. Dr.-Ing. Michael Sinapius Prof. Dr.-Ing. habil. Dr. h.c. Ulrich Gabbert Promotionskolloquium am 26. Februar 2013

Zusammenfassung

Der zunehmende Einsatz von Kohlenstofffaserverbundwerkstoffen als Strukturmaterial dient dem Ziel leistungsfähigere, effizientere und somit ökologisch verträglichere Strukturen und Strukturkomponenten zu realisieren. Zunehmendes Interesse seitens der Automobilindustrie, sowie signifikant steigende Stückzahlen in der Luftfahrt, wobei erstmals über 50 Flugzeuge/Monat gefertigt werden sollen, resultieren in stetig wachsenden Anforderungen an die faserverbundspezifischen Fertigungsverfahren und deren Abläufe.

Eine wesentliche Herausforderung ist es dabei Faserverbundstrukturen in sehr engen geometrischen Toleranzen zu fertigen um so einen problemlosen und damit spannungsreduzierten Zusammenbau zu realisieren. Dies ist besonders für Großbauteile, wie sie in der Luftfahrt zu Einsatz kommen, von besonderer Bedeutung.

Gegenwärtig sind fertigungsinduzierte Deformationen ein immanentes, kostentreibendes Problem in der Faserverbundfertigung. Diese ungewollten Deformationen sind auf die richtungsabhängigen Materialeigenschaften des Verbunds zurückzuführen, die zum einen zu exzellenten spezifischen Eigenschaften führt, zum anderen jedoch zu komplexen und vergleichsweise schwer vorstellbaren Effekten im Fertigungsprozess.

Im Zusammenbau resultieren diese Formabweichungen der Einzelkomponenten in unzulässig hohen Spaltmaßen und Zwischenräumen, die mittels des Einsatzes von Hard- und Softshim manuell ausgeglichen werden müssen. Bauteilabhängig kann eine Montage sogar unmöglich sein, so dass signifikante Ausschussraten die Folge sind. Sowohl das manuell durchgeführte Shimming, als auch nachträgliche Werkzeugmodifikationen sind mit einem enormen Kosten- und Zeitaufwand verbunden. Hinzu kommt, dass diese Aktivitäten nur bedingt planbar sind und so den Status des 'kurzfristigen Problemlösens' nicht überschreiten.

Die vorliegende Arbeit verfolgt das Ziel eine Methodik bereitzustellen, welche es erlaubt die unvermeidlichen, da materialspezifischen, und somit zu erwartende fertigungsinduzierten Deformationen vorherzusagen, um diese Information im Bauteilentwicklungsprozess nutzbar zu machen. Auf diesem Weg können Fertigungseffekte im der strukturellen Auslegung eines Bauteils aber vor allem im Werkzeugdesign Anwendung finden, um so bereits im Vorfeld entsprechende Kompensationsmaßnahmen virtuell ableiten zu können.

Ein wesentlicher Kernpunkte der Arbeit ist die umfangreiche, experimentelle Charakterisierung der auftretenden verformungsinduzierenden Effekte Warpage, Spring-in (-back), sowie die am Beispiel durchgeführte Charakterisierung des forced-interaction Effekts. Die experimentellen Untersuchungen verfolgen dabei das Ziel, die genannten Phänomene hinsichtlich relevanter Bauteilund Prozessparameter, wie z.B. des Lagenaufbaus oder des Werkzeugmaterials, zu charakterisieren. Die Entwicklung eines methodischen, simulationsgestützten Vorgehens zur Vorhersage zu erwartender Fertigungsverformungen, bildet den zweiten, wesentlichen Kernpunkt der Arbeit. Wesentliche Neuerung dieser Methodik ist die Kondensierung einer Vielzahl prozessrelevanter

Parameter in einem einzelnen L-Probekörper. Basierend auf der experimentell ermittelten Verformung dieser Probekörper gelingt es mittels einer entwickelten analytischen Transfervorschrift äquivalente Simulationsparameter zu berechnen, welche in Kombination mit konventionellen Schalenelementen innerhalb der FEM Anwendung finden. Auf diesem Weg werden Modell-größenlimitierungen, sowie der außerordentlich hohe Parameterbedarf phänomenologisch motivierter Prozesssimulationsprogramme umgangen. Den Abschluss der Arbeit bildet eine Reihe experimenteller Validierungen, welche die Eignung der Methodik verifizieren.

Abstract

The increasing application of carbon fiber reinforced plastics as a structural material pursues the aim to realize high-performance structures with improved efficiency and reduced ecological impact. Increasing interest of the automotive industry and significantly increasing quantities for modern aircrafts in aerospace, targeting at more than 50 aircrafts/month, generates steadily increasing challenges for composite-specific manufacturing strategies and related processes.

The compliance of narrow geometrical tolerances is one essential challenge in order to achieve a simple and structure-friendly assembly process. This is of particular importance for large CFRP structures as they are used in aerospace applications.

Currently, manufacturing-induced distortions are an inherent, cost-driving issue within composite manufacturing. These undesired distortions are induced by the composite's anisotropic material properties in combination with the commonly used high-temperature processes.

On the one hand this anisotropy enables the superior specific mechanical properties, while on the other hand these properties induce the complex shape-changing effects during manufacturing. Within the assembly, these shape deviations result in inadmissible large gaps between mating parts which must be compensated with soft- or hardshim. For some structures, assembly can become impossible which results in increasing scrap rates. Manual shimming as well as tool re-work, often referred to as non-added value operations, are related to significant time and cost efforts.

The present thesis pursues the aim to provide a methodology to predict the unavoidable, manufacturing-induced distortions in order to use this data within an improved part development chain. This enables the consideration of manufacturing effects within the structural sizing and in particular the tool design as appropriate compensation measures can be derived on a virtual level prior the first part or tool is fabricated.

A comprehensive experimental investigation of the distortion-inducing effects warpage, spring-in (-back) and forced-interaction represents the first essential part of this thesis. The main aim of the experimental studies is to elaborate the main drivers of the single effects. Furthermore, a phenomena-specific characterization is performed which focuses on relevant part and process parameters such as layup or tool material.

The development of a prediction methodology for expectable process-induced distortion represents the second essential part of this thesis. The major novelty of this approach is the integration of a multitude of process-relevant parameters within one L-shaped specimen. Measured manufacturing-induced distortion of this small specimen is analytically transferred to an equivalent scale-independent simulation parameter while the structural FE model uses conventional shell elements.

Thus, model-size limitations and the extraordinary large parameter requirements of phenomenologically-based state of the art process analysis tools are bypassed which lead to a very quick and efficient simulation strategy.

The thesis concludes with a set of case studies which verify the suitability of the developed approach numerically and experimentally.

Vision is the art of seeing what is invisible to others

Jonathan Swift, 1667-1745

Acknowledgments

The research presented in this thesis was carried out during my time as a research assistant at the Institute of Composite Structures and Adaptive Systems in Braunschweig which is part of the German Aerospace Center (DLR).

My special thanks go to Prof. Michael Sinapius for the valuable and very interesting discussions throughout the whole preparation time of the thesis and the eventual academic supervision of this work. Moreover, I thank Prof. Ulrich Gabbert for the co-supervision, Prof. Michael Scheffler for the leadership of the examining board and Prof. Klaus Rohwer for sharing his expertise with me.

Particular thanks is due to Dr. Christian Hühne, head of department Composite Design, and deputy head Heiko Assing, for providing an ideal research environment that allowed me to dedicate myself fully to the investigation of process distortion inducing phenomena.

Special thanks are due to Daniel Stefaniak, who supported me with excellent work within the warpage investigations and with his extensive knowledge in the field of composites. Thank you for the variety of discussions on- and off-topic and for the proofreading of this thesis. Another thank you goes to Robert Prussak, who supported me with his warpage investigations of thin and simply curved UD laminates.

I would like to thank my former office colleagues Hardy Köke for countless conversations about any topic imaginable and Arne Stahl for supporting me with the 'small' Catia issues I encountered every now and then. I really enjoyed our time together in R065. Moreover I would like to thank Dr. Markus Kleineberg for a variety of highly interesting discussions and for the sharing his expertise with me. In addition, I thank Dirk Holzhüter, leader of the team 'Partanalysis', for supporting me with proofreading of the one or other publication.

I thank Ary Zipfel, who supported me with the great number of full-field measurements which are content of this thesis and in particular for the unbureaucratic scheduling. Further, I thank Mareike Stegmaier for her support in the pre- and the post processing of my specimens.

Apart from the academic stimulation and support mentioned above, a heartfelt thank you must go to my family who has given and still is providing me support in all the steps of my life. A thank you is due to my father Michael and in particular my mother Birgit for her enormous strength an patience in bring up a guy like me.

I would also like to give special thanks to my girlfriend Jessica Preuß for supporting and encouraging me over the last years and for tolerating long working days, extended fishing trips and other time-consuming activities.

Finally, I will dedicate this thesis to my grandfather Oskar Kappel who unfortunately passed away in May 2012. Thank you for your lifelong encouragement, for all you were as a grandfather and of course thank you for the 'long' walks around the Oberteich.

Braunschweig, February 2013

Erik Happel

Erik Kappel

Contents

Lis	of Acronyms	ix
Lis	of Symbols	xi
Int	duction	1
1	the Problem's Topicality and Relevance Nowadays The Problem's Topicality Goals of the Thesis Phenomena Spring-in and Warpage: A Definition Relevance and Consequences of Manufacturing Deformations Strategies to Counteract Process Distortions Review of the Literature Essence and Cognitions of the Review	7 12 16 18
2	esearch Objectives and Thesis Outline	33
3	haracterization of the Warpage Phenomenon 1 Preliminary Remarks on Warpage Experiments	40 41 45 50 51
4	Analytical Pre-examination of the Spring-in Effect Preliminary Remarks on Experimental Investigations Experimental Investigation on Spring-in Affecting Parameters Statistical Analysis on obtained Spring-in Angles Extended Radford Approach Experimental Quantification of Contributing Spring-In Fractions Spring-in of Doubly Curved Areas and Nonlinear-Swept Profiles Cognitions of the Spring-In Investigations	65 68 74 80 90 93
5	uperposition of Distortion Mechanisms 1 Process Distortions of an Integral Composite Box Structure	106 114
6	Semi-Numerical Prediction Approach 1. Intention of the Model and its Area of Application	123

	6.2	Model Derivation for Warpage of Flat Laminates	123
	6.3	Model Derivation for Spring-In of Single- and Double-Curved Sections	127
	6.4	Advanced Model Formulation	130
	6.5	Limitation and Transferability	131
7	Verif	fication by Means of Numerical and Experimental Studies	133
	7.1	Application and Extension of the Warpage Prediction Approach	133
	7.2	Numerical Verification for Warpage of Curved Specimens	135
	7.3	Compensation of C-profile Process Distortions	137
	7.4	Spring-in Simulation for a Curved L-profile	141
	7.5	Spring-in of Curvature-Changing Structures	144
	7.6	Verification of the T-joint Tool by Experimental Means	149
	7.7	Prediction of Process Distortions for the Integral CFRP Box Structure	150
	7.8	Consequences of Process Scattering on Box Distortions	157
	7.9	Process Distortions of a Highly Integrated CFRP Upper-Wing Cover	159
	7.10	Feasibility of the Tool-Compensation Approach	165
8	Cond	clusions and Outlook	169
Αŗ	pend	ix	173
	A	Verification of the Advanced Model Formulation	173
	В	Experimental Study on Interply Slippage	175
	\mathbf{C}	Spring-in Prediction Tool in MATLAB	176
	D	Shrinkage - isotropic, anisotropic $\dots \dots \dots$	178
Bi	bliogr	aphy	181
O۱	vn Pu	ublications	187
Cι	ırricul	um Vitae	190

List of Acronyms

ACT Advanced Composite Tool

ATOS Full-field measurement system

 C_{Ai} Configuration i fabricated on Aluminum

 C_{Ii} Configuration i fabricated on Invar

CAD Computer Aided Design

CAE Computer Aided Engineering

CFRP Carbon Fiber Reinforced Plastics

CLT Classical Laminate Theory

CPE Coefficients of process expansion

CTE Coefficient of Thermal Expansion

CV Coefficient of Variation

DoC Degree of Cure

DoF Degree of Freedom

FE Finite Element

FEA Finite Element Analysis

FEP Fluorinated Ethylene Propylen

FRP Fiber Reinforced Plastics

GOM Company - Gesellschaft für optische Messtechnik

GUI Graphical User Interface

HTS High Tenacity S

Invar Steel with a nickel content of 36% (1.3912.0)

 \tilde{K} Reference condition

K Actual condition

MRCC Manufacturer's Recommended Cure Cycle

OoA Out of Autoclave

Prepreg Preimpregnated fibers

PSD Part-Specification document

QI Quasi Isotropic

RTM Resin Transfer Molding

 T_g Glass transition temperature

TMA Thermo Mechanical Analysis

UD Unidirectional

List of Symbols

Latin

Symbol	\mathbf{Unit}	Description
<u>A</u>	N/mm	Extension stiffness matrix
a	mm	Web area warpage
A_{ij}	N/mm	Coefficient ij of the A matrix
A_K	-	K plies of orientation A
A_w	g/m^2	Area weight
$(B,-B)_M$	-	M plies of orientation B and -B
<u>B</u>	N	Coupling stiffness matrix
B_{ij}	N	Coefficient ij of the B matrix
B_a	mm	Actual outer arc length
C_L	-	L plies of orientation C
<u>D</u>	Nmm	Bending stiffness matrix
d	mm	Connecting dimension
D_{ij}	Nmm	Coefficient ij of the D matrix
d_a	mm	Change in flange distance due to web area warpage a
d_f	mm	Distance flange-to-flange
$E_{F,L}$	MPa	Fiber Young's modulus in longitudinal direction
E_{glass}	MPa	Young's modulus of the resin in glassy state
E_{rub}	MPa	Young's modulus of the resin in rubbery state
E_i	MPa	Young's modulus in i-direction
E_R	MPa	Resin's Young's modulus
G_{ij}	MPa	Shear modulus
L	mm	Length of the warpage specimen
L_c	mm	Critical length according to Twigg
\underline{M}	N	Vector of bending moments

M_i^*	N	Equivalent moment in i direction
\underline{N}	N/mm	Vector of normal forces
$ec{n}_i$	-	Normal vector i
N()	1/°	Normal (gaussian) distribution
p_a	MPa	Absolute pressure inside the autoclave
P_a	mm	Path a on the tool
P_{i}	-	Probability for interval $\pm i \cdot s_{\Delta \varphi}$
ppm	-	Parts per million 10^{-6}
$\underline{\underline{\bar{Q}}}_k$	MPa	Stiffness matrix of the k-th layer in global coordinates
$\underline{\underline{Q}}$	N/mm^2	Ply stiffness matrix in local coordinates
$R_{0,\varphi}$	mm	Nominal radius in direction of φ
$R_{0,\vartheta}$	mm	Nominal radius in direction of ϑ
R_{glob}	mm	Global part radius
R_{loc}	mm	Local part radius
R_a	μm	Average Roughness
R_i	mm	Actual inner radius
s	mm	Measured deviation due to spring-in
$s_{\Delta arphi}$	0	Standard deviation for measurand $\Delta\varphi$
S_{ii}	MPa	Stress tensor component ii
$\underline{\underline{T}}_{i}^{-1}$	-	Inverted rotation matrix of angle i
$\underline{\underline{T}}_i$	-	Rotation matrix of angle i
t	mm	Actual thickness
T_{Hp}	K	Heating plate temperature
t_{il}	mm	Thickness of interleaf layers
t_{ply}	mm	Nominal ply thickness
T_{Sp}	K	Specimen temperature
U_i	mm	Deflection in i-direction
UR_i	mm	Rotation around in i-axis
V_f	%	Fiber volume fraction
$ar{w}$	MPa	Average warpage deflection of multiple specimens

w mm Measured warpage deflectio	n
---------------------------------	---

 \tilde{x} - Tilde parameters refer to the reference condition

Greek

Symbol	\mathbf{Unit}	Description
α^*	ppm/K	Equivalent CTE of shrinkage induced strain
$lpha_i^*$	ppm/K	Modified thermal expansion parameter in i-direction
$lpha_{Alu,Steel}$	ppm/K	Thermal expansion of aluminum or invar tools
α_{cer}	ppm/K	Thermal expansion of a ceramic tool
α_{CFRP}	ppm/K	Thermal expansion of carbon fiber tools
$lpha_{F,L}$	ppm/K	CTE of the fiber in longitudinal direction
$lpha_{F,T}$	ppm/K	CTE of the fiber in transverse direction
$lpha_i$	ppm/K	Coefficient of thermal expansion in i-direction
α_m	ppm/K	Resin's CTE
$lpha_R$	ppm/K	Thermal expansion in radial direction
$lpha_T$	ppm/K	Thermal expansion in tangential direction
eta_i	-	Strain due to moisture swelling
Δl	mm	Length change
ΔT	K	Temperature Difference
Δt_i	s	Duration of stage i
ΔV	%	Resin's cure shrinkage
Δx	mm	Deflection in x-direction
Δy	mm	Deflection in y-direction
Δy_m	mm	Measured flange shape deviation in y-direction
$\Delta arphi$	0	Spring-in angle according to definition $\Delta \varphi = \varphi - \tilde{\varphi}$
$\Delta arphi_{FEM}$	0	Predicted spring-in using 2D FE analysis
$\Delta \varphi_{iso}$	0	Spring-in for isotropic materials
$\Delta \varphi_{max}$	0	Maximum spring-in derived from the minimum d_f
$\Delta arphi_{R,C}$	0	Radial spring-in fraction due to chemical shrinkage
$\Delta arphi_{R,T}$	0	Radial spring-in fraction due to thermal contraction
$\Delta \varphi_{Radford}$	0	Predicted spring-in using the radford approach

$\Delta \varphi_{T,C}$	0	Tangential spring-in fraction due to chemical shrinkage
$\Delta arphi_{T,T}$	0	Tangential spring-in fraction due to thermal contraction
$\Delta arphi_R$	0	Spring-in fraction driven by radial parameters
$\Delta \varphi_T$	0	Spring-in fraction driven by tangential parameters
$\overline{\Delta arphi}$	0	Average spring-in angle
$\dot{\varepsilon}_b$	1/s	Average strain rate during stage b
$arepsilon^*$	-	Equivalent strain in the transverse plane
$arepsilon^0$	-	Membrane strains
$arepsilon_{Ch}$	-	Chemical strain component
$arepsilon_{eff}$	-	Effective strain
$arepsilon_{froz}$	-	Residual (frozen) strain in the resin
$arepsilon_{glass}$	-	Resin strain in glassy state
$arepsilon_{int}$	-	Strain due to tool-part interaction
$arepsilon_{lam}$	-	Expansion of the laminate
$\varepsilon_{rubbery}$	-	Resin strain in rubbery state
$arepsilon_{Th}$	-	Thermal strain component
$\varepsilon_{thermal}$	-	Strain due to thermal heating
$arepsilon_{tool}$	-	Expansion of the tool
$arepsilon_i$	-	Strain in i-direction
$arepsilon_R$	-	Strain in radial direction
$arepsilon_T$	-	Strain in tangential direction
×	$1/\mathrm{mm}$	Membrane curvatures
λ	-	Ratio of thermal expansion for two different V_f contents
$ u_{ij}$	-	Poisson ratio in ij-plane
ϕ	0	Global section angle
$\partial \varphi/\partial s_{\varphi}$	$^{\circ}/\mathrm{mm}$	Angle change along the arc length $s=f(\varphi)$
φ	0	Actual section angle
$arphi_{chem}$	0	Chemical fraction of Spring-in
$arphi_{eff}$	0	Effective spring-in angle
$arphi_{tem}$	0	Thermal fraction of Spring-in
$arphi_0$	0	Initial section angle

\vec{n}_i	_	Normal	vector	i

 φ_{enc} ° Actual enclosed angle (flange-to-flange)

 φ_{sec} ° Actual section angle

 ψ ° Local section angle

 ρ kg/dm^3 Density

 $\sigma_{ass.}$ MPa Stress due to the assembly process

 $\sigma_{man.}$ MPa Residual stress due to manufacturing

 σ_i MPa Stress in i-direction

 Ξ - Constant

 ξ_i - Strain due to chemical shrinkage in i-direction

Introduction

Efficiency is one essential requirement for modern products. Particularly in context of mobility, the striving towards eco-efficient vehicles, which demand an intelligent light-weight-design, has opened the market for high-performance materials. Carbon fiber reinforced plastics (CFRP) are the material of choice for various branches of industry to meet those requirements. Innovative car manufacturers such as BMW respond to the increasing demand for electro-mobility and its associated demand for significant weight reduction, with car concepts as the I3, where the structural entire body of series vehicle is made of composite material for the first time. Within the aircraft industry the use of CFRP has been developed from a component solution to the material of choice for the majority of the structural body. Modern civil aircrafts such as the Boeing 787 or the Airbus A350XWB consist of CFRP material to over 50 %. The main reason for the use of CFRP materials, is their low density combined with high moduli and strength properties. Furthermore, current composite manufacturing technologies allow the fabrication of almost arbitrary geometries, which become more and more important considering design issues. Market forecasts of car manufacturers as well as leading aircraft companies predict a significantly increasing demand of mobility for the near future [1, 2, 3]. Within the aerospace environment catchwords such as 'ramp-up', which stand for a rapid increase of fabricated aircrafts per month, become omnipresent [4]. Consequently, manufacturing processes are challenged in order to realize demanded production rates. Reproducibility, narrow geometrical tolerances, process cycle times and ease of assembly are key-demands of those required high efficient manufacturing processes. Currently, especially the compliance of narrow geometrical tolerances is still a challenge for CFRP manufacturers. Nowadays, missing geometrical exactness leads to increased efforts in the assembly process as costly shimming becomes necessary to fill gaps between mating parts. In addition, the violation of geometrical tolerances leads to a non-negligible amount of scrap parts. Consequently, geometrical fidelity is directly linked to an immense cost-saving potential as shimming becomes dispensable and the scrap rates can be reduced significantly, whether parts are manufactured without undesired deviations from the designed shape.

In academia it is generally acknowledged that undesired process-induced deformations of CFRP structures are due to the anisotropic material properties of the composite. Autoclave supported fabrication processes, as they are common in state of the art aircraft manufacturing, deteriorate deformation inclination due to curing at high temperatures. However, even manufacturing at low curing temperatures leads to significant manufacturing deformations induced by the resin's chemical shrinkage during the ongoing curing process. Those deviations between the manufactured and the desired nominal geometry is often referred to as spring-in. As will be shown in this thesis, this definition turns out to be slightly inaccurate, as multiple drivers of fabrication induced deformations are acting in parallel.

Therefore, within this thesis, it is distinguished between warpage, induced due to extrinsic parameters as tool-part interaction for example, and spring-in induced due to intrinsic parameters as the composite's anisotropy. Moreover, the forced-interaction effect is regarded which is relevant for certain part shape and tooling materials. Deformations induced due to asymmetric laminate stacking are out of scope of this research as corresponding deformations are not a direct consequence of the manufacturing process.

As process-induced distortions are inevitable for current composite-process combinations, the search for suitable countermeasures is an issue for research as well as for producing companies 2 Introduction

for years.

In industry, the lack of economic and reliable procedures applicable within the industrial environment, have led to an establishment of widely empirical procedures, which are based on worker's experience and rule-of-thumb. Although CFRP producers gained a wealth of expertise, this procedure is susceptible for multiple reasons: The quality of compensation is directly linked to the quality and quantity of the worker's experience; experiences gained for one structure are hardly transferable to other dissimilar geometries; the risk increases massively with the part's complexity and scale; counteracting based on a loop of tool-rework, prototype manufacturing and prototype measurement in order to subsequently reduce process-distortions induces massive costs for tool machining and prototype manufacturing; an experience-based compensation is hardly implementable into CAE supported product-development chains.

According to the aforementioned increasing requirements for modern composite structures in automotive and aerospace, this procedure becomes contemporary and needs to be structured and a standard process should be established.

In academia, different approaches are proposed for the prediction of process-induced distortions. On the one hand side analytics-based strategies, as proposed by Radford [5] e.g., represent the most simple approaches. However, due to the limitation to cross-section analysis, those approaches reach their limits when part complexity increases. Furthermore, an implementation into FEA supported process-chains is difficult. Nevertheless, analytics-based models can give a quite good estimation of process-distortions for simple structures.

On the other hand numerical approaches using finite element analysis are developed accounting for the entire manufacturing process as for example proposed by Johnston [6]. Therein, different physical processes are modeled by constitutive models. As usual, each modeled physical process demands corresponding simulation parameters. Thus, extensive material characterizations are necessary for the model setup. Due to the modeled time-dependent curing process, heat-transfer or heat generation, transient calculations are required, while fine solid-element meshes are used for discretization. Although computing performance have increased massively within the last years, model-size and the high amount of necessary parameters remain the limiting factors for those numerical approaches. According to the aforementioned issues, numerical-based prediction approaches have not yet reached a state of the art status in part or tool design.

Within this thesis a new, more focused approach is developed that targets mainly on process-distortions. It pursues the idea that global deformations of a complex part can be explained with characteristic deformations obtained from simple laboratory-scale specimens. Utilizing that, the presented approach overcomes the aforementioned drawbacks of analytical and numerical prediction-strategies by a combination of experimental, analytical and numerical steps. The main objective is the significant reduction of required parameters for the prediction of the part's manufacturing distortions even for large components. Therefore, this thesis investigates acting mechanisms and main drivers of process-induced distortions. Following the physically based idea of the approach, a straightforward shell-element-based simulation strategy is developed, applied and experimentally validated.

1 The Problem's Topicality and Relevance Nowadays

1.1 The Problem's Topicality

Carbon fiber reinforced plastics have become the material of choice for high-performance applications due to their outstanding mechanical properties. In addition, almost arbitrary geometries can be fabricated with current manufacturing processes, which is a significant advantage in contrast to equivalent metal solutions. However, especially the compliance of narrow geometrical tolerances is still a challenge for CFRP manufacturers. Nowadays, as outlined by Campbell [7], missing geometrical exactness leads to increased efforts in the assembly process as shimming is necessary. Furthermore, the violation of geometrical tolerances leads to a not negligible amount of scrap parts. Consequently, geometrical fidelity is directly linked to an immense cost-saving potential when shimming becomes dispensable and the scrap rate reduces significantly. Indirectly, assembly costs can be reduced due the reduction of manual work as a consequence of improved geometrical fidelity.

Geometric measurements of fabricated parts often reveal massive deviations between the fabricated shape and the aspired nominal geometry. In academia it is widely acknowledged that those undesired process-induced deformations are due to the anisotropic material properties of fiber-reinforced composites. Autoclave supported fabrication exacerbates the extent of those deformations, as the composite cures at high temperatures while the autoclave pressure compacts the laminate and induced considerable normal forces against the tool surface. But even out-of-autoclave (ooA) manufacturing strategies lead to distortions due to the resin's cure shrinkage. In academia and in practice, those process-induced deviations are often referred to as spring-in.

It will be shown in this thesis that this definition is inaccurate, as multiple drivers of fabrication induced deformations are acting in parallel. This thesis distinguishes between warpage and spring-in distortions which is in accordance with Albert and Fernlund [8].

According to the authors, warpage is dominated by extrinsic process parameters such as the tool material and the bagging arrangement. Stefaniak et al. [9] outlined a significant dependency of the warpage deformations of thin flat composite specimens from tool-surface roughness and the prepreg material itself. Radford [5] showed that a single-sided mold concept may induce fiber volume fraction (V_f) gradients in laminate thickness direction. Those gradients can result in distortions similar to that one due to layup-asymmetry, as the V_f massively affects the in-plane ply properties. In contrast, spring-in deformations are driven by intrinsic material properties of the composite. A strong through-thickness anisotropy of common multi-angle laminates induced by anisotropic thermal expansion properties and the significant resin cure shrinkage leads to shape changes in curved areas of a part during processing. According to Fernlund et al. [10] and Twigg et al. [11] there is another indirect effect of the autoclave pressure. This effect is often referred to as forced-interaction. It leads to gradients of in-plane stresses in throughthickness direction of the part. Thereby, the autoclave pressure induces massive normal forces on the laminate, which are commonly desired for the compaction purposes. In combination with certain tooling and/or part geometries, these normal forces lead to a geometrical locking, when the composite's CTE is significantly smaller than the tool's CTE ($\alpha_{alu.steel} > \alpha_{CFRP}$). This effect is attributed to the warpage effect in this thesis, as it is driven by the tool's expansion which represents an extrinsic process parameter. In consequence, forced-interaction is of particular

relevance for steel and aluminum tools and will likely diminish for composite or invar tools as those materials have similar CTEs to the CFRP part $(\alpha_{Invar} \approx \alpha_{CFRP})$.

In contrast, the spring-in effect is driven by the composite's anisotropy. It induces distortions in curved laminate sections. Consequently, it is relevant for the majority of CFRP components such as profile structures or even curved skins. As warpage is only observed for thin flat laminates according to Twigg et al. [11] and Stefaniak et al. [9] it is only relevant for certain parts. However, forced-interaction induced distortions can superpose spring-in when tools with considerable CTE are used such as aluminum or steel.

1.2 Goals of the Thesis

As process distortions are inevitable for autoclaved state of the art carbon-duromere composites, they must be considered within a sophisticated design-process to improve the part's geometrical fidelity in the future. This is shown in the following flowchart schematically.

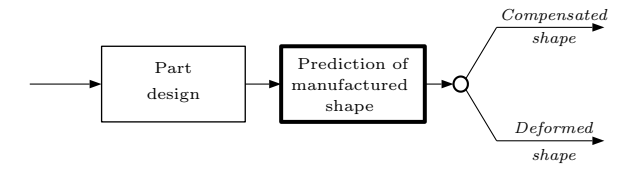


Fig. 1.1: Sophisticated part development due to consideration of CFRP-specific manufacturing deformations

According to Wille et al. [12] different approaches can be pursued in order to predict manufacturing-induced deformations: empirical, simulation-based and combined semi-numerical ones. In industry, mainly empirical strategies are established which depend mainly on the worker's experience. Often, a loop containing tool-rework and prototype-manufacturing is performed until the geometrical fidelity of the part is satisfying. Although composite manufactures already have a wealth of experience, the empirical approach is inefficient as it is time-consuming, cost-intensive and risky in particular for large structure. Furthermore, it reaches its limit when part complexity increases and the experience transfer from one shape to another dissimilar one is uncertain. Thus, no funded shape-independent knowledge can be built up using this approach.

In academia, considerable effort has been put into simulation-based approaches modeling the complex processes during the composite manufacturing process. Proposed strategies are not focused on process-distortions as comprehensive results are derived such as degree of cure (DoC) for example. Phenomena, such as inhomogeneous temperature distribution on the part surfaces, autoclave pressure, chemical shrinkage and exothermic heat, heat conduction, tool-part interaction as well as curing related property changes are only a selection of aspects being regarded simultaneously within such simulations on micro-level. According to the multitude of parallel acting mechanisms and their interaction, efforts for parameter determination are very high. In addition, due to time-dependency and local variability, transient calculations utilizing fine solid-element meshes are necessary which results in laborious modeling and long computation times.

Considering that part and tool design are located at an early stage of the development chain where it is common that neither the part's final geometry, the final composite material, nor the final layup is known. Thus, the efforts necessary for the set-up of a numerical-based model are disproportional high.

Furthermore, although computing performance has increased, model-size is still a limiting factor for simulation-based approaches especially for large structures as degree of freedoms (DoF) increases highly nonlinear with part scale driven by recommended FE aspect-ratio limitations.

Within this thesis a new, widely different strategy for the prediction of process-induced distortions is pursued, trying to overcome drawbacks of empirical and simulation-based approaches. Therein, the fundamental model considerations are related to the contents of a part-specification document (PSD) which contains the part's geometry and material-, tooling- and process-specific guidelines. The pursued approach differentiates between the nominal-part shape and the part's 'configuration', while the term 'configuration' contains all information of a PSD except the part's geometry. Thus, it is physically reasonable that the configuration-specific behavior during manufacturing is independent from the part's shape and scale. Hence, the knowledge of the configuration-specific behavior promises the predictability of process-induced distortions for the whole part-scale range without a limitation to a specific geometry. Consequently, the new approach follows this idea and uses laboratory-scale specimens for the evaluation of configuration-specific manufacturing distortions. Figure 1.2 shows a flow chart of the proposed strategy which represents the 'Prediction of manufactured shape' block in Figure 1.1.

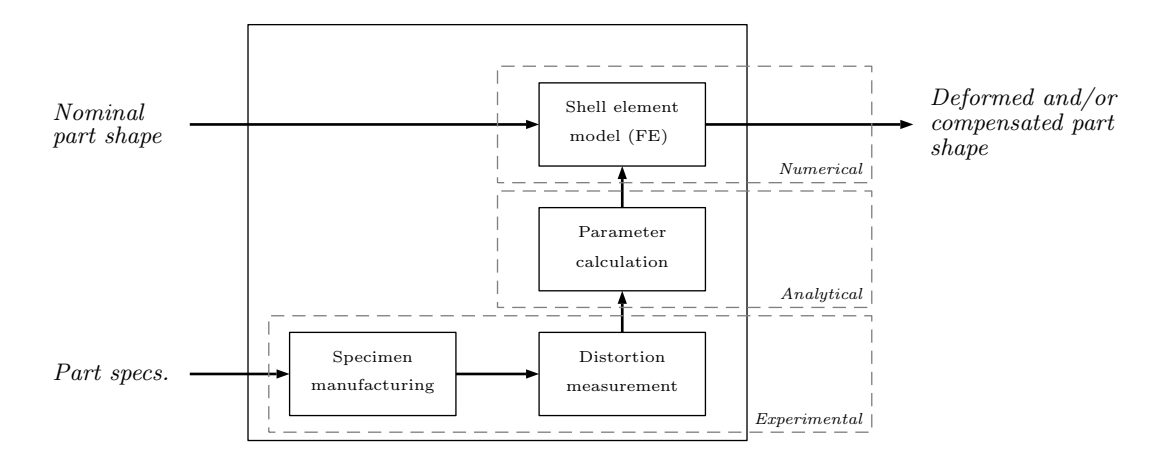


Fig. 1.2: Flow chart of the proposed semi-numerical simulation methodology

One essential advantage of that approach is that fabricated specimens inherently contain information about the material **and** the manufacturing process. Thus, a characterization of each acting physical process, as it is necessary for simulation-based strategies, is substituted by geometrical measurement of the specimen shape. That is supposed to be less erroneous, as the number of parameters and corresponding uncertainties is massively reduced. Furthermore, geometrical measurement using state-of-the-art techniques is comparably simple compared to comprehensive material characterizations.

Hence, the main goal of this thesis is the formulation of a semi-numerical compensation methodology according to Figure 1.2. To achieve this, the main goal is subdivided into three sub-goals which are 'preliminary experimental and numerical investigations', 'model derivation and application' and 'experimental validation'.

1. The idea is to work out the main drivers of spring-in and warpage experimentally and to quantify their impact. Therefore, the spring-in effect is investigated utilizing L-profile specimens similar to those used by Kleineberg [13]. In addition, a new experimental technique, similar to the one presented by Garstka et al. [14] is developed which allows an estimation of expectable spring-in distortion by use of the approach presented by Radford [5]. The warpage phenomenon is investigated, while specimens are similar to that ones used by Twigg et al. [11]. The forced-interaction effect is investigated exemplary for one critical box structure. In parallel to the experimental work, results are reviewed and compared to preliminary numerical studies in order to validate their plausibility.

- 2. Focusing on the fundamental idea of a straightforward procedure, an analytical model is developed which transfers measured distortions on specimen level to corresponding simulation parameters. The analytical model is suitable for warpage of flat and slightly curved geometries as well as spring-in of single- and double-curved geometries. The use of common shell elements within the FEA environment is one essential innovation of the new concept. In addition, an extension of Radford's [5] model is proposed as an alternative input source for the parameter calculation and to provide a kind of a handbook-formula.
- 3. For sake of verification, the developed approach is applied to multiple sample cases and experimentally validated. The idea of a compensation within the tool geometry is experimentally validated for a straight C-profile geometry. Transferability of the findings for extruded profiles to double-curved profiles is examined. The approach is applied to a complex CFRP box structure and predictions are compared to measurement results. Finally, the approach is applied to a highly integral CFRP upper wing cover and results are compared to three manufactured parts.

1.3 Phenomena Spring-in and Warpage: A Definition

In the literature a multitude of different nomenclatures are used to describe process-induced distortions. This leads to an inconsistent and therefore unclear wording within this field of research. The synonyms spring-forward (e.g. [15]), spring-back (e.g. [16]), spring-down (e.g. [17]), warpage (e.g. [18]) as well as spring-in (e.g. [19]) are used synonymously by different authors, describing manufacturing deformations. Neither a phenomena-based distinction with respect to the part's geometric properties nor a distinction into material specific (intrinsic) and material unspecific (extrinsic) effects is consistent.

This thesis distinguishes between two main phenomena: spring-in and warpage which is shown in Figure 1.3. The former describes process-distortions due to the intrinsic anisotropic material properties, the part's geometry and the process conditions, whereat the latter one is driven by extrinsic parameters such as tool-part interaction during processing or effects due to single-sided tooling. This is in accordance with Albert and Fernlund [8] who have shown that different phenomena affects the manufactured shape and therefore occurring deviations of composite parts.

Literature

Springforward, Springback, Spring-In and Warpage are used synonymously for fabrication-induced deformations

This Thesis

Spring-In: Shape changes due to intrinsic material properties. Predominant for parts with angled cross sections

Warpage: Shape changes due to extrinsic effects. Predominant for flat, thin or geometrically constrained parts

Fig. 1.3: Denotation of the acting effects used in this thesis

In general, spring-in and warpage effects act in parallel. The relevance of each effect depends massively on the part's geometry. As will be shown in this thesis, profile-like composite parts with angled cross sections are dominated by spring-in deformations. Flat laminates, fabricated on metallic single-sided tools with considerable thermal expansion such as steel of aluminum, are affected by the warpage phenomenon. Forced-interaction which is also driven by the tool's thermal expansion, can occur even for complex integral structures. Thus, it is very similar to the warpage effect. In the following, the phenomena spring-in, warpage and forced-interaction are described briefly.

The Spring-In Phenomenon

According to Albert and Fernlund [8], spring-in is induced due to the different material properties of the composite laminate in the in-plane directions and the through-thickness direction. Figure 1.4 shows that relationship qualitatively.

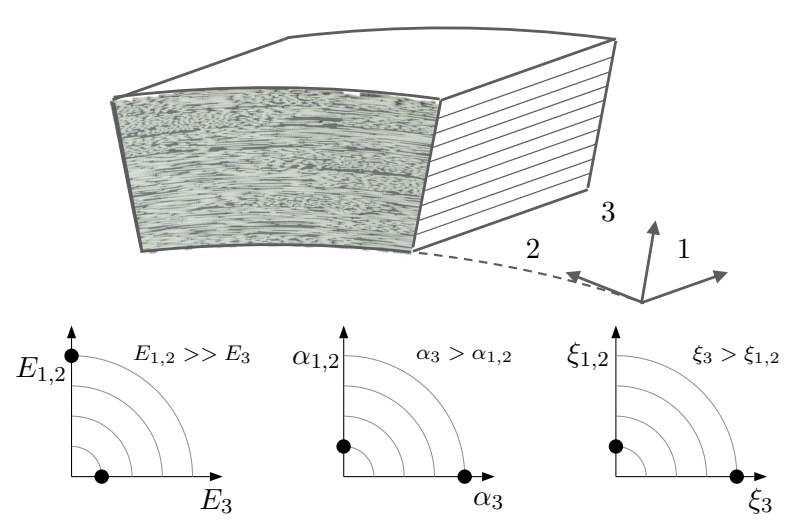


Fig. 1.4: Anisotropic material properties of a quasi-isotropic laminate. E_i , α_i and ξ_i denote the laminate's homogenized Young's modulus, CTE and the strain due to chemical shrinkage in i-direction, respectively.

During processing, the ongoing curing process leads to volumetric shrinkage of the resin which is observed mainly in thickness direction as the fibers constrict it in the laminate plane. A similar behavior is observed for the thermal fraction of the spring-in, which lead to deformations when the cured part is cooled down from curing to room temperature. As outlined by Nelson et al. [20], that mismatch between the through-thickness and the laminate-plane direction leads to shape changes only in curved laminate areas.

Figure 1.5 shows a schematic for the initial configuration \tilde{K} and the deformed configuration K.

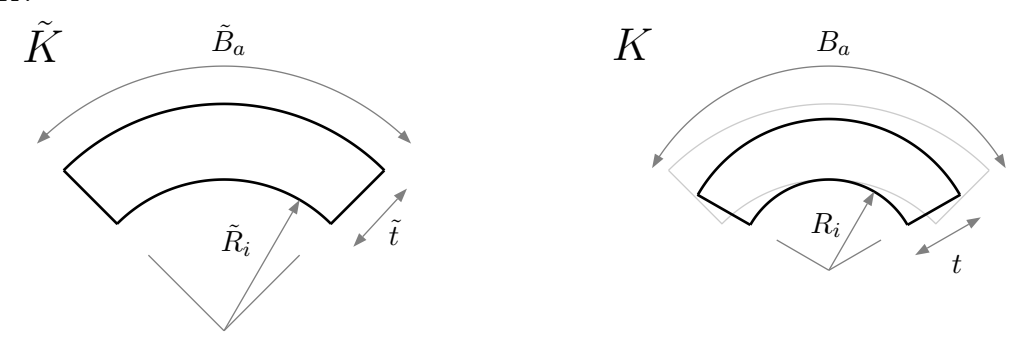


Fig. 1.5: Angle change due to inhomogeneous strains in the cross section plane.

Equation 1.1 derives the deformed angle φ with respect to anisotropic strains in tangential ε_T and radial ε_R direction and the initial angle $\tilde{\varphi}$.

$$\varphi = \frac{1 + \varepsilon_T}{1 + \varepsilon_R} \cdot \tilde{\varphi} \quad \text{from} \quad \begin{cases} B_a = \tilde{B}_a \cdot (1 + \varepsilon_T) \\ B_a = (R_i + t) \cdot \varphi \\ \tilde{B}_a = (\tilde{R}_i + \tilde{t}) \cdot \tilde{\varphi} \\ (R_i + t) = (\tilde{R}_i + \tilde{t}) \cdot (1 + \varepsilon_R) \end{cases}$$
(1.1)

In accordance with Radford [5] the spring-in angle $\Delta \varphi$ is given by Equation 1.2 wheres the strains ε_2 and ε_3 refer to Figure 1.4.

$$\Delta \varphi = \varphi - \tilde{\varphi} = \frac{\varepsilon_2 - \varepsilon_3}{1 + \varepsilon_3} \cdot \tilde{\varphi} \tag{1.2}$$

This equation excellently demonstrates that spring-in distortions are only relevant for anisotropic materials. Assuming isotropy, strain components in circumferential and thickness direction are identical $\varepsilon_2 = \varepsilon_3$ which results in no spring-in distortions because of $\varepsilon_2 - \varepsilon_3 = 0 \to \Delta \varphi_{iso} = 0$.

Analogously to the contradiction concerning the denotation of the spring-in effect, there is some contradiction about the denotation of the spring-in angle itself. Therefore, a short definition is following, which is used within this thesis. Considering a curved section with an arbitrarily selected section angle of 90°, as shown in Figure 1.6, two angles $\tilde{\varphi}_{enc}$ and $\tilde{\varphi}_{sec}$ can be identified for the initial configuration \tilde{K} . The angle $\tilde{\varphi}_{enc}$ corresponds to the enclosed angle between both flange directions, whereas $\tilde{\varphi}_{sec}$ corresponds to the section angle between both flange normal directions. For the perpendicular oriented flanges depicted in figure 1.6 both angles are equal in the initial configuration.

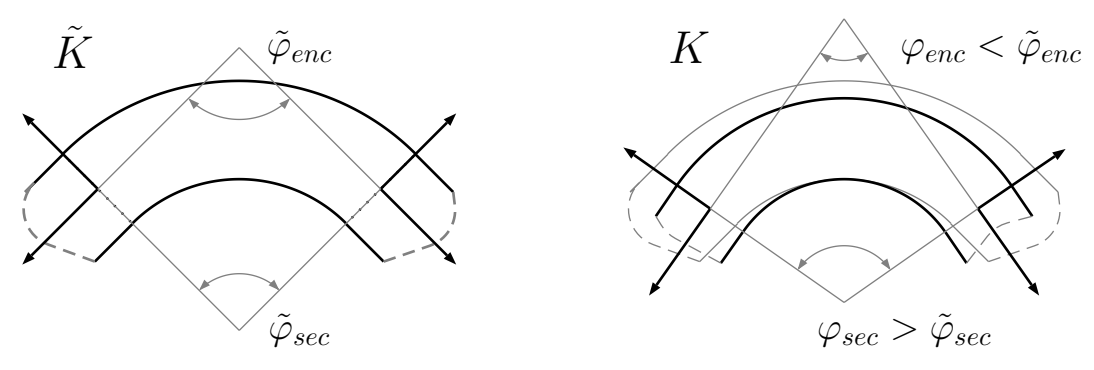


Fig. 1.6: Spring-in phenomenon: Definition of the enclosed φ_{enc} and the section-angle φ_{sec}

Generally, both angles allow the definition of the spring-in angle $\Delta \varphi$. The inspection of the deformed configuration K shows that the enclosed angle decreases $\varphi_{enc} < \tilde{\varphi}_{enc}$ while the section angle increases $\varphi_{sec} > \tilde{\varphi}_{sec}$. Hence, the spring-in angle $\Delta \varphi$ is defined as followed:

$$\Delta \varphi = \varphi_{sec} - \tilde{\varphi}_{sec} = \tilde{\varphi}_{enc} - \varphi_{enc} \quad . \tag{1.3}$$

Thus, a positive spring-in angle $\Delta \varphi$ corresponds to a decrease of the flange-to-flange angle about the same magnitude. For sake of clarity, the manifestation of the spring-in effect is illustrated for a C-profile geometry in Figure 1.7.

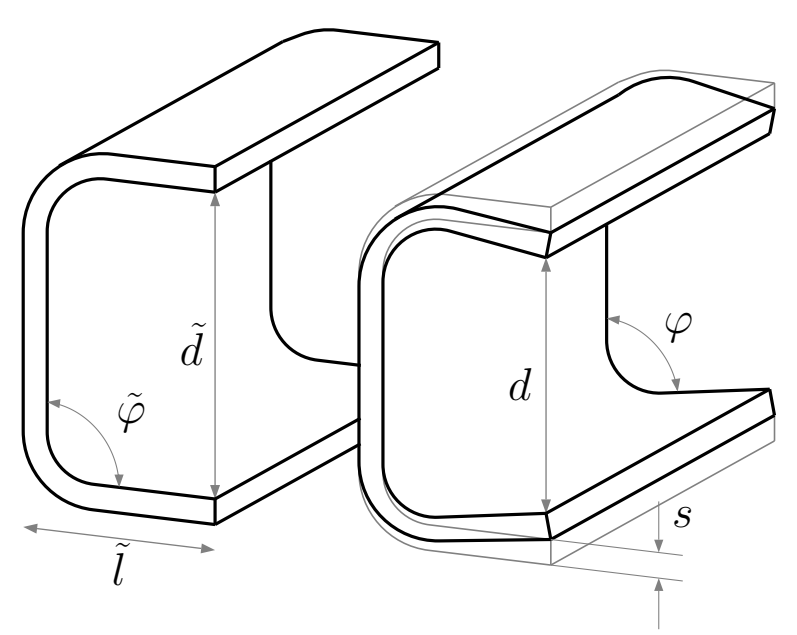


Fig. 1.7: Nominal (left) and manufactured shape (right) of a C-profile schematically. Connecting dimension d changes depending on the spring-in angle $\Delta \varphi$ and the profile's flange length \tilde{l}

An evaluation of the shape changes in Figure 1.7 by the following equations strikingly illustrates the relevance of spring-in, as connecting dimension d depends on the spring-in angle **and** the part dimensions.

$$s = \tilde{l} \sin \Delta \varphi$$
 and $d = \tilde{d} - 2\tilde{l} \cdot \sin \Delta \varphi$ with $\Delta \varphi = \tilde{\varphi} - \varphi$ (1.4)

Thus, spring-in deviations s scales linearly with the part dimensions, which underlines the importance of a spring-in compensation in particular for large composite structures.

Warpage Phenomenon

Warpage is related to extrinsic process parameters such as the tool or the bagging arrangement. Typically, a convex-up warpage is observed after demolding the parts. Two main drivers are conceivable sources which are V_f gradients and tool-part interaction. Both effects are related to the single-sided mold concept as outlined by Fernlund et al. [21] and Radford [5]. During processing a resin-rich laminate area can develop at the tool-side of the part while a resinpoor layer develops at the bag side likely promoted by the use of peel-plies. According to the CLT and considering that the ply's expansion and stiffness properties depend massively on the V_f , those gradients result in a inhomogeneous stress distribution in thickness direction which manifests in the part during the curing process. Tool-part interaction is mainly driven by the tool properties, whereas tool-surface roughness and thermal expansion properties are supposed to be the main drivers. Different CTEs of the tool and the applied laminate lead to a strain mismatch between the part and the tool, which is often referred to as a thermal incompatibility. Consequently, warpage depends directly on the curing temperature as it defines the magnitude of the strain mismatch. Thus, metallic tools made of aluminum or steel are more prone to induce warpage distortions when high-temperature process are uses as $\alpha_{Alu,steel} >> \alpha_{CFRP}$. Normal forces, induced by the applied vacuum or the autoclave pressure, enforce friction between the differently expanding materials while the tool-surface roughness affects the acting stress transfer as outlined by Stefaniak et al. [9, 22] and Ersoy et al. [23]. In contrast CFRP or invar tools are supposed to induce no warpage as $\alpha_{CFRP,invar} \approx \alpha_{CFRP}$. Figure 1.8 illustrates the warpage

effect for flat laminates fabricated with a high-temperature process on a tool with considerable thermal expansion.

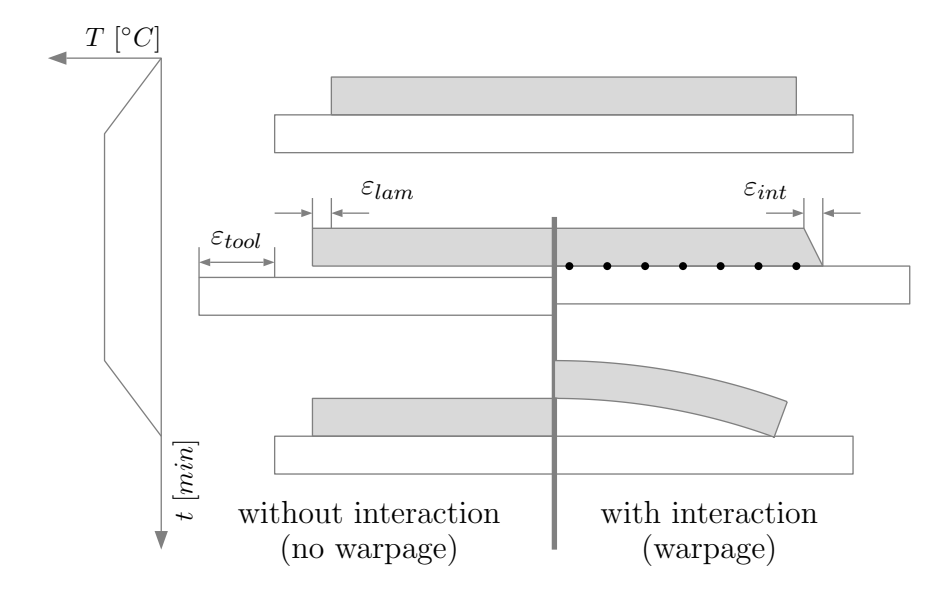


Fig. 1.8: Warpage mechanism for a high-temperature process using a tool with considerable thermal expansion

As the interaction only affects a small fraction of the laminate the magnitude of induced stresses is limited. Thus, the effect is only of particular relevance for thin laminates as those have a very small bending stiffness. As will be shown in this thesis warpage of flat laminates almost diminishes when thickness exceeds 1.5 mm.

Forced-Interaction

The forced-interaction phenomenon is very similar to warpage of flat laminates as it is mainly driven by the tool's expansion enforced by autoclave pressure. However, that effect is observed even for integral structures what increases its relevance. According to Fernlund et al. [10] forced-interaction is an indirect effect of the autoclave pressure or the vacuum as it compacts the composite plies against to tool surface. As pressure is applied throughout the entire manufacturing process it forces the laminate to follow the tool's expansion. Figure 1.9 shows that schematically.

Due to the acting normal forces the interaction between the tool-sided ply and the tool surface is enforced while outer plies are not directly affected. Assuming a certain viscosity, induced inplane stress relaxes in thickness direction until the gradient is frozen after the resin passes the gel point. After demolding the inhomogeneous stress state results in shape changes of the part. In academia forced-interaction is comparably less investigated. Studies on thin specimens are performed by Wisnom et al. [24], Potter [25]. L- and C-profiles are investigated by Fernlund et al. [8] whereas the latter ones show approximately 30% greater spring-in angles which is likely due to forced-interaction effects. As will be shown in the following, those findigs are in accordance with experimental results of this thesis. However, within another study Albert and Fernlund [8] contradict the aforementioned findings as fabricated L- and C-profiles show almost identical spring-in angles. A clear assessment on those contradicting results is not possible. Thus, the phenomenon is one issue within this thesis which is experimentally investigated in Section 5.1.

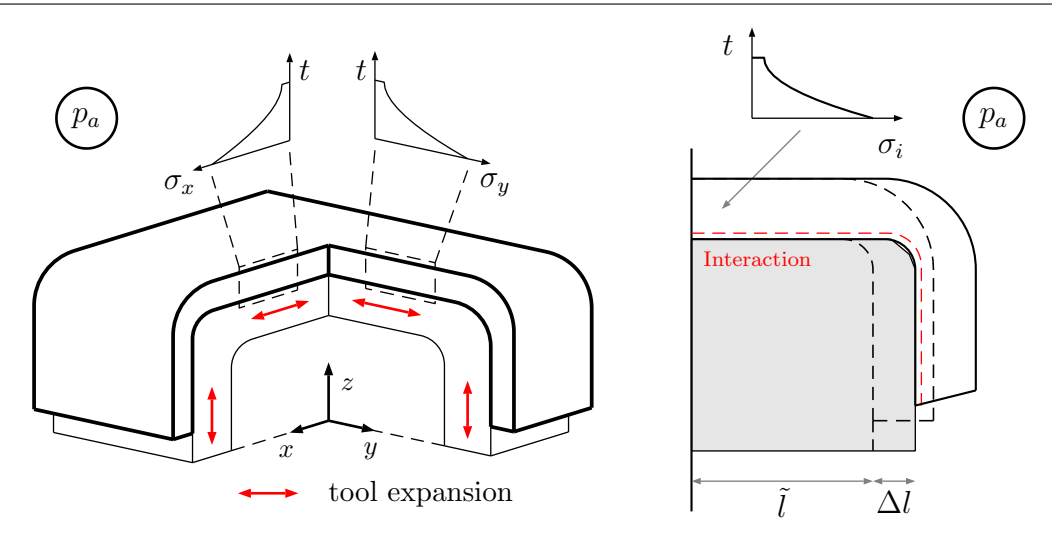


Fig. 1.9: Trough-thickness stress gradients induced by forced tool-part interaction. Tool expansion and autoclave pressure p_a enforce the effect.

1.4 Relevance and Consequences of Manufacturing Deformations

As documented by composite manufacturing companies, manufacturing-induced distortions of CFRP structures are of considerable relevance nowadays. The consequences of those undesired deformations are complex, as they affect wide areas of the part's production process starting from the tool-design up to the final assembly. In the end, manufacturing distortions induce significant costs within the production process.

Regarding the assembly process of complex parts, manufacturing deformations are a direct as well as an indirect cost driver. Considering an aircraft's fuselage or a wing's structure as sketched in Figure 1.10, the multitude of parts lead to a considerable tolerance chain.

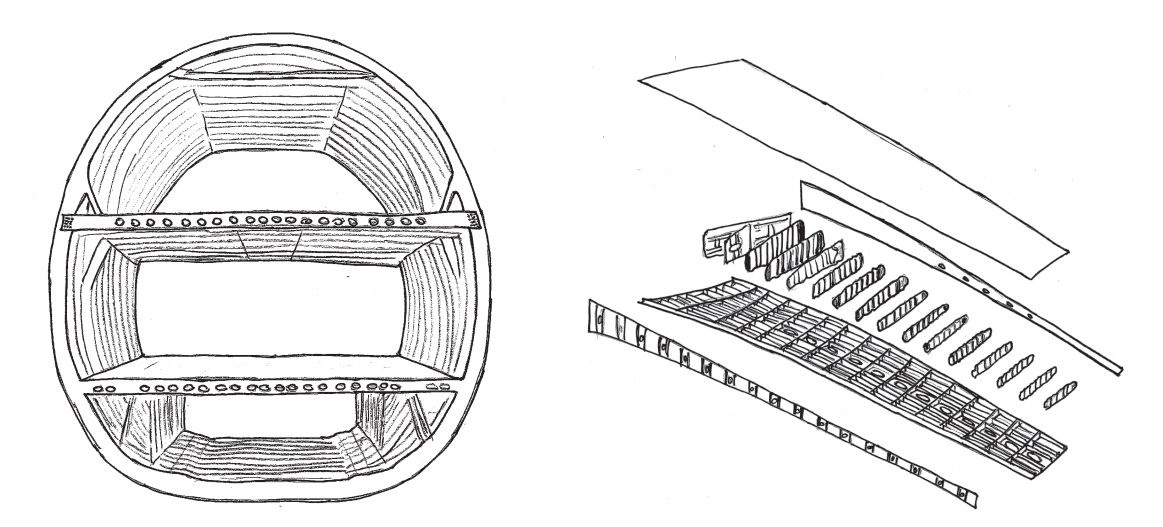


Fig. 1.10: Complex assemblies such as a fuselage and a wing's structure have a considerable tolerance chain

According to Fernlund et al. [8] process-induced deformations can be addressed by design-, assembly- or mold compensation. The first approach contradicts the philosophy of striving for highly-integral composite structures, while the second approach is insufficient from an economical point of view as soft and hard shiming commonly demand cost-intensive manual work and increase the structure's weight without increasing its performance. Figure 1.11 shows the

different shimming strategies using hard and moldable shims of variable size.

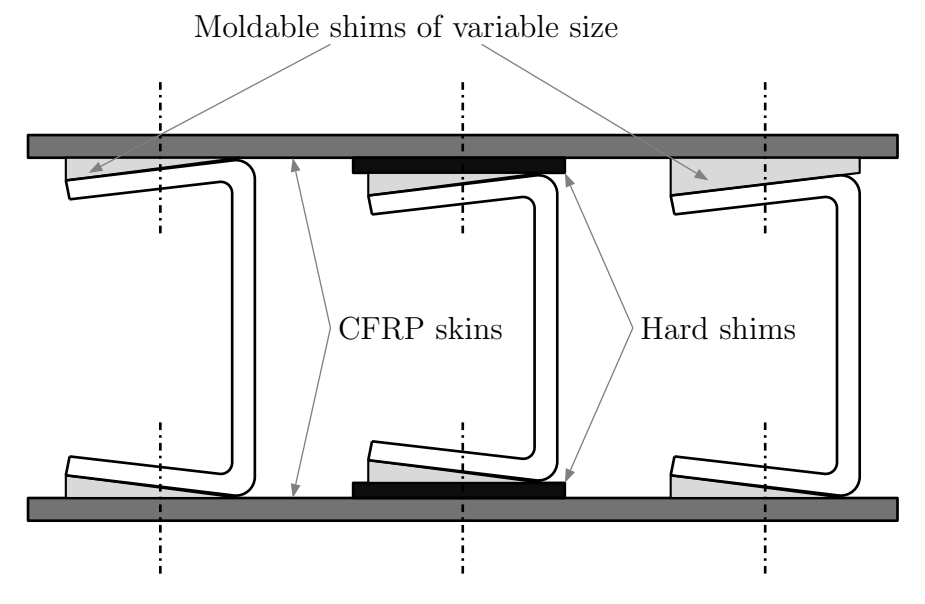


Fig. 1.11: Assembly strategies using hard and moldable shims according Fernlund et al. [10]

The third approach, mold compensation, promises good integrability into the part's development chain, as only the tool design is affected. Figure 1.12 shows the general idea of mold compensation. The use of compensated tools promises a fabrication without undesired distortions as it is common in the conventional manufacturing.

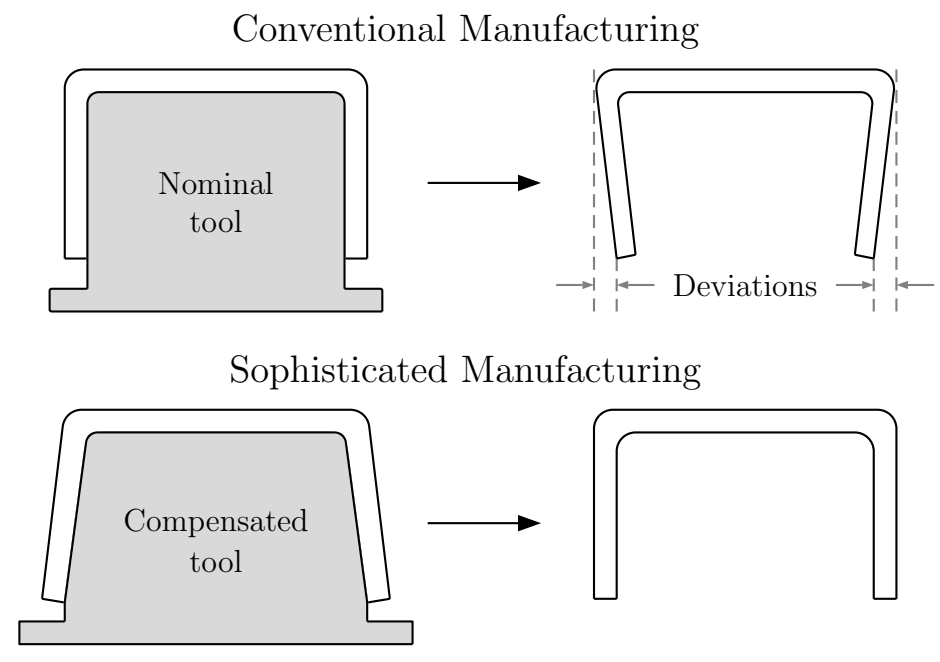


Fig. 1.12: Sophisticated manufacturing due to mold compensation

Due to the lack of straightforward prediction tools for the global part level, shiming is still state of the art within the assembly process of complex parts. Due to the high fraction of manual work, these efforts stand in contradiction to aspired highly automated production processes, which are necessary to achieve increased production rates. Furthermore, shiming directly induce additional costs as shims must be purchased from suppliers.

Estimation of Assembly-Induced Stresses in Spring-In Affected Components

Another consequence of process deformations is the part's increased internal stress level σ_i . Based on the assumption that not all deformations can be compared by shiming efforts a certain 're-deformation' is necessary to enable mounting of different components. Considering a certain amount of manufacturing-induced stresses $\sigma_{man.}$ due to process, material and stacking parameters, 're-deformation' of deformed parts adds assembly-related stresses $\sigma_{ass.}$ to the part's internal stress level. Figure 1.13 shows that schematically.

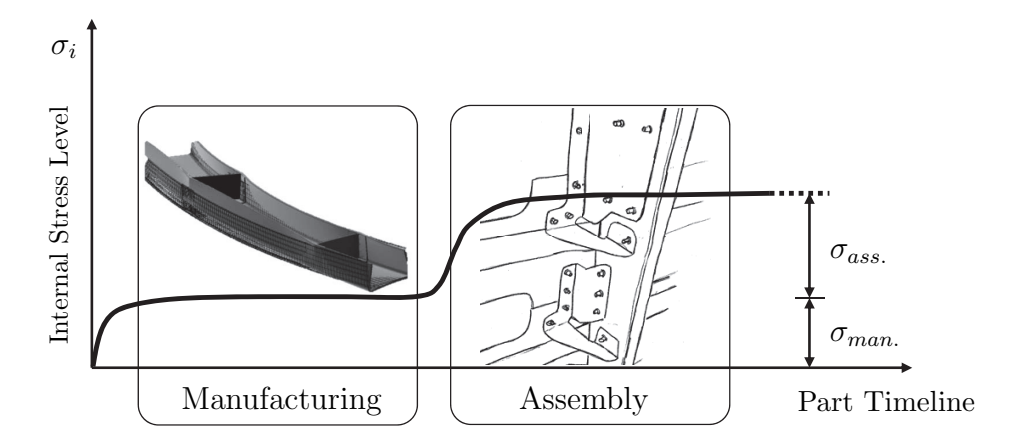


Fig. 1.13: Assembly loads increase part's internal stress level (C-spar taken from [26])

As outlined in Section 1.3 manufacturing deformations of stiffener structures such as spars and stringers are spring-in dominated. During the assembly-process stresses are induced due to manual re-deformation in order to fix mating parts.

A finite element model of a curved laminate section with a section angle of 90° is used. This cut-out is representative for often used profiles with Z-,C- or L-shape. The parameterized model is used to estimate the maximum assembly stresses. Within the model, the parameters are the inner Radius R_i , the mechanical material properties, layup, ply thickness and the section width W. The 're-deformation' is modeled by appropriate boundary conditions. Therein a realistic spring-in angle of $\Delta \varphi = 1.5^{\circ}$ is imposed while the cross-sections in circumferential directions are forced to remain plane. Figure 1.14 shows a schematic of the FE model and the 0° orientation.

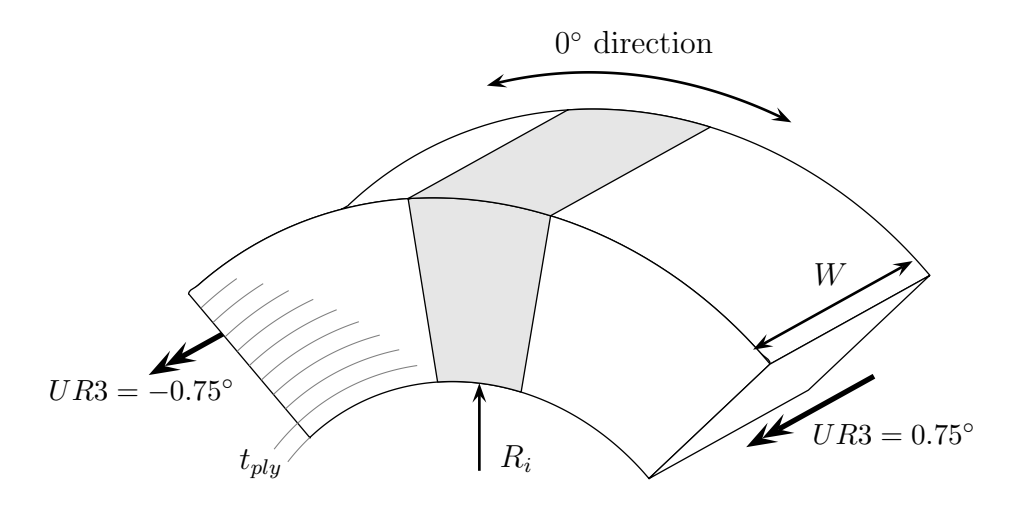


Fig. 1.14: Schematic picture of the used parameterized FE model

Within the following study each ply consists of 2250 elements with five elements used in thickness direction. The inner radius R_i is held constant to 4 mm, whereat the section width W is set to 6 mm. In order to blank out boundary edge effects stresses are evaluated for the light-gray area depicted in Figure 1.14. As the stress distribution within a composite is dependent from laminate stacking, the model is applied for a selection of layups. Therein, three stress components are evaluated ply wise. Components S_{11} , S_{22} and S_{33} denote stresses in fiber direction, in-plane transverse direction and in laminate thickness direction, respectively. For sake of clarity, an evaluation utilizing a failure criterion is not given here. The underlying material properties used within this study are outlined in Table 1.1.

Material	E_1 [GPa]	$E_{2,3}$ [GPa]	$\nu_{12,13}$ [-]	$\nu_{23} \ [-]$	$G_{12,13} [{\rm GPa}]$	G_{23} [GPa]	t_{ply} [mm]
T300/977-2	149.94	11.00	0.25	0.45	6.00	3.70	0.188

Tab. 1.1: UD properties of T300/977-2 prepreg material taken from Nguyen [27]

Figure 1.15 shows the evaluation of the stress components S_{11} , S_{22} and S_{33} for a $[0,90]_{2s}$ laminate exemplary. Within Table 1.2 the maximum and minimum of each stress component S_{ii} is

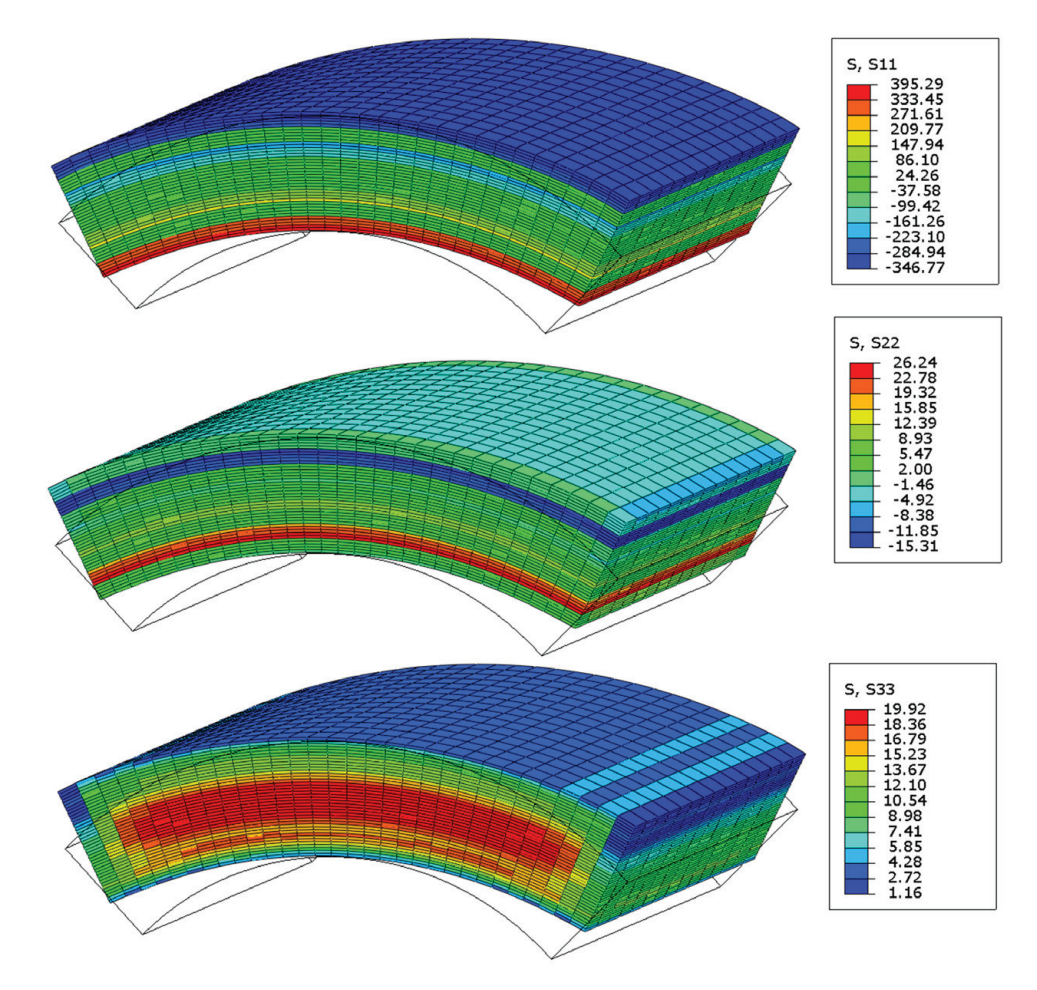


Fig. 1.15: Ply-wise stress evaluation for a $[0, 90]_{2s}$ curved laminate subjected by an angle increase of $\Delta \varphi = 1.5^{\circ}$

listed for multiple layup configurations. Depending on the laminate stacking obtained maximum and minimum stresses differ significantly. According to Jumahat [28] the tensile strength of the 977-2 resin is about 81 MPa. According to Torayca [29], tensile and compression strength of a T300/180°C Epoxy resin configurations with a $V_f=60\%$ are about 1760 MPa and 1570 MPa

respectively. Comparions of the derived ply stresses with those strength values are given in the brackets in Table 1.2. Values which exceeds 25 % of the material strength in the corresponding direction are marked red.

Layup	$S_{11,max}$	$S_{11,min}$	$S_{22,max}$	$S_{22,min}$	$S_{33,max}$	$S_{33,min}$
$[0]_{4s}$	397 (23 %)	-333 (21 %)	7 (9 %)	-12 (15 %)	29 (<mark>36 %</mark>)	1 (1%)
$[0]_{10s}$	780 (44 %)	-518 (33 %)	17~(~21~%~)	-22 (27 %)	98 (121 %)	1 (1%)
$[0, 90]_{2s}$	395 (22 %)	-347 (22 %)	26 (32 %)	-15 (19 %)	19 (23 %)	1 (1%)
$[0, 90, 45, -45]_s$	396 (23 %)	-371 (24 %)	26 (32 %)	-16 (20 %)	17 (21 %)	0 (0 %)
$[45, -45, 90, 0]_s$	170 (10 %)	-164 (10 %)	21 (26 %)	-18 (22 %)	9 (11 %)	-3 (4 %)
$[45, -45, 90, 0]_{2s}$	441 (25 %)	-431 (27 %)	47 (58 %)	-38 (47 %)	32 (40 %)	-10 (12 %)
$[45, -45]_{2s}$	156 (9 %)	-107 (7 %)	20 (25 %)	-18 (22 %)	8 (10 %)	-2 (2 %)
$[45, -45]_{3s}$	207 (12 %)	-108 (7 %)	24 (30 %)	-22 (27 %)	15 (19 %)	-2 (2 %)

Tab. 1.2: Stress evaluation for different laminates subjected to bending (Unit of S_{ii} [MPa])

According to the preceding table, significant stress levels are induced to the re-deformation mode. Regarding multi-angle quasi-orthotropic laminate configurations, assembly stresses in fiber direction are up to 25 % of the tensile strength. Regarding stress components in thickness direction S_{33} reveal significant amounts as well, which decrease the laminate's sustainability against unfolding which is mainly driven by a failure due to interlaminar normal stresses, which can, in some cases, lead to considerable material efforts. Although the preceding numerical investigation is a kind of worst case scenario it, clearly substantiates that manufacturing deformations induce considerable stresses within part.

Usability of Manufacturing-Induced Deformations

Beside the negative aspects of manufacturing distortions outlined above, there are a handful of selected applications where those distortions can be used. A CFRP wing upper cover concept striving for natural laminar flow in cruise conditions at it is regarded in Section 7.9. There, manufacturing deformations can counteract in-service deformations due to aerodynamic loads. Thus, the in-flight shape of the wing's upper cover can meet requirements for natural laminar flow.

1.5 Strategies to Counteract Process Distortions

As manufacturing deformations are inevitable for current composites fabricated with state of the art process cycles a strong demand for appropriate counter measures is the consequence. Process-induced distortions can be compensated on two different levels, whereat the first one uses design and tool related modifications while the second one uses material and process modifications.

Fernlund et al. [10] focused on the first level and outlined three different conceivable strategies. The first, very conservative approach, avoids curved CFRP sections within the part design. This, massively contradicts the philosophy of striving for integral composite structures. Furthermore, weight-saving potential is lost due to the need of metallic fittings. The second approach considers manufacturing distortions within the design and accounts for it with moldable or hard shims in the assembly. Whereas, this approach could work for small components fabricated in small quantities it is inefficient for large assemblies as the weight-specific in-service structural performance decreases due to the shims. Furthermore, additional costs are induced as shims have to be purchased from suppliers and the assembly demands additional manual work. The third approach, proposed by Fernlund, is geometrical tool compensation. This approach promises good integrability in the part's development chain, as only the tool-design is affected. However, it demands a high-quality prediction of the manufactured shape without any prototypes manufactured. Another approach proposed by Huang [30, 31] uses morphing composite tools. Therein,

anisotropic tool material and thus anisotropic thermal expansion is used in order to adjust the tool geometry according to the nominal part shape.

The second level of counteracting strategies uses modifications on material or process level. Radford [5] e.g. proposed an alternative compensation strategy which utilizes asymmetry effects, wherein locally asymmetric layups are used in curved laminate areas. Thus, asymmetry-induced distortions are adjusted by layup modifications in order to compensate process-induced deformations. In contrast, Spröwitz [32] e.g. investigated the effect of varying dwell times on the spring-in deformation of RTM L-profile specimens.

Figure 1.16 gives an outline of the different strategies.

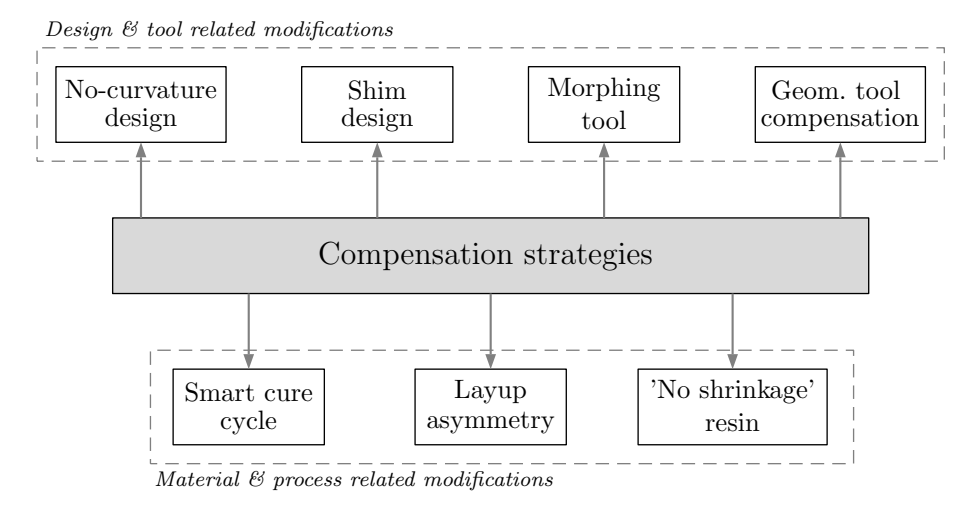


Fig. 1.16: Approaches counteracting manufacturing-induced deformations

Advantages and Shortcomings of the Different Compensation Strategies

Radford as well as Spröwitz are able to demonstrate within their studies that occurring deformations can be massively decreased with the proposed strategies. Even the use of nano particles in context of a 'no-shrinkage' resin is supposed to reduce manufacturing distortions. However, from an industrial point of view, these approaches are not feasible for multiple reasons. Radford's approach is able to reduce spring-in distortions but the local laminate modification leads to a considerable extension-bending coupling which affects the in-service performance under mechanical loads. Furthermore, the laminate modification within bent sections is hardly realizable in an automated manufacturing process as plies become to small. According to Spröwitz, extended dwell stages lead to decreased manufacturing distortions. However, from economical and environmental reasons, increased process times are not desirable. On the contrary, rapid cure cycles are aspired to shorten manufacturing time massively. In addition, it is not experimentally validated that extended process times are able to eliminate process-distortion entirely. From an industrial point of view the production rate in [kg/h] of those strategies decrease. In addition, they open new issues in context of certification. In contrast 'design & tool' modifying approaches do no affect the composite's material properties. From an industrial point of view this represents an advantage, as mechanical parameters which are used for the design must not be characterized for modified process conditions. Nevertheless, the first approach outlined by Fernlund is very conservative as one major benefit of composite structures, its design freedom is eliminated by the use of flat laminates mounted with metallic fittings. The second approach is less efficient due to increased assembly costs and the increased structural weight. Using morphing composite tooling as proposed by Huang does not solve the problem of manufacturing distortions. Instead it shifts it toward the tool design, where asymmetry effects as well an manufacturing effects need to be considered simultaneously. Moreover, this strategy is limited to composite tools which are not state of the art within industry due to their reduced durability compared to metallic tools. In contrast, geometrical mold compensation represents a promising approach. From an industrial point of view, excellent integrability into running process development chains is given. This is supported by the findings of Jain et al. [33], who outlined that manufacturing distortions are commonly limited to a narrow range between 1° to 2.5° for L-shaped composite profiles. Considering that tool compensation is already established in industry, this process should be extended by a prediction of manufacturing distortions on CAE level. According to the focus outlined above, this thesis pursued the aim to predict manufacturing distortions in order to derive appropriate mold-compensation measures. Moreover, the predicted manufactured shapes can be used within the structural analysis to assess the consequences of these distortions. Other compensation strategies described in the preceding remain disregarded in this thesis.

1.6 Review of the Literature

An excellent review of the literature in the field of residual stresses in composites and their consequences is composed by Parlevliet et al. [34],[35],[36]. Although those papers focus on thermoplastic resin systems, the effects are similar for the thermoset resins which are investigated in this thesis. Within the following literature review the scope is sharpened towards the phenomena of manufacturing deformations of carbon fiber/duromere composites. For those materials spring-in deformations are inevitable as outlined by Jain et al. [19]. The authors investigate UD and fabric prepreg materials as well as RTM injection technology. They outline that anisotropic thermal expansion and the resin's chemical shrinkage are the main drivers of the spring-in phenomenon. In accordance with experimental investigations of this thesis, the authors results show that spring-in is independent from tooling material. Furthermore, analytical investigations reveal that cross-ply laminates $[0, 90]_{2s}$ show a constant spring-in angle for radius > thickness configurations. While the derived analytical relations match the experimental findings for multiangle quiet well laminates with plies oriented in direction of curvature, significant deviations of the model are obtained for $[\phi, -\phi]_s$ laminates such as $[30, -30]_s$ or $[45, -45]_s$. Contrary to the theory, UD laminates with plies oriented in the profile's extrusion direction, reveal a radius dependent spring-in angle between $0.20^{\circ} < \Delta \varphi < 0.75^{\circ}$. That is in accordance with experimental findings of this thesis described in Section 4.3. Kollár [37] obtain similar results for that special layup. However, scattering for UD ply-based specimens is extraordinary high which suggests obscurities in the specimen manufacturing process. This is in accordance with results of this thesis as 90° specimens show process distortions and large scattering as will be shown in Section

Huang and Yang [38] investigate spring-in deformations with the aim to improve geometrical accuracy and shape fidelity of advanced composite tools (ACT). The authors investigate the effect of different tool angles and tool radii based on unidirectional laminates. They obtain an approximately linear increase of the spring-in angle with increasing enclosed angle of the part, which is expected when reflecting the findings of Radford [5]. Fiber volume fraction analysis reveals a slight gradient in, whereas the ply nearest to the mold show 10 % smaller V_f than the plies nearest to the bleeder. Due to the limitation to UD laminates, the relevance for common composite parts with multi-angle laminates is rather limited. In context of a tool-design issue the transferability to complex tooling geometries remains undiscussed.

The effects of processing condition on the spring-in deformations are investigated by Sarrazin et al. [16]. The authors regard different layups, different mold types and different types of vacuum bagging arrangements for different temperature cycles. As specimens are fabricated with vacuum-only conditions and with asymmetric layups only, a comparison to the experimental findings of this thesis are hardly possible, as especially asymmetry induced distortions commonly dominate shape variations due to bagging or V_f gradients. Furthermore, vacuum-only conditions often

result in laminates with poor compaction which results in voids and porosity.

Within an analytical study Nelson and Cairns [20] investigate spring-in deformations with a strain-based strategy. They account for the effects of thermal tool expansion, thermal anisotropy of the composite and effects due to chemical shrinkage. They obtain an expectable spring-in angle for a 90° L-profile of $0.63^{\circ} < \Delta \varphi < 1.93^{\circ}$ which is similar to the findings of Jain et al. [33, 19]. Based on the assumption that the resin's volumetric cure shrinkage ΔV is between 3.5 % and 5.0 % the authors quantified the spring-in fraction due to chemical shrinkage to 30 % $< \Delta \varphi_{Ch} < 60$ %. The main aim of the developed strategy is to support tool designers in their daily work in order to improve the preliminary design process. This is in good accordance with the experimental results of this thesis shown in Section 4.6.

Yoon et al. [39] investigate the contribution of thermal anisotropy and chemical shrinkage on process-induced deformations of curved CFRP laminates with $[\pm \theta]_{2s}$ layups. The authors propose a model based on CLT, whereas properties in laminate thickness direction are assumed to be equal to transverse properties of the single UD plies. Obtained numerical results show reasonable good accuracy, wherein the discrepancy to experimental results is between 20% and 55%. The thermal fraction of the obtained spring-in is reported to 42 % for the majority of laminates. Unfortuneately, the fiber volume fraction V_f of the investigated parameters remain unknown, which hinders an quantitative comparison to other experimental results. The results are in accordance with the findings of Section 4.6. Furthermore the magnitude is in the range of the results of Nelson and Cairns [20]. As experiments are conducted for $[\pm \theta]_{2s}$ layups only the transferability to multi-angle laminates containing 0° and 90° plies is limited.

Darrow and Smith [40],[18] investigate the effect of the resin's cure shrinkage, mold expansion and V_f gradients on warpage and spring-in deformations. The authors support the thesis that warpage is mainly induced by tool-part interaction and/or gradients in fiber volume fractions. Cognitions gained for warpage specimens are used within a FE study in order predict the springin deformation of L-profiles with a 13 mm radius. Although accuracy of the FE predictions is quite good, the obtained spring-in angles up to 5.5° are unique in its magnitude within the literature. Those results are contrary to the experiments of this thesis, which reveal a spring-in angle of approximately 1.4° for a similar configuration. As neither details about the manufacturing process nor about the bagging and tooling material are documented, an interpretation of the origins of these massive spring-in deformations is not possible. Nevertheless, the study supports the striving for a straightforward strategy, similar to the aim of this thesis, wherein experimental findings are used in combination with a constitutive simulational model. Metallographic analysis technique is used by Radford [41] in order to attribute spring-in deformations to a gradient in V_f as it is sometimes obtained for vacuum-bag processed composite parts. The work focuses on the differences in spring-in obtained for male-tool and female-tool fabrication. The average measured distortions of the investigated laminate $[0,90]_{2s}$ is $1.05^{\circ} \pm 0.10^{\circ}$ for concave (female) tooling and $1.50^{\circ} \pm 0.10^{\circ}$ for convex (male) tooling which is in the range of the experimental findings of this thesis presented in Section 4.3. Radford uses equivalent flat plate curvatures. which are proposed by Radford and Diefendorf [42] earlier for analysis purposes.

Garstka et al. [14] develop an experimental technique to measure through-thickness-strains during composite manufacturing. Using this methodology, effects of thermal expansion, laminate consolidation and cure shrinkage is captured simultaneously. The authors show that preconsolidation affects the total amount of through-thickness strains massively. Jig-, vacuum and no pre-consolidation configurations are investigated. The authors substantiate that UD laminates exhibit larger thickness changes compared to cross-ply laminates, which is likely due to fiber-washing tendencies of UD laminates. A similar experimental technique is developed in this thesis which promises a simplified parameter derivation for the semi-analytical approach presented in Section 4.5.

Jain et al. [33] investigate spring-in deformations of an aileron rib which are manufactured

with a compression molding technology. The authors conclude that spring-in deformations of parts with angled cross sections can be limited to a range of $1^{\circ} < \Delta \varphi < 2.5^{\circ}$. They point out that a reliable and effective prediction of the spring-in angle should support the tool-design process as it promises a massive reduction of prototype manufacturing.

Syanberg and Holmberg [43, 44] describe manufacturing deformations as an omnipresent issue for composite manufacturers. The authors investigate RTM fabricated glass fiber/epoxy laminates. Although glass fibers are isotropic and therefore not comparable to carbon fibers, the effect of different process-cycle paths can be transferred to CFRP laminates. The authors developed a state-dependent numerical model wherein the rate (change/time) dependency is replaced by a path dependency. Thus, computational effort is reduced. An experimental validation of the proposed model is given by Svanberg and Holmberg in [45]. The model turns out to be able to account for varying process conditions. However, the spring-in angle is overestimated but the qualitative agreement is quite good. Although computational efforts are reduced significantly, the amount of necessary parameters is still large as mechanical, thermal and chemical parameters for each state are demanded. Another linear model is developed by Bapanapalli and Smith [46]. The authors claim that an accurate spring-in prediction is possible without a complete resin characterization. They worked out, that up to 75 % of the spring-in deformations are induced by the resin's cure shrinkage which is approximately 15 % above the prediction of Nelson and Cairns [20] and Yoon et al. [39]. Furthermore, they claim, that effects due to mold stretching diminishes for parts with a thickness above 2.5 mm. Salomi [47] investigate spring-in deformations of thermoplastic C-channel profiles fabricated using female tooling. An optical laser reflection measurement technique is used in order to determine the thermo-elastic fraction of the spring-in angle. Results indicate that the spring-in behavior of thermoplastic-based composites is similar to the one of duromere composites. The authors extend Radford's [5] model accounting for the a change in expansion properties when passing the glass transition temperature T_q . Contrary to experimental findings of this thesis and the Radford-model, which substantiate no dependence of the spring-in angle from the part's radius, a significantly different spring-in angle is obtained by the authors for specimens with 16 mm and a 32 mm corner radius. However, deviations are traced back to inhomogeneous fiber distribution and corner wrinkling within the thermoplastic composite. As the material differs significantly from the one investigated in this thesis, obtained spring-in angles and corresponding thermo-elastic fractions are not comparable. Nonetheless, a similar measurement technique, using a full-field 3D measurement system, is used within this thesis for the determination of the thermo-elastic spring-in fraction of the investigated carbon fiber/ duromere prepreg systems.

Spröwitz et al. [48, 32] investigate spring-in deformations of RTM fabricated L-profiles made of a HTS Fiber/ RTM6 composition. The effects of different process cycles are investigated for multiple V_f contents. The authors develop a combined shell-solid element simulation strategy with the aim of reducing computational effort focusing on the simulation of large geometries. Therefore, curved cross section areas are modeled with solid elements while flat flange areas are modeled with shell elements. Rigid bar elements are utilized to achieve kinematic consistency between both element types. Equivalent CTEs are used within the simulations which consider volume change due to chemical shrinkage. The developed strategy is applied to a Z-spar geometry. However, neither the derived deformations are analyzed in detail nor they are validated against measurement results from fabricated parts. Thus, a quantitative evaluation of the acting phenomena and their magnitudes is not meaningful. Nevertheless, the proposed strategy represents a first step towards a straightforward procedure to simulate extended structures based on properties gained on simple laboratory-scale test specimens.

Ersoy et al. [23] characterize the development of the spring-in angle during processing by utilizing a cure quench technique. They show that spring-in angle before vitrification is larger than after reaching the vitrification point, which is used later by Wisnom et al. [24]. That is

due to the resin's larger CTEs in rubbery state in comparison to the glassy state. Consequently, they modify the Radford's [5] approach in order to account for the shift of CTEs when passing the glass transition temperature T_q .

Ding et al. [49] develop an analysis procedure for thin and thick angled composites utilizing solid finite elements. Simulation results show good agreement with analytical results obtained by Jain et al. [19]. The thermo-elastic fraction of the spring-in is obtained to be 37 % which is similar to the fractions obtained in Section 4.6 of this thesis and in the range of the findings of Yoon et al. [39] and Bapanapalli [46]. The authors proof the independence of the spring-in angle from mid-plane radius of the curved section for radii larger than 1 mm. Regarding eight-ply laminates with a thickness of 1.6 mm the authors show that different materials and different manufacturing procedures (dry-fiber and prepreg) lead to different spring-in angles while a radius independence remains. The authors point out that the proposed strategy is sufficient for most composite structures whenever R>>h is fulfilled. In accordance with Radford and Rennick [50], the authors show that the spring-in angle increases nearly linear with the enclosed angle of the section.

Nyman et al. [51] distinguishes shape distortions of a complex composite structure in local and global phenomena such as local spring-in, global spring-in, global twist and bending. The authors point out the increasing demand of compensation techniques due to the increasing complexity. Furthermore, they criticize current tool-compensation procedures as they are based on rule of thumb combined with production trials. The authors pursue two methods of different complexity in order to calculate manufacturing deformations. Within the so-called 'simplified' way the authors introduce coefficients of process expansion (CPE), which corresponds to strains due to chemical shrinkage. Based on a process trial the CPE is obtained to be 1.6 times the CTE which is about 61 % of the total expansion. That correlates with experimental findings of this thesis which are documented in Section 4.6. The significance of the presented simulations and the necessary efforts cannot be assessed entirely due to several open questions: Utilized subroutines are not documented in detail; parameters affecting the draping simulation remain unknown; boundary conditions seems to be over-constrained. The obtained deformation results are hard to interpret as the selection of the displayed variable U_1 is not meaningful for the assessment of manufacturing deformations.

Radford [42] uses equivalent flat plate curvatures as mentioned above to account for spring-in deformations. Furthermore, he proposes locally asymmetric layups as a suitable counter-measure to reduce spring-in deformations. The main drawback of this approach is the increase of thermal instability of the part within those areas due to layup asymmetry as those laminates show a coupled behavior between extension and bending effects which is commonly not desired for structural components.

Albert and Fernlund [8] perform comprehensive experimental investigations to examine the effect of design and process parameters on spring-in and warpage of composite layups with symmetric layups. The investigated design parameters are: part shape, lay-up, flange length, part thickness and part section angle, whereas the process parameters are tool material, tool surface and cure cycle. Albert and Fernlund use toughened T800H/3900-2 duromere prepreg material. The authors show that a combined FEP ply/ release agent configuration decreases spring-in significantly in comparison to a release-agent-only setup. Furthermore, the authors work out that flange warpage needs to be considered as it affects the measured spring-in angle. A clear distinction between the single effects is only possible to a limited extent, as the parameters part shape, flange length, tool material and tool surface are varied simultaneously. Consequently, only single configurations are compared, whereas each configurations is characterized by the part's shape, flange length, tool material and the tool surface and cure cycle.

As neither experiments of this thesis nor those of other researchers reveal massive flange warpage, the origin of that effect can only be suspected. The comparison of experimental results by the authors with analytically derived spring-in values utilizing the relation proposed by Radford [5] are not convincing as effects of volumetric cure shrinkage of the resin are only roughly estimated. Results by the authors contradict the experimental findings of this thesis presented in Section 4.6. However, an interesting conclusion of the authors is that the effect of the part's shape (C or L profile) is of lower importance.

Within a companion paper, Fernlund et al. [21] describe an experimental and numerical study accounting for spring-in affecting parameters. One major finding of the investigation, which will be substantiated within this thesis, is, that plies oriented in direction of curvature dominate the amount of spring-in massively. Furthermore, differences in spring-in angle up to 50 % are obtained for the two different prepreg systems 8552/AS4 and 3900-2/T800H. That is contrary to the findings of this thesis which shows almost identical spring-in angles for different prepreg systems as outlined in Section 4.3. A considerable flange warpage, as it is stated in Albert and Fernlund [8], is not verified in this study which is in accordance with the experimental investigations of this thesis. Wisnom et al. [52] derive an analytical relation accounting for spring-in deformations of curved thermoset matrix composites taking into account the low shear stiffness of the material during the rubbery state. Experimental results show a significant thickness dependence for the fabricated specimens which do not match measurement results obtained in this thesis. Potential sources of the deviations are the used composite tooling which has a comparably small thermal expansion in combination with the silicon rubber diaphragm which has a comparably large thermal expansion.

Fernlund [53] develops a simple analytical model which accounts for the spring-in behavior of curved sandwich laminates. The model is similar to the one for monolithic composite laminates proposed by Radford [5]. A comparison between the analytical model and a detailed finite element based model utilizing COMPRO shows excellent agreement, which underlines the relevance of the Radford model. However, an experimental validation based on a fabricated panel is lacking.

Zeng and Raghavan [54] utilize finite element analysis to assess the effect of tool-part interaction on an autoclave-processed composite fairing. Interaction between the tool and the part is modeled using contact elements whereat a degree of cure dependent frictional coefficients are implemented. Abaqus user-routines are used within the model. The effect of sandwich-areas on the part deformations remain ambiguous. The authors name two major effects which contribute to the total deflection: Shape changes of tool and part during processing and process-induced stress due to constrained deformation of the tool and the part.

Another approach based on Bayesian statistical considerations is proposed by Fernlund [55]. The approach uses prior knowledge, prototype data and model results. Fernlund develops a Bayesian methodology using a probability density function of the outcome which account for the reliability of the data sources. Considering scattering in geometrical accuracy, which is still an issue for composite manufacturers, the presented strategy represents a promising approach. Nevertheless, it still depends strongly on experience parameters which are hardly to determine.

While spring-in deformations are subject of multiple studies, the warpage phenomenon is not investigated to that extent. In the following, relevant literature is discussed. Comprehensive investigations, accounting for warpage due to tool-part interaction is performed by Twigg et al. [11],[56],[57]. Therein, shear interaction is measured directly with strain gauges applied to a thin aluminum mold. The experimental findings show that interaction occurs despite the use of liquid release agent and FRP release films, whereat the effect is smaller for the latter one. Within the experimental part [56], the authors point out that part aspect ratio has a greater influence on warpage deformations than the autoclave pressure. The authors obtain no significant effect of the tool surface condition, which represents a direct contradiction to the experimental findings presented in this thesis. The geometric properties of the specimens investigated in this thesis are equal to the one used by Twigg. A significant variation from batch to batch is

documented by the authors, which raise open questions about the reproduceability of the used manufacturing process. However, within the numerical part of the investigations by Twigg et al. [57] it is shown that an elastic shear layer modeling is not able to predict the lengthwise stress distribution due to tool-part interaction. As expected, specimens fabricated on invar tooling show smaller deformations as specimens fabricated on aluminum tooling ($w_{invar} < w_{steel} < w_{aluminum}$) which is likely due to the lower CTE of the invar material. Melo and Radford [58] distinguish between thermoelastic and non-thermoelastic effects which affect the final shape of flat symmetric laminates.

Within a developed analytical model they introduce originally unknown friction coefficients C_1 for the laminate-tool interface and C_2 for the ply-to-ply interfaces. Specimens fabricated on aluminum tooling $\alpha_{al} = 22.7$ ppm/K show approximately a fourfold higher deformation than parts fabricated on ceramic tooling $\alpha_{cer} = 5.82$ ppm/K. At a first glimpse that is analogous to the ratio of expansion coefficients. However, those results are affected by the surface properties, which are different for both tool materials. Therefore, the obtained results cannot be directly linked solely to the expansion properties. The presented experimental result does not allow the determination of one unique set for C_1 and C_2 . Thus, the relevance of the approach is questionable as a single set of coefficients would be physically meaningful.

Zhang et al. [59] investigate different types of modeling surface stress on rectangular beams analytically. The numerical model uses the Euler-Bernoulli beam theory. Comparison of the analytical results given by the authors allow a comparison to experimental results for the warpage specimens of this thesis. Similar investigations are conducted by Kopmaz and Gündogdu [60]. The authors compare linear and nonlinear theories of the curvature of the Euler-Bernoulli beam for large deformations. According to Potter et al. [61] many factors lead to geometrical variability of curved composite parts while part/tool interaction is one major effect. The authors obtain a significant variability for UD specimens fabricated with a no-bleeding technique, using FEP films at the part-breather and the part-tool interface. Humidity experiments approve the nonelastic character of the obtained warpage deformations. The reproduceability of the presented experimental result is rather good, as the influence of prepreg selection dominates the obtained warpage deformations significantly. Cross section inspections, which might allow a substantiated interpretation, are not given so that the V_f remain unknown. Jung et al. [62] try to counteract warpage deformations of hybrid composite booms with tool compensation measures. Therein, the boom's laminate asymmetry as well as effects due to chemical shrinkage overlay each other. Thus a clear assessment is not possible.

Ersoy et al. [63] experimentally investigate the friction process at ply-to-ply and ply-to-tool interfaces. They show that prepreg-prepreg interfaces show shear stresses in a range of 0.02 - 0.25 MPa whereas prepreg-tool interfaces show only 0.01-0.1 MPa. Both effects are rate and layup dependent. Supported by the experimental findings it is assumed that warpage deformations are induced by a shear strain gradient in thickness direction. According to the authors, a simple stretching of the ply adjacent to the tool is not possible as the transferable shear stress from the tool to the ply is smaller than it is necessary to overcome the ply-to-ply shear stress capability. Within Section B that assumption is experimentally validated based on C-profile tests.

Arafath et al. [64],[65] develop a 2D analytical closed form solution for the prediction of process-induced stresses and deformations of flat and simply curved structures. The model matches results gained by FE analysis and experimental results by Twigg et al. [11],[56],[57] quite well. A shear layer is utilized whereat layer thickness and layer properties are used to match experimental findings. In context of a tool design process, accounting for different prepreg materials, the model's applicability is rather limited as property fitting of the shear layer is demanded. Furthermore, the applicability is limited to extruded structures.

Within a case study Fernlund et al. [10] investigate the applicability of coupled 2D/3D simulation techniques using the COMPRO simulation tool. The main aim of this study is to evaluate

the exactness of the simplified strategy. Therein, a shoe-box-like structure is manufactured and the deformed shape is geometrically measured. Within the initial state after manufacturing the deformed shape of the structure is mainly dominated by spring-in deformations. However, the proposed measurement technique turns out to be likely inaccurate as will be discussed in detail in Section 5.1. Measurements reveal clearly that the flange spring-in varies along the length of the shoe-box due to the structure's shape. After sectioning constant spring-in angles are obtained for the sectioned ribs, which are similar to the ones derived with COMPRO 2D simulations. The author's show that the applied 2D/3D simulation technique is suitable for the prediction of manufacturing deformations of complex parts. However, the amount of necessary parameters is still significant, as heat transfer, pressure and part-tool interaction is considered within the 2D simulation. Nevertheless, experimental results reveal a transferability from specimen level to part level which is a fundamental bases of the approach developed in this thesis.

1.7 Essence and Cognitions of the Review

The preceding literature review reveals a wealth of experimental and numerical investigations which focus mainly on process-induced deformations. There are a lot of similarities obtained. However, the comparability between different experimental results is rather limited as process conditions and/or manufacturing strategies differ between the single studies. Nevertheless, important statements, limitations as well as fundamental experimental findings are summarized and set in context with the aims of this thesis.

Thus, it is widely acknowledged that the spring-in effect is mainly dominated by through-thickness anisotropy of common composite laminates. According to multiple authors such as Fernlund [55], Radford [5], Nelson and Cairns [20], Jain et al. [33], Wisnom et al. [24] and Svanberg et al. [45] the effect is mainly dominated by anisotropic thermal expansion as well as the resin's chemical shrinkage.

Supported by experimental findings of Jain et al. [33], Nelson and Cairns [20], Radford [41] and experimental findings of this thesis, occurring spring-in angles of FRP composite parts can be roughly limited to a range of $1.0^{\circ} < \Delta \varphi < 2.5^{\circ}$.

This cognition represents a 'positive' information as no severe non-linearities of the spring-in angle are to be expected. Due to the limitation to a narrow area of magnitude the spring-in effect shows a good-natured character.

In the context of appropriate countermeasures, the limited magnitude promotes the approach of a tool compensation strategy as proposed by Jung et al. [62] e.g.. Furthermore, as documented by multiple authors such as Radford and Rennick [50] e.g., the spring-in angle changes linearly with temperature. In addition, spring-in also depends linearly from the section angle as experimentally validated by Huang and Yang [38] and analytically predicted by Radford [5]. Another essential statement is given by Jain et al. [33], who experimentally validate the transferability of spring-in magnitudes from specimen to part scale. Consequently, it can be assumed that cognitions made on specimen level can be directly used for predictions on part level as it is the idea of the proposed approach of this thesis.

According to main drivers of the spring-in effect, multiple authors have investigated the corresponding fractions of the total spring-in angle. Hence, Kollár [37] and Yoon et al. [39] show that the thermal spring-in fraction is about 42 % for multiple laminates while Nelson and Cairns [20] limit the possible fraction to an area of 40 % to 70 % of the total spring-in angle. Although this is not valid for all laminate configurations, it gives a quite good estimation. Experiments conducted in this thesis substantiate the proposed area of Nelson and Cairns, whereat it shows a significant layup dependency within this range.

An interesting statement focusing on the handling of the spring-in phenomenon is formulated by multiple authors such as Jain et al. [33], Nelson and Cairns [20] and Svanberg and Holmberg

[43]. They criticize the absence of comprehensive models and appropriate design tools which can support the preliminary and the tool-design phase due to the consideration of spring-in issues. A first step towards a simplified simulation strategy is proposed by Spröwitz et al. [48],[32] who use combined shell-solid modeling accounting for spring-in of a Z-spar structure. Therein, solid elements are used for curved sections of the profile accounting for the through-thickness effects causing spring-in deformations.

The preceding literature review shows the multifaceted nature of composite manufacturing and the different simulation approaches. For sake of clarity, the investigated specimens and their manufacturing process is set in context to the generic term 'composite manufacturing'. Thus, the experimental results presented in this thesis are directly transferable for structures fabricated with similar materials. Analogous to the manufacturing part, the multitude of simulation approaches proposed in the literature are discussed from a tool-designer's point of view. This should give the reader a clear understanding of the differences, advantages and drawbacks of a numerical-based approach and the semi-analytical one proposed here. This is complemented by a short discussion of scattering in the geometrical fidelity of produced composite parts as this is a relevant issue today.

Classification of the Investigated Specimens

Composite manufacturing contains a variety of facets, whereas fiber materials, resin, process parameters and even process techniques can vary significantly. Thus, the experiments documented in this thesis are set in context to this topic. Experiments conducted for this thesis focus on autoclave-processed thermosetting/carbon fiber prepreg materials which are cured on single-sided metallic molds. Therein, different mold materials are used to account for the effect of differing coefficients of thermal expansion. Monolithic laminates are investigated composed of different state of the art prepreg materials available on the market.

Figure 1.17 gives an outline of different strategies in composite manufacturing and shows the combination regarded here.

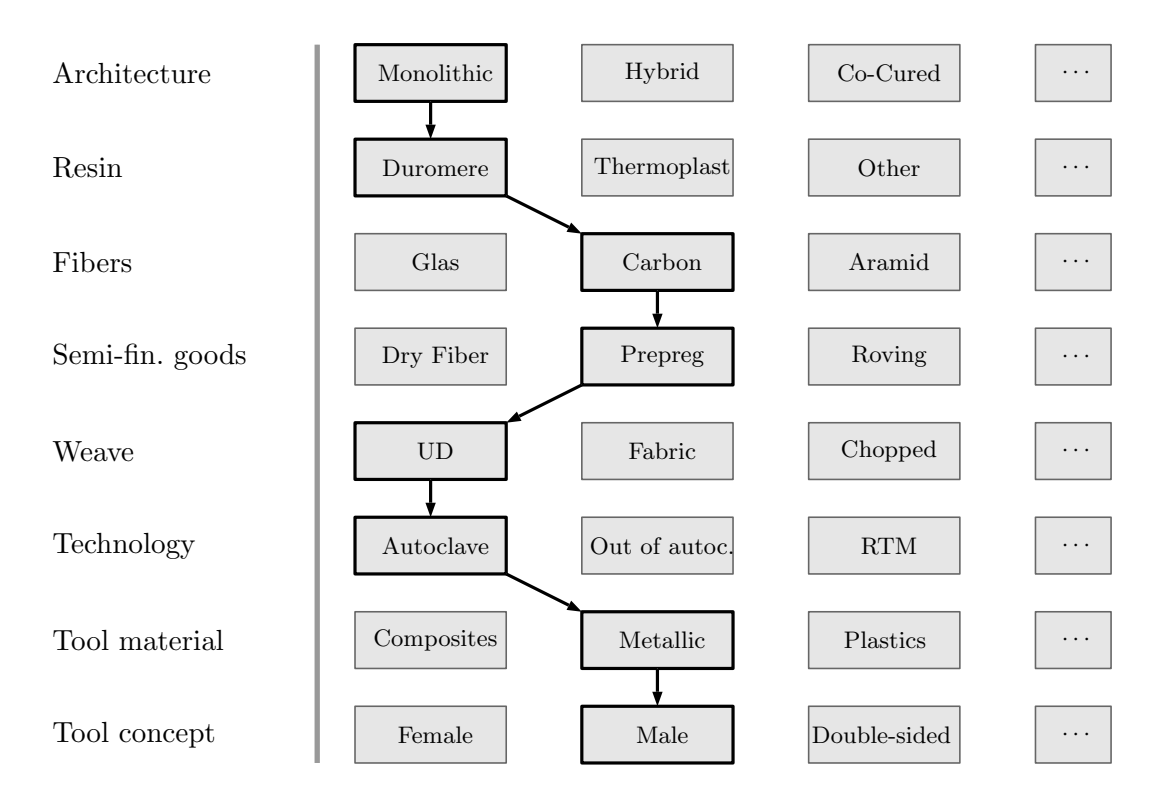


Fig. 1.17: Classification of the investigated specimens of this thesis in the context of composite manufacturing

That restriction is necessary in order to compare experimental results stated in the literature with the work presented here. Generally, it cannot be assumed that the characteristic mechanisms acting during the manufacturing process are the same for different types of processes.

Conceivable Simulational Strategies

Within the following section the aforementioned mold compensation is discussed whereas the focus is on different simulation strategies. As outlined in Section 1.5 compensation of the nominal tool geometry demands the knowledge of characteristic manufacturing deformations prior the first part is fabricated. Figure 1.18 shows a flow chart of a tool design process, as it is often used in the industrial environment. Tool design is performed based on the nominal part geometry which is commonly generated by the construction office supported by CAD systems. After the first part is fabricated geometrical measurements allow an assessment of manufacturing deformations and the deduction of appropriate counter measures. Currently, this process is supported by existing experience of the workers and is conducted based on rule of thumb. The dashed blocks in Figure 1.18 directly depends on the quality of the workers' experience. Thus, this block is related to massive cost saving potential providing that reliable compensation methods are available. Especially for large extended structures and the corresponding large tools, multiple rework loops induce immense costs and undesired delays. Furthermore, responsibility of the workers and the financial risk for the company are high. Moreover, the knowledge within one company is directly linked to particular workers and commonly not documented satisfyingly.

Within a more sophisticated process chain, the tool design is supported by an additional block which is called 'Deformation prediction'. Therein, the nominal part geometry of the construction office is updated and modified based on the knowledge of the expectable manufacturing deformation of the composite structure at hand. This is analogous to Figure 1.1 on the part level. Nonetheless, deviation measurement of the first fabricated part is still necessary in context of

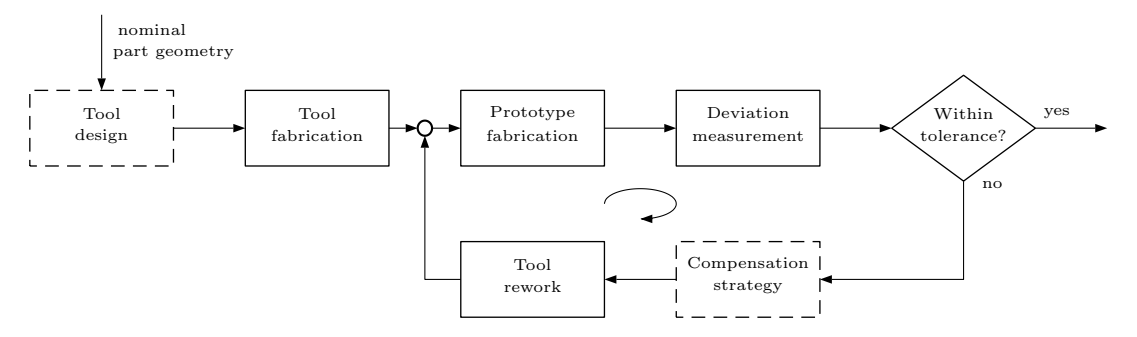


Fig. 1.18: State of the art tool compensation procedure. Dashed blocks are supported by fabrication experience

quality control issues and to validate the conducted compensation modifications.

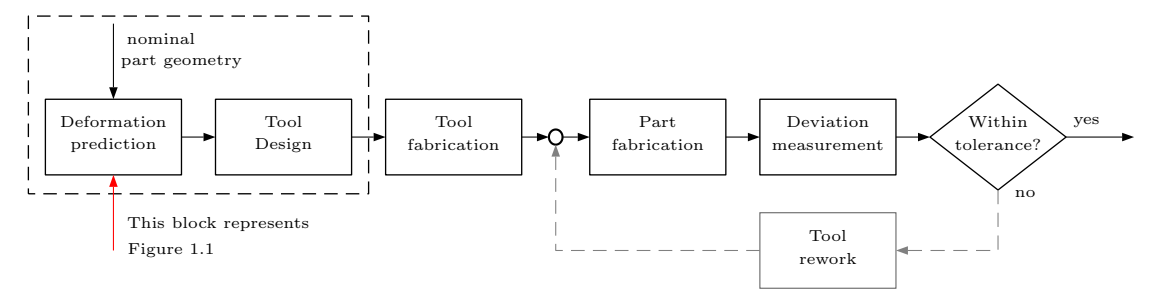


Fig. 1.19: Sophisticated compensation strategy in order to avoid (reduce significantly) process distortions

Generally, the aim is to achieve a first-time-right production, but however, especially for very complex structures it has to be proven that this can be achieved by simple straightforward compensation measures. Therefore, a block 'Tool rework' is illustrated in light-colors within Figure 1.19, which has to be understand as an optional process step.

State of the Art Process Simulation

The incorporation of a geometry modification step, wherein the nominal geometry is adapted according to predicted manufacturing deformations, represents a promising approach in order to improve geometrical fidelity of composite parts. Consequently, the main key for a sophisticated design process is to have a reliable prediction procedure. As outlined by Wille et al. [12] simulation-based and combined semi-numerical strategies can be pursued for the prediction of process-induced distortions. Within the last decades, detailed simulation-based models have been developed by a variety of researchers accounting for the composite manufacturing process. However, the strategies as well es their development do not focus on part deformations solely. Instead, they try to model the entire production process characterized by a multitude of different physical processes. Thus, degree of cure, residual stresses, chemical shrinkage due to ongoing chemical reaction, flow and compaction of the laminate, exothermic heat development as well as heat transfer are in the focus of the models proposed in the literature Svanberg [26], Johnston [6], Wijskamp [66] and Hubert [67]. Figure 1.20 illustrates the complex interactions which needs to be regarded for capturing the entire curing process of a composite structure. Therein, the parameters in each block of the flow chart denote a direct dependence to the given parameters where t, T, p and H denote time, temperature, autoclave pressure and process-history dependence, respectively.

The simulation of curing process of a composite structure inside an autoclave represents a

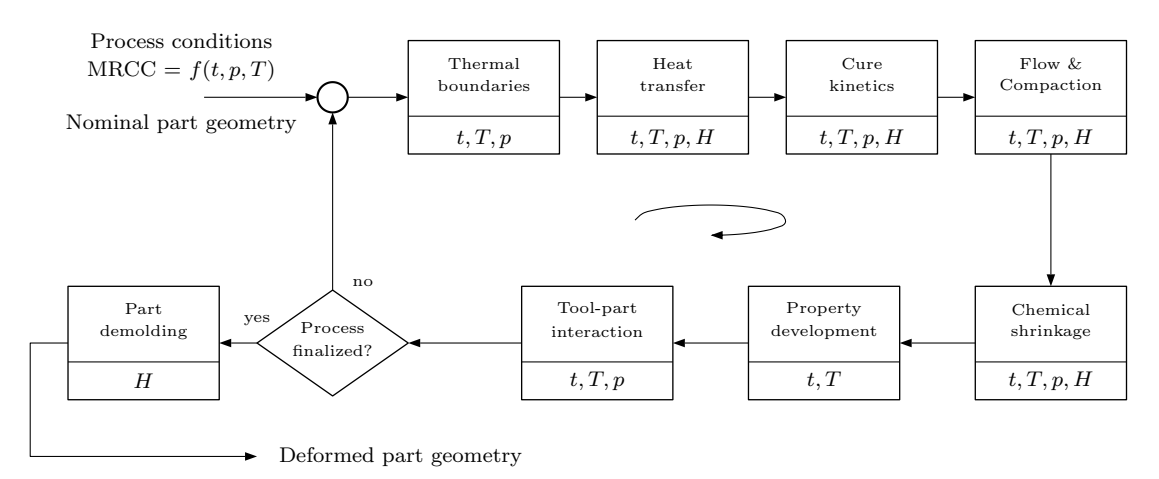


Fig. 1.20: Simulation of a composite manufacturing process. Parameter t, T, p and H denote time dependence, temperature dependence, pressure and process history dependence, respectively.

challenging modeling exercise. To clarify the number of necessary simulation parameters the single process steps are described step by step in the following whereas prepreg material is assumed. The MRCC is characterized by a certain temperature profile T = f(t) and a pressure profile $p_{abs} = f(t)$ as it is schematically illustrated for a two-dwell phase cycle in Figure 1.21. Magnitudes and lengths of the single process steps are material specific.

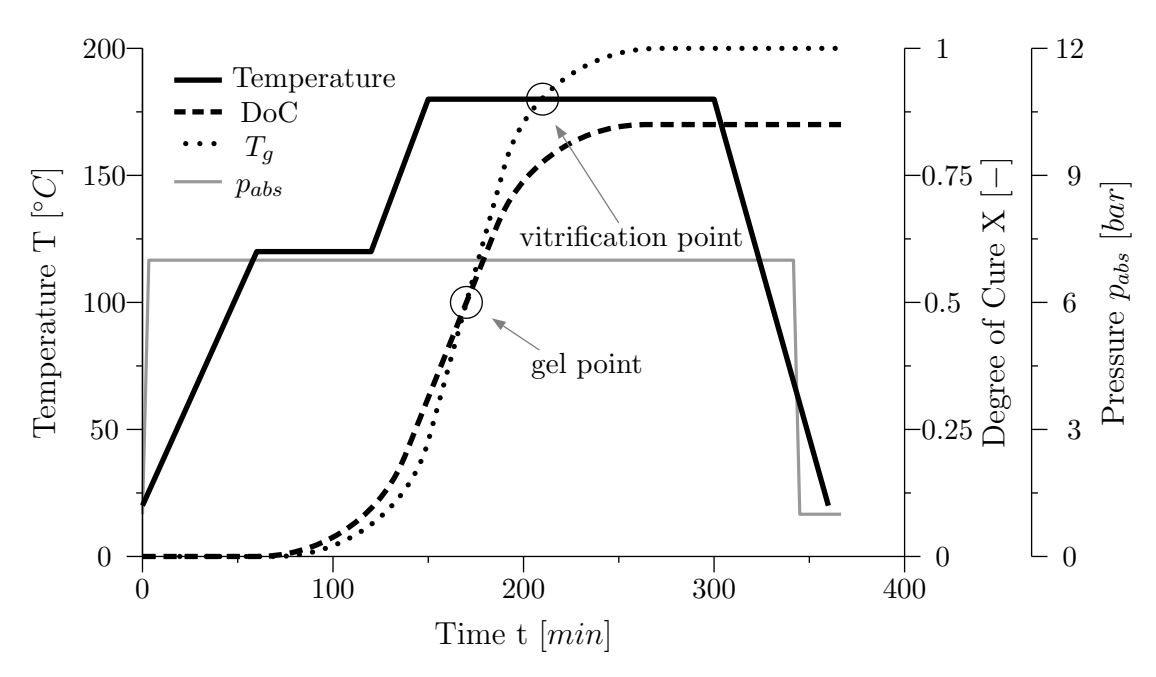


Fig. 1.21: Temperature, degree of cure and glass transition temperature during a common 180° cure cycle used for aircraft composites.

After the process has started, hot air (or nitrogen) is pumped into the autoclave to compact the laminate. Parallel, temperature is increased by a certain rate (e.g. $2^{\circ}C/min$). As the air cycles due to the autoclave fan, heat is transferred from the air to the tool and the laminate by convection. Correct heat-transfer coefficients are essential for the simulation as they affect the introduced heat into the part. The heat capacity of the constituents and the heat conduction

properties, which might be isotropic for the resin and transversal orthotropic for the fibers needs to be experimentally determined in order to model a correct heat conduction inside the part. Furthermore, this must be done multiply as a liquid resin e.g. shows other heat-transfer properties than a resin in the rubbery or glassy state as shown by Svanberg [26].

The introduced heat decreases the resin's viscosity which directly affects the interaction between the single plies as shown by Sun [68]

Exothermic heat is another issue, which is a critical problem especially for thick composite parts. It is induced due to the poor thermal conductivity of the resin, which leads to property degradation within the hot-spot area. The amount of degradation must be experimentally determined in order to model it correctly. The progress of the curing reaction and the corresponding viscosity of the resin depends directly on the current process step and its magnitude as well as the already passed process history. The degree of cure X, schematically depicted in Figure 1.21, affects the property development of the resin's Young's modulus directly. As common process simulations utilizes homogenized material properties on ply level, rules of mixture are implemented into the simulation strategy. A variety of different rules exist, for example Hill [69], Tsai [70], Hashin [71] and Chamis [72], where some are based on micro-mechanics and others are additionally modified by empiric or 'experimental' factors. However, applicability especially for the liquid and the rubbery state remain questionable. Moreover, the fiber volume fraction V_f , which is controlled by the amount of applied peel-plies in a prepreg process, needs to be regarded since it affects the rules of mixture significantly.

Another challenging issue is tool-part interaction induced by thermal mismatch between the composite and the metallic tool. Analogous to the mechanical properties, the interaction behavior depends directly on the resin properties. Interaction coefficients for the part-tool interface as a function of degree of cure are necessary to model those interactions correctly. Within the demolding block of the simulation strategy, mechanical boundary conditions which represent the constraint by the tool for example are disabled in the FE model. Thus, residual stresses due to chemical shrinkage, constrained thermal expansion and gradients in fiber volume fraction deform the part. The part demolding process block directly depends on the history of the manufacturing process which is denoted by the H in Figure 1.20. Consequently, the correct prediction of the deformed part geometry can only be expected when all the preceding process blocks work and interact correctly and when all simulation parameters are determined accurately.

Table 1.3 summarizes selected issues for the single blocks shown in Figure 1.18.

Block	Issues
Thermal boundaries	Temperature distribution due to autoclave air flow
	Heat transfer coefficients of the parts surface
	Heat transfer coefficients of the tool part interface
	Heat transfer coefficients of the tool-base interface
	Exothermic heat due to ongoing chemical reaction
Heat transfer	Isotropic heat conduction properties of the resin
	Anisotropic heat conduction properties of the fibers
	Heat transfer between tool and part
Cure kinetics	Developing degree of cure (isotropic)
	Resin viscosity
Flow & Compaction	Ply-to-ply interaction
	Resin viscosity and trapped air
Chemical shrinkage	Isotropic shrinkage of the resin due to chemical reaction
	Resulting Laminate shrinkage (anisotropic)
Property development	Change in Young's modulus of the laminate
	Thermal expansion property changes
Tool-part interaction	Interface conditions
	Tool expansion
Micromechanics	Rules of mixture

Tab. 1.3: Essential physical issues within a composite manufacturing process simulation

As outlined above, the single process steps interact nonstop and are dependent from the passed process history. That underlines the necessity of time dependent simulations when striving for all-embracing process simulational models. Simplifications are proposed by Svanberg [43] e.g., who divided the entire curing process into the three discrete phases: liquid, rubbery and glassy. Thus, time-dependency is substituted by a state-dependency. Nevertheless, even for this strategy the parameter efforts are high.

Reflecting the initial aim of this thesis, the part's manufacturing deformations are the subject of particular interest. Regarding numerical based approaches, described above, the part deformation is the final result of a multitude of different process steps demanding a variety of hard to determine simulation parameters. Due to the complexity of the necessary constitutive models failure-cause analysis is hardly possible. Considering the aim to predict part's manufacturing deformations within the early part design, the efforts for the experimental parameter determinations are disproportional.

Straightforward Prediction Approach

As a consequence of the aforementioned limitations of numerical-based approaches a novel seminumerical strategy is pursued in this thesis which focuses on part deformations only. The conceptual key idea of the approach is described in the following. The overall aim of the methodology is to provide a prediction of the manufactured shape with best possible accuracy based on as few parameters as possible.

One key-idea of the semi-numerical approach is to shift process dependencies of each process-block and thus the corresponding parameters towards one geometrical measurand of the fabricated specimen. That is based on the assumption that characteristic manufacturing deformations of one configuration are independent from part scale. Thus, the determined set of parameters is applicable for small as well as extended structures. Figure 1.2 shows a flowchart of the proposed approach. Although a multitude of different specimen shapes are conceivable, isosceles L-profiles are used within this thesis for multiple reasons: First, investigations by Kleineberg and Spröwitz

[13],[48] have proven the suitability; second, manufacturing is comparably simple; third, a right-angled L-profile represents an often to find cut-out of typical structural components such as stringers and spars; fourth, comparison to experimental results obtained by other researchers is comparably simple.

As shown in Figure 1.2 only the process-block 'Specimen manufacturing' depends on the process-related parameters. The subsequent steps are material unspecific. Thus, from this point the methodology is applicable for prepreg and infusion/injection technologies. The transfer of measured specimen deformations to one parameter set using an analytical formula considers the use of shell elements within the simulation part of the methodology. Thus, the prediction of process-distortions is close to the shell-element based design process of the majority of all parts, which corresponds to a massive reduction of modeling efforts compared to SoA process-simulation tools.

Scattering of Process Distortions

Scattering of the geometrical fidelity of composite structures is a known issue for manufacturers and in research. However, the magnitude and the relevance have only been studied rarely. The proposed approach allows a quick estimation of the expectable geometrical scattering on the part level based on the scattering obtained on specimen level. This represents an easy step in order to assess the magnitude of variability for the macro level part.

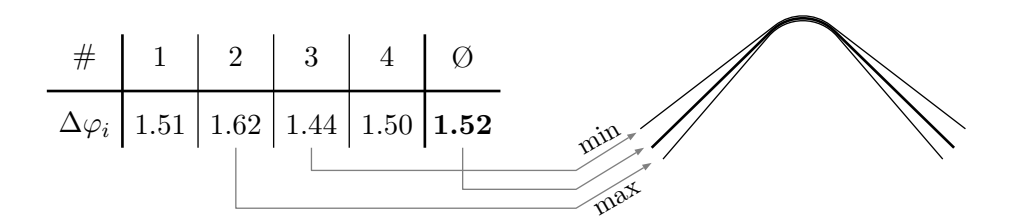


Fig. 1.22: Estimation of expectable scattering: Average, maximal and minimal configuration

Assuming that four specimens (#=1,...,4) are manufactured at once on an appropriate tooling, the obtained spring-in deformations commonly show a certain magnitude of scattering. As each measurand corresponds to an equivalent simulation parameter, the derivation of an expectable deformation envelope becomes simple within the FEA. Figure 1.22 shows that exemplary. Within Section 5.1 this is demonstrated for a integrally manufactured CFRP box structure. In contrast, current simulation-only strategies demand the derivation of the probability functions for each parameter in order to set-up a FE based probability-analysis. Related costs and numerical efforts are of another scale in contrast to the simple strategy described above.

2 Research Objectives and Thesis Outline

This thesis focuses on manufacturing-induced distortions which are an issue within composite manufacturing. The main aim of this work is to establish a straightforward methodology for the prediction of occurring manufacturing deformations on part level. A profound knowledge of the acting mechanisms and their magnitudes is gained by experimental means.

Therein, the two main contributors warpage and spring-in are within the scope. Both effects are characterized according to fundamental process and process-related parameters such as laminate layup, composite material, process cycle, tooling material, tool surface roughness, part thickness and part radii in order to substantiate and extend experimental results documented in the literature. Moreover, the forced-interaction effect are characterized for a CFRP box structure.

Simple analytical models are derived to validate and extrapolate experimental findings. Thus, thermal and chemical fractions of manufacturing deformations as well as their dependence from V_f is characterized.

The experimental program of this thesis is conducted with carbon fiber - duromere prepregs. Different state of the art materials are used in order to assess material dependency and transferability of the occurring effects. Tools made from steel, aluminum and invar are used in order to investigate the effect of the tool's CTE. All specimens and parts are fabricated using autoclave processes with a single-sided male mold concept. Obtained measured spring-in angles are statistically analyzed and evaluated.

In order to facilitate the consideration of manufacturing deformations within the part's and/or the tool's CAE supported design phase, a semi-numerical shell-element-based simulation methodology is developed. A massive parameter reduction and efficient shell-element modeling are the main innovations of that approach, as single laboratory scale L-profile specimens are the only input data necessary to predict the 'as-manufactured' shape of an entire part. Due to the use of test specimens for the parameter derivation, the prediction methodology itself is material independent and thus directly transferable to other manufacturing processes such as RTM or ooA methods.

One major aspect of this thesis is the validation of the idea of a mold-compensation to counteract process distortions. The developed methodology and its work flow is verified via a number of test-cases in specific frame-like, integral and highly integral structures. Predicted 'as-manufactured' shapes are compared with full-field optical measurements of manufactured structures in order to verify the area of application.

Structure of the Thesis

This thesis contains eight chapters. Each chapter is described briefly in the following for sake of the reader's convenience:

Chapter 1 introduces into the topic and the aim of this thesis and outlines the relevance of manufacturing deformations for current composite manufacturing. Acting phenomena and sources are characterized according to their origin and the two main effects spring-in and warpage are introduced. Different counteracting strategies are discussed focusing on the compensation of process-deformations. As an essence, the major findings of an extensive literature review are summarized and interpreted. The investigated manufacturing technique and the proposed approach are set in context of state of the art manufacturing processes and numerical based simulation procedures, respectively.

Chapter 2 summarizes the research objectives resulting from the literature review and gives an outline about the scientific approach pursued in this thesis. The fundamental questions which should be answered within this thesis are formulated.

Chapter 3 deals with the warpage phenomena. After a definition of the characteristics of the warpage phenomenon detailed experimental investigations are presented and discussed. Therein, three different state of the art prepreg systems are regarded, whereas flat as well as curved specimens with varying layups serve as the experimental basis. Results are interpreted and experimental findings are assessed according to their relevance for current and future composite structures within aerospace and automotive industry.

Chapter 4 summarizes the conducted spring-in investigations. After analytical pre-examinations of the effect, conducted experiments are described and results are presented. Therein, the search for the main contributors of the spring-in effect is in the focus. A new experimental methodology is presented which allows a spring-in estimation and/or the parameter calculation based on most simple specimens with dimensions of a few millimeters. Simple L-profiles as well as curved L-profiles serve as the experimental basis. Analytical and numerical findings are summarized and assessed with respect to their relevance. A statistical analysis of the measured spring-in angles is conducted.

Chapter 5 is dedicated to structures which are simultaneously affected by springin, warpage and in particular the forced-interaction effect. Within this section an integrally fabricated prepreg-made box structure is investigated in order to characterize the occurring process-induced manufacturing distortions. Experimental findings are compared to predictions within Section 7.7. In addition, a numerical study is presented which focuses on the gusset fillet and its effect on part waviness of T-joint connections.

Chapter 6 contains the derivation of the semi-analytical simulation model. The main aim of this model is to transfer measured specimen spring-in angles and/or warpage deflections to equivalent simulation parameters which are applicable with the shell-element based simulation methodology. The model is based on the classical laminate theory. It is derived in detail for flat, simple and double-curved laminates.

Chapter 7 is dedicated to the application and validation of the developed methodology, based on multiple test cases. In specific, a C-profile structure, an integrated box structure and an highly integrated upper wing cover are regarded. Model predictions are compared in detail with measured distortions of manufactured parts. Advantages as well as limitation of the developed strategy are discussed in detail. A prediction of expectable scattering of process-distortions based on variations obtained on L-profile concludes this chapter.

Chapter 8 contains a brief summarization of the major findings of experimental and numerical investigations of this thesis. Concluding remarks about the proposed simulation methodology, its applicability within a CAE supported design process, and its limitations are given. A technical outlook completes the present thesis.

3 Characterization of the Warpage Phenomenon

Within this chapter the warpage phenomenon is experimentally characterized in order to assess its relevance for structural components in context of a sophisticated design process. Therefore, experiments with three different state of the art prepreg materials, varying part aspect ratios and varying tool conditions are performed to identify material, geometrical and process dependencies of the phenomenon. Moreover, the transferability between warpage distortions of flat and simply curved shapes is experimentally investigated.

Under certain conditions flat laminates autoclaved with a single-sided mold concept show undesired warpage distortions after the manufacturing process. In particular, very thin composite structures are prone to show these process-deformations. In academia, two major sources are named as possible origins of warpage which are gradients in V_f and a mechanical interaction between the tool and the part during the ongoing curing process. Within this section effects due to V_f gradients are neglected as fabricated specimens do not show a measurable gradient of multiple percent as it is reported by Radford [5]. However, due to the uncertainty of the measurement technique, it is not concluded that there is no gradient due to the single-side mold concept. Instead, it is assumed, that the affectation is indifferent for the investigated UD laminates and is therefore assumed to be constant.

Tool-part interaction is enforced by the autoclave pressure which induces massive forces on the laminate. This is commonly desired for compaction purposes in order to reduced pore volume and therefore the pore content. However, this pressure forces the laminate against the tool surface which leads to a frictional contact when the tool expands during processing as the laminate's CTE is significantly smaller ($\alpha_{CFRP} \approx 2 \text{ ppm/K}$). Thus, the effect directly depends on the strain mismatch between the tool and the part. Parts fabricated on aluminum tools ($\alpha_{alu} \approx 24 \text{ ppm/K}$) are supposed to show larger warpage distortions than parts fabricated on steel ($\alpha_{steel} \approx 12 \text{ ppm/K}$) or invar ($\alpha_{invar} \approx 2 \text{ ppm/K}$) tools. As the effect is driven by a frictional contact the tool-surface properties are of particular relevance. While former research focused on different release agent techniques using liquid agents or FEP plies, the effect of the tool-surface roughness on occurring warpage distortions is of particular interest within this thesis. This section summarizes the essence of an comprehensive test program which is described in detail by Stefaniak et al. [9].

3.1 Preliminary Remarks on Warpage Experiments

Specimens geometries investigated in this thesis are similar to those used by Twigg [56] what ensures comparability between the experimental results. In short: specimen lengths L are in the range of 600 < L < 1200 mm and specimen thickness t is in the range of 0.5 < t < 1.75 mm. A solid steel tool is used for the fabrication of all specimens. Prior to the first manufacturing cycles preliminary tests are performed in order to verify the tool expansion properties and the tool surface roughness. Due to the production process of the tool raw material (rolling) a certain anisotropy in thermal expansion properties is conceivable. Expansion measurement by means of strain gauges reveals slight differences in thermal expansion between the longitudinal (grinding

direction in Figure 3.2) and the lateral direction. That difference is in the range of 0.5 % while the longitudinal CTE is determined to 12.015 ppm/K as shown in Table 3.1. As this difference is

Direction	$\varepsilon_{thermal} \ [\mu m/m]$	$\Delta T [K]$	$\overline{\text{CTE} [ppm/K]}$
longitudinal	75	61.74	12.015
lateral	71	61.74	11.949

Tab. 3.1: Measured tool expansion coefficients

small compared to the CTE difference between the tool and part CTE, it is neglected within this thesis. For sake of simplicity the thermal expansion of the tool is assumed to be constant although Gorenc [73] reports a slight nonlinear character for increasing temperatures. This simplifies the analytical relations derived in the following. However, those equations can be derived for a temperature dependent tool CTE analogously.

Another important issue is the peripheral grinding process of the tool surface which commonly leads to a certain anisotropy in roughness between the grinding direction and the lateral direction. Coarseness measurements at the initial state, utilizing a Mahr Perthometer M1, reveal significant differences. Tool surface roughness in grinding direction is obtained to be four times smaller than in the lateral direction. Table 3.1 gives an outline of the measured coarseness values for different configurations which are explained in the following. Therein, parameter R_a represents the arithmetic roughness index according to Hoischen [74].

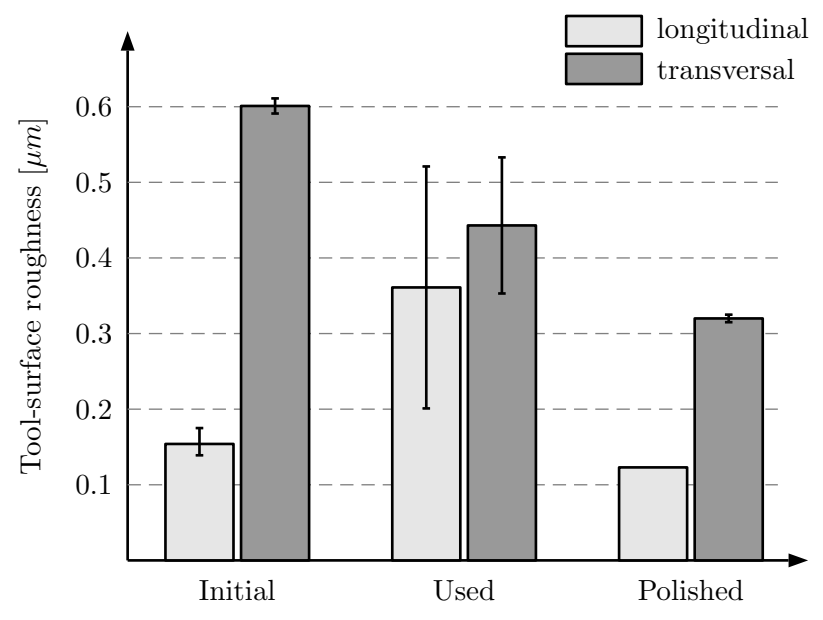


Fig. 3.1: Average tool-surface roughness R_a [μm] in the tool's longitudinal and lateral direction

On the one hand, this anisotropic coarseness is undesired as it demands additional attention within the specimen manufacturing process. On the other hand, it allows the detailed investigation of the coarseness dependence of the warpage effect.

Thus, different alignments of the specimens on the tool allows the characterization of this roughness effect. Figure 3.2 depicts differently aligned specimens of various lengths as well than the obtained convex warpage deformations schematically.

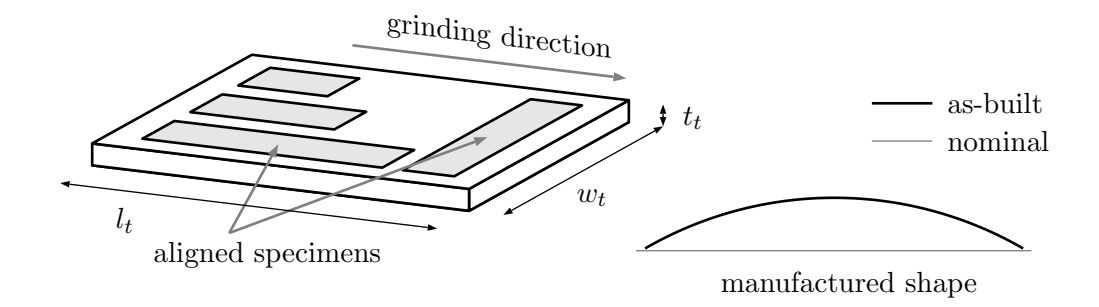


Fig. 3.2: Flat laminates of various lengths differently aligned on the steel tool where tool dimension are $l_t = 1300$ mm, $w_t = 1000$ mm and $t_t = 15$ mm

Warpage Deformation Measurement

Warpage deformations are characterized by a convex shape, whereas the center of the composite part moves away from the tool surface what is shown in Figure 3.2. The shape of the manufactured part depends on the magnitude of interaction effects. Generally, specimen distortions show neither a quadratic or circular nor a harmonic shape. Thus, two different approaches are conceivable to characterize the occurring warpage deflections. The first one examines the maximum deflection of the part while the second one uses multiple measurements along the part length. Within this thesis the maximum deflection approach is pursued as it represents a straightforward procedure and as it was also used by Twigg [56].

Due to the small thickness of the laminates the bending stiffness around the width-axis of the fabricated specimens is very small. Thus, gravity affects the part shape massively. Consequently, this effect needs to be blanked out within the evaluation of the warpage distortions. Figure 3.3 shows the chosen measurement arrangement as it is used in this thesis. Therein, specimen width-axis is aligned parallel to the gravity axis \vec{g} . A heavy fixture serves as an arrester for the specimen,

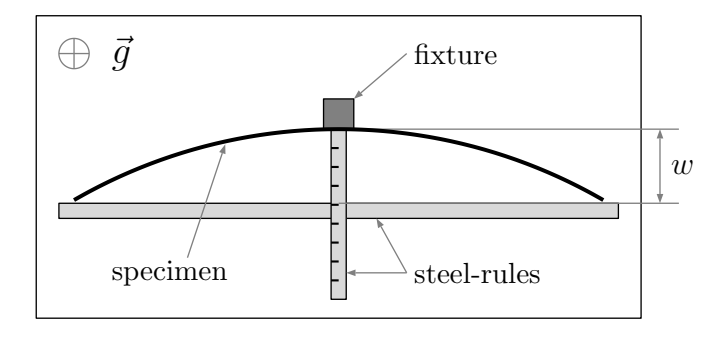


Fig. 3.3: Deflection measurement assembly for warpage specimens

while two steel rules are used to determine the maximum deflection w as illustrated in Figure 3.3. For very thin specimens with $t\approx 0.5$ mm an adhesive spray is used to fix the specimens on the flat table. In order to validate the reproducibility of that procedure, each specimen was positioned and measured three times on each longitudinal edge. The measurements revealed an accuracy of ± 0.1 mm for the measured warpage deflection.

Investigated State-of-the-Art Prepreg Materials

Warpage experiments presented in this section are performed with three state-of-the-art prepreg materials: HexPly®-8552/194/AS4, HexPly®-M21E/134/IMA and HexPly®-8552/134/IM7.

Table 3.2 gives the major physical and mechanical properties taken from available supplier data sheets. The assigned abbreviations are used within the following sections. The main differences

Prepreg	$V_f[\%]$	t [mm]	$Aw [g/m^2]$	$\rho \ [g/cm^3]$	$E_{11}[GPa]$	$G_{12}[GPa]$	Source
8552/IM7	59.2	0.184	194	1.58	160	4.6	[75]
8552/AS4	57.4	0.195	194	1.58	141	3.9	[75]
M21E/IMA	-	0.127	134	1.58	154	4.2	[76]
M21/T800	-	-	-	1.80	171	5.1	[77]

Tab. 3.2: Investigated prepreg materials and nominal suppliers data. Note, M21/T800 is used with Section 4.3

between the three investigated prepregs are obtained for the Young's modulus in fiber direction which is due to the different fiber characteristics. Differences in the area weight (Aw) and therefore the nominal cured ply thickness t are compensated due to appropriate layups in order to achieve comparable thicknesses. All three prepreg system are processed with 180° C cure cycles. This is important, as the tool expansion is temperature dependent. Consequently, it is assumed that the maximum tool expansion is equal for all three materials.

3.2 Effect of Tool Surface Coarseness on Warpage Deflections

Eight specimens are manufactured to characterize the effect of the tool-surface roughness on the warpage deflections. Specimens have a length of 900 mm and are composed of four or eight UD plies which corresponds to a thickness of 0.5 mm and 1.0 mm, respectively. Indifferent

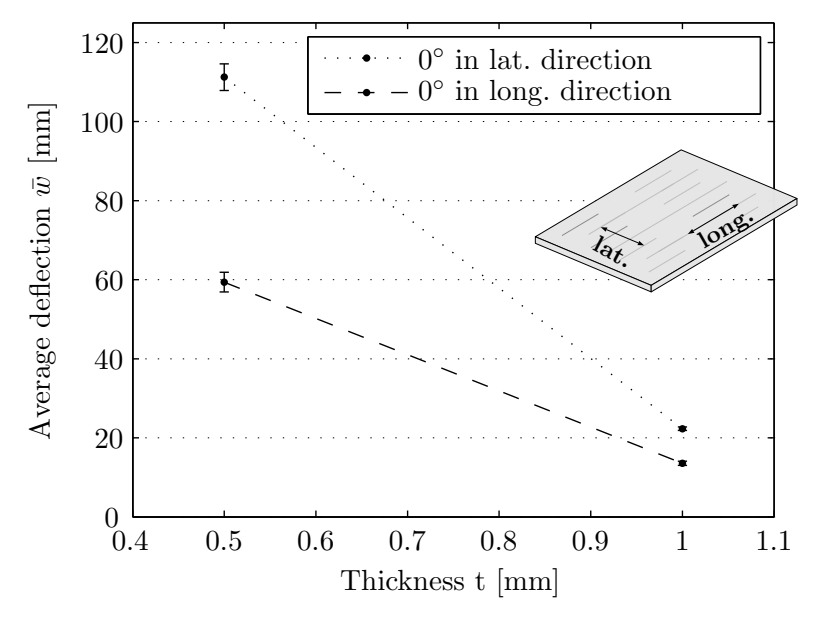


Fig. 3.4: Effect of surface coarseness on warpage deformations of M21E. \bar{w} denotes the average deflection of three nominal identical specimens.

from the prepreg material, specimens aligned in the tool's lateral direction show larger warpage deflections. However, M21E/IMA specimens show significantly larger warpage deflections than the other two specimens. Within the following, measurement results of the M21E/IMA specimens are evaluated. According to Figure 3.4 warpage deflection of the lateral aligned specimens is almost as twice as high as the deflection of longitudinally aligned ones. Regarding the 1 mm thick specimens, lateral aligned ones show a 60 % larger warpage deflection as the longitudinal aligned ones. An overall interpretation of the measurement results reveals a massive thickness

dependence, as e.g. the warpage deflection of the lateral aligned specimens decreased about 77 % while the thickness doubles. As only two thicknesses of one layup are manufactured, results are connected linearly in Figure 3.4. Therein \bar{w} denotes the average deflection of three nominal identical specimens. As will be shown in the following this turns out to be incorrect, as warpage distortions does not scale linearly with the part thickness. Further examinations are given in Stefaniak et al. [9].

The experimental findings described above substantiate the assumption that tool-surface coarseness affects warpage deformation significantly. The sources for the different magnitudes between the single prepreg materials remain unknown up to this point. Thus, all fabricated specimens are fabricated aligned parallel to the longitudinal tool direction. That is due to the aim to fabricate 1200 mm long specimens, since the tool width in lateral direction is only approximately 1000 mm. For each prepreg material nine different configurations are fabricated, whereas three lengths of 600, 900 and 1200 mm are combined with three thicknesses of approximately 0.5, 1.0 and 1.5 mm. Thus, the warpage deflections are characterized according to the geometrical parameters part length and part thickness. Alternatively to length-based description, a curvature-based analysis is possible as presented by Rohwer et al. [78].

Effect of a Double-Sided Tooling Concept

The aforementioned experimental investigations substantiate the assumption that manufacturing deformations are mainly dominated by the tool thermal expansion and the tool surface properties. Consequently, a double sided tooling would lead to a double-sided introduction of interaction effects into the laminate which would not lead to a warpage distortion after manufacturing. In order to validate that assumption, two specimens are manufactured according to the arrangement depicted in Figure 3.5. Therein tool#2 has the same thickness, identical surface properties and is made of the same material as the already described flat base tool.

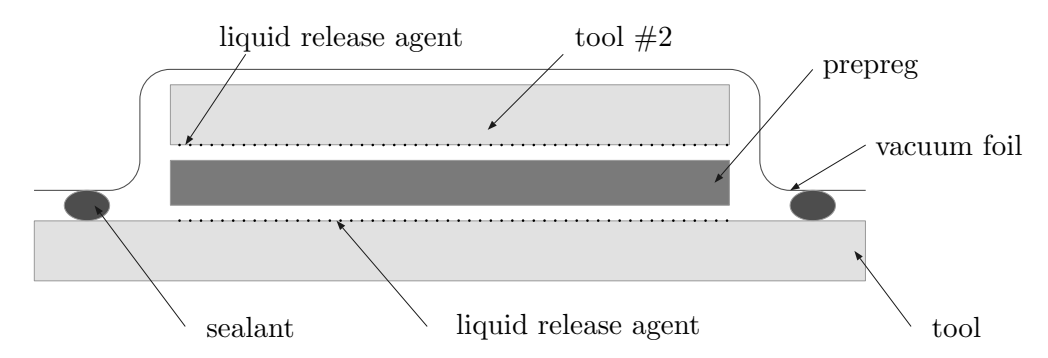


Fig. 3.5: Vacuum bagging arrangement with a double-sided tooling concept

The fabricated test specimen revealed no measurable deflection after manufacturing, what substantiates the general model assumption illustrated in Figure 1.8.

3.3 Warpage Deflections of Flat Unidirectional Specimens

Specimens Fabricated from 8552/AS4 Prepreg

The maximum deflection obtained for 8552/AS4 unidirectional specimens is about 17.5 mm. Generally, warpage deflection increases with increasing part length and decreases with increasing part thickness. Neither a linear nor a distinct nonlinear relation can be derived from the experimental findings. Specimens with a thickness larger than 1 mm show comparatively

small scattering, while 0.5 mm thick specimens scatter significantly as indicated by the standard deviation illustrated in Figure 3.6.

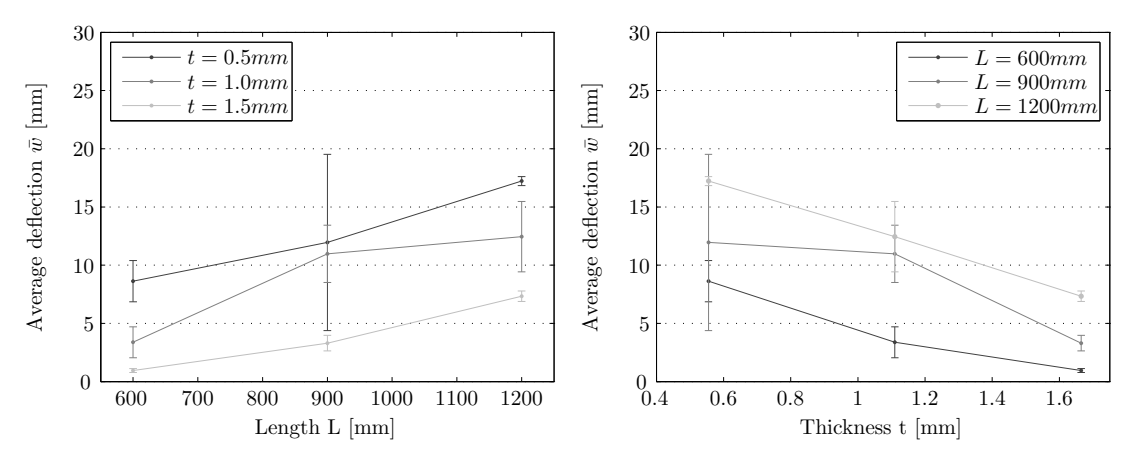


Fig. 3.6: Warpage deformations of 8552/AS4 specimens as a function of part-thickness (left) and as a function of part-length (right)

For illustration purposes the average deflections \bar{w} of the different thickness-length combinations are illustrated in Figure 3.7 with bilinear surfaces as proposed by Gao. [79].

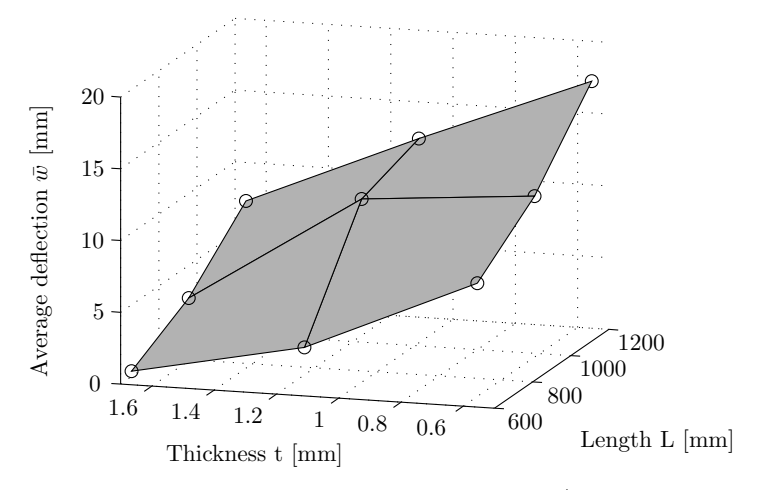


Fig. 3.7: Illustration of average warpage deflections \bar{w} of 8552/AS4 specimens using bilinear surfaces

Specimens Fabricated from M21E/IMA Prepreg

Specimens made from M21E/IMA show significantly higher warpage deflections compared to the 8552/AS4 specimens. The maximum average deflection is obtained to 76 mm for the 1200 mm long specimens with a thickness of 0.5 mm. This is four times the maximum deflection of the 8552/AS4 specimens. Less scattering is obtained compared to the 8552/AS4 specimens. Nevertheless, the major characteristics are similar to the 8552 specimens as thin, long parts show the largest warpage deformations.

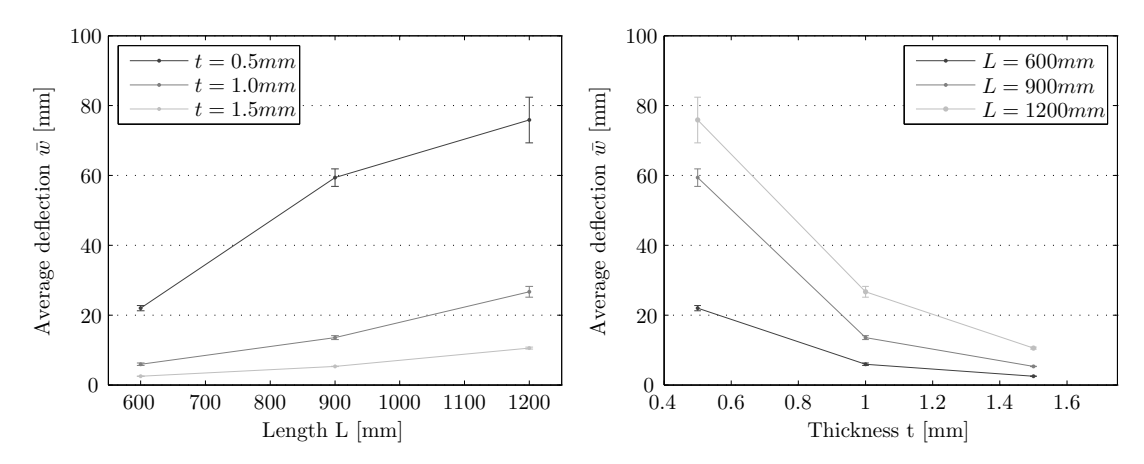


Fig. 3.8: Warpage deformations of M21E/IMA specimens as a function of part-thickness (left) and as a function of part-length (right)

Measurement results of the 0.5 mm thick specimens are conspicuous, as the qualitative deflection development is contrary to specimens with other thicknesses. A possible explanation of that phenomenon is proposed by Twigg [56] who obtain similar striking measurement results. He introduces a critical part length L_c , whereat he assumed that for parts longer than L_c sticking conditions between the expanding tool and the composite part are present. Consequently, no shear stress is introduced in the area $L_c < x < L$. Hence, L_c represents a kind of upper bound of the obtained deformations. An experimental validation by fabrication of a longer part was not possible due to geometrical limitation of the tool at hand. Figure 3.9 shows a bilinear surface interpolation of the obtained average warpage deformations \bar{w} .

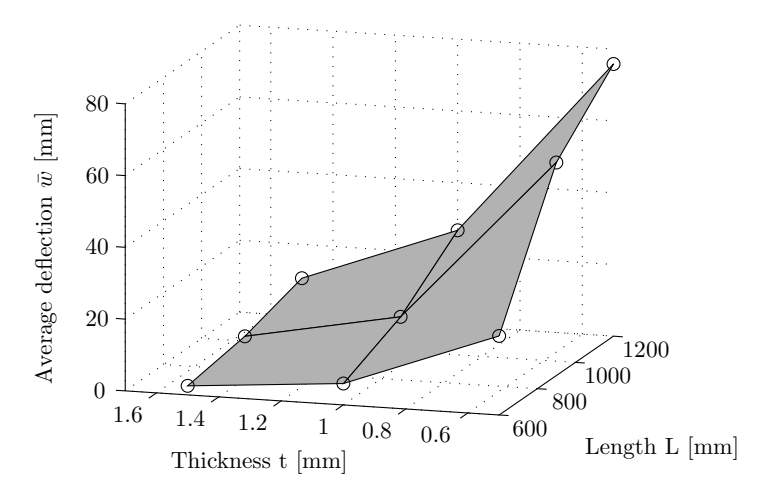


Fig. 3.9: Bilinear illustration of average warpage deflections \bar{w} of M21E/IMA specimens

Specimens Fabricated from 8552/IM7 Prepreg

At the first glance, 8552/IM7 specimens show very similar characteristics as the M21E/IMA specimens while the maximum part deflection is in between the deflection of the aforementioned materials. However, it should be noted that tool surface conditions have changed prior to fabrication. While M21E/IMA and 8552/AS4 specimens are manufactured contemporary after the tool delivery and therefore the initial coarseness measurement, the 8552/IM7 specimens are fabricated at a clearly later point of time. Within the meantime a multitude of parts are manufactured on the tooling. A repeated coarseness measurement reveals significant changes in tool roughness anisotropy. While in the initial state the lateral R_a was four times the longitudinal R_a in grin-

ding direction, repeated measurement reveals a considerable approximation of both coarseness values, what is depicted in Figure 3.1 with the shortcut 'used'. That adulterates a quantitative

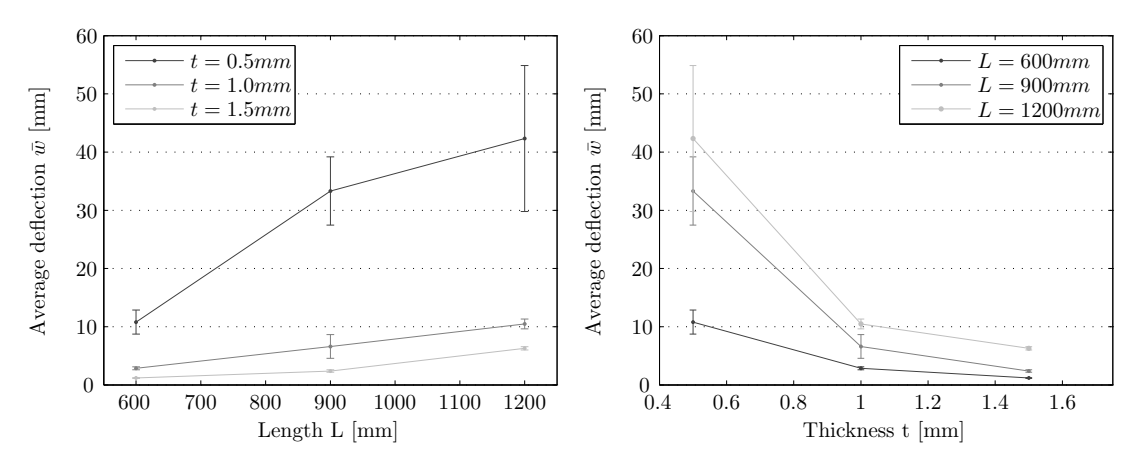


Fig. 3.10: Warpage deformations of 8552/IM7 specimens as a function of part-thickness (left) and as a function of part-length (right)

comparison significantly, as the coarseness affects the occurring warpage deformations as substantiated in Section 3.2. Thus, this must be kept in mind when comparing the experimental results. Nevertheless, the approximation of the longitudinal and the lateral coarseness represents an interesting experimental result, which is probably induced due to resin residues and a certain layer of release agent which built-up with the number of manufactured parts. Those residues fill coarseness cavities step-by-step. This suggests that a kind of equilibrium state of the surface roughness is conceivable after a certain amount of fabricated parts. To assess this interesting effect more thoroughly it needs further experimental investigation. As it is out of the major scope of this thesis it is not further investigated here. However, an additional set of experiments in specimen-scale should be performed to substantiate and quantify the effect. Analogously to the preceding material, Figure 3.11 shows the average warpage deflection \bar{w} obtained for the 8552/IM7 specimens.

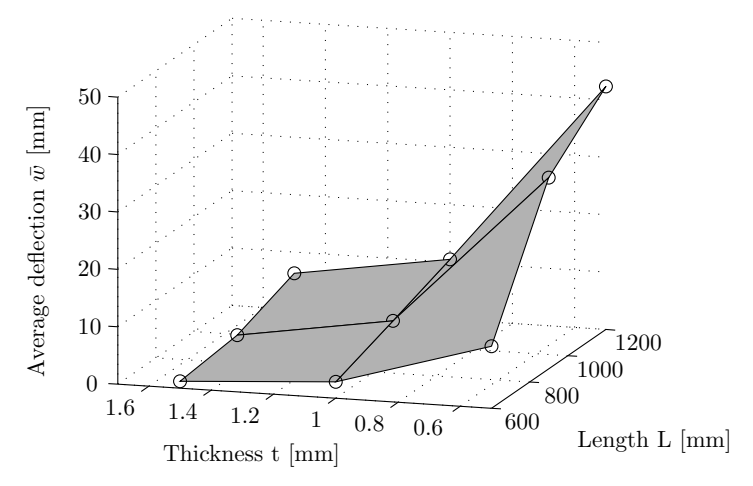


Fig. 3.11: Bilinear illustration of average warpage deflections \bar{w} of 8552/IM7 specimens

Up to this point the interpretation of the experimental findings is difficult. Figure 3.12 shows the obtained average warpage deflections for the three investigated prepreg materials. Results clearly show that warpage deflections increase nonlinearly with increasing part length and decreasing part thickness.

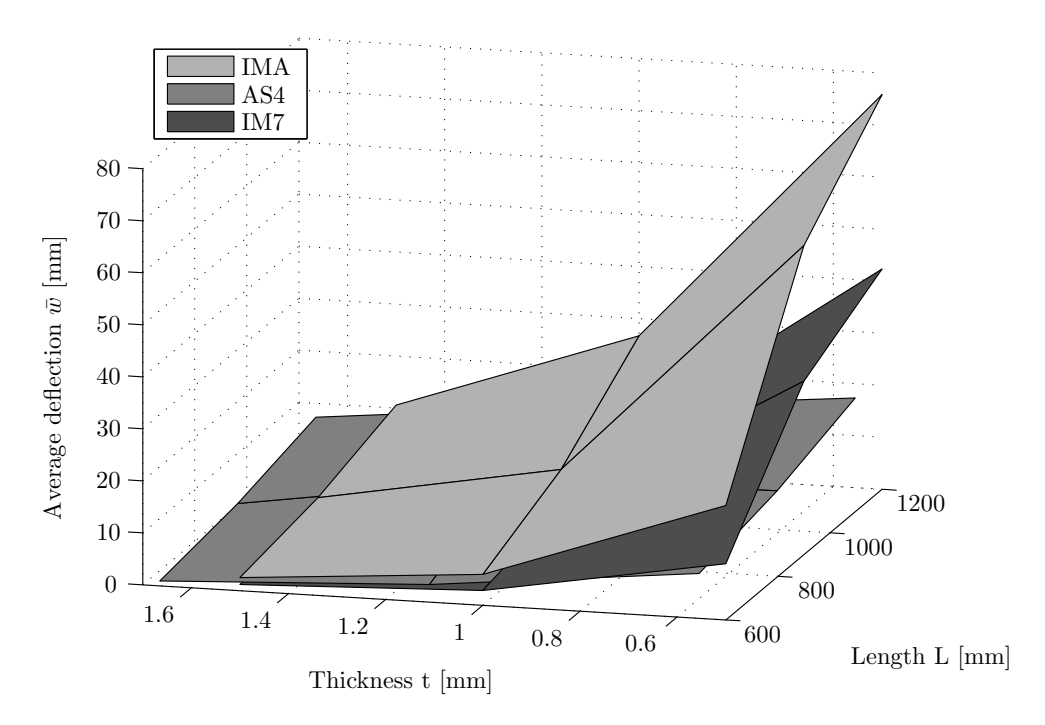


Fig. 3.12: Comparison of warpage deflections \bar{w} for the three material combinations

However, differences between the single materials are significant, as the deflection of M21E/IMA specimens increase deflections of the 8552/AS4 specimen by a factor of four. This was not expected, as the warpage effect was assumed to be driven by the thermal tool expansion mainly. As all prepreg materials are cured with an 180 °C process there must be another effect which induces the massive difference in deflection. The obtained magnitudes clearly suggest that warpage is only relevant for applications using laminates with thicknesses smaller than 1.5 mm. In context of a compensation, it should be balanced between a modified curved tool surface, simple re-deformation of the part within the assembly or a tool solution using invar. Considering common structural components such as spars, stringers or ribs, the warpage phenomenon is of minor relevance as laminate thickness of those components is commonly above a thickness threshold of 1.5 mm.

Nevertheless, the inspection of the experimental findings clearly reveals that M21E/IMA specimens show the largest distortions. At this point the origin of this difference is not clear. Resin and fiber properties of the materials at hand differ slightly as shown in Table 3.2, but not to a degree that justifies the obtained differences in \bar{w} . When focusing on the 8552/AS4 and M21E/IMA warpage deflections, since tool surface properties can be assumed as identical for those specimens, experimental results are striking.

Micro section analysis are performed in order to account for potential differences in the part's inner structure induced due to the different ply thickness, a V_f gradient or neat resin layers for example. Within the following section, the conducted micro section analysis results are presented and discussed.

3.4 Inspection of Laminate's Architecture by Means of Microsection Analysis

Tool Surface properties during the manufacturing of the M21E/IMA and the 8552/AS4 specimens are assumed as equal, since the manufacturing of the specimens are conducted within a small time period. Considering the significant differences of the obtained warpage deformations

for the investigated materials, it is suspected that the slight fiber property differences outlined in Table 3.2 are not the only explanation.

To substantiate that guess, micro-section analysis are performed for selected specimens of the same thickness. Figure 3.13 shows representative micro sections for the investigated unidirectional specimens of the three prepreg materials at hand. A comparison reveals massive divergences in the laminates architecture. Almost no interply borders are detectable for the 8552/AS4 specimen while the 8552/IM7 specimens partially show ply boundaries.

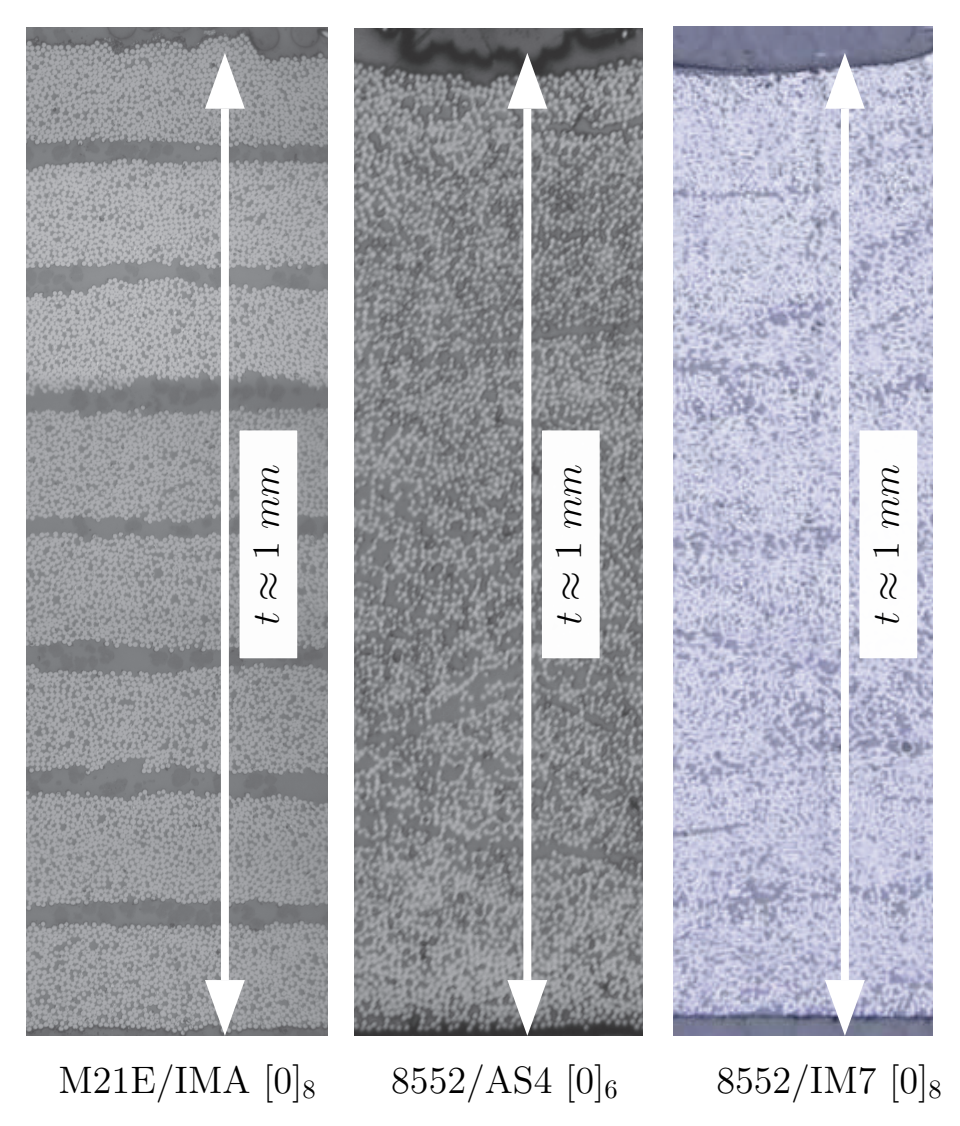


Fig. 3.13: Microsections of the investigated laminates

In contrast, the M21E/IMA specimen shows conspicuous interply regions, what can be excellently seen in Figure 3.13. A detailed cut-out of two adjacent layers is given in Figure 3.14. The manifestation of those so-called interleaf layers is supported by thermoplastic particles which are part of toughening concepts of modern prepreg materials. Those concepts aim for improved damage tolerance properties as outlined amongst others by Marsh [80]. Regarding such an interleaf layer in Figure 3.14, different gray scales indicate neat resin (less dark) and thermoplastic particles (darker).

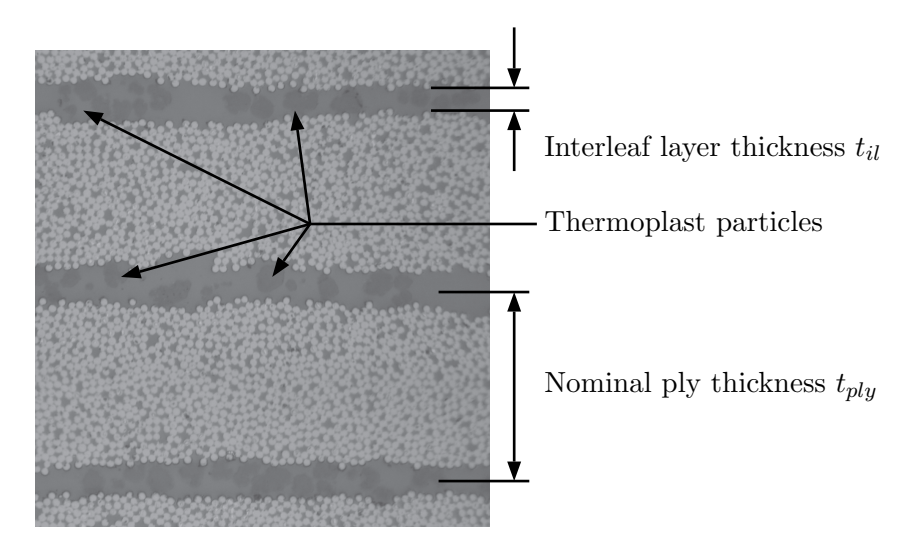


Fig. 3.14: Detailed view on distinct interleaf layers obtained for the M21E specimens

The nominal ply thickness t_{ply} of one M21E/IMA ply is about 0.127 mm. Micro section inspection reveals interleaf-layer thicknesses t_{il} of approximately 0.025 mm which is approximately one fifth of the total ply thickness t_{ply} . As the appearance of the cross sections are that different, it is assumed that those interleaf layers abet the development of warpage deformations significantly.

Nevertheless, ply-wise V_f inspections are conducted to account for conceivable gradients. Since, those inspections reveal no volume fraction or void gradient from ply to ply no detailed presentation is given here. However, experimental results are comprehensively described by Stefaniak et al. [9].

Summarizing it should be noted that laminates with interleaf layers show larger warpage deflections compared to non-interleaf laminates, when similar fiber properties and identical tool and process properties are given.

A common modeling approach is based on the theoretical assumption of interply slippage. Melo and Radford [58] assume that slippage between the fibers abet the development of a stress gradient, since plies distant from the tool relieve stresses as sliding between the plies is possible. However, this is contrary to experimental findings of Ersoy et al. [63] who showed for 8552/AS4 prepreg material that prepreg/prepreg interfaces have better stress transfer properties than prepreg/tool interfaces. Furthermore, own experiments, described in section B, substantiate Ersoy's [63] findings. In contrast, Sun et al. [68] experimentally show that ply slippage occurs already at low temperatures between 40 °C and 80 °C when absolute pressure is about 0.1 MPa. Sun et al. [68] use these effects within a prepreg-based diaphragm-forming process. This suggests that interply-slippage is a direct function of normal forces induced by the pressure difference which is analogously to the Coulomb friction. As laminates investigated in this thesis are autoclaved, interply slippage is excluded as a potential mechanism inducing warpage deformations as specimens are fabricated with an absolute pressure of almost 0.7 MPa.

Constitutive Model Explaining the Interleaf-Layer Effect

The expanding tool transfers interfacial stresses at the tool/part interface. Considering a homogeneous material, this leads to a shear-stress gradient in laminate-thickness direction as depicted in Figure 3.15 (left). As long as linear-elastic material properties are assumed, such a gradient will not result in residual stresses after the cool down to room temperature.

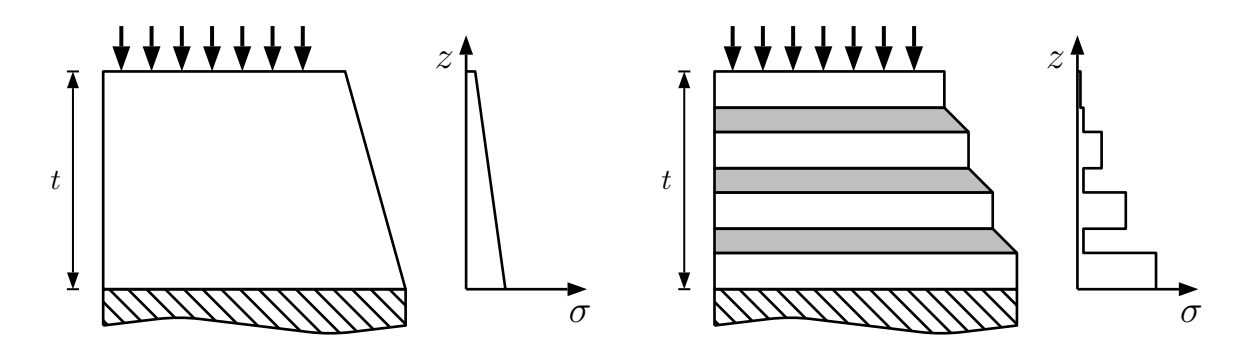


Fig. 3.15: Post-gelation stress distribution within the laminate for layups with interleaf layers (right) and without interleaf layers (left)

Regarding the interleaf-layup configuration in Figure 3.15 (right), the comparably soft interleave layers potentially lead to a more distinct stress gradient, as shear deformation of the resin-similar areas impede the stress transfer between the plies. Nevertheless, no residual stresses due to tool-part interaction would remain after the cool-down. Present models give no substantiated explanation for the obtained deformations as they do not account for property changes due to the ongoing curing process. Thus, a new explanatory model is developed which can explain the differences between interleaf and non-interleaf prepreg systems.

During the curing process resin properties change significantly. Garstka et al. [14], Ersoy et al. [23] and Gigliotti et al. [81] investigate the property development during cure of 8552/AS4 prepreg and showed that the gel point is reached during the second ramp when processing the MRCC. Moreover, Ersoy et al. [82] show that vitrification is observed approximately 45 minutes after reaching the second dwell phase. Generally, the resin's modulus develops during the rubbery state, which is between the gel point and the vitrification, and increases instantaneously at the point of vitrification. The underlying mechanism can be explained based on Figure 3.16 (left).

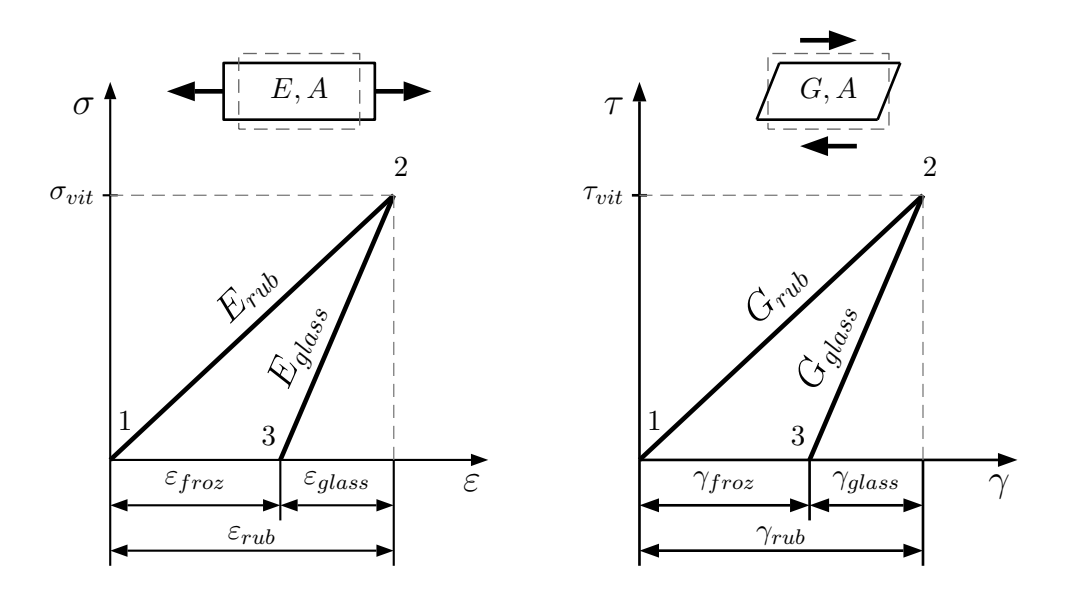


Fig. 3.16: Illustration of the constitutive model

After reaching the gel point the resin is in rubbery state and is able to transfer stresses between fibers and plies. Within this state, the resins's modulus is denoted E_{rub} . Commonly,

gelation and vitrification are timely spaced within the manufacturing process. As the gel point is reached during the second ramp, additional thermal strain is induced by the tooling until the second dwell phase is achieved. Therefore, the laminate exhibits a kind of elastic pre-loading, whereat the corresponding strain is denoted at ε_{rub} . When reaching the vitrification within the second dwell phase, the Young's modulus of the resin increases instantaneously. After reaching the vitrification the resin is in glassy state and no relaxation is possible any more. At the end of the process, the cool down to ambient conditions induces thermal contraction of the tooling. Due to the instantaneous property change the resin's modulus in glassy state E_{glass} becomes significantly higher that E_{rub} . Due to this difference, the strain due to the cool down ε_{glass} is smaller than ε_{rub} which results in a certain residual strain fraction. Due to their residual character these strains are referred to as frozen strains ε_{froz} in this thesis. At this point, frozen strains are responsible for the development of manufacturing deformations but however the relation of interleaf layer thickness to magnitude of deformation still remains unclear.

As the resin is assumed to have isotropic properties throughout the entire curing process, shear stiffness is proportional to Young's modulus $G \sim E$ as, where a change of the poisson's ratio is disregarded.

Therefore, the aforementioned characteristics of the Young's modulus can be transferred to the shear properties. This is shown in Figure 3.16 (right). A direct comparison of the cross section characteristics of the M21E/IMA and the 8552/AS4 specimens given in Figure 3.13 abets an explanation why laminates containing interleaf layers exhibit larger deformations than non-interleaf laminates. Due to the finite thickness of the interleaf layers, which have neat resin similar material properties, the development of a distinct stress gradient is supported, as indicated in Figure 3.15 (right). Figure 3.17 illustrates the effect of frozen strains in Figure 3.16.

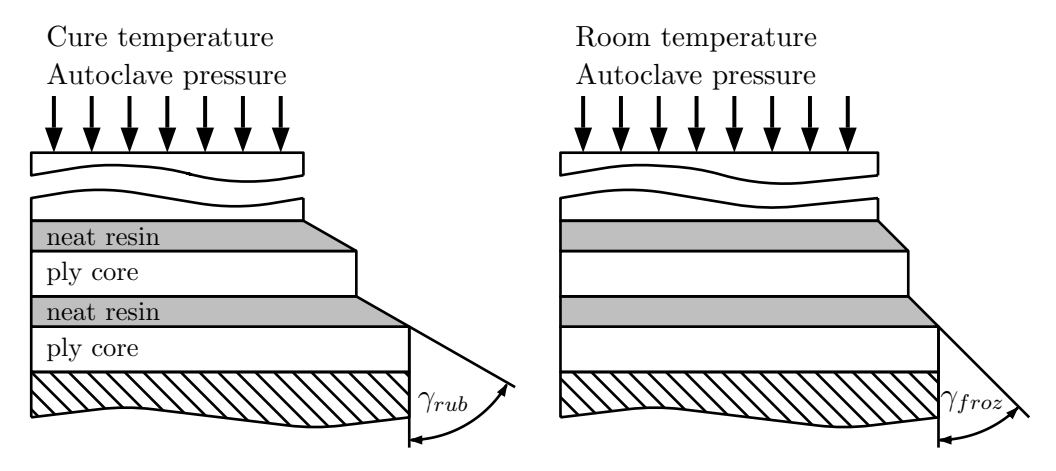


Fig. 3.17: Frozen strains in neat resin layers support manufacturing deformations

As these strains induce a more distinct stress gradient in laminate thickness direction the resulting residual moment M, which is derived according to Equation 3.1, is larger than for a homogeneous laminate.

$$M = \int_{-t/2}^{t/2} \sigma(z) \cdot z \cdot dz \tag{3.1}$$

As the relevance of the warpage phenomenon for common structural elements is comparably small due the aforementioned geometrical limitations, the preceding constitutive model is not further pursued in this thesis. Nevertheless, it provides a physically reasonable explanation why manufacturing-induced warpage distortions of interleaf-layer prepreg systems exceed distortions of non-toughened systems.

3.5 Warpage Deflections of Flat Multiangle Specimens

Up to this point, experiments are performed with UD laminates only. Due to their weak mechanical properties in transverse direction those laminates are rather less relevant in technical applications. To assess the relevance of warpage distortions for technically relevant laminates composed of multiple differently aligned plies, a set of warpage test specimens is manufactured.

The set consists of four different layups manufactured from M21E/IMA prepreg. Layups are $[0, 90]_s$, $[90, 0]_s$, $[45, -45, 90, 0]_s$, $[45, -45, 0, 90]_s$, whereas three specimens of each layup are manufactured. All specimens are 900 mm long and 100 mm wide and are fabricated aligned in tool longitudinal direction. According to the layup, the specimens thickness is between 0.5 mm and 1.0 mm. Figure 3.18 elucidates the measured warpage deflections for these configurations.

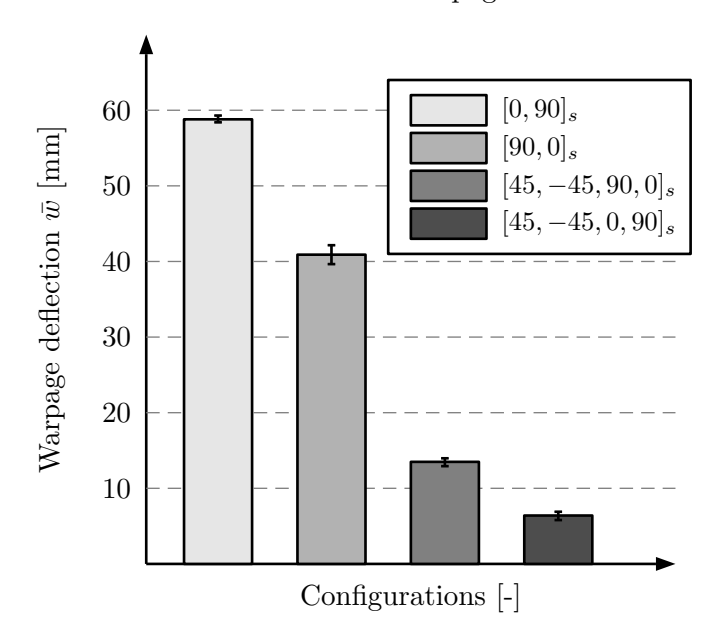


Fig. 3.18: Average warpage deflections of selected multi-angle laminates

The comparison of the average warpage deflection of the multi-angle laminates shown in Figure 3.18 with that one of the unidirectional laminates given in Figure 3.8, abets a few simple conclusions. The obtained warpage deflections of the unidirectional and the $[0, 90]_s$ laminates are of almost the same magnitude, whereas \bar{w} of the $[90, 0]_s$ is only approximately 70 %. This can by explained with findings by Bapanapalli and Smith [46] who numerically analyse the warpage effect for UD laminates. They derive the theoretical thickness of the laminate fraction affected by tool-part interaction. They derive a thickness of 0.013 mm for aluminum molds and 0.03 mm for invar molds, whereat both thicknesses are less than one ply thickness. Thus, it is assumed that the 0° ply in the $[90,0]_s$ is not directly affected by the expanding tool which leads to a smaller stress gradient and therefore a smaller deflection.

This indicates that the number of UD plies does not dominate the warpage deformations solely. Instead, it is a balance between the position of the outer 0° plies and the total bending stiffness of the specimen.

Warpage deflection for the $[45, -45, 90, 0]_s$ is almost identical to that one of the eight ply UD specimens. Nevertheless, $[45, -45, 0, 90]_s$ show only half of the warpage deflection than the $[45, -45, 90, 0]_s$ specimens. At a first glimpse, this finding contradicts the relations above, where the outer 0° ply dominates the occurring warpage deflections. Considering that the affected laminate fraction is less than two times the ply thickness, it is assumed that the tool expansion leads to an identical stress transfer for both eight-ply laminates. As this introduced residual stress

is responsible for the bending of the specimens after the demolding, it acts against the bending stiffness of the specimens. As the bending stiffness of the $[45, -45, 0, 90]_s$ layup is larger than that one of the $[45, -45, 90, 0]_s$ specimens, the expectable warpage is lower. This explanation is supported by investigations of Arafath et al. [64].

3.6 Warpage of Curved Thin Specimens

In the preceding, the warpage effect is characterized for flat unidirectional and multi-angle laminates. In this section warpage is investigated for simply-curved laminates with a considerable radius of R=350 mm.

Due to the geometrical shape of the structure it is potentially affected by warpage and the spring-in effect as is has a reasonable curvature and is still thin.

The main issue of this section is to answer the question whether a simply curved composite part is dominated either by the spring-in phenomenon or the warpage effect, or whether both effects equal each other.

Figure 3.19 shows the used tooling geometry schematically. Roughness measurements are performed with a Perthometer M1 in extrusion direction of the tool. A measurement in circumferential direction is not possible with the used Perthometer M1 due too the massive curvature. However, the coarseness in transverse direction is obtained to $R_a = 1.46 \ \mu m$ and $R_a = 1.24 \ \mu m$ for two arbitrary selected positions on the tool surface which is significantly higher than that one of the flat tooling.

As that tooling has been fabricated out of rolled steel sheet metals which commonly have no grinded surface, no direction dependence of the surface roughness is obtained.

Depending if warpage or spring-in is dominating, two different deformation shapes are conceivable after demolding the part from the tool.

In case #1, the spring-in effect is dominating which leads to an increase of the enclosed angle but a decrease of the part radii according to Figure 3.19. Case #2 is dominated by the warpage effect, which results in a convex-down curvature of the part in tool direction, what is accompanied by a decrease of the enclosed angle and an increase of the part's radius.

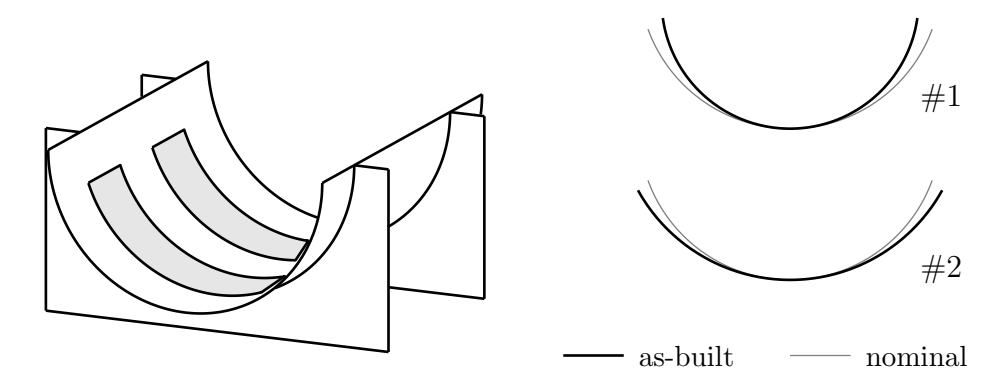


Fig. 3.19: Constantly curved (R=350mm) flat laminates: #1 spring-in dominated configuration; #2 warpage dominated configuration

To assure a transferability, the used length and width of the curved specimens should be identical to those of the flat unidirectional laminates. Thus, the length of the specimen is set to 900 mm whereby an eight-ply laminate is used ($t \approx 1$ mm). The bagging arrangement is equal to that one of the flat-plate experiments as illustrated in Figure 4.13. Three specimens are fabricated at the same time in order to blank out batch-to-batch variability similar to the flat-plate manufacturing. While the maximum deflection is an appropriate measurand for the flat

specimens, it is insufficient for the curved specimens. Therefore, part deformation is measured with respect to the coordinate system illustrated in Figure 3.20. The specimen coordinates are measured for fifteen points along the arc length, while Δx and Δy represent components of the maximum deflection vector comparable to the measurand w for the flat specimens.

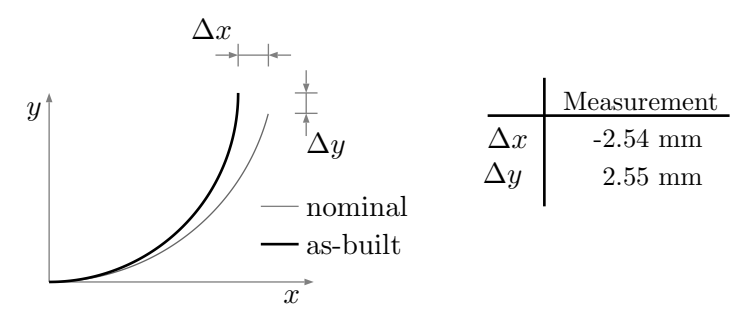


Fig. 3.20: Measured deformation of the curved specimens. Signs correspond to axes orientations

The signs of the measured deformation in Figure 3.20 are related to the depicted coordinate system. The comparison with the two cases shown in Figure 3.19 reveals that the deformation of the curved specimen is dominated by the spring-in effect.

Within Section 7.2 an informative numerical comparison is presented, applying the new modeling strategy which is introduced in Chapter 6. In order to compare the measured as-built shape with the nominal tool shape, best-fit circles are derived from the 15 points along the arc length of each specimen. It should be noticed that a malfunction of the used diamond saw damaged specimen 2. Therefore, the specimens number one and three are utilized for evaluation purposes only. Table 3.3 gives the derived best-fit diameter.

Specimen	Meas. points	Best-fit Ø[mm]	max dev. [mm]	arc length [mm]	
nom.	-	700.00	0	900	
1	15	687.58	1.46	900	
2	15	700.27	1.74	913	
3	15	687.76	1.93	900	

Tab. 3.3: Best-fit circle derivation based on measurement results

Evaluation of the arc-length relation $s=r\varphi$ for the nominal configuration reveals an enclosed angle of 147.33° for a radius of 350 mm. Application of the arc-length relation to the average asbuilt configuration gives an enclosed angle of 149.97° with a corresponding radius of 343.84 mm. That corresponds to the definition of the spring-in phenomenon which suggested the assumption that manufacturing deformations of curved thin composite specimens are dominated by that effect.

3.7 Cognitions from the Experimental Warpage Investigations

The relevance of the warpage effects directly depends on the structural application. Experimental results clearly verify that tool-part interaction can lead to massive deflections of thin flat laminates. Experiments further verify that the warpage effect occurs only for single-sided mold manufacturing techniques as a double-sided mold with identical surface and tool properties on both sides produces no measurable warpage deflection. Moreover, warpage is directly related to the tool's CTE and in particular to the mismatch between the tool's and the part's CTE.

Regarding specimens with identical lengths, a clear nonlinear relation is obtained as the warpage deflection significantly decreases with increasing laminate thickness. This is consistently observed for the investigated 8552/AS4, M21E/IMA and M21/T700 prepreg materials.

The qualitative behavior is identical for all three prepreg materials, as increasing specimen lengths lead to larger warpage deflections. However, a significant dependency from the prepreg system is observed as M21E/IMA specimens produce almost twice times higher warpage deflections compared to the other systems.

Microsection inspections show significant differences in the laminate's architecture, as M21E/IMA shows well established interleaf layers with distinct thermoplastic particles. In contrast, M21/T700 and 8552/AS4 specimens only show slight interleaf-layer tendencies respectively no interleaf layers.

Figure 3.21 shows a selection of different specimens. As can be seen, deflections can reach considerable magnitudes.

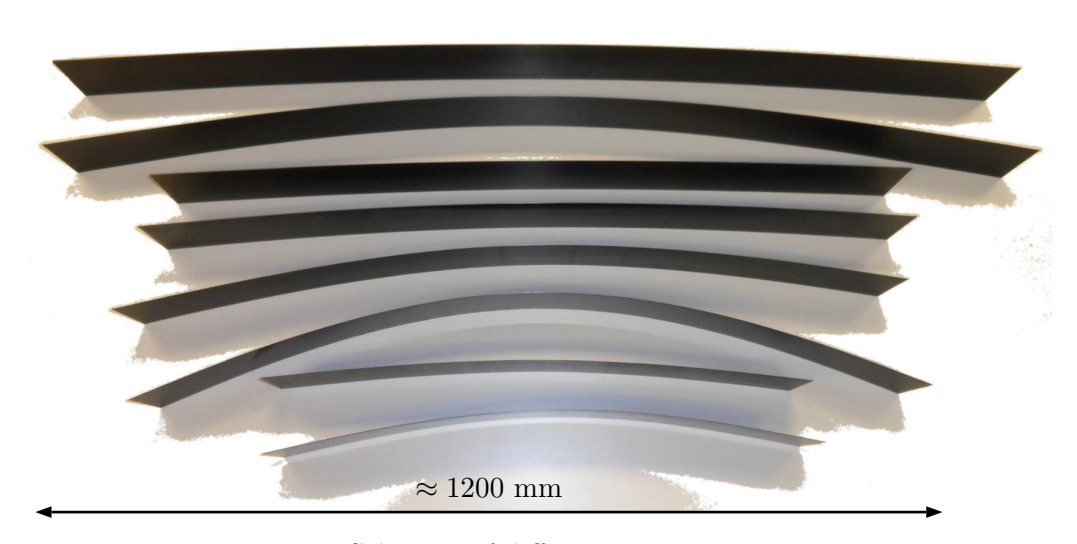


Fig. 3.21: Selection of different warpage specimens

The surface roughness of the tooling turned-out to have a massive impact on the obtained warpage deflections. Thus, a surface roughness of R_a of 0.15 μm results in a 50 % warpage reduction compared to a surface roughness R_a of 0.6 μm for nominal identical specimen properties. These are common values for tools fabricated with a circumferential grinding process. Interestingly, measurements show that the surface roughness tends to equalize after the fabrication of multiple structures.

Warpage measurements with different multi-angle specimens reveal that warpage deflections are dominated by the outer 0° plies in combination with the overall bending stiffness of the part.

Warpage measurements for unidirectional flat circular curved specimens reveal, that the warpage effect is not the main driver for curved shapes, as obtained deflections are contrary to the expected, warpage typical distortions. The simulation shown in Section 7.2 substantiates this experimental finding.

In terms of appropriate counteracting measures it remains questionable if a tool compensation in form of an 'inverted' curved tool surface is able to compensate warpage distortions. According to the curved-warpage investigations, it must be expected that fabrication on a curved tool surface leads to spring-in dominated shape variations and thus, no complete compensation. Therefrom, it is concluded that warpage can only be counteracted by use of a double-sided mold concept even when aluminum or steel with their high CTEs is used.

If a single sided mold concept is demanded, invar or CFRP tools provide similar CTE's as the composite part which will avoid warpage distortions.

4 Investigation of the Spring-In Phenomenon

In this chapter the spring-in effect is investigated by means of geometrical measurements of fabricated test specimens. The aim is to work out the main drivers of the effect. Therefore, part specific parameters such as section-radii, part-thickness and layup as well as tool specific parameters as surface roughness and tool material are varied. Furthermore, the effect of a process cycle with modified dwell stages is investigated. Spring-in angles obtained for different prepreg materials are compared to identify the characteristics of each prepreg material. A comprehensive statistical analysis is conducted based on the obtained spring-in angles. The experimental quantification of thermal and chemical spring-in fractions finalizes this chapter

4.1 Analytical Pre-examination of the Spring-in Effect

Composite manufacturing is characterized by an almost infinite number of parameter configurations. Due to this complexity, it is neither possible to quantify the magnitude of expectable spring-in angles nor to estimate the amount of scattering without focusing on a certain parameter combination or a parameter group. As outlined in the literature review given in Section 1.6, a lot of research has been conducted in the last decades. Unfortunately, fundamental differences in experimental setups hardly preclude a distinct quantitative comparison between the obtained experimental findings. Therefore, the investigations reported in this chapter focus on prepreg materials similar to the ones used for the warpage investigations.

Therefore, this focus on state of the art prepreg materials similar to the warpage investigation. Thus, the results presented here are evident for the selected prepreg systems. Specimens are fabricated with the MRCC with use of a certain bagging arrangement while the tool preparation procedure is equal. As this preliminary study is performed to receive a good approximation of the expectable spring-in angles, the straightforward approach proposed by Radford [5] is utilized. Numerical approaches on detail level, as they are described in the preceding, remain disregarded, as the parameter characterization efforts are disproportional within the context of a preliminary study.

The Radford Approach

Orthotropic material properties, such as direction dependent coefficients of thermal expansion lead to inhomogeneous shape changes of a part when subjected to a thermal load for example. Based on that cognition, Radford proposed a simple analytical model for the calculation of anisotropy-related shape changes of curved sections. A brief derivation of Radford's equations is given in Section 1.3.

The model is based on the assumption that angle changes of a curved section can be described by a strain mismatch in the cross-section of the part. Hence, Radford's model is two-dimensional, whereat the inspection plane is equal to a section-cut perpendicular to the centerline of the curvature as indicated in Figure 4.1. Radford distinguishes between strains in tangential direction ε_T and strains in radial direction ε_R which are depicted in Figure 4.2. Based on these strain components, the current section angle φ as well as the corresponding spring-in angle $\Delta\varphi$ are given as a function of the nominal section angle φ_0 .

$$\varphi = \frac{1 + \varepsilon_T}{1 + \varepsilon_R} \cdot \varphi_0 \quad \text{and} \quad \Delta \varphi = \varphi - \varphi_0 = \frac{\varepsilon_T - \varepsilon_R}{1 + \varepsilon_R} \cdot \varphi_0$$
(4.1)

In the original form, Radford's approach is formulated for homogeneous orthotropic material.

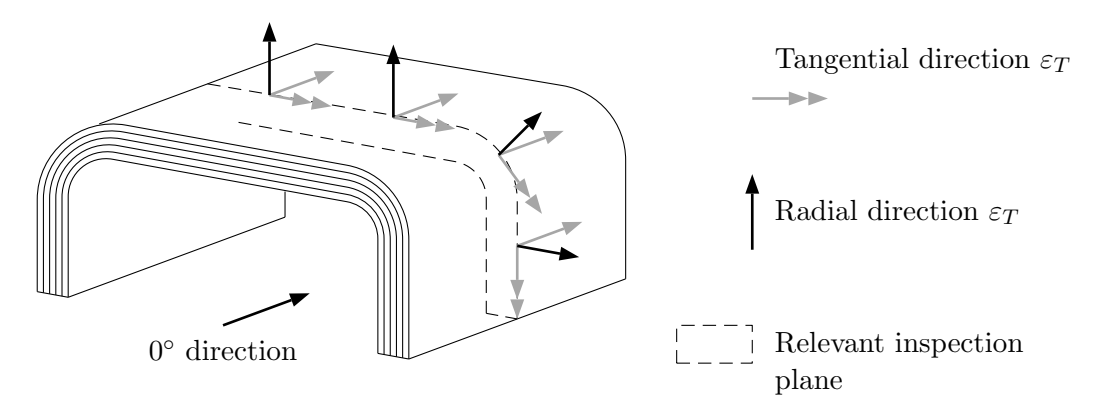


Fig. 4.1: Inspection plane of Radford's approach

Regarding a composite laminate composed of differently oriented unidirectional plies, the cross-section cannot be regarded as a homogeneous material. Utilizing homogenization approaches, as they are part of the CLT, allow the application of the Redford approach, since the ply properties of the single plies are transferred to equivalent properties of the laminate.

In order to prove that the Radford approach is applicable for layered composites, a ply-wise plain-stress FE model is compared with the analytic Radford approach, whereat homogenized material properties are used for the latter one.

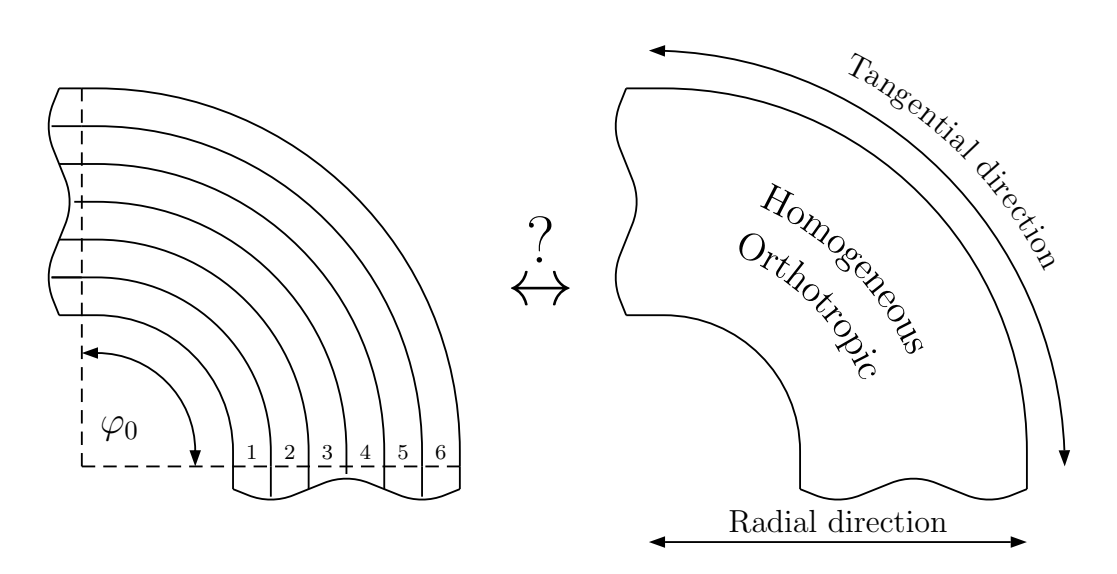


Fig. 4.2: Application to homogeneous and layered materials: Is that possible?

The special behavior of a layered composites is illustrated in Figure 4.3. Therein, the laminate has a $[+45, -45, (90, 0)_2]_s$ layup, whereat the 0° direction is normal to the depicted cross-section. Interaction between the single plies is disabled. Consequently, the different expansion properties of each ply lead to different thermal expansions of the different plies. A 15° segment of a corner area is modeled within the FE model.

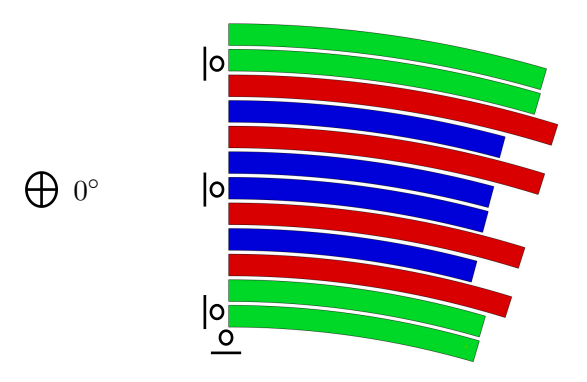


Fig. 4.3: Thermal expansion of single plies disregarding interaction $[+45, -45, (90, 0)_2]_s$

Applying tie conditions between the single layers and introducing boundary conditions, which force the free end to remain plain, the FE model deforms like a homogeneous orthotropic material. That is necessary in order to compare the predictions of the Radford model with the FE predictions.

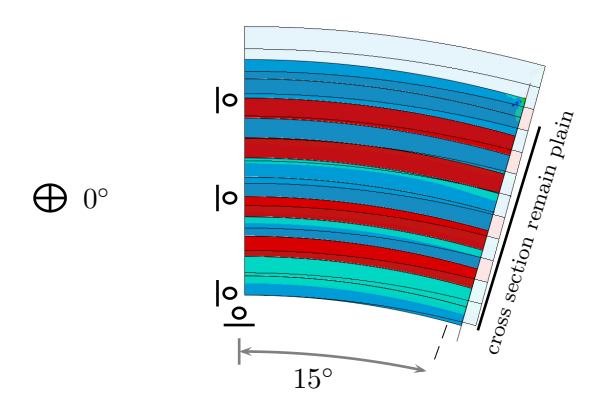


Fig. 4.4: Corresponding FE model of angle section (15°)

For sake of simplification, the comparison is conducted by regarding the deformation behavior for a thermal load of $\Delta T = -160^{\circ}C$ for a laminate composed of 0° and 90° plies. Within the FE model, each ply is modeled with three elements per ply in thickness direction, while material properties in laminate's tangential direction are derived by CLT. Material properties in thickness direction are assumed to be equal to the unidirectional ply properties in transverse direction. With other words, material properties in tangential direction depend on the layup whereat properties in thickness direction are equal to the ply's transverse properties.

The thermal expansion properties in tangential direction α_T and in radial direction α_R are given in Table 4.1. These parameters are derived with ESAComp. The iinsertion of $\varepsilon_T = \alpha_T \cdot \Delta T$ and $\varepsilon_R = \alpha_R \cdot \Delta T$ into Equation 4.1 and a nominal angle of 15° gives the corresponding springin angle $\Delta \varphi_{Radford}$ predicted by the Radford approach. The spring-in angle derived by FEM is denoted with $\Delta \varphi_{FEM}$.

0° plies [%]	Layup	$\alpha_T \text{ ppm/K}$	$\alpha_R \text{ ppm/K}$	$\Delta \varphi_{Radford} [^{\circ}]$	$\Delta \varphi_{FEM}[^{\circ}]$
0	[90] ₁₂	28.1	28.1	0	0
16.7	$[0, 90_5]_s$	5.82	28.1	0.32	0.32
33.4	$[0_2, 90_4]_s$	2.95	28.1	0.36	0.37
50	$[0_3, 90_3]_s$	1.82	28.1	0.38	0.38
66.7	$[0_4, 90_2]_s$	1.21	28.1	0.39	0.39
83.3	$[0_5, 90_1]_s$	0.803	28.1	0.39	0.40
100	$[0]_{12}$	0.281	28.1	0.40	0.40

Tab. 4.1: Radford predictions and simulation results

A comparison of both strategies based on Table 4.1 verifies the expectation that the Radford approach is equivalent to the FE simulation when constraining edge-effects by appropriate boundary conditions as shown in Figure 4.4.

Based on that finding, the Radford approach represents a suitable strategy to investigate spring-in fractions on a preliminary level. Therefore, it is utilized within a Matlab routine in order to quantify thermal and chemical spring-in fractions for a variety of layups. This allows a limitation of the expectable spring-in angles to a certain range as will be shown in the following.

Magnitude of the Expectable Spring-in Angles

As a first issue, the effect of the fiber volume fraction is investigated for a quasi isotropic layup $[45, -45, 90, 0]_s$. Subsequently, the spring-in fractions are derived for a variety of conceivable layups, whereat the regarded V_f is held constant. The Matlab tool, which has been programmed in context of this thesis, is described briefly in Section C. As outlined in the definition of the spring-in phenomenon, thermal expansion and chemical shrinkage are regarded as the main sources of the spring-in deformations. Both effects are resin dominated as the fibers have a considerably smaller thermal expansion as well as no chemical shrinkage. Up to this point chemical shrinkage of the resin is blanked out for sake of clarity. However, due to the similarities between thermal and chemical effects, chemical shrinkage is regarded analogously to the thermal expansion within the Radford approach. The derivation of corresponding 'quasi-thermal' parameters are demanded in order to incorporate chemical shrinking within the Radford model.

Considering a brick-shaped continuum with the edge-lengths a, b and c and volume change ΔV [%] is given by Equation 4.2.

$$\Delta V = \varepsilon_a \varepsilon_b \varepsilon_c + \varepsilon_a \varepsilon_b + \varepsilon_a \varepsilon_c + \varepsilon_b \varepsilon_c + \varepsilon_a + \varepsilon_b + \varepsilon_c \tag{4.2}$$

For an isotropic material strain is direction independent $\varepsilon_a = \varepsilon_b = \varepsilon_c = \varepsilon$. Consequently, Equation 4.2 gives

$$\Delta V = \varepsilon^3 + 3\varepsilon^2 + 3\varepsilon \tag{4.3}$$

The preceding equation represents the often cited relation $\varepsilon \approx \Delta V/3$ which relates volume change with corresponding strains. That is derived when disregarding higher-order terms of ε . Regarding a transversal isotropic material, as a unidirectional ply for example, the transverse plane is resin dominated. Thus, it is assumed that chemical shrinkage acts in that plane, as no physical constrains are present. Due to the high fiber stiffness no elongation in fiber direction occurs. Considering Equation 4.2 that is given when $\varepsilon_a = 0 \wedge \varepsilon_b = \varepsilon_c = \varepsilon^*$ is used.

$$\Delta V = \varepsilon^{*2} + 2\varepsilon^* \tag{4.4}$$

Solving for ε^* gives the corresponding strain induced by a volume change of a transversal-isotropic material.

$$\varepsilon^* = -1 \pm \sqrt{1 + \Delta V} \tag{4.5}$$

The second solution (-) remains disregarded as it has no physical interpretation. In context of a composite laminate Equation 4.5 needs to be expanded by the V_f as only the resin content of the laminate shrinks according to the preceding equation. The corresponding shrinkage of a laminate with a fiber volume fraction of V_f is described by the following equation.

$$\varepsilon^* = -1 + \sqrt{1 + (1 - V_f)\Delta V} \tag{4.6}$$

As the interpretation of ε^* is difficult, the derived ε^* values are described as an 'quasi-thermal' parameter. Therefore, ε^* is divided by the acting temperature change ΔT which gives a corresponding quasi-thermal expansion coefficient α^* . Thus, parameters α^* , α_T and α_R are quantitatively comparable.

In order to investigate the expectable spring-in fractions, a simple Matlab routine is developed which enables a spring-in prediction based on the Radford approach, wherein effects due to chemical shrinkage are considered as outlined above. Figure 4.5 gives a flow chart of the Matlab tool. A detailed explanation with further explanation of the underlying equations is given in Section C. The input data for the routine is separated into a material related fraction, wherein fiber and resin properties are defined, and a layup and process related fraction, wherein resin shrinkage and curing temperature are defined. Based on the input data, the local ply properties are derived with respect to micro-mechanics given by Schürmann [83]. Subsequently, the local ply properties are transferred to the laminate coordinate system. Homogenization allows the derivation of the resulting homogenized thermal and chemical parameters of the inspected laminates.

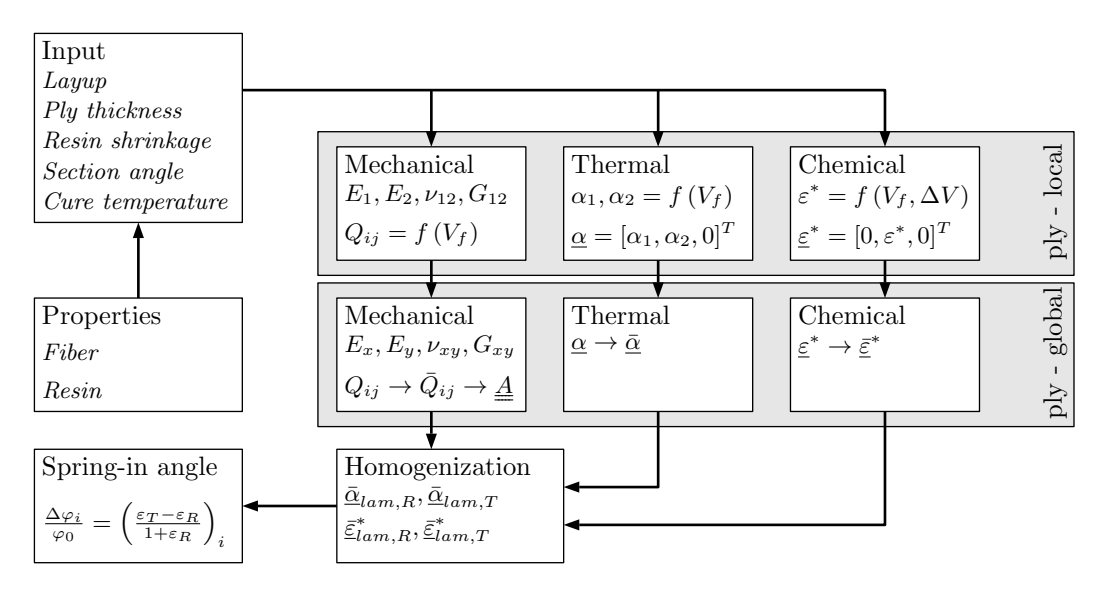


Fig. 4.5: Matlab routine schematically

Finally, Equation 4.1 is implemented in order to derive the spring-in angle fractions as a function of fiber volume fraction V_f . For sake of clarity, only selected layups are depicted here. Table 4.2 gives the used material properties which are mainly taken from the literature. Although parameters are taken from the literature and are not validated by experiments, the derived spring-in fractions allow a limitation of the expectable magnitude of spring-in.

Parameter	Value	Unit	Reference
$\overline{E_{f1}}$	231000	MPa	[75]
E_{f2}	21000	MPa	[75]
v_{12f}	0.25	-	[75]
G_{12f}	28000	MPa	[75]
α_{f1}	-0.63	ppm/K	[75]
$lpha_{f2}$	7.2	ppm/K	[84]
$\overline{E_m}$	4670	MPa	[85]
v_m	0.37	-	[86]
G_m	1704	MPa	[86]
α_m	65	ppm/K	[86]
ΔV	$-2 < \dots < -7$	[%]	-

Tab. 4.2: Material parameters of AS4 fibers and 8552 resin utilized within the Matlab routine

As depicted in Figure C3 in the Appendix, those parameters can be easily adapted within the tool. The resulting spring-in angle and its fractions for an $[+45, -45, 90, 0]_s$ laminate are shown in Figure 4.6 as a function of the V_f .

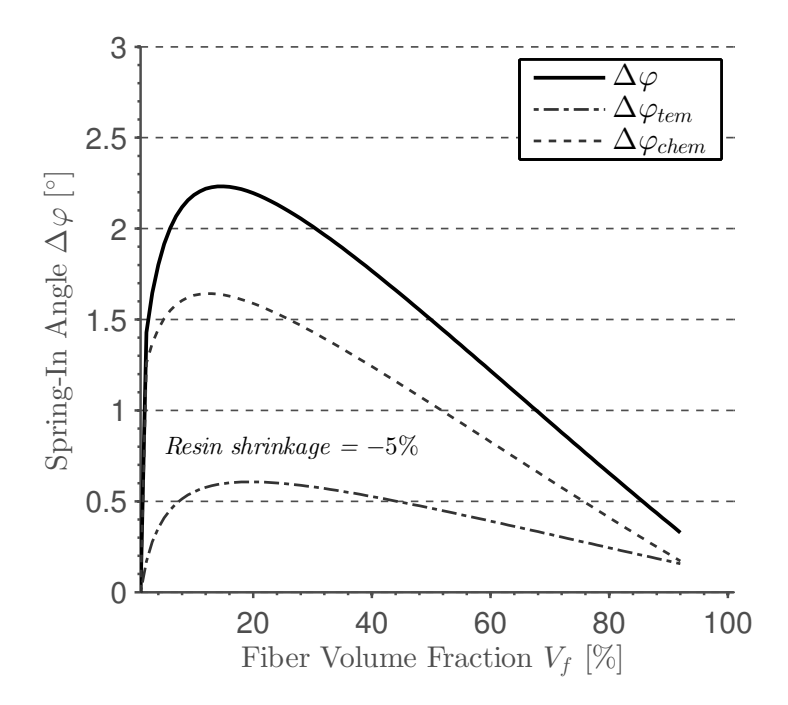


Fig. 4.6: Spring-in fractions of a quasi - isotropic $[45, -45, 90, 0]_s$ laminate with $\Delta V = -5 \%$

Therein, the resin's cure shrinkage is set to $\Delta V = -5$ %, whereat Figure 4.7 shows the resulting spring-in angles for $\Delta V = -2$ %, -3 % and -7 %. The ply thickness t_{ply} is 0.25 mm and the nominal section angle is $\varphi_0 = 90^{\circ}$ referring to experiments presented in the following.

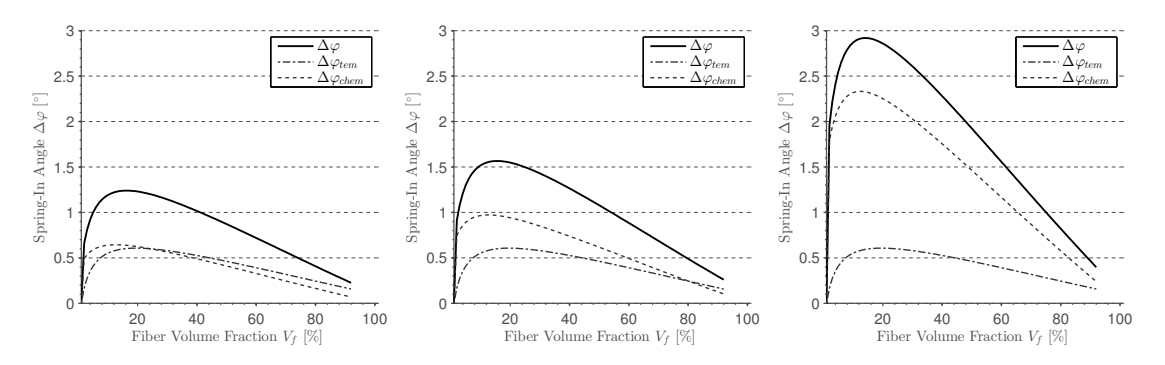


Fig. 4.7: Spring-in fractions of a quasi - isotropic $[45, -45, 90, 0]_s$ laminate for $\Delta V = -2 \%, -3 \%$ and -7 %, respectively

Figure 4.8 gives the derived spring-in fractions for a $[0,90,0,90]_s$ laminate, wherein $\Delta V=-3$ % , -5 % and -7 %.

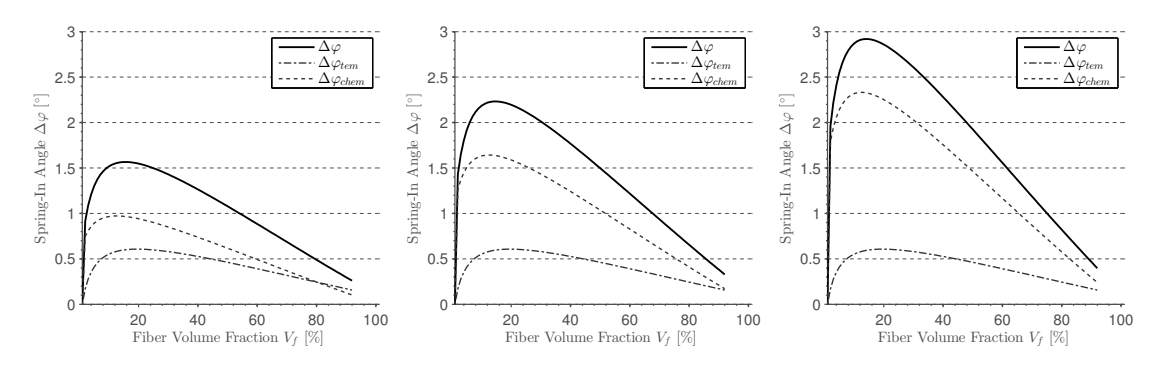


Fig. 4.8: Spring-in fractions of a $[0, 90, 0, 90]_s$ laminate for $\Delta V = -3\%$, -5% and -7%, respectively

Figure 4.9 gives the derived spring-in fractions for a $[(45, -45)_2]_s$ laminate, wherein $\Delta V = -3$ %, -5 % and -7 %.

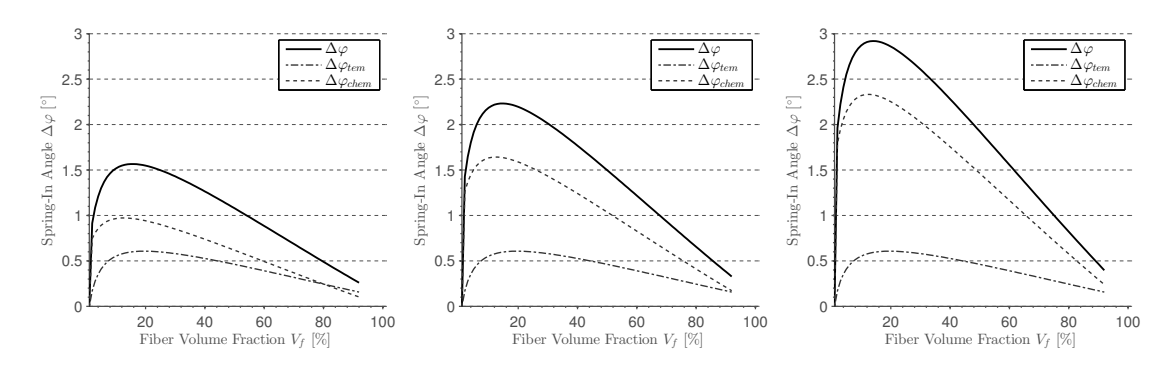


Fig. 4.9: Spring-in fractions of a $[45, -45, 45, -45]_s$ laminate for $\Delta V = -3 \%, -5 \%$ and -7 %, respectively

Comparison of the results depicted in the preceding figures, allows the cognition that the magnitude of spring-in can be limited to $0.8^{\circ} < \Delta \varphi < 2.5^{\circ}$ for a technically relevant fiber volume fraction range of 40 % $< V_f < 70$ %. However, the assumed chemical shrinkage is essential for this range.

Although a slight uncertainty must be expected due to the non-validated material parameters, the predicted range of spring-in deformations corresponds to own experimental results as well

as data given by Fernlund and Twigg.

As indicated by the Figures 4.6, 4.7, 4.8 and 4.9 slight changes between the single layups are obtained, whereat the sensitivity to chemical shrinkage is the main difference.

Spring-in Angle as a Function of Laminate Stacking

The presented approach is applied to a multitude of different laminates. Therein, V_f remains constant while the layup varies. The investigated layups are described by the parameterized notation $[A_K(B, -B)_M C_L]_s$, wherein A, B and C denote certain angles. Within the study presented here A, B, C correspond to $0^{\circ},45^{\circ}$ and 90° ply orientations, respectively. The coefficients K, L, M denote the number of plies or plygroups of a certain orientation.

It should be noted that the stacking of the plies does not affect the equivalent laminate parameters as $\underline{\underline{A}} = \sum \underline{\underline{Q}}_i \cdot t_i$. Therein, $\underline{\underline{A}}$, $\underline{\underline{Q}}_i$ and t_i denote the laminates extension stiffness matrix, the ply stiffness of ply i in global coordinates and the thickness of ply i, respectively. Therefore, the number of plies of a certain orientation is regarded in the parameterized laminate only. According to Equation 4.1, the tangential $\Delta \varphi_T$ and a radial fraction $\Delta \varphi_R$ are defined as followed.

$$\Delta\varphi_i = \frac{\varepsilon_T - \varepsilon_R}{1 + \varepsilon_R} \cdot \varphi_0 = \frac{\varepsilon_T}{1 + \varepsilon_R} \cdot \varphi_0 + \frac{-\varepsilon_R}{1 + \varepsilon_R} \cdot \varphi_0 = \Delta\varphi_T + \Delta\varphi_R \tag{4.7}$$

Considering that this distinction is possible for the thermal and the chemical fraction, the springin angle $\Delta \varphi$ is equal to the sum of the four fractions.

$$\Delta \varphi = \Delta \varphi_{T,T} + \Delta \varphi_{T,C} + \Delta \varphi_{R,T} + \Delta \varphi_{R,C} \tag{4.8}$$

A meaningful illustration is difficult due to the number of acting parameters. Within Figure 4.10 is a derivation based on the assumption that K equals L, which leads to a reduced degree of freedom. Thus, the illustration as a surface plot is possible. Other configurations with a higher degree of freedom are not illustratable as a surface plot.

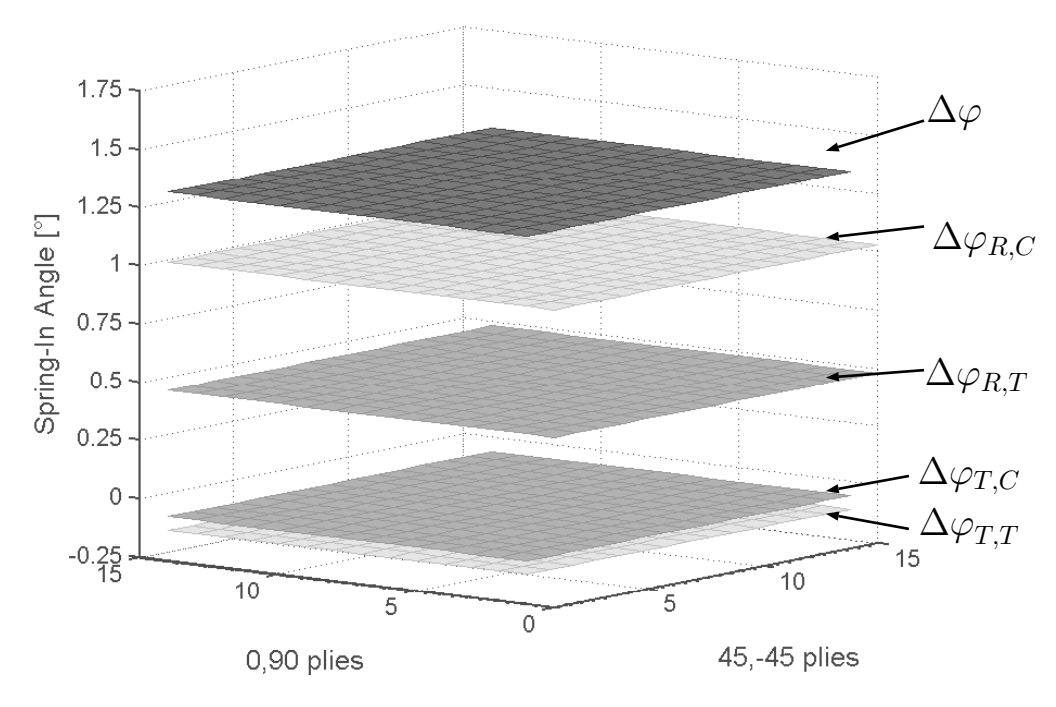


Fig. 4.10: Spring-in fractions for the parametric layup $[A_K(B, -B)_M C_K]_s$, wherein A,B and C denote $0^{\circ},45^{\circ}$ and 90° , respectively.

An investigation of a parameterized layup $[A_K(B, -B)_M C_K]_s$ with a V_f of 60 % reveals interesting results. For $1 \le K \le 14$ and $0 \le M \le 15$ layups contain up to 116 plies. However, the spring-in angle is obtained independent from the number of 0/90 plies, which is due to the quasi orthotropic material properties. The following set of equations verifies this for this particular layup.

$$\underline{N}_{i} = \underline{\underline{A}} \cdot \underline{\varepsilon}_{i} \quad \text{with} \quad \begin{cases} \underline{\underline{A}} = \sum_{k=1}^{n} \underline{\underline{Q}}_{k} \cdot t_{k} \\ \underline{\varepsilon}_{T} = \underline{\bar{\alpha}}_{lam} \cdot \Delta T \end{cases} \tag{4.9}$$

The laminate's homogenized coefficient of thermal expansion and the expansion due to chemical shrinkage is derived according to Equation 4.9. With respect to the parameterized layup, the extension stiffness matrix $\underline{\underline{A}}$ and the total width specific normal forces due to a thermal load is given by equations 4.10 and 4.11, respectively.

$$\underline{\underline{A}} = 2t_k \left[K \cdot \left(\underline{\underline{T}}_0^{-1} \cdot \underline{\underline{Q}} \cdot \underline{\underline{T}}_0 + \underline{\underline{T}}_{90}^{-1} \cdot \underline{\underline{Q}} \cdot \underline{\underline{T}}_{90} \right) + M \cdot \left(\underline{\underline{T}}_{45}^{-1} \cdot \underline{\underline{Q}} \cdot \underline{\underline{T}}_{45} + \underline{\underline{T}}_{-45}^{-1} \cdot \underline{\underline{Q}} \cdot \underline{\underline{T}}_{-45} \right) \right] \quad (4.10)$$

$$\underline{N}_{T} = \left[K \cdot \left(\underline{\underline{T}}_{0}^{-1} + \underline{\underline{T}}_{90}^{-1} \right) + M \cdot \left(\underline{\underline{T}}_{45}^{-1} + \underline{\underline{T}}_{-45}^{-1} \right) \right] \cdot \underline{\underline{Q}} \cdot \underline{\alpha} \cdot \Delta T \cdot 2t_{k}$$
(4.11)

Equation 4.11 can be simplified as follows:

$$\underline{N}_T = (K+M) \cdot \begin{bmatrix} 1 & 1 & 0 \\ 1 & 1 & 0 \\ 0 & 0 & 0 \end{bmatrix} \cdot \underline{\underline{Q}} \cdot \underline{\alpha} \cdot \Delta T \cdot 2t_k \quad . \tag{4.12}$$

Deriving the homogenized laminate's coefficients of thermal expansion given by $\bar{\alpha}$ reveals constant parameters although the laminate stacking and the laminate thickness changes significantly.

$$\underline{\bar{\alpha}}_{lam} = \frac{1}{\Delta T} \cdot \underline{\underline{A}}^{-1} \cdot \underline{N}_{T} \tag{4.13}$$

The single fractions depicted in Figure 4.10 show that the radial components of the total spring-in angle $\varphi_{R,i}$ dominate spring-in angle $\Delta\varphi$ massively. Consequently, that cognition is used within a new experimental approach for the derivation of expectable spring-in angles presented in Section 4.5

It should be noted that, non-quasi-orthotropic laminates, as for example $[A_{2K}(B, -B)_M C_K]_s$, reveal a layup-specific spring-in angle which is depicted in Figure 4.11. However, the obtained variability is limited.

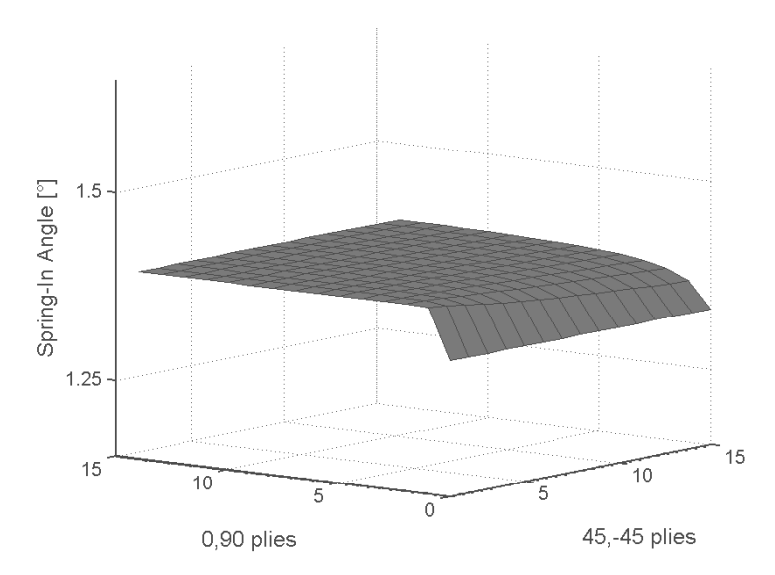


Fig. 4.11: Spring-in fractions for the non-quasi orthotropic parametric layup $[A_{2K}(B,-B)_M \ C_K]_s$, wherein A, B and C denote 0° , 45° and 90° , respectively.

Findings of the Numerical Pre-examinations of the Spring-in Phenomenon

Within the preceding section, the expectable magnitude of spring-in is investigated, pursuing the aim to define a quantitative range of the expectable spring-in angles. Therefore, the two-dimensional approach proposed by Radford [5] is utilized. As that approach is proposed for orthotropic homogeneous materials, it is applicability to layered composites which are not homogeneous. This is validated by means of finite element analysis. Therefore, homogenized layup expansion properties used with the Radford approach are compared to ply-wise FEM analysis. Both strategies reveal the same result when appropriate boundary conditions are applied within the FE analysis. That boundaries represent a kind of cyclic symmetry which prevents edge effects as depicted in Figure 4.4.

Providing this transferability, a Matlab routine was developed, which enables a spring-in estimation based on the Radford approach. Therein, the resin's volumetric shrinkage ΔV is transferred to corresponding strains. Expansion in transverse direction only is assumed. Thus, 'quasi-thermal' strains are derived based on simple volumetric considerations. Subsequently, the routine is applied for different layups for the range $0\% \leq V_F \leq 90\%$. The used material mechanical and thermal properties are taken from the literature. The magnitude of resin's volumetric shrinkage is varied in a realistic range of $2\% \leq \Delta V \leq 7\%$ in order to quantify the effect on the spring-in angle. It should be noted that all stated spring-in angles are referred to a nominal angle $\varphi_0 = 90^\circ$ as this allows a direct comparison to the experimental results presented in the following. Although slight uncertainties are related to the mechanical properties taken from the literature, the values of the parameters are representative. Thus, the expectable spring-in of the φ_0 angle can be limited to a range of $0.8^\circ < \Delta \varphi < 2.5^\circ$ for a technically relevant fiber volume fraction of $40\% < V_f < 70\%$.

In order to widen the significance of this study, the Matlab routine is used for an parameterized layup $[A_K(B, -B)_M C_L]_s$. Therein, A,B and C are taken as $0^{\circ},45^{\circ}$ and 90° , respectively. The parameters K, L and M denote the number of plies or ply-groups. As the number of parameters is to large for a clear illustration within a surface plot, it is exemplary depicted for the selected configuration where K equals L.

Thus, the derived spring-in angle can be limited to 1.33° for a V_f of 60 %. Regarding non-quasi-orthotropic laminates as $[A_{2K}(B, -B)_M \ C_K]_s$ for example layup dependencies are obtained.

Those findings clearly substantiate that the expectable amount of spring-in is within a small range, at least for the carbon epoxy prepreg materials similar to that one used for this study. In context of a straightforward compensation strategy, those findings are essential, as expectable tool modifications will be within a small range as well even when a significant chemical shrinkage is considered.

4.2 Preliminary Remarks on Experimental Investigations

In order to investigate the influence of part-specific properties such as, for example, part thickness, section radii, laminate layup, a tool geometry is designed enabling the fabrication of L-profile test specimens with different geometrical properties. In order to determine the effect of the tool material, the tool design is fabricated twice, whereat one is made from aluminum, which has a comparably high thermal expansion ($\alpha \approx 24 \text{ ppm/K}$) and one is made from invar, which has a similar thermal expansion as a cured laminate in in-plane direction of $\alpha \approx 2 \text{ ppm/K}$. Figure 4.12 shows both tools and a detailed sketch of the cross section of a single L-profile. As illustrated by Figure 4.12 the tool-shape provides four male radii ($R_{i,m} = 4, 6, 8, 12 \text{ mm}$) and three female radii ($R_{i,f} = 4, 6, 8 \text{ mm}$). However, within this thesis the male-tooling concept is pursued. The geometrical properties of the L-profiles are similar to those used by Kleineberg [13]. The specimens are equal-sided, whereat the side length is L = 40 mm. A picture of tools and specimens is given in Figure 4.12.



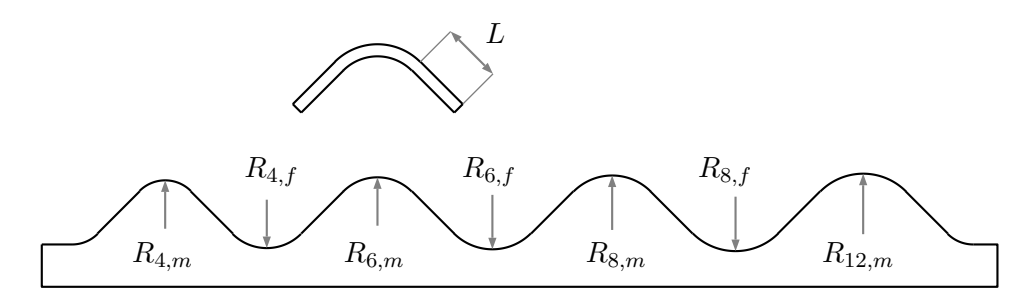


Fig. 4.12: Cross section of the utilized angle-tools

According to previous experience, specimens show slight batch-to-batch variations in geometrical deviations when they are fabricated at different dates although the cure cycle is nominally identical. In order to blank out this variability, the tool is designed that way that at least four specimens of each configuration R_i are fabricated simultaneously. Thus, it can be assumed that each prepared specimen experiences exactly the same environmental condition during processing. Due to the small size of the tool, effects due to inhomogeneous heat conduction are disregarded.

Specimen Manufacturing

Composite manufacturing provides a wealth of more or less different procedures. As the chosen process cycle as well as the utilized consumables, such as bleeder a peel-ply for example, might affect the resulting part shape as outlined by Radford et al. [41], all specimens investigated within this thesis are fabricated with respect to a single processing instruction similar to the MRCC given in [75]. If the manufacturing process deviates from the MRCC, it is clearly announced within this thesis. Thus it is achieved that measured spring-in angles are without a certain contribution due to varying bagging or process conditions.

Figure 4.13 shows the principal bagging assembly, which is used for all specimens.

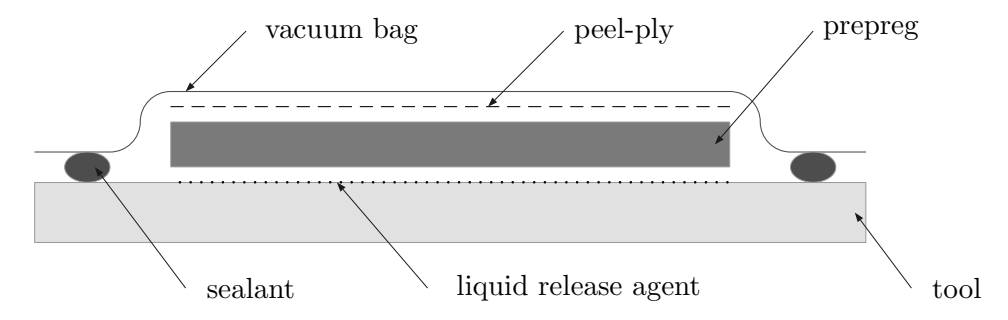


Fig. 4.13: Vacuum bagging arrangement utilized for all specimens investigated in this thesis

First, the tool surface is thoroughly cleaned (two times) with acetone in order to remove grease deposits from handling. Subsequently, liquid release agent Chem-Trend Chemlease® is applied three times in order to achieve preferably constant surface properties for all specimens. Prior to the first manufacturing tests, liquid release agent has been applied to the tool and subsequently oven dried for multiple hours at a temperature of approximately 180°C. Thus, a certain starting configuration is generated, whereat a thin layer of release agent stays on the tool surface even after the use of cleaning agents. The prepreg is applied ply by ply, whereat after each ply it is consolidated with a hand roller. On top of the laminate a peel-ply is applied to absorb excess resin and to allow homogeneous vacuum suction. The bagging is completed by a vacuum bag which is sealed with tacky-tape at the boundaries.

Measurement Procedure and Uncertainty

The measurement of the fabrication induced deviations is performed with a high resolution full-field ATOS measurement system. Since parts are fabricated with a single-sided mold concept the tool-sided surfaces are used for sake of inspection. As the ATOS system works best when reflection-free surfaces are inspected, the measurement-relevant surfaces are sprayed with an appropriate contrast medium which is provided by GOM. Thus, undesired reflections which falsify the measurement are eliminated. The thickness of the very thin sprayed contrast-medium layer is assumed to have no adulterating effect since it is applied homogeneously. An ATOS scan gives a high density point-cloud, whereat the density depends on the camera resolution and the used measuring-field size. For the L-profiles investigated in this thesis a point-density of approximately $0.35 \, \text{pt}/mm^2$ is achieved.

As aforementioned, the spring-in is defined as the angle change $\Delta \varphi$ of a section with a nominal angle $\tilde{\varphi}$ induced by manufacturing effects. Thus, the orientation of the L-profile's flanges is an appropriate measurand. In order to transfer the geometrical information of the point-cloud into a corresponding spring-in angle, a local area of the point-cloud is selected at each flange of the profile. Based on all selected points a best-fit plane is derived for each profile leg. Subsequently, the spring-in angle is derived as the angle between the two plane-normals. Figure 4.14 illustrates

that schematically.

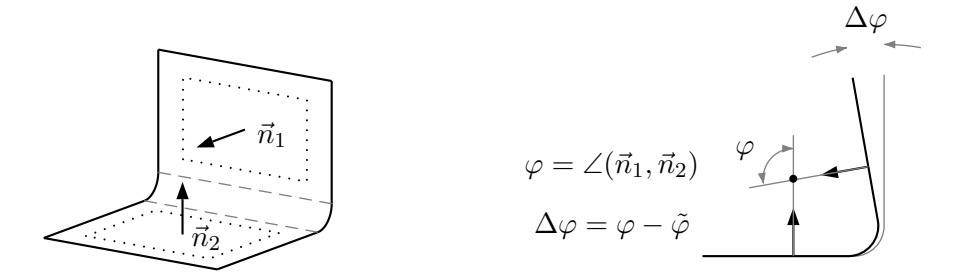


Fig. 4.14: Angle measurement using best-fit planes generated from ATOS point-cloud. Nominal angle is $\tilde{\varphi}$

As indicated in Figure 4.14 the orientation of a calculated best-fit plane is directly dependent on the selected points. Each point-cloud of a measured test-specimen is unique and therefore a automated geometrical inspection has not been possible. Thus, the area for the best-fit plane generation is selected manually. In order to reduce adulteration, boundary areas and the transition zone for the single-curved radius area to the flange area is excluded for the plane calculation as indicated by the dotted plane boundaries in Figure 4.14. Nevertheless, that manual work-step is accompanied by an uncertainty which needs to be regarded within the evaluation. In order to quantify the magnitude of that uncertainty, the spring-in angle has been measured fifteen times (n = 15), whereat each calculation is based on a new generated set of best-fit planes. The obtained measurement uncertainty is 0.02° . As this measurement uncertainty is significantly smaller than the obtained part-specific scattering it is disregarded in the following.



Fig. 4.15: Measured L-profile point cloud with constructed best-fit planes and angle measurement

Within the following sections, the measurement results are illustrated, whereat the ordinate values are given by the average spring-in angles and the corresponding standard deviations. In Section 4.4 the geometrical scattering of fabricated L-profiles is discussed in detail.

Therein, the average values \bar{x} and the standard deviations s_x are calculated with the following

equations given by Row [87].

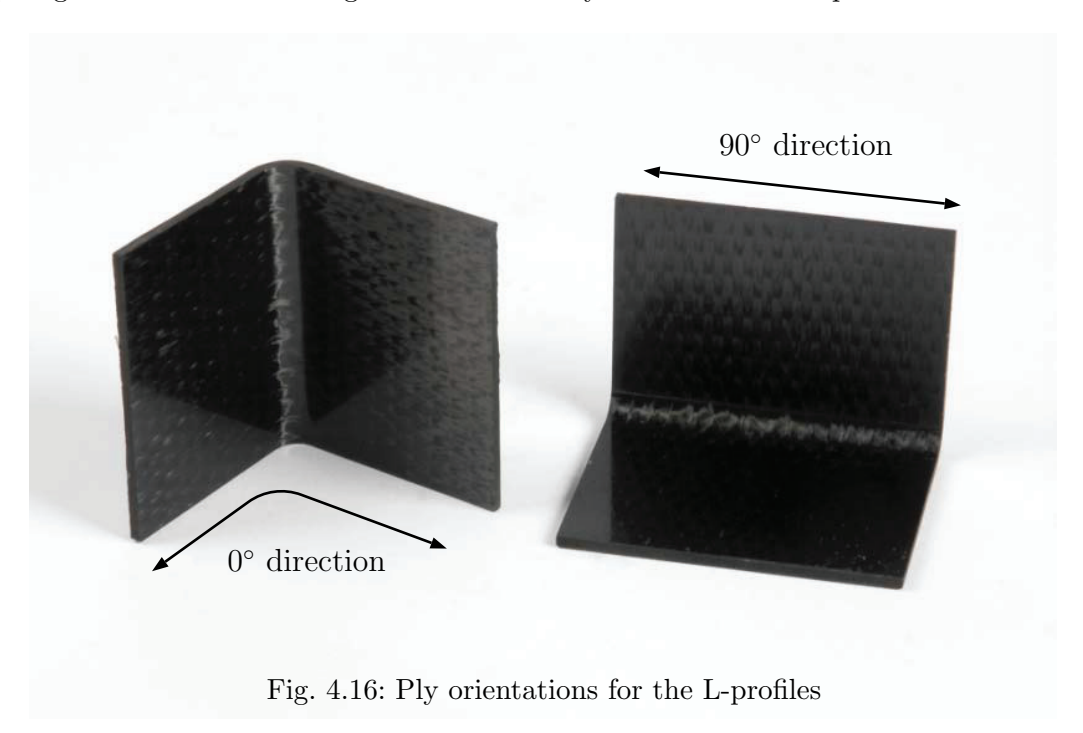
$$\bar{x} = \frac{1}{n} \sum_{k=1}^{n} x_k$$
 , $s_x = \sqrt{\frac{1}{n-1} \sum_{k=1}^{n} (x_k - \bar{x})^2}$ (4.14)

4.3 Experimental Investigation on Spring-in Affecting Parameters

Composite manufacturing is sensitive to environmental effects, since the composite characteristic properties arise during the manufacturing process. Beside that, a variety of part specific parameters influence the manifestation of process-induced distortions. Those are:

- 1. Part thickness
- 2. Section radius
- 3. Laminate layup
- 4. Tool material
- 5. Tool surface roughness
- 6. Process cycle
- 7. Prepreg material selection

Therefore, the following issues are investigated by experimental means, in order to work out the main drivers, respectively the essential parameters of occurring spring-in deformations. The idea is to quantify the single contributions and to gain substantiated knowledge of the origins which can be purposeful used for the model derivation in Section 6. As the ply-by-ply composition of common laminates allows a target oriented adaptation of mechanical properties according to given loads on the one hand, the multitude of conceivable layups makes it hard to develop general statements about the main drivers on the other hand. Thus, a statement according to the thickness dependency of the spring-in effect can only be formulated with respect to a certain layup. Figure 4.16 contains the global coordinate system used for all specimens in this section.



Regarding a symmetric eight-ply laminate for example, wherein ply orientations are limited to 45° , -45° , 90° and 0° , $4^{4} = 256$ different layups are possible. As this multitude of different layups

cannot be investigated entirely, it is focused on selected layups in this section. Nevertheless, a certain transferability between different laminates is given for quasi orthotropic laminates as outlined in Section 4.1.

Spring-in - A Function of Part Thickness?

An effect of part thickness is only evident for layups consisting of one fiber direction only. Thus, unidirectional four and eight-ply layups are fabricated from 8552/AS4 pregreg material. This is done on the available aluminum and invar tools. Each set consists of four specimens with four different radii. Tool cross section and bagging arrangement are given in Figure 4.12 and Figure 4.13, respectively. Note that the four-ply specimens with the radius of 8 mm are not listed, due to a problem during the manufacturing process. Thus, Figure 4.17 depicts measurement results of these 60 specimens.

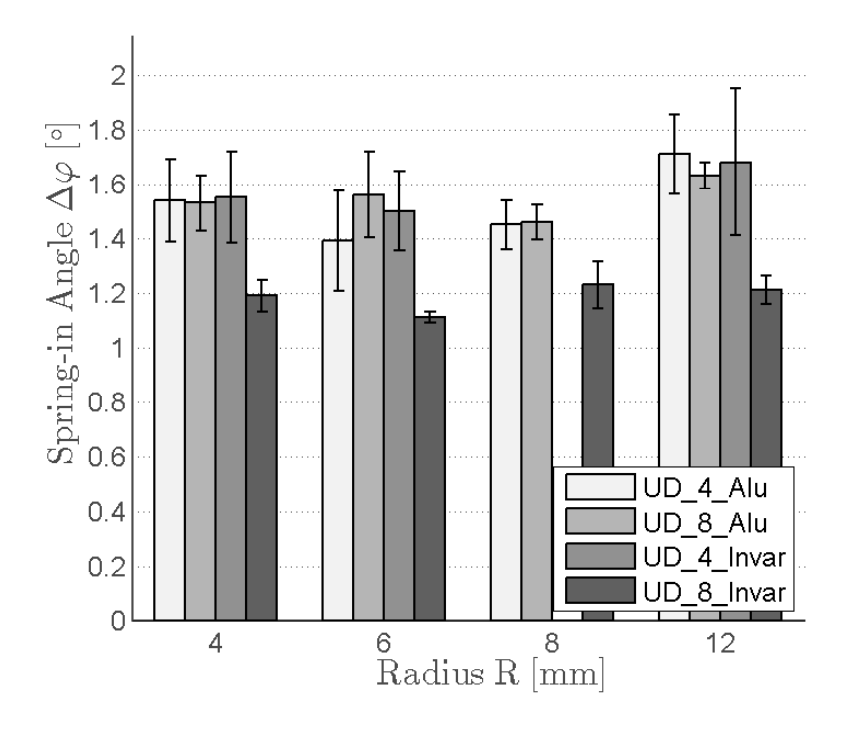


Fig. 4.17: Obtained spring-in angles of unidirectional laminates fabricated on aluminum and invar tooling with different radii

These measurements show that whether the tool-radius nor the laminate thickness affects the spring-in angle significantly. However, a slight increase of the spring-in angle is obtained for the R_{12} specimens, what is consistent with experimental findings of Hamamoto [88], who reported a slight increase in spring-in of up to 10 % for increasing radii. Nevertheless, this is contrary to the aforementioned Radford model as this is radius independent.

A comparison of spring-in angles for specimens fabricated on the aluminum and the invar tool reveals striking results. Regarding four-ply laminates, specimens made on invar show comparable spring-in as specimens fabricated on aluminum tooling. This is expected, as spring-in is induced by through-thickness strains and therefore theoretically independent from tool expansion. However, regarding the eight -ply specimens, and in particular those ones made on invar the tool, obtained distortions are approximately 20 % smaller.

This is conspicuous, as it is not consistent for all specimens. In addition, results of the following subsection do not show this difference between specimens made on aluminum and invar. At this point no convincing explanation can be given for the observed behavior. As no experimental

results for carbon-epoxy prepreg L-profiles made on invar are available in the literature the results obtained here cannot be compared to the ones of other researchers. As further experiments conducted in this theses do not substantiate this finding it should be treated with caution. It is recommended to repeat the corresponding experiments in order to verify the results. Nevertheless, the magnitudes of the obtained spring-in angles, even for the R_8 specimens made on invar, are slightly higher than those ones obtained by Fernlund et al. [21] who measured an average value of approximately 1.06°. However, Fernlund uses release film, which impedes the direct comparability between the results. Flanagan [89] for example, obtained an average spring-in angle of three specimens of 1.75° with a considerable large scattering of 14 %.

Spring-in - A Function of Tool Coarseness and Tool Material?

Another set of specimens is fabricated in order to quantify the effect of different tool coarseness. Therefore, half of both tool surfaces is polished by hand until an extremely fine surface is achieved. Coarseness is estimated using a micro-finish comparator to $R_a \approx 0.1 \ \mu m$, whereat the initial condition is about $R_a \approx 0.25 \ \mu m$. That is similar to the 'Initial' configuration obtained for the warpage tool. The following bar plot is based on two specimens of each tool material-coarseness-radii configuration. A quasi-isotropic $[45, -45, 90, 0]_s$ layup is used for all specimens.

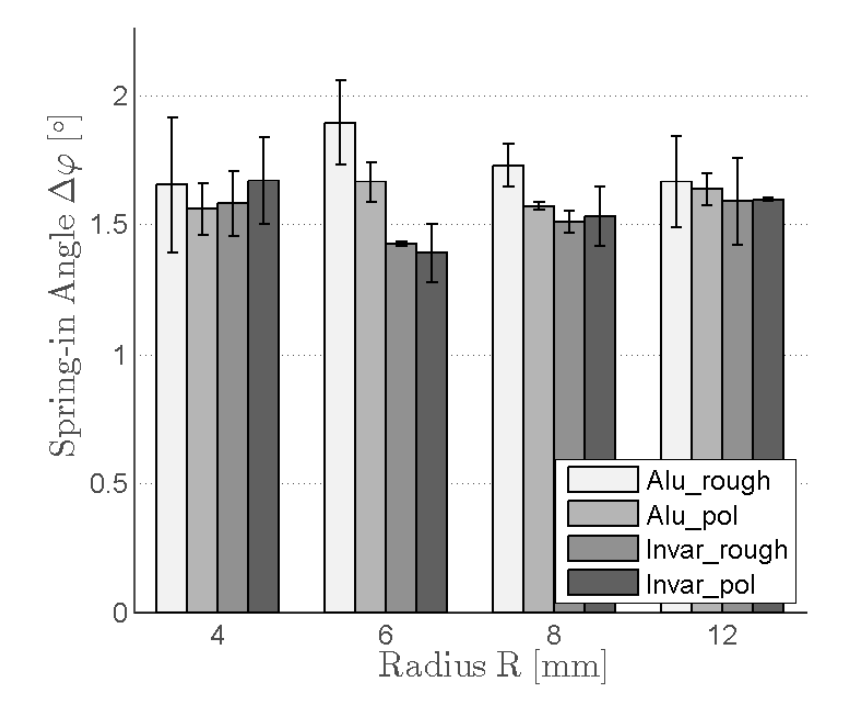


Fig. 4.18: Spring-in angles of a $[45, -45, 90, 0]_s$ layup fabricated on different tooling materials for two different tool surface coarsenesses

Contrary to the findings of the experimental warpage investigations, tool surface properties have no significant effect on the developing spring-in angles. It is conspicuous that scattering is smaller than for the unidirectional specimens, although only two specimens of each configuration are manufactured. That might be due to a reduced fiber washing tendency (ASTM - 5687) of the multi-angle laminates compared to the UD laminates. Although the R_6 specimens fabricated on aluminum tend to show larger deformations, a clear effect cannot be developed from the experimental findings. These findings indicate that the tool surface roughness does not effect the development of spring-in angles significantly as long it is in a common tool-quality range. A slight increase of the average spring-in angle for increasing tool radii is obtained, similar to the

UD laminates discussed above.

Spring-in - Depending on the Prepreg Selection?

As the preceding results are obtained for 8552/AS4 prepreg material, it is an interesting issue if spring-in angles are transferable even when different prepreg systems are used. As shown within the warpage experiments outlined in section 3.4, material selection can affect manufacturing deformations significantly, particularly due to different chemical shrinkage. Within this section, it is experimentally validated whether the spring-in phenomenon is even sensible to changing epoxy-based prepreg systems. Therefore, M21/T800 and M21E/IMA specimens are fabricated and compared to the 8552/AS4 specimens. Selected material properties are given in Table 3.2.

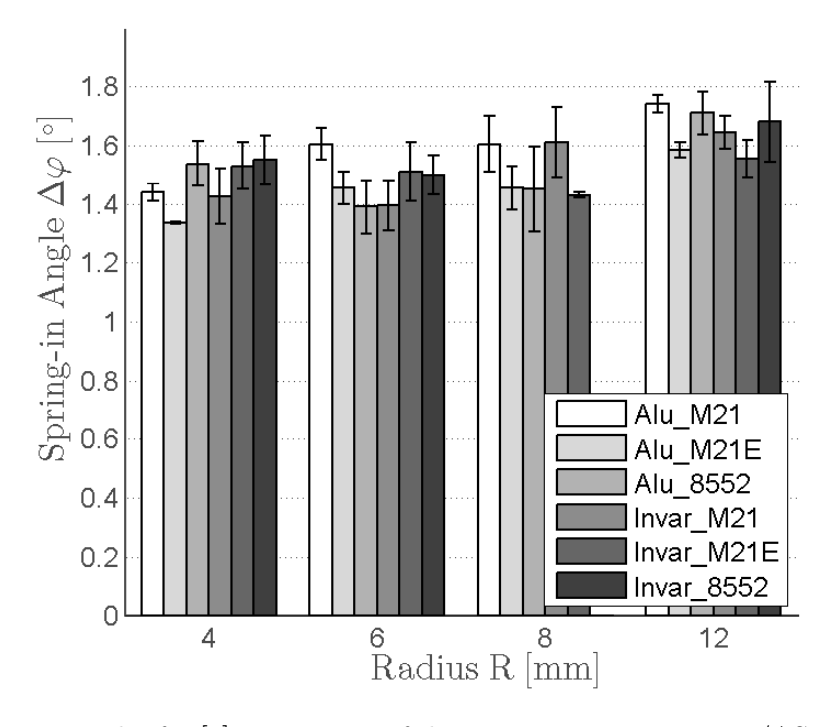


Fig. 4.19: Spring-in angles for $[0]_4$ specimens of three prepreg systems 8552/AS4, M21/T800 and M21E/IMA

The dependency from the prepreg material, obtained in the warpage investigation, cannot be obtained for the spring-in phenomenon. Neither clear differences between the single materials nor a consistent tendency can be derived from the experimental results. Only the slight increase of the spring-in angle for the increased tool radius is consistent to the findings presented above. Although characteristics of the M21 process are completely different compared to the 8552 cycle, as it has only one dwell phase at 180°C (ref. [76]), obtained deformations are in the same range for all three materials investigated here. The findings of the preliminary numerical investigations given in Section 4.1 indicate that thermal expansion as well as chemical shrinkage of the M21 resin must be similar to the 8552 resin. Although it is not further investigated in this thesis, the later introduced extended Radford approach should be a suitable experimental approach to verify that assumption. In summary it should be said that the magnitudes of the spring-in angles are comparable between the prepreg systems at hand, although cure cycles differ significantly. That offers a certain potential in context of a straightforward simulation strategy, as experimental results may be transferred from one material to another. This would be conceivable particularly in a preliminary spring-in estimation, as the deviations between the single materials are approximately 20 %. However, this demands additional statistical investigation.

At least in context of a preliminary spring-in estimation that would be conceivable, as the deviations between the material are approximately 20 %.

Spring-in - Is it Process-Cycle Dependent?

Within another set of experiments, 8552/AS4 specimens are fabricated whereat the M21 process cycle is used. That allows the inspection, whether the process cycle characteristics affect the spring-in angles significantly. All specimens have a four-ply UD layup. Specimens fabricated with the regular 8552 MRCC are denoted with the index 'reg' while the index 'proc' denotes specimens fabricated with the M21 cure cycle.

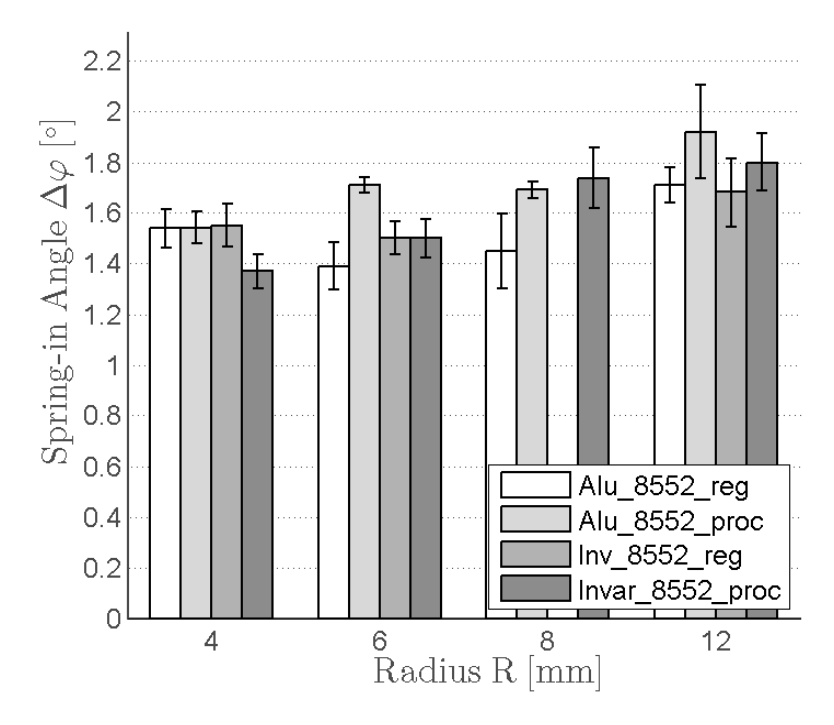


Fig. 4.20: Spring-in angles for $[0]_4$ specimens of 8552/AS4 fabricated with the one-dwell-phase M21 process cycle

Although it is not completely consistent for all radii configurations, specimens fabricated with the M21 one dwell-stage cure cycle tend to show slightly increased spring-in angles. However, for the R_4 configuration it remains almost constant. Scattering is comparable between the single configurations. Nevertheless, the statistical confidence is weak. Therefore, additional experiments are recommended to verify these tendencies.

Spring-In Deformations of multiple UD and Multi-Angle Layups

For sake of comparison, Figure 4.21 gives a comprehensive outline of spring-in angles for various layup configurations. Therein, seven configurations are fabricated on the aluminum tool and five are fabricated on the invar tool. The former are denoted as C_{Ai} and the latter are denoted with C_{Ii} . The corresponding layups are given in Table 4.3.

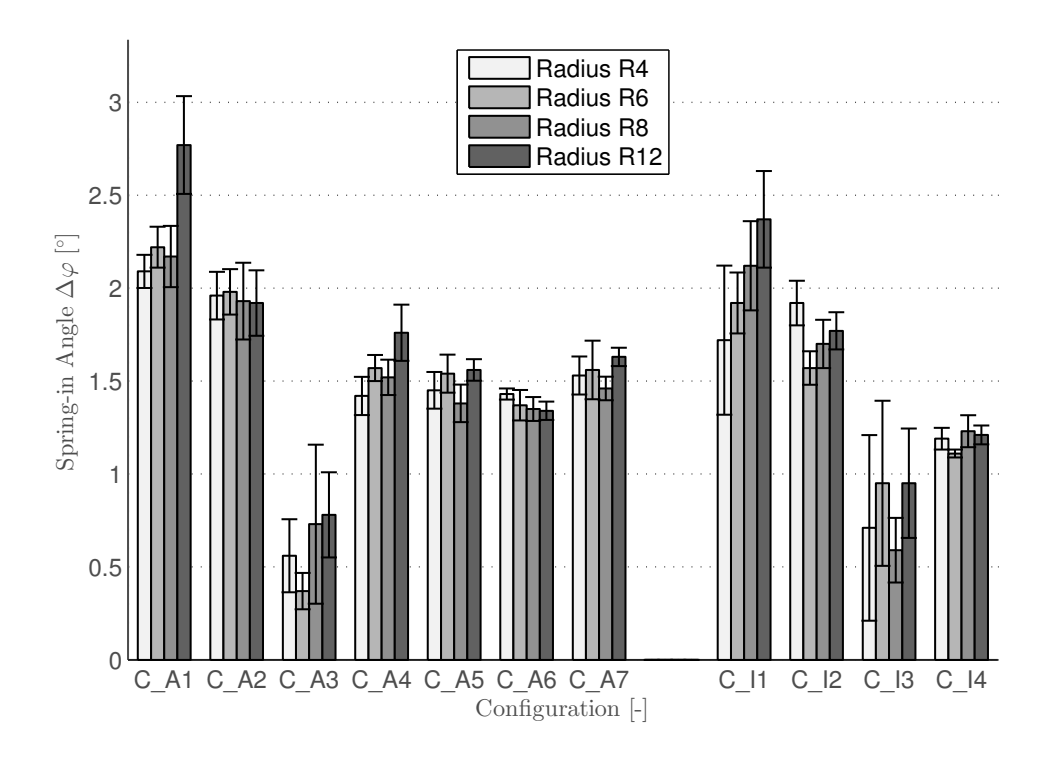


Fig. 4.21: Spring-in deformations for different configurations. Corresponding layups are listed in table 4.3

Results depicted in Figure 4.21 allow a few conclusions. Laminates with a $[45, -45]_s$ layup show larger spring-in distortions compared to the other layups. Thus, the average spring-in angles for the specimens manufactured on aluminum and invar are $\overline{\Delta\varphi}_{C_{A1}} = 2.28^{\circ}$ and $\overline{\Delta\varphi}_{C_{I1}} = 2.05^{\circ}$. High standard deviations of $s_{C_{A1}} = \pm 0.29^{\circ}$ and $s_{C_{I1}} = \pm 0.34^{\circ}$ are observed. This large scattering is likely layup-induced as no fibers are aligned in circumferential direction of the profiles. When touching these specimens, their low mechanical stiffness is striking. Therefrom it is concluded that these specimens are extraordinary sensitive to ply misalignment inducing twist or a certain asymmetry in the layup. Nevertheless, this layup is selected for the verification of the tool compensation idea as it shows the largest average spring-in angle. This is content of Section 7.3.

Similar results are obtained for the 90° specimens. The specimens show a certain spring-in angle although this is contrary to the Radford theory presented in the preceding. A possible explanation for this behavior represents the forced-interaction effect which is discussed in Chapter 5. This effect introduces a stress gradient into the resin at the tool side of the specimens analogous to the warpage principle.

As no load-carrying plies are oriented in circumferential directions, this slight gradient is able to deform the part. However, the stiffness of the specimens is negligible. Specimens of preliminary experiments are already damaged during the demolding process and the removal of the peel ply.

Configuration	Layup	Tool-material
C_{A1}	$[45, -45]_s$	Aluminum
C_{A2}	$[0, 90]_s$	Aluminum
C_{A3}	$[90]_4$	Aluminum
C_{A4}	$[45, -45, 90, 0]_s$	Aluminum
C_{A5}	$[45, -45, 0, 90, 0]_s$	Aluminum
C_{A6}	$[45, -45, 0_2, 90, 0_3]_s$	Aluminum
C_{A7}	$[0]_{8}$	Aluminum
C_{I1}	$[45, -45]_s$	Invar
C_{I2}	$[0, 90]_s$	Invar
C_{I3}	$[90]_4$	Invar
C_{I4}	$[0]_{8}$	Invar

Tab. 4.3: L-profile layup configurations depicted in Figure 4.21

Cross-ply laminates with a $[0, 90]_s$ layup shows a deviating average distortion of $\overline{\Delta \varphi}_{C_{A2}} = 1.95^{\circ}$ for the aluminum configuration and $\overline{\Delta \varphi}_{C_{I2}} = 1.73^{\circ}$ for the invar configuration. Scattering for both configurations is in the same range of $\pm 0.15^{\circ}$.

A comparison of the remaining laminates shows that expectable spring-in angles are in narrow tolerances. In particular, the results of C_{A4} , C_{A5} and C_{A6} are almost identical although the layups are different.

4.4 Statistical Analysis on obtained Spring-in Angles

This section contains a statistical analysis of the experimentally obtained spring-in angles of the preceding section. The main aim of this study is to characterize the spring-in effect in terms of probability. A total of 289 different, prepreg-made L-profile specimens are considered as the basis. Specimens are sub-divided into distinct groups and averages as well standard deviations for each group are derived and evaluated.

Table 4.4 shows the investigated configurations and their assignment to the groups All, With θ° , Multiangle, UD, $\theta/90$ and \pm 45, respectively. The underlying group definition is based on essential findings of the preceding section as the spring-in angle is independent from tool radius and tool material for example. Therefore, the groups investigated here do not distinguish between different prepreg materials or different tool conditions. As an exception, the spring-in angle of a single layup fabricated with three different prepreg materials is compared at the end of this section.

Table 4.4 shows the regarded configurations and the assignment to the aforementioned groups.

Config.	Layup	All	With 0°	UD	Multiangle	0/90	±45	90°
	$[0]_4$	√	√	✓				
	$[0]_{8}$	\checkmark	\checkmark	\checkmark				
	$[90]_4$	\checkmark						\checkmark
8552/AS4	$[45, -45, 90, 0]_s$	\checkmark	\checkmark		\checkmark			
Aluminum	[0] ₄ *	\checkmark	\checkmark	\checkmark				
	$[0, 90]_s$	\checkmark	\checkmark			\checkmark		
	$[45, -45]_s$	\checkmark					\checkmark	
	$[45, -45, 0_2, 90, 0_3]_s$	\checkmark	\checkmark		\checkmark			
	$[45, -45, 0, 90, 0]_s$	\checkmark	\checkmark		\checkmark			
	$[0]_4$	✓	\checkmark	\checkmark				
	$[0]_{8}$	\checkmark	\checkmark	\checkmark				
8552/AS4	$[90]_4$	\checkmark						\checkmark
Invar (Ni36)	$[0]_4^*$	\checkmark	\checkmark	\checkmark				
	$[0, 90]_s$	\checkmark	\checkmark			\checkmark		
	$[45, -45]_s$	✓					✓	
M21/T800	$[0]_4$	✓	\checkmark	\checkmark				
Aluminum	[0]4	,	,					
M21/T800	$[0]_4$	\checkmark	\checkmark	\checkmark				
Invar (Ni36)	[0]4		•					
M21E/IMA	$[0]_4$	✓	\checkmark	\checkmark				
Aluminum	[~]4	•	•					
M21E/IMA	$[0]_4$	\checkmark	\checkmark	\checkmark				
Invar (Ni36)	[0]4	<u> </u>	<u> </u>	•				
8552/AS4	$[45, -45, 90, 0]_s$	\checkmark	\checkmark		\checkmark			
Alu. rough	[-0, -0,00,0]8		<u> </u>		·			
8552/AS4	$[45, -45, 90, 0]_s$	\checkmark	\checkmark		\checkmark			
Alu. pol	[-0, -0,00,0]8				·			
8552/AS4	$[45, -45, 90, 0]_s$	\checkmark	\checkmark		\checkmark			
Inv. rough	[- / - / - / -]8	· 			-			
8552/AS4	$[45, -45, 90, 0]_s$	\checkmark	\checkmark		\checkmark			
Inv. pol				100		0.1	0.0	90
\square \squar	nens per group	289	261	122	76	31	30	30

Tab. 4.4: Investigated L-profile configurations assigned to specific groups. Specimens marked with * are fabricated using the M21E/IMA process

A histogram is derived to investigate whether the measured data can be described by a normal (gaussian) distribution. Therefore, the area of obtained spring-in angles $0.13^{\circ} \leq \Delta \varphi \leq 3.07^{\circ}$ is divided into ten intervals. Measured results are assigned to these intervals. Figure 4.22 shows their relative frequency of occurrence and a corresponding scaled normal distribution derived based on the average obtained spring-in angle for the group All $\overline{\Delta \varphi} = 1.55^{\circ}$ and its standard deviation $s_{\Delta\varphi} = 0.40^{\circ}$. Note that this procedure is contrary to the original idea of a normal distribution as not all specimens of the regarded population have one identical expected springin angle. Moreover, the statistical analysis for each configuration is not meaningful as for some configurations only two specimens are fabricated. Nevertheless, the approach is used in order to outline group specific tendencies and to show differences.

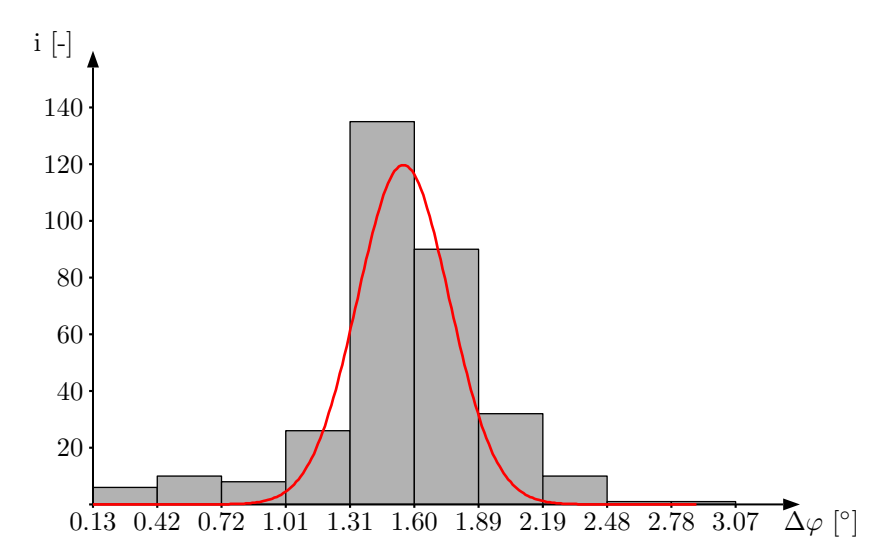


Fig. 4.22: Histogram for all fabricated specimens with corresponding normal distribution

A comparison between the obtained histogram and the normal distribution suggests that the measured spring-in data can be described with this kind of distribution. However, this is checked by a second analysis wherein the group $With \ 0^{\circ}$ is considered. This is due to the reason as the group All contains $[45, -45]_s$ and $[90]_4$ specimens. When evaluating the spring-in angles of these configurations shown in Figure 4.21 the massive scattering and variability indicated by the large standard deviations is conspicuous. When deriving the coefficient of variability CV = deviation/mean values up to 0.7 are obtained especially for the $[90]_4$ specimens what clearly indicates the lack of reproducibility. Therefore, these configurations are excluded for the following cases.

Figure 4.23 shows the derived histogram, whereat the area of magnitude of the spring-in angles reduces to $1.09^{\circ} < \Delta \varphi < 2.23^{\circ}$. The corresponding normal distribution derived from $\overline{\Delta \varphi} = 1.57^{\circ}$ and its standard deviation $s_{\Delta \varphi} = 0.22^{\circ}$ substantiates that the measured data can be described with the normal distribution.

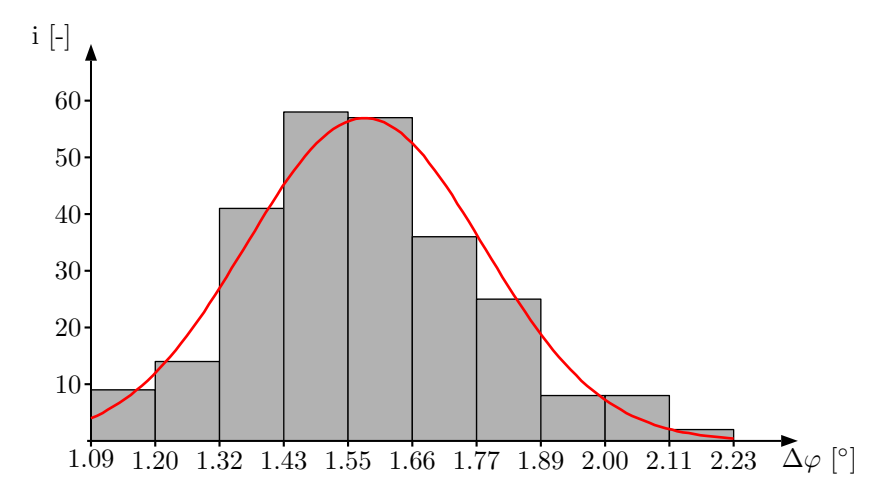


Fig. 4.23: Histogram for specimens of the group With 0° and corresponding scaled normal distribution

However, for the sake of verification a Q-Q plot for both groups is given in Figure 4.24. Within this Q-Q plot predictions z(p) and measurements $\Delta \varphi(p)$. The obtained plots show asymptotic behavior to the angle bisector what clearly substantiates the presumption that the measured

results are gaussian distributed. Consequently, this kind of function is used in the following for the characterization of the group-specific spring-in results.

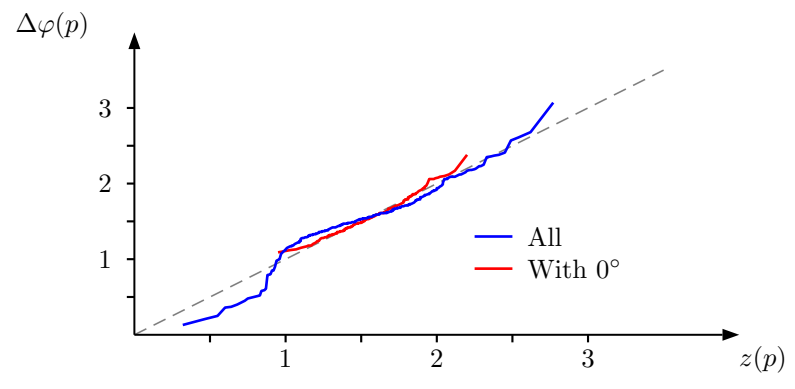


Fig. 4.24: QQ-plot for All and With θ° configuration

Group-Specific Spring-in Characterization

The comparison between a group-specific normal distribution and one of all experimental results allows a quantitative evaluation in terms of the group-mean value and its standard deviation. The normal distribution is given by Equation 4.15, where $\overline{\Delta \varphi}$ and $s_{\Delta \varphi}$ are the group-specific mean value and the group-specific standard deviation.

$$N\left(\Delta\varphi; \overline{\Delta\varphi}, s_{\Delta\varphi}\right) = \frac{1}{s_{\Delta\varphi}\sqrt{2\pi}} \cdot e^{-\frac{1}{2}\left(\frac{\Delta\varphi - \overline{\Delta\varphi}}{s_{\Delta\varphi}}\right)^2}$$
(4.15)

The All group shows a comparatively large standard deviation of $s_{\Delta\varphi} = 0.40^{\circ}$ which is approximately 28 % of the measured mean value. Group With θ° shows a comparable mean value while the standard deviation is only 14 %.

As aforementioned this effect is induced by the $[45, -45]_s$ and the $[90]_4$ layups. Figure 4.25 shows the specific normal distributions for these groups. The comparably wide shape of the bell function indicates a large standard deviation for $[45, -45]_s$ and the $[90]_4$ group.

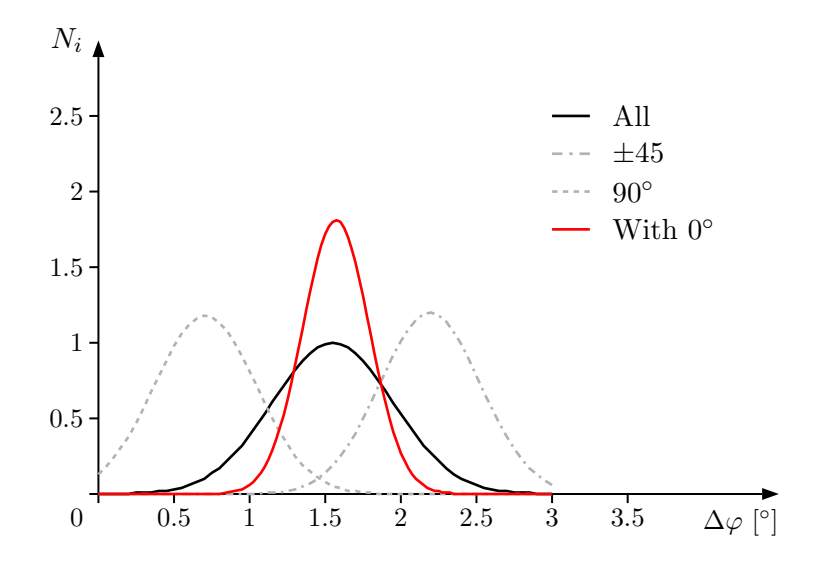


Fig. 4.25: Differences between normal distribution of the All and the With θ° group are due to the consideration of $[45, -45]_s$ and $[90]_4$ layups

Table 4.5 contains the obtained average spring-in angles $\overline{\Delta\varphi}$ and the corresponding standard deviations $s_{\Delta\varphi}$ for all investigated groups. In addition, three intervals with a probabilty P_i of 68.3 %, 95.5 % and 99.7 % are derived according to Equation 4.16.

$$P_{i}(\overline{\Delta\varphi} - i \cdot s_{\Delta\varphi} < \Delta\varphi < \overline{\Delta\varphi} + i \cdot s_{\Delta\varphi}) = \begin{cases} 68.3\% & \text{for } i = 1\\ 95.5\% & \text{for } i = 2\\ 99.7\% & \text{for } i = 3 \end{cases}$$

$$(4.16)$$

These intervals are derived based on Equation 4.17 taken from [90].

$$P_i\left(|\Delta\varphi - \overline{\Delta\varphi}| < i \cdot s_{\Delta\varphi}\right) = \int_{\overline{\Delta\varphi} - i \cdot \Delta\varphi}^{\overline{\Delta\varphi} + i \cdot \Delta\varphi} N\left(\Delta\varphi; \overline{\Delta\varphi}, i \cdot s_{\Delta\varphi}\right) d\Delta\varphi \tag{4.17}$$

Groupname	Specimens	$\overline{\Delta \varphi}$ [°]	$s_{\Delta \varphi} \ [^{\circ}]$	$P_1 = 68.3 \%$	$P_2 = 95.5 \%$	$P_3 = 99.7 \%$
All	289	1.55	0.40	1.15 - 1.95	0.75 - 2.35	0.35 - 2.75
With 0°	229	1.57	0.22	1.35 - 1.79	1.13 - 2.01	0.91 - 2.23
UD	122	1.53	0.22	1.32 - 1.75	1.10 - 1.96	0.89 - 2.18
Multiangle	76	1.53	0.16	1.37 - 1.69	1.21 - 1.84	1.06 - 2.00
0/90	31	1.83	0.19	1.65 - 2.02	1.46 - 2.21	1.27 - 2.40
± 45	30	2.19	0.33	1.86 - 2.53	1.53 - 2.86	1.19 - 3.19
90°	30	0.71	0.34	0.37 - 1.05	_	_

Tab. 4.5: Group-specific mean values, standard deviations and probability intervals P_i

A comparison between normal distributions of the groups All, $With 0^{\circ}$, UD, Multiangle and 0/90 is given in Figure 4.26. Inspection of the average values shows that 0/90 specimens show a higher mean spring-in, while the standard deviation for all groups is in the range of 0.20°. It is conspicuous that specimens with a 0° ply aligned in circumferential direction show less scattering which results in a higher reproducibility.

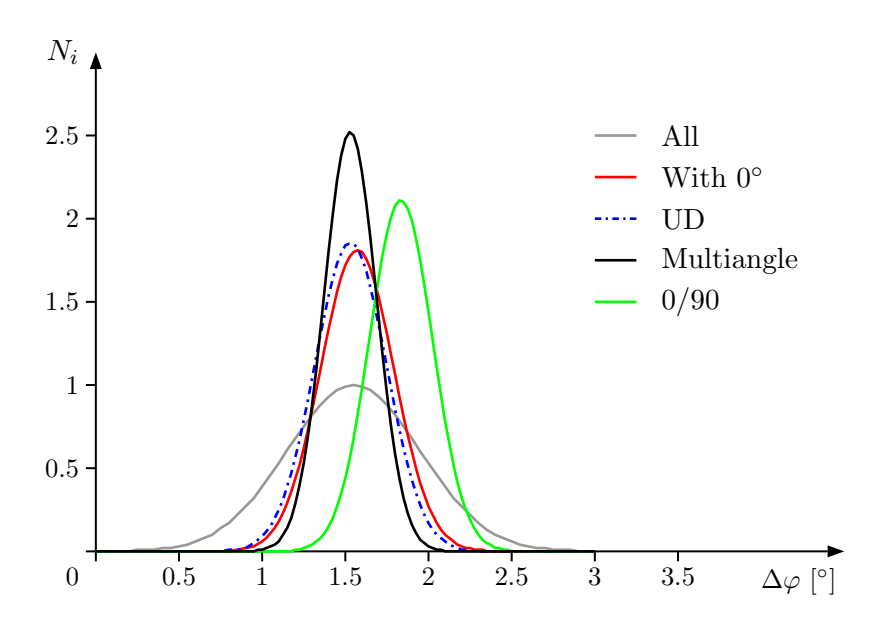


Fig. 4.26: Normal distributions of the groups

One configuration with an unidirectional $[0]_4$ layup is fabricated from three different prepreg materials 8552/AS4, M21/T800 and M21E/IMA. Thus, a direct comparison between the springin angles is done here. As these specimens are a subgroup of the UD group they are separately defined in Table 4.6. The mean values obtained for the three subgroups are very similar between 1.46° and 1.60° while the standard deviations are between 0.09° and 0.20° which is slightly less than obtained for the other groups.

Configuration	Specimens	$\overline{\Delta \varphi}$ [°]	$s_{\Delta\varphi}$ [°]	P = 68.3 %	P = 95.5 %	P = 99.7 %
M21/Inv	8	1.52	0.15	1.37 - 1.67	1.21 - 1.82	1.06 - 1.98
M21/Alu	8	1.60	0.13	1.47 - 1.73	1.34 - 1.86	1.21 - 1.99
M21E/Inv	8	1.51	0.09	1.41 - 1.60	1.32 - 1.69	1.23 - 1.78
M21E/Alu	8	1.46	0.11	1.35 - 1.57	1.24 - 1.67	1.13 - 1.78
8552/Inv	12	1.58	0.20	1.38 - 1.77	1.18 - 1.97	0.99 - 2.16
8552/Alu	16	1.55	0.18	1.38 - 1.73	1.20 - 1.91	1.02 - 2.08

Tab. 4.6: Unidirectional subgroups made from three different prepreg materials on aluminum and invar tools

Figure 4.27 illustrates this graphically. The standard deviation of all subgroups is significantly smaller than that one from the All group which is illustrated as well. This study substantiates the preceding findings as the obtained spring-in angles are almost identical for different prepreg systems. Therefrom it is concluded that neat resin dominated interleaf layers, as they are present for the M21E/IMA laminates, do not have a significant impact on spring-in distortions.

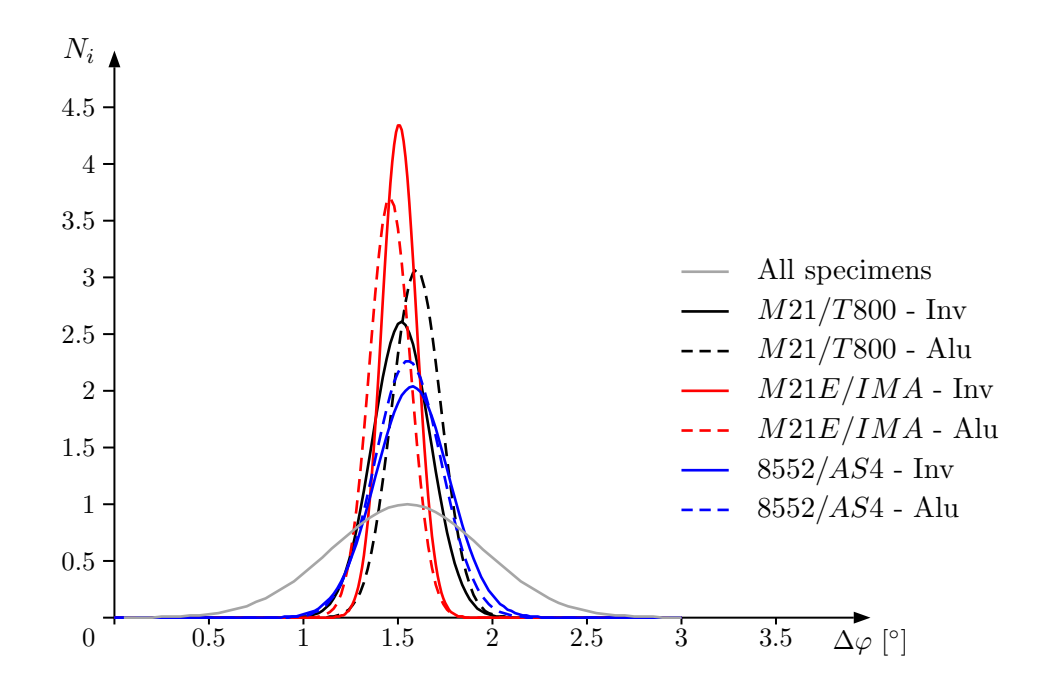


Fig. 4.27: Normal distributions of [0]₄ specimens made from three different prepreg materials manufactured on invar and aluminum tools

Conclusions

The preceding study analyzes the experimentally obtained spring-in angles of the preceding section. It is that the measurement data can be described by a gaussian distribution. The

definition of seven groups is driven by the cognitions of the preceding section. Hence, groups are defined by their layup, disregarding tool material, part-radii and process informations as the spring-in angle is widely independent of these parameters. It is shown that laminates with no plies aligned in circumferential direction, in particular the $[45, -45]_s$ and $[90]_4$ configurations, have significantly deviating mean spring-in values and standard deviations. The mean spring-in angle of all 289 specimens is obtained to 1.55° . This magnitude turned out to be representative even for different prepreg materials. However, the $\theta/9\theta$ configuration show a higher average spring-in angle of 1.83° which is likely induced due to the missing transverse stiffness of the 90° plies. Overall, when regarding the widely representative With θ group, a standard deviation of 0.22° is obtained which is approximately 14 % of the total spring-in average. Results of smaller subgroups which contains only one material show standard deviations starting from of 0.09° which is approximately 6 % of the group-specific average angle. When regarding specimen sets of one specific radius and one prepreg material, standard deviations of less than $\pm 0.05^{\circ}$ are realistic. The relevance of the obtained scattering is exemplary investigated for a CFRP box structure in Section 7.8.

4.5 Extended Radford Approach

According to the hypothesis of this thesis distortions obtained on L-profile level are a suitable parameter for a straightforward simulation approach. Nevertheless, L-profile manufacturing is a hurdle. In this section it is investigated whether a very simple measurement technique can be used as an alternative parameter source. The main reason for this study is the aim to reduce necessary costs for the parameter derivation to a minimum. The fundamental idea of the experimental technique based on Radford's [5] approach represented by Equation 4.18. The character of the experimental technique is developed based on essential findings of the preliminary numerical study on spring-in given in Section 4.1, as will be shown in the following.

$$\Delta \varphi_i = \frac{\varepsilon_{Ti} - \varepsilon_{Ri}}{1 + \varepsilon_{Ri}} \cdot \varphi_0 \tag{4.18}$$

Therein the index i represents thermal, moisture and chemical fractions, while the entire spring-in angle is given by the sum of the single fractions $\Delta \varphi = \sum_i \Delta \varphi_i$ as shown by Equation 4.8. Regarding a unidirectional prepreg ply, certain direction dependent properties are present as the material is transversal isotropic. Figure 4.28 elucidates that schematically. The fiber direction is characterized by high fiber modulus E_1 , very small thermal expansion α_1 , very small moisture sensitivity β_1 and very small elongation due to chemical shrinkage ξ_i . That is based on the assumption that chemical shrinkage acts mainly in the transverse plane as no constraints by the fibers are present, similar to the thermal expansion. A detailed derivation of that assumption is given in Section D of the appendix.

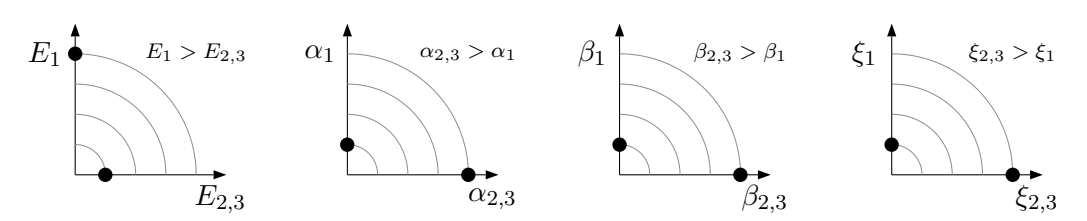


Fig. 4.28: Unidirectional ply properties schematically

When regarding a non-unidirectional laminate such as $[0,90]_s$ for example, the characteristic properties change, whereat properties in thickness direction differ significantly from the properties in laminate-plane directions. Figure 4.29 shows that schematically.

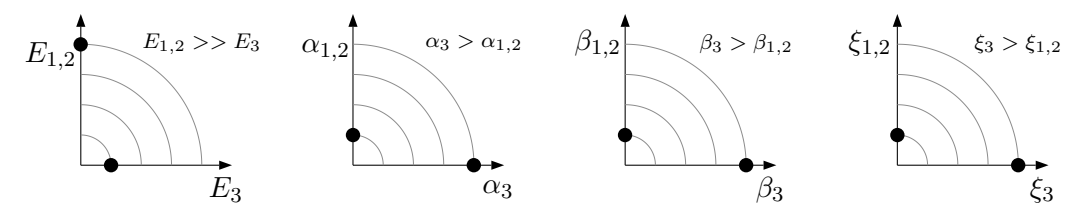


Fig. 4.29: $[0, 90]_s$ laminate properties schematically

As the laminate-plane has fiber dominated mechanical properties the expectable thermal expansion for example should be in the same range as that one of the unidirectional ply. Analogous, the laminate thickness direction has a comparable high thermal expansion since it is resin dominated. As a first approach, which has already been applied in the literature, Radford's equation is modified. Often strains in tangential direction are neglected what can become comprehensible when inspecting Figure 4.10 thoroughly. Therein, it is obvious that strain in tangential direction does not significantly contribute to the overall spring-in angle. Within this thesis, a modified expression of the original relation given by Equation 4.18 is used which promises smaller deviations. Therein, the tangential effect is indirectly considered.

General Idea

Regarding micro-mechanics based equations, which correspond to simple rheologic models of parallel and serial acting springs, for the derivation of the expansion property of a unidirectional ply, it becomes obvious that those expansion properties are determined by the fiber stiffness in longitudinal direction $E_{F,L}$, the resin's modulus E_R , the fiber volume fraction V_f , the resin's coefficient of thermal expansion and the thermal expansion of the fiber in its fiber longitudinal $\alpha_{F,L}$ and transversal direction $\alpha_{F,T}$. These parameters are very similar for a variety of different fibers and resins. Consequently, a kind of interaction coefficient ξ is introduced which is a measurand for the laminate's anisotropy. Providing that, equation 4.18 can be modified as shown in equation 4.19.

$$\Delta \varphi_i = \frac{-\varepsilon_{Ri}}{1 + \varepsilon_{Ri}} (1 - \xi) \cdot \varphi_0 \quad \text{with} \quad \xi = \frac{\varepsilon_{Ti}}{\varepsilon_{Ri}}$$
(4.19)

At a first glimpse, this equation solely depends on the radial strain component. However, the ratio ξ still depends on tangential strains. The Ratio ξ can be either derived from thermal or chemical parameters. Here, thermal parameters are used as these are easy to derive using micro mechanics.

Based on the parameters given in Table 4.7 the coefficients of thermal expansion in fiber and transverse direction are derived as a function of the V_f . Therefore, the simple relations given by Schürmann [83] are utilized as a first step. However, it should be noted that more sophisticated micro mechanics based rules of mixtures can be applied alternatively.

Parameter	Value	Source
$\alpha_{F,L}$	-0.9 ppm/K	Anghelescu and Alam [91]
$\alpha_{F,T}$	$7.2~\mathrm{ppm/K}$	Anghelescu and Alam [91]
α_m	45.45 pmm/K	Own measurement
$E_{F,L}$	206.8 GPa	Anghelescu and Alam [91]
E_R	$4.67~\mathrm{GPa}$	Hexcel [75]

Tab. 4.7: Material parameters used for the derivation of ξ

Figure 4.30 depicts the corresponding coefficients of thermal expansion in fiber direction α_{11} and in transverse direction $\alpha_{22,33}$ as a function of the V_f . Furthermore, the ratio ξ is derived.

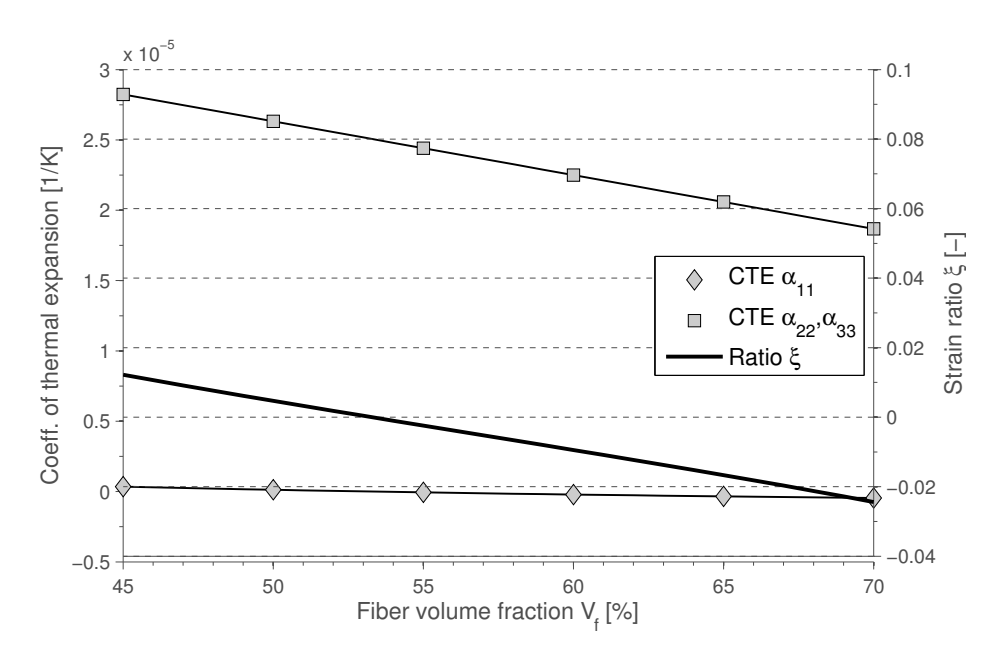


Fig. 4.30: Ratio ξ of longitudinal α_{11} and transversal $\alpha_{22.33}$ properties.

That calculation allows a distinct limitation of the ratio ξ for a realistic range of V_f . For a realistic range of 50 % $\leq V_f \leq$ 70 % the corresponding ratio is 0.005 $\geq \xi \geq$ -0.024. According to equation 4.19, the error due to disregarding tangential properties is quantifiable to -2.4 % up to 0.05 %.

When considering an arbitrary spring-in angle of 1.5°, as it is conceivable for a variety of layups, that corresponds to an error of 0.03° per fraction, which is smaller than a common scattering obtained for the L-profiles presented in Section 4.3.

Based on this verification, the hope is justified that a good prediction of the spring-in behavior can be derived based on the measurement of through the thickness strains during processing. Consequently, an experimental setup is developed to measure the through-thickness strains during manufacturing.

Experimental Setup

A common thermo mechanical analysis (TMA) device is used as it is able to measure strains in thickness direction. Commonly, thermal expansion of consolidated materials is measured using a TMA. As this device is able to provide nearly arbitrary temperature ramps it is used for the curing of prepreg specimens.

In contrast to the prepreg's MRCC no compaction force is applied during the curing. At a first glimpse that limits the suitability of this approach. However, as will be shown in the following, the lack of compaction force affects the obtained through thickness strains only in early stages of the cure cycle as convincingly documented by Garstka et al. [14].

Nevertheless, the missing compaction and its effect on the laminate quality is discussed in this section. In the following it is assumed that chemical shrinkage and thermal expansion after the gelation of the resin, which are responsible for the manufacturing deformations, remain unaffected.

Figure 4.32 shows the utilized specimen exemplary. Several plies of uncured prepreg material are stacked according to the layup at hand. Subsequently, circular specimens are stamped out with a stamping tool and placed between two silica glass disks of a thickness of 0.5 mm. These disks are necessary as they prevent the sensing element from indenting into the laminate. The specimens have a diameter of 5 mm and a thickness of two silica disks plus the inspected layup

specific value. For an eight-ply layup of 8552/AS4 with a nominal ply thickness of 0.125 mm the specimen thickness is 3 mm for example.



Fig. 4.31: Size of the utilized specimens

Although the expansion of those glass disks is very small, it is considered for all conducted measurements. Therefore, a TMA run with two applied silica disks is conducted. The obtained strain curve is subtracted from all other measurements. Thus, the resulting strain plots discussed here are induced by the prepreg material only.

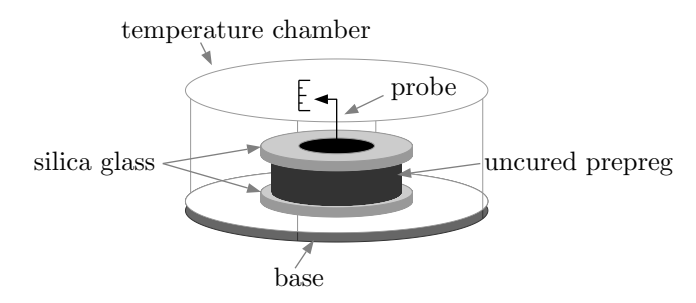


Fig. 4.32: Schematic illustration of the specimen used in the TMA device

Two configurations for the specimen preparation are conceivable. The first one, denoted with 'simple setup', is quiet simple as the layup is simply put between two silica disks. The drawback of this method might be that neat resin can be washed out during process resulting in a bubble-shaped form as indicated in Figure 4.33 (left). Another more improved setup prohibits that, by a small cup depicted in 4.33 (right). This cup and the top-plate are made from aluminum, which again demands the subtraction of a compensation TMA run. The results presented here are gained utilizing the simple setup. Optical inspection of cured specimens reveals no neat resin excess at the sides of the specimens which is likely due to the missing compaction. However, V_f has been determined for the fabricated specimens for sake of verification.

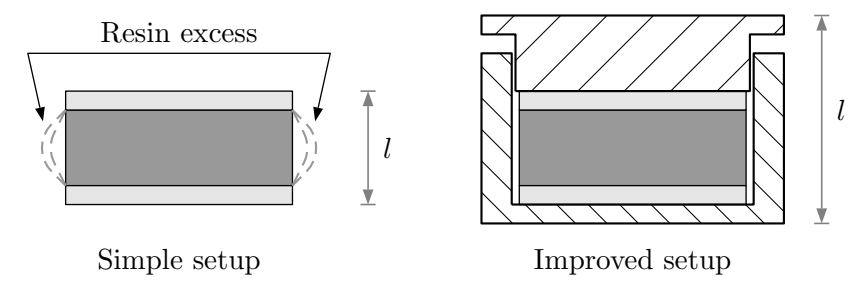


Fig. 4.33: Simple and improved setup of the specimens utilized within the TMA device

The characteristic of the gained strain-graph is depicted in Figure 4.34. This is based on a common two dwell stage cure cycle. Elongation in thickness direction is measured and strain is derived according to $\varepsilon = \Delta l/l_0$. For sake of inspection, the time axis is divided into different sections, whereat each section is related to a certain configuration of the material. That division

is similar to the one proposed by Garstka et al. [14]. Within phase a thermal expansion and

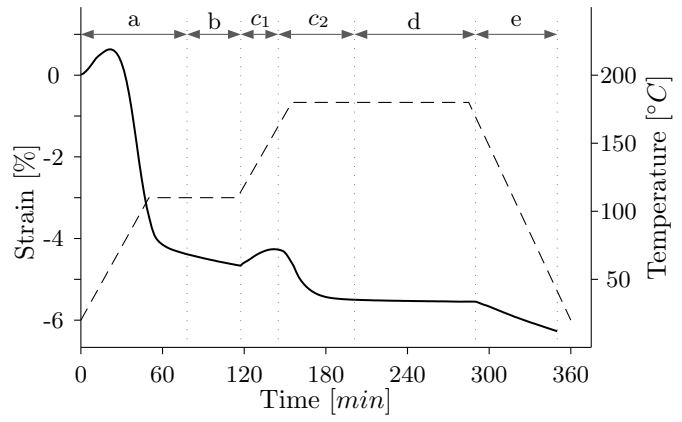


Fig. 4.34: Representative measurement result for a two dwell phase cycle utilizing the TMA based approach

consolidation processes are acting parallel. Phase b is affected by an ongoing consolidation process and small amount of chemical shrinkage as the cross-linking reaction has started slowly. Strains due to thermal expansion are not present as the temperature is constant. Within phase c_1 and c_2 the temperature increases. Thus, effects of thermal expansion are co-acting with chemical shrinkage and consolidation effects. The transition from c_1 to c_2 is equivalent to the gel point of the resin, which has been proven by Garstka with by pull-out tests. The observed instantaneous change in slope at the beginning of stage c_2 is due to cure shrinkage and a significant reduction of the coefficient of thermal expansion which occurs when the resin transforms from liquid to rubbery state. Within stage d the resin is almost completely cured. Due to the constant temperature, the observed strain is related to chemical shrinkage only. Assuming that the resin is cured at the end of stage d, the evaluation of the cool down process gives the final coefficient of thermal expansion of the layup at hand. It should be noted that the transitions from stage a to stage b and from stage c_2 to d do not match to the corresponding changes in the thermal profile. Due to the conducted fragmentation, the evaluation of shrinkage rates during both dwell stages has more relevance as they are approximately linear as transition zones are blanked out.

Influence of the Consolidation Pressure

The approach presented here does not utilize any explicit consolidation pressure. The aim of this approach is to provide a strategy which enables the determination of through-thickness strains. According to Garstka et al. [14] the stages up to the $b-c_1$ transition are dominated by the competing mechanisms of thermal expansion, consolidation and chemical shrinkage. Nevertheless, the resin is in liquid phase up to the gel point. Therefore, differences in obtained strains up to stage c_1 do not affect the magnitude of strains after the gelation, as will be demonstrated in the following.

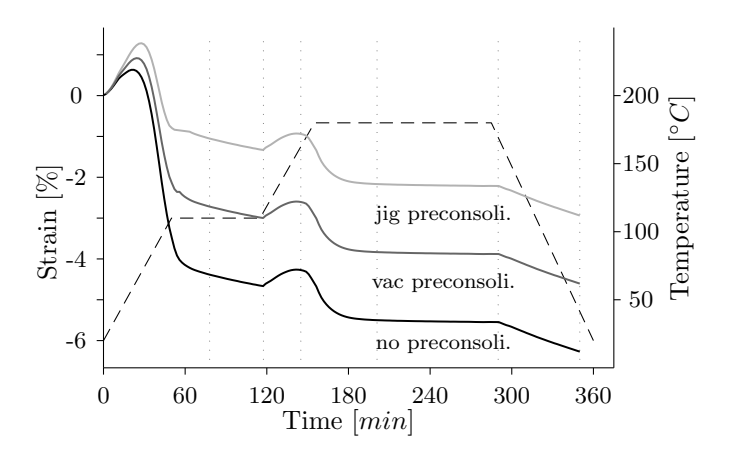


Fig. 4.35: The effect of different pre-consolidation strategies on the measured strains. Redrawn after Garstka et al. [14]

In Figure 4.35 this is illustrated, whereby three different types of consolidation are depicted schematically. Based on the cognition that residual stresses can build up after passing the gelpoint, it is assumed that the effect of pre-consolidation, which occurs in an earlier phase, does not affect the final strain after gelation. Therefore, it is blanked out.

Through-Thickness Strains Obtained for Certain Laminates

Three different laminates are investigated utilizing the proposed technique: $[0]_8$, $[0,90]_{2s}$ and $[45,-45,90,0]_s$. Two specimens are fabricated for the $[0]_8$ layup, whereat four specimens are manufactured for the others. Figure 4.36 compares the average measured strains for the given layups. However, this illustration is limited only to a limited extent as variations of the single measurements due to pre-consolidation effects are considered within the derivation of the averages. Nevertheless, clear differences are obtained for the different laminates.

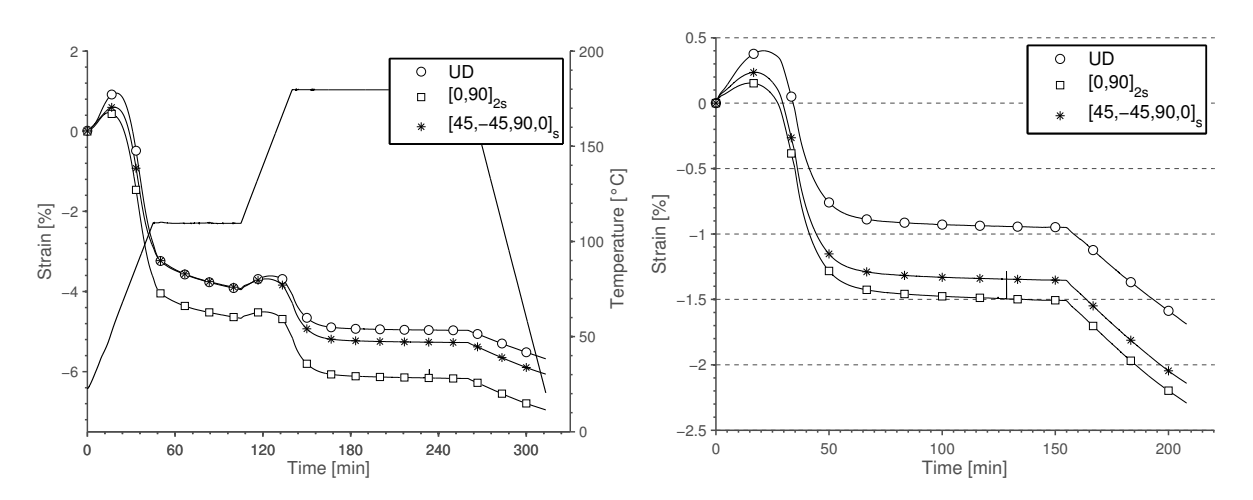


Fig. 4.36: Average strains determined for the layups at hand (left): Zeroed at the start of stage c_1 (right)

When zeroing the obtained curves at the beginning of stage c_1 , which is equal to the start of the second temperature ramp, these differences become more explicit. Figure 4.36 shows that. Nevertheless, the evidence is still rather limited due to the averaging. According to the assumption that the resin is able to transfer stresses when the gel-point is achieved, a zeroing at this point is promising. The gel point is characterized by a significant density increase of the

resin which results in a considerable volume shrinkage as the mass is constant. Regarding the measured curves, this happens shortly after starting the second temperature ramp. Commonly, a linear increase of strain is expected for linear increasing temperature. However, in stage c_1 this linear increase is superposed by the massive chemical shrinkage. This results in a local maximum in the measured strain graph. The comparison of all specimens shows a high reproducibility of this behavior. Therefore, this local maximum is considered as the gel-point although it must be expected that the gel-point is reached slightly earlier. Within the following, all curves are zeroed at this point. The, position of the extrema is calculated based on the measurement data as the differential quotient is equal to zero at this point. Figures 4.37 and 4.38 show the obtained strain measurements for all specimens. Graphs are zeroed at the derived local maximum.

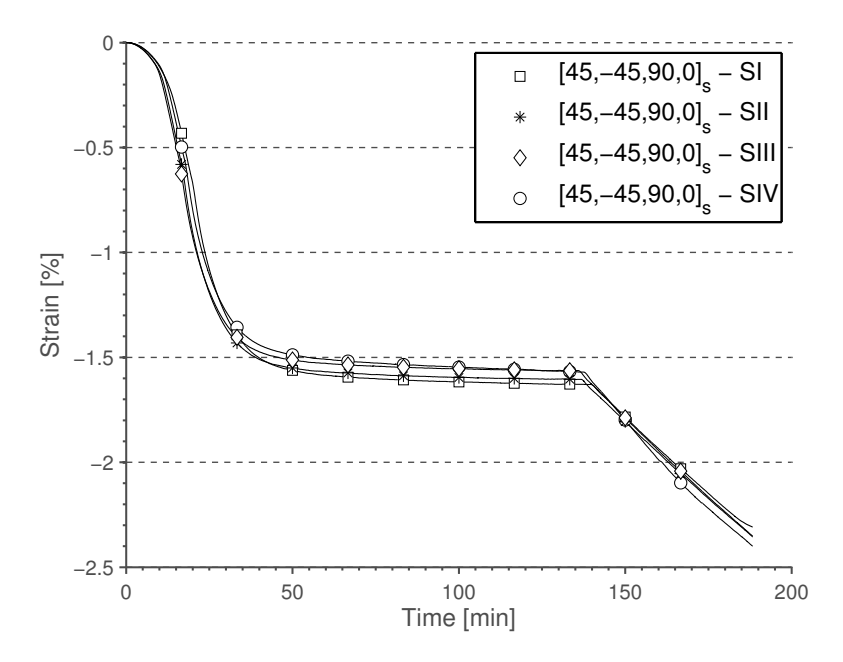


Fig. 4.37: Through-thickness strain measurement for the $[45, -45, 90, 0]_s$ layup, zeroed at the transition point from liquid to rubbery state

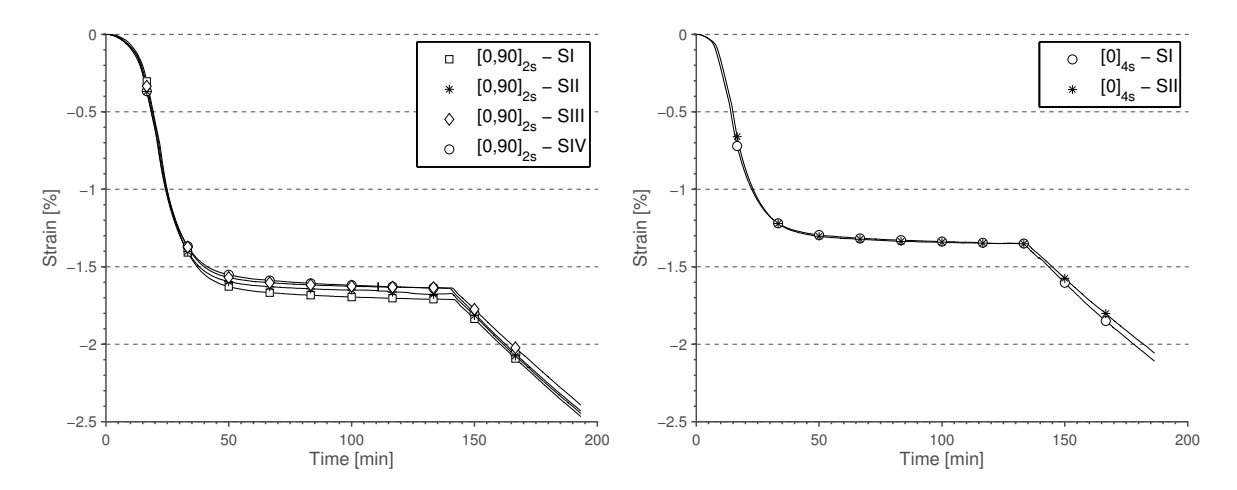


Fig. 4.38: Through-thickness strain measurement for the $[0]_8$ and the $[0,90]_{2s}$ layup, zeroed at the transition point from liquid to rubbery state

The strain measurements shown in the Figures 4.37 and 4.38 allow the determination of multiple parameters. Figure 4.39 shows the evaluated parameters exemplary. Therein, ε_{Ch} and

 ε_{Th} correspond to strains due to chemical shrinkage and thermal expansion, respectively. The time segments Δt_d and the not depicted Δt_b correspond to the duration of the aforementioned stages d and b, whereat those stage-lengths are utilized for the computation of the corresponding averaged strain rates $\dot{\varepsilon}_b$ and $\dot{\varepsilon}_d$ by $\dot{\varepsilon}_i = \Delta \varepsilon / \Delta t_i$. As the stages b and d are isothermal it is assumed that measured increase of strains induced by chemical shrinkage. However, the ongoing consolidation process in stage b adulterates the significance to a certain amount. The time fragment Δt_e is directly related to a certain temperature change in stage e which is given by the cool-down temperature ramp. Assuming that the resin is fully cured at the end of the second dwell phase, the cool down step allows the determination of the coefficient of thermal expansion of the cured laminate by $\alpha_{lam} = \varepsilon_{Th}/\Delta T_e$.

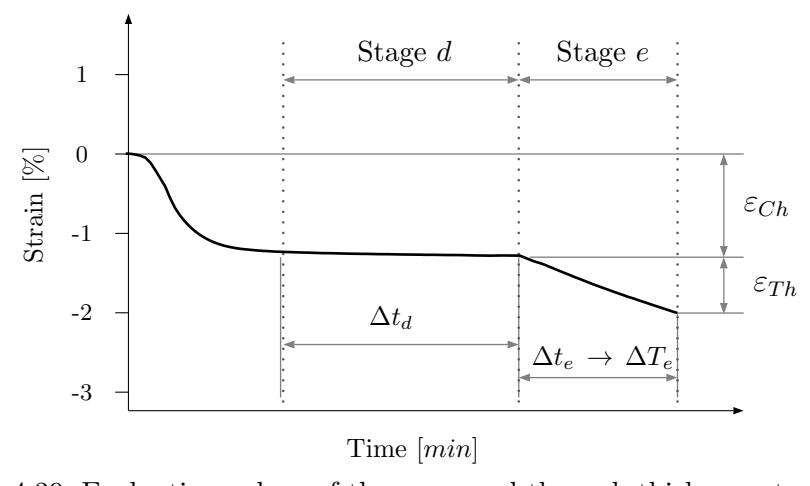


Fig. 4.39: Evaluation values of the measured through-thickness strains

Within Table 4.8 the evaluated measurands are depicted. One specimen of the $[45, -45, 90, 0]_s$ configuration remains disregarded due to a malfunction of the TMA device. Regarding the average CTE for all layups, the multi-angle laminates show slightly higher expansion properties in the range of 48.9 ppm/K whereat the unidirectional specimens show 46.4 ppm/K. Curing rates, which give an impression about the amount of strain during one stage are comparable for all layups, while they are in the range of $-0.0070 \le \dot{\varepsilon}_b \le -0.0092$ [%/min].

Layup	Value	I	II	III	IV	Average	Std.Dev.
	$\dot{\varepsilon}_b \ [\%/min]$	-0.0082	-0.0102	-	-	-0.0092	-
$[0]_{8}$	$\dot{arepsilon}_d \ [\%/min]$	-6.163E-4	-5.175E-4	-	-	-5.669E-4	-
	$\alpha_t[1/K]$	4.770E-5	4.506E-5	-	-	4.638E-5	1.83E-6
	$\dot{\varepsilon}_b \ [\%/min]$	-0.0077	-0.0065	-0.0065	-0.0072	-0.0070	_
$[0, 90]_{2s}$	$\dot{arepsilon}_d \ [\%/min]$	-6.425E-4	-6.475E-4	-5.125E-4	-7.585E-4	-6.403E-4	-
	$\alpha_t[1/K]$	4.883E-5	4.916E-5	4.824E-5	4.962E-5	4.896E-5	0.58E-6
	$\dot{\varepsilon}_b \ [\%/min]$	(-0.0078)	-0.0098	-0.0086	-0.0081	-0.0088	-
$[45, -45, 90, 0]_s$	$\dot{arepsilon}_d \ [\%/min]$	(-8.075E-4)	-5.525E-4	-4.975E-4	-4.825E-4	-5.108E-4	-
	$\alpha_t[1/K]$	(5.433E-5)	4.768E-5	4.868E-5	5.041E-5	4.892E-5	1.38E-6

Tab. 4.8: Obtained coefficients of thermal expansion α_T of the cured laminates as well as isothermal dwell phase strain rates $\dot{\varepsilon}_b$ and $\dot{\varepsilon}_d$

The results of the evaluation of the conducted strain measurements are summarized in Table 4.9.

$$\Delta \varphi_i = \frac{-\varepsilon_i}{1 + \varepsilon_i} \cdot \varphi_0 \quad \text{with} \quad \varphi_0 = 90^\circ \text{ and } \xi = 0$$
 (4.20)

As a first step Radford's simplified Equation 4.20 is used to derive spring-in fractions due to chemical $\Delta \varphi_{Ch}$ and to thermal contraction $\Delta \varphi_{Th}$ and the resulting spring-in angle $\Delta \varphi_{eff}$

Layup	Spec.	$\varepsilon_{Ch} \left[-\% \right]$	$\varepsilon_{Th} \left[-\% \right]$	$\varepsilon_{eff} \left[-\% \right]$	$\Delta \varphi_C [^{\circ}]$	$\Delta \varphi_{Th} [^{\circ}]$	$\Delta \varphi_{eff} [^{\circ}]$
[0]8	I	1.388	0.653	2.041	1.267	0.592	1.875
[0]8	II	1.359	0.710	2.069	1.240	0.644	1.901
	I	1.642	0.765	2.407	1.502	0.694	2.220
$[0, 90]_{2s}$	II	1.690	0.799	2.489	1.547	0.725	2.297
$[0, 90]_{2s}$	III	1.678	0.778	2.456	1.536	0.706	2.266
	IV	1.639	0.767	2.406	1.500	0.696	2.219
	I	1.571	0.864	2.435	1.436	0.784	2.246
$[45, -45, 90, 0]_s$	II	1.630	0.700	2.330	1.491	0.634	2.147
	III	1.605	0.775	2.380	1.468	0.703	2.194
	IV	1.565	0.802	2.367	1.431	0.728	2.182

 $\Delta \varphi_{Th} + \Delta \varphi_{Ch}$. Therein, the initial angle φ_0 is 90°.

Tab. 4.9: Strain measurement results for all fabricated specimens. Corresponding spring-in angle fractions are derived using equation 4.20

Inspecting the derived spring-in angles $\Delta \varphi_{eff}$, the unidirectional laminate shows smaller spring-in angles than the multi-angle laminates which show comparable spring-in angles. However, $[0,90]_{2s}$ specimens show slightly more spring-in. That is not surprising, as the global mechanical behavior of UD laminates is still transversal isotropic. With other words, volumetric shrinkage of the resin can develop in the transverses direction and is not constrained by the fibers of the plies underneath. Obtained tendencies are comparable to the findings of the experimental Section 4.3, although derived absolute angles are approximately 30 % to high.

Due to the good reproducibility, averaged values are regarded in the following, whereat the standard deviation can be seen in Table 4.10

Layup	$\overline{\Delta \varphi}_{Ch} [^{\circ}]$	$\overline{\Delta \varphi}_{Th} [^{\circ}]$	$\overline{\Delta\varphi}_{eff}\left[^{\circ}\right]$	$s\left(\overline{\Delta\varphi}_{Ch}\right)$	$s\left(\overline{\Delta\varphi}_{Th}\right)$	$s\left(\overline{\Delta\varphi}_{eff}\right)$
[0]8	1.253	0.618	1.888	0.019	0.037	0.019
$[0, 90]_{2s}$	1.521	0.705	2.250	0.024	0.014	0.038
$[45, -45, 90, 0]_s$	1.457	0.712	2.192	0.028	0.062	0.041

Tab. 4.10: Average spring-in fractions and corresponding standard deviations for the layups at hand

Comparing the results of the strain-measurement-based spring-in, the estimation given in Table 4.10 with the experimentally gained values, shown in Figure 4.21, reveals differences, whereat experimental values are approximately 30 % below the predicted ones utilizing strain measurement. This may have two potential origins. First, V_f of the TMA specimens are lower than those of the fabricated specimens which leads to more spring-in as shown in Section 4.1. Second, the selected maximum is not a suitable reference point for the derivation of the shrinkage induced strains.

TMA measurements are performed using incineration techniques in order to compare V_f of L-profiles. The evaluation of the TMA specimens using incineration is slightly more complex, due to the two silica glass disks which are part of the cured specimens. As those disks do not incinerate, their mass must be considered when evaluation the remaining ash. A set of three specimens is incinerated whereat an average fiber volume fraction of 57.2 % and a standard deviation of 3.8 %. This is a common value as it is expected for this kind of prepreg material.

Consequently it must be assumed that the selected local maximum is not suitable for the derivation of expectable spring-in angles. To experimentally validate this, additional specimen sets are necessary. However, a reverse analysis allows estimating the location of a suitable zeroing point. Regarding the $[45, -45, 90, 0]_s$ L-profile specimens for example, the measured average spring-in is obtained to 1.57° .

This angle is transferred to an equivalent radial strain ε_R according to Equation 4.19 while $\xi = 0$ is assumed.

$$\varepsilon_R = -\frac{\Delta \varphi}{\Delta \varphi + \varphi} \quad \rightarrow \quad \varepsilon_R = -\frac{1.57}{91.57} = -1.7145 \%$$
(4.21)

This strain is illustrated in Figure 4.40. Considering that the thermal fraction is given in Table 4.9 the resulting chemical fraction ε_{Ch^*} is derived according to the following equation.

$$\varepsilon_{Ch^*} = \varepsilon_R - \varepsilon_{Th} \quad \to \quad \varepsilon_{Ch^*} = -1.7145 \% - (-0.785) \% = -0.9295 \%$$
 (4.22)

Therein, the average thermal strain $\overline{\varepsilon}_{Th}$ of -0.785 % is used which is derived from the four $[45, -45, 90, 0]_s$ specimens given in Table 4.9.

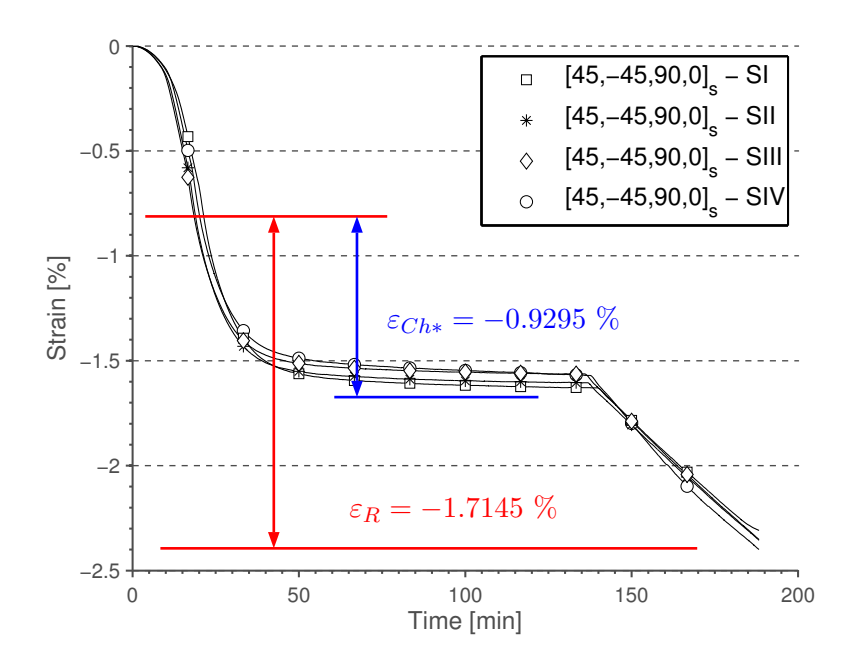


Fig. 4.40: Reverse spring-in analysis for $[45, -45, 90, 0]_s$ specimens

The evaluation of the thermal and the chemical fraction is given by the following equation. Therefrom, the reversible thermal fraction is derived to $\Delta \varphi_{Th} = 45.8 \%$ while the chemical fraction is derived to $\Delta \varphi_{Ch} = 54.2 \%$

$$\Delta \varphi_{Ch} = \frac{\varepsilon_{Ch^*}}{\varepsilon_R} = 54.2 \% \text{ and } \Delta \varphi_{Th} = \frac{\varepsilon_{Th}}{\varepsilon_R} = 45.8 \%$$
 (4.23)

This results are within the area obtained by Yoon et al. [39] and Nelson and Cairns [20] but slightly above the experimentally measured ones described in the next section. However, the findings verify that the originally selected local maximum is not the correct choice as it leads to an over prediction of expectable spring-in distortions as shown in Table 4.9.

The results of a reverse analysis show that a point on the strain ramp shortly after passing the local maximum is more appropriate for a spring-in prediction. As a first approximation the inflection point on the ramp might be a suitable choice. This point is described by the following Equation.

$$\frac{\partial^2 \varepsilon}{\partial t^2} = 0$$
 and $\frac{\partial^3 \varepsilon}{\partial t^3} > 0$ (4.24)

This statement is not further validated in this thesis. Nevertheless, the obtained results promise to be an efficient way for a spring-in prediction. However, the experimental technique must be enhanced in order to account for pressure during the process. This would lead to an improved

laminate quality as the current specimens show small poorly impregnated areas within the laminate, which is due to the missing compaction force. Figure 4.41 shows a representative microsection of a single specimen.



Fig. 4.41: Microscopic analysis of one TMA-cured specimen

At least an experimental investigation is necessary to assess whether a pressurize curing is required. In addition, pull-out tests as performed by Twigg et al. [11] can help to find relevant reference point on the strain ramp.

4.6 Experimental Quantification of Contributing Spring-In Fractions

Spring-in distortions are driven by two main contributors, the chemical shrinkage during the ongoing curing process and the thermal contraction when the part is cooled down from the curing temperature to the room temperature. While the chemical fraction has an irreversible character as the resin's morphology changes during the ongoing curing process, the thermal fraction has a thermo-elastic character.

As the material properties of the composite are assumed as constant after finishing the second dwell stage, a re-heating to the curing temperature of the specimens leads to a reduction of the spring-in angle. In this study, specimens are fabricated with a 180° process. The change of the spring-in angle corresponds to its thermal fraction. Consequently, it can be assumed that the measured spring-in angle at a temperature of 180°C represents the irreversible chemical fraction as $\Delta \varphi = \Delta \varphi_{th} + \Delta \varphi_{ch}$.

The investigated layup configurations of this study are listed in Table 4.11.

Name	Layup	Thickness [mm]	V_f [%]
C1	$[0]_{8}$	1.50	59.6
C2	$[0, 90]_s$	0.75	52.8
C3	$[45, -45, 90, 0]_s$	1.50	70.2
C4	$[45, -45]_s$	0.75	59.1

Tab. 4.11: Investigated configurations of the spring-in fraction study

A used measurement setup consists of a controllable heating plate, a temperature measurement device and a GOM ATOS 3D full-field measurement system [92]. Figure 4.43 shows the setup schematically.

The GOM Atos system is utilized to measure the geometry of the L-profile specimens at different temperature levels. The controllable heating plate is used to heat up the specimens to the aspired temperature, whereat the temperature measurement device is used to detect the specimen temperature accurately as it deviates from the heating plate temperature due to radiation and convection effects. Figure 4.42 shows a photo during a similar measurement.



Fig. 4.42: Specimens applied on the hot-plate during the measurement

As spring-in distortions develop in the curved area of the profile the temperature sensor detects the specimen temperature T_{Sp} in this area. Geometry measurements are performed at certain temperature steps in order to obtain the spring-in angle as a function of specimen temperature $\Delta \varphi = f(T_{Sp})$.

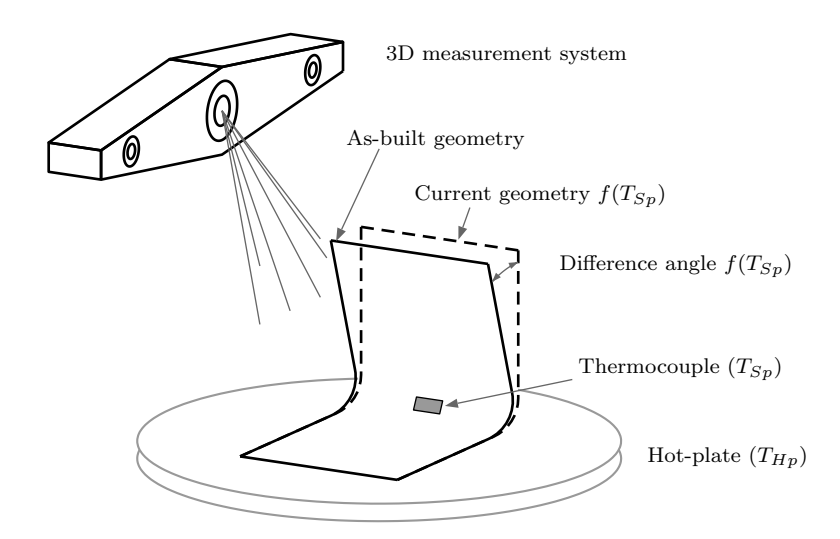


Fig. 4.43: Experimental setup for quantification of the thermal fraction of spring-in deformations

The measurement is affected by heat convection, as the temperature difference of the specimen to the environment is considerably large. Thus, the heating plate temperature must be above the aspired specimen temperature $T_{Hp} > T_{Sp}$ in order to compensate loss of temperature. The detected specimen temperature T_{Sp} as a function of the heating plate temperature T_{Hp} is

described by the following equation. Therein, the offset temperature T_{offset} represents the linear interpolation of the measurement results.

$$T_{Sp} = T_{Hp} - T_{offset}$$
 with $\Delta T_{offset} = 0.3673 \cdot T_{Hp} - 8.1651^{\circ}C$ (4.25)

Evaluating Equation 4.25 shows that a hotplate temperature of approximately 200°C is necessary to achieve a specimen temperature of 130°C. Consequently, experiments are stopped approximately at this temperature in order to prevent the resin from degrading due to temperatures above the glass transition temperature T_g . However, as will be seen in the following, measurement results can be excellently extrapolated as the change in spring-in angle shows a clear linear character.

As outlined by Hubert and Poursatip [93] and substantiated by the preliminary spring-in investigations shown in Section 4.1, the V_f is an important parameter for the spring-in angle. Especially the V_f in the curved section which is often referred to show considerable scattering due to corner thinning or corner thickening as outlined by Hubert and Poursatip [93], is of interest. Therefore, the V_f of each specimen is measured and results are shown in Table 4.11. This is done by incineration of small laminate sections taken from the curved L-profile areas.

From former experiments with similar specimens it is known that the V_f along the circumferential length of the L-profile is constant. Thus, a homogeneous V_f within the curved laminate area is assumed. Figure 4.44 shows the measurement results and the derived linear extrapolations. At a first glimpse the configuration c1 shows a deviating slope, while slopes of the other configurations are quiet similar. This effect is clearly related to the layup of configuration C1 which is unidirectional. Thus, fibers are aligned in circumferential direction of the L-profile only. Therefore, the specimen freely expands in the transverse plane. Consequently, only a certain fraction of the thermally-induced volume expansion induces a change of the spring-in angle.

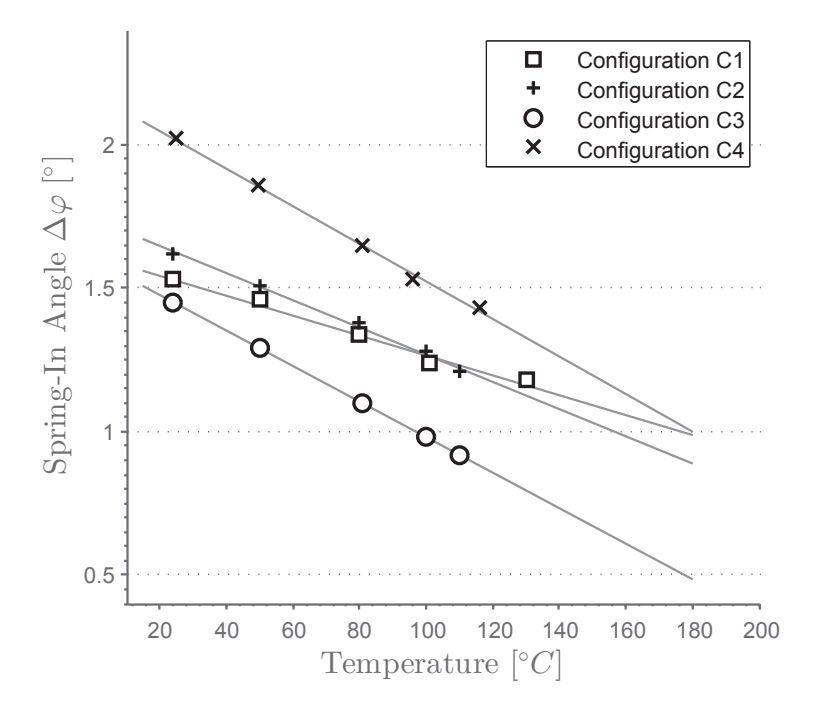


Fig. 4.44: Linear interpolation of the Spring-in angle $\Delta \varphi$ as a function of temperature for each configuration. Specimens are fabricated on the 6 mm toll radius

The evaluation of the derived linear regressions of the measurement results allows the determination of thermal and chemical fraction and their percentage of the total spring-in angle. Therein, the thermal fraction is derived by $\Delta \varphi_{Th} = \Delta \varphi(20^{\circ}C) - \Delta \varphi(180^{\circ}C)$ while the chemical

fraction is derived with $\Delta \varphi_{Ch} = \Delta \varphi(180^{\circ}C)$. Similar to the obtained spring-in angles differences between the single layups are obtained which is in accordance with the experiments described in Section 4.3.

Name	$\Delta \varphi$	$\Delta \varphi_{Th} \ [^{\circ}]$	$\Delta \varphi_{Ch} \ [^{\circ}]$	$\Delta \varphi_{Th}/\Delta \varphi$ [%]	$\Delta \varphi_{Ch}/\Delta \varphi$ [%]
C1	1.55	0.56	0.99	36.1	63.9
C2	1.65	0.75	0.90	45.4	54.6
C3	1.47	0.99	0.48	67.3	32.7
C4	2.05	1.06	0.99	51.7	48.3

Tab. 4.12: Measured results of the investigated configurations

The thermo-elastic fraction of the spring-in angle is obtained for 36 % $\leq \Delta \varphi_{Th} \leq$ 67 %. This is in accordance with Yoon et al. [39] who experimentally verifies a thermal fraction of 42 % and with Nelson and Cairns [20] who limited the possible thermal fraction to an area between 40 % and 70 %.

The magnitude of thermal variability of the spring-in is an important cognition for part and tool designers as this thermal effect must be considered when a structure is designed to a certain operating point with a certain operating temperature. For example, a wing of a commercial aircraft is subjected by thermal loads between -50 °C up to +100 °C. However, due to the linear character of the spring-in effect shown here, this variability can be well estimated starting from a spring-in angle measured at room temperature. Although the linearity of the effect is convincing, it is recommended to perform further experiments with this experimental set-up to secure this assumption statistically.

4.7 Spring-in of Doubly Curved Areas and Nonlinear-Swept Profiles

Up to now, spring-in is analytically described by a two-dimensional approach proposed by Radford. Considering doubly curved geometries, part's shape is affected by a combined deformation mechanism, as different curvatures are present. Regarding a section of a spherical segment, two main deformation modes are conceivable whereat superposition gives the total part deformation. Figure 4.45 depicts the nominal configuration denoted with tilde-parameters \tilde{R}_{gl} , \tilde{R}_{loc} , $\tilde{\phi}$ and $\tilde{\psi}$, which correspond to the initial global radius, the initial local radius, the section angle, and the local segment angle, respectively. With respect to the findings presented so far, complex shape changes are expected for the structure at hand, whereat the geometric parameters of the deformed configuration change to R_{gl} , R_{loc} , ϕ , ψ .

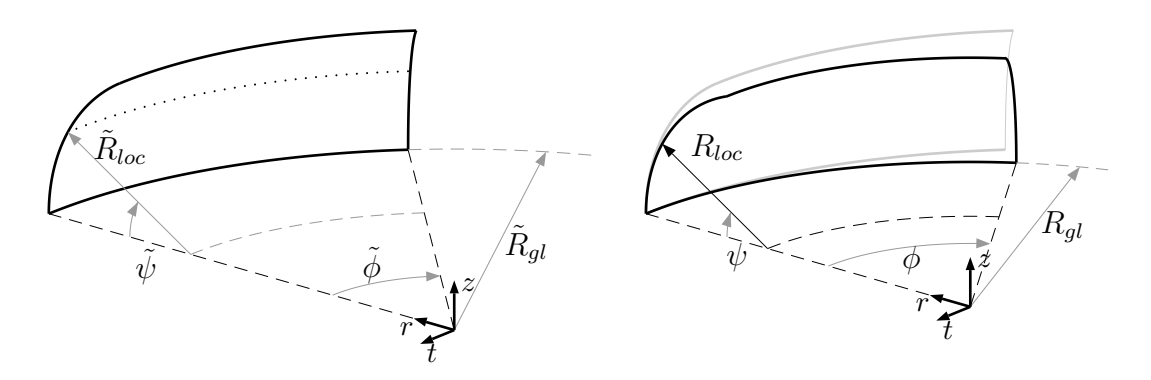


Fig. 4.45: A spherical segment section in reference configuration (left) and in deformed configuration (right)

As spring-in spring-in deformations develop in the curved part areas, the two curvatures of the reference configurations in Figure 4.45 indicate that two mechanisms are competing, whereat one is due to the local curvature and the other is due to the global curvature. Both deformation modes are depicted in Figure 4.46, where the local spring-in dominated mode is shown on the left side. It is characterized by the change in the local radius $\tilde{R}_{loc} \to R_{loc}$ and the segment angle $\tilde{\psi} \to \psi$, whereat the global radius and the section angle remain constant.

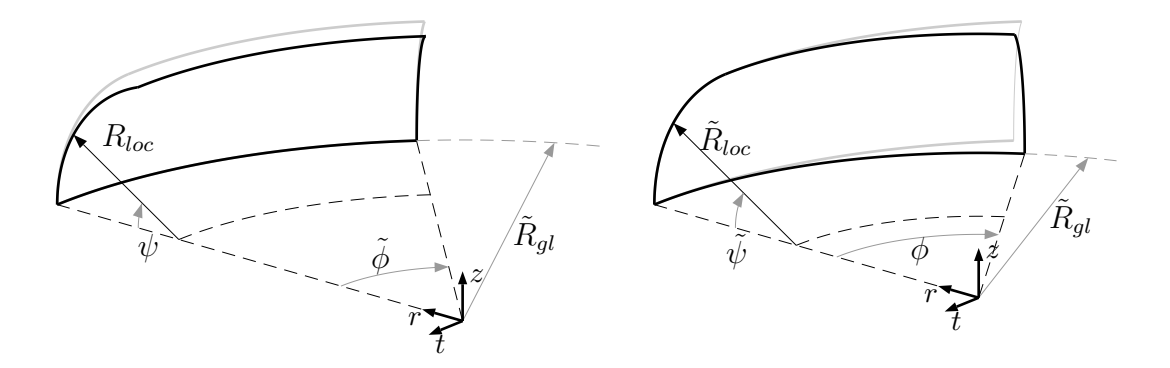


Fig. 4.46: Separation to local and global spring-in fraction of a doubly curved spherical segment section

The second mode, dominated by the global radius, is characterized by constant local radius and segment angles and changing global radius $\tilde{R}_{gl} \to R_{gl}$ and $\tilde{\phi} \to \phi$.

Within this section, the main goal is to find out whether the total deformation of a part containing doubly curved areas is either dominated by the global spring-in or by the local spring-in. Experimental investigation have been conducted based on two curved L-profiles, which have been fabricated on an aluminum male tooling whereat the bagging arrangement is identical to that one shown in Figure 4.13.



Fig. 4.47: Aluminum tool for curved L-profile specimens

The section angle of the profile is 74° whereat the nominal inner part radius is 492.1 mm. The local nominal radius of the part's cross section is 4 mm with a segment angle of 90°. Thus, dimensions of the global and local radii are of different scale which is a common situation when considering common aircraft parts such as spars for example. Those spars commonly have a very large global flange radius up to 3 m and local radii in the range of 3 mm to 15 mm in the web-to-flange transition areas. In context of a spring-in prediction supported by experimental efforts, it has to be proved whether simply curved L-profile specimens or the extended Radford approach is suitable for parameter derivation. The profile's layup is [45, -45, 90, -45, 45, -45, 90, 45]_s, whereat it is fabricated out of 8552/AS4 prepreg material with a nominal ply thickness of 0.125 mm. The layup coordinate system is depicted in Figure 4.48. Prior to manufacturing, tool dimensions have been validated based on 3D surface measurements. Flatness as well as radii match the nominal data exactly. Thus affectations due to bad tooling quality can be excluded.

For sake of evaluation, the tool-sided surface of the fabricated specimens is 3D scanned using the GOM Atos system. GOM Inspect software is used for evaluation of the obtained point cloud. The boundaries of the nominal geometry, which are engraved into the tool surface, and thus visible in the fabricated parts, are used for the construction of the initial center axis of global curvature. Subsequently eight cutting planes are defined to generate eight section cuts of the point cloud. Figure 4.48 illustrates that schematically, whereat the section cuts are denoted with SC_{1-8} . The generated cuts are inspected manually. A representative as-built shape of the cross

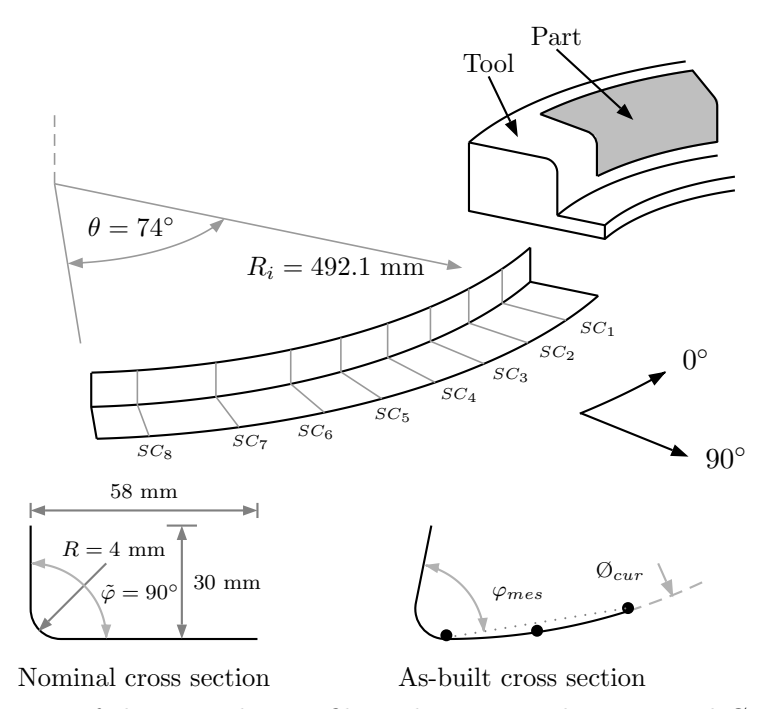


Fig. 4.48: Dimension of the curved L-profile and measurands $\varphi_m es$ and \emptyset_{cur} . The 0° direction is defined by the global curvature of the profile

section cuts is depicted in Figure 4.48 schematically. Therein, the short flange does not show a measurable curvature, whereat the long flange comes with a measurable curvature. However, the obtained curvatures are very small compared to the part's dimensions. Conceivable sources for the obtained curvature of the long flange are the absence of unidirectional plies in circumferential 0° direction and warpage interactions between the aluminum tool and the composite part. Within Section 7.4 that is validated utilizing the later introduced simulation strategy. Regarding the obtained spring-in angles in circumferential direction of the curved L-profile given in Table 4.13, they clearly show that the obtained angles are in the range of the specimens presented in Section 4.3. Thus, a transferability is given although the geometry is curved. As the bagging is similar to that one used for the simple L-profiles, a direct comparison to that obtained spring-in angle is possible.

Regarding the spring-in angles of the specimens C_{A4} , C_{A5} and C_{A6} given in Figure 4.21, a good match is observed. It should be noted that the reference coordinate systems of the curved specimen is different to that one of the regular L-profiles. Thus, a 90° ply within the layup of the curved L-profile corresponds to a 0° ply of the regular L-profile specimen. Thus, comparability is given. Spring-in angles of the simple profiles are obtained to $\Delta \bar{\varphi}_{C_{A4}} = 1.42^{\circ}$, $\Delta \bar{\varphi}_{C_{A5}} = 1.43^{\circ}$ and $\Delta \bar{\varphi}_{C_{A6}} = 1.45^{\circ}$, whereat the average spring-in angle of the curved profiles are obtained to $\Delta \bar{\varphi}_{CL,II} = 1.41^{\circ}$ and $\Delta \bar{\varphi}_{CL,II} = 1.44^{\circ}$ which is almost identical. That excellent matching allows the cognition that the magnitude of spring-in angles obtained for simple L-profiles is directly transferable to curved geometries.

Material parameters ESA Comp $E_X = 47760 \text{ MPa}, E_Y = 23590 \text{ MPa}, G_{12} = 29130 \text{ MPa}, v_{12} = 0.792$

	#	SC_1	SC_2	SC_3	SC_4	SC_5	SC_6	SC_7	SC_8	$\bar{\varphi}_{mes}$	$s_{arphi_{mes}}$
$\Delta \varphi_{loc}$ [°]	1	1.44	1.48	1.30	1.33	1.41	1.35	1.49	1.46	1.41	0.07
$\Delta arphi_{loc}$ [°]	2	1.62	1.44	1.30	1.37	1.46	1.41	1.42	1.53	1.44	0.10
$2/\varkappa$ $[mm]$	1	8077	15919	16101	13319	15382	17970	9900	5390	12757	-
$2/\varkappa$ $[mm]$	2	18267	14780	18155	13221	15654	21878	15010	13250	14322	-

Tab. 4.13: Section cut spring-in angles and obtained flange curvatures for the curved L-profiles

The experimental findings documented in the preceding are compared and numerically validated with the use of the developed simulation strategy of this thesis within Section 7.4.

Difficulties in the Comparison of CAD, FEA and Measurement data

A common strategy to assess the significance of FE predictions is the comparison of the FE results to nominal CAD data or to 3D full-field surface measurements. Whereat that comparison is simply applicable for simple geometries such as the linear extruded L-profiles described in Section 4.2 it is a bit deceiving when applied to more complex structures as the curved L-profile for example. The main source of error is induced within the alignment process of the different data sets. Within the following, the difficulties are demonstrated, based on the curved L-profile geometry, whereat a comparison of nominal data to FE result data is conducted. Therefore, one point cloud of the nominal FE model and one of the resulting deformed FE model is imported into the GOM Inspect software in order to compare both part shapes geometrically. Thereby, each point cloud consists of approximately 2900 points, whereat both polygonized surfaces show a circumferential gap which seems to be an error of the utilized software. However, this is neglected as it is not detrimental in achieving the goal of this section.

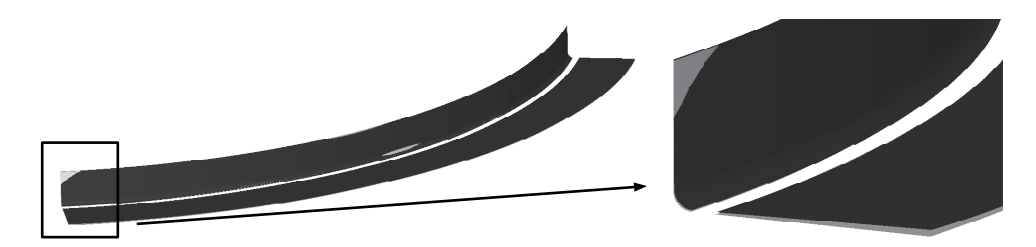


Fig. 4.49: Deformed (dark gray) and nominal shape (light gray) aligned according to the boundary conditions of the FE model. Spring-in deviation is visible on the detail picture on the right

The comparison of nominal CAD data to simulation results or to measurement results demands an appropriate alignment of the data sets towards each other. Considering the curved L-profile of this section, different alignment options are present. The alignment according to the boundary condition assigned in the software represents the first solution presented here. It allows a description of the deviation between both shapes whereat an assessment whether the inner radius or the global orientation changes is hardly possible. The second and the third option utilize the flange section of the L-profiles. Within Figure 4.50 the options are depicted. Using the short flange for alignment, which is indicated by the white triangles, results in deviations shown on the left bottom side. Using the long flange for alignment, indicated by the white circles, produces a completely different deviation shape, as shown on the right bottom side.

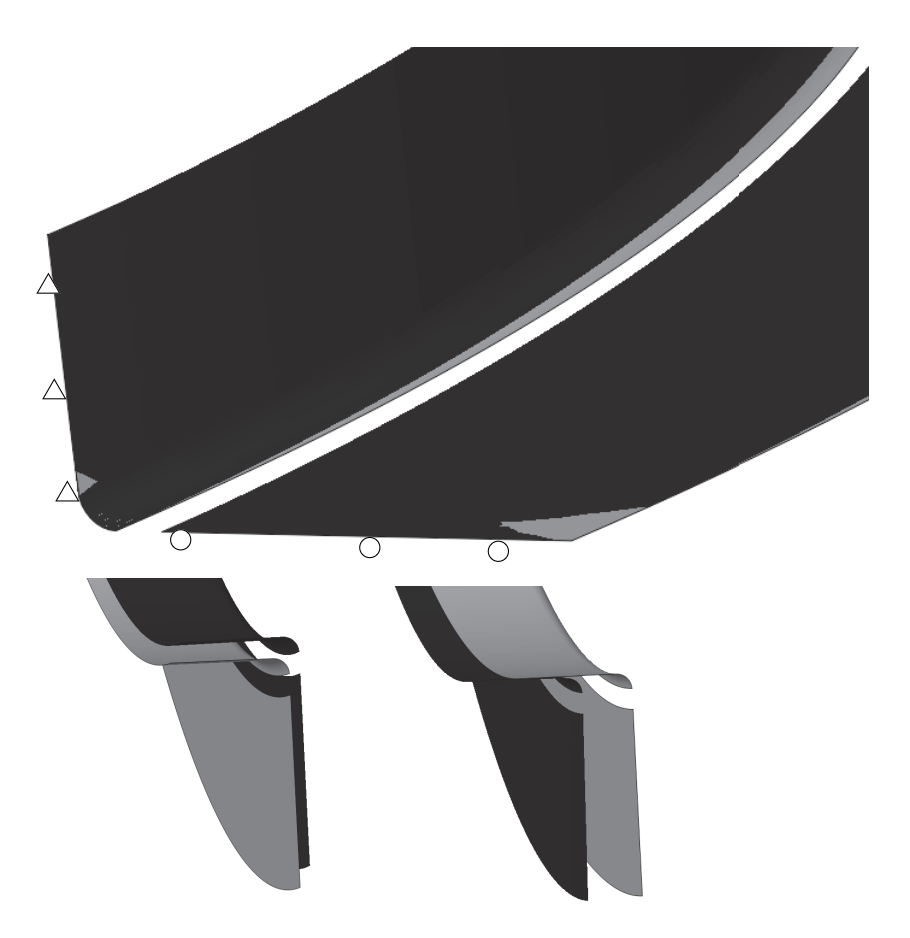


Fig. 4.50: Different alignment strategies for the curved L-profile give apparently different types of deformations although the numerical result is identical for both alignments

Considering that the FE data is identical for all three presented alignments, the significant differences are conspicuous. That clearly underlines the sensitivity to appropriate alignment of quantitative comparisons between nominal shape to FE or measurement data.

Therefore, the evaluation of the curved L-profile is limited to the spring-in evaluation based on cross section cuts at this point. However, appropriate 'alignment strategies' should be investigated and formulated in the future in order to reduce/avoid incorrect cognitions induced by manual misalignment. Simple 'best-fit' alignments, as they are commonly used, are often inappropriate for the to assessment manufacturing deformations. Thus, a cross section based evaluation, as it is conducted in the preceding, is rather suitable, since it is independent from the part's alignment.

4.8 Cognitions of the Spring-In Investigations

Preliminary analytical studies are in accordance with experimental results of Kleineberg [13] as the spring-in angle is linearly dependent on the V_f when regarding fractions of 40 % up to 75 %. Numerical studies with a parameterized layup clearly demonstrate that the spring-in effect is majorly driven by the strains acting in laminate thickness direction. Moreover, these studies substantiate the narrow range of expectable spring-in distortions.

The comprehensive experimental study gives insight into the magnitude of occurring processinduced spring-in distortions. The laminate thickness of unidirectional laminates turned out to have no direct impact on the measured spring-in distortions. Moreover, the tool material as well as the tool surface roughness does not affect the obtained angles significantly. However, eight-ply specimens, fabricated on the invar tool, show conspicuous results as they produce approximately 20 % less spring-in than the specimen fabricated on aluminum tools. As this result is not verified by other experiments further investigation is demanded to assess this result thoroughly. The investigation of the effect of the tool radius respectively the part radius revealed no clear relation. For some layups a slight increase for the 12 mm radius is observed which is in the range of a spring-in increase of 5 %. A remarkable result is that three different SoA prepreg materials produce almost identical spring-in angles for one layup. This is contrary to the findings within the warpage investigations where a strong material dependency is observed. However, these results verify that expectable spring-in angles are widely material independent as long as carbon-epoxy prepregs are considered.

All 289 specimens are used for a statistical evaluation. Five groups of specimens are defined for sake of characterization. Histogramms show that measured spring-in angles can be described with a gaussian normal distribution although the groups contain specimens made from different prepreg materials. The average spring-in angle for all specimens is obtained to $\overline{\Delta \varphi}_{All} = 1.55^{\circ}$ with a standard deviation of $s_{\Delta \varphi} = 0.40^{\circ}$ which is quite high. These high scattering can be traced back to significant scattering of selected layups. Evaluating specimens with at least two 0 °plies in direction of curvature reveals an average spring-in angle of $\overline{\Delta \varphi}_{with~0^{\circ}} = 1.57^{\circ}$ and a significantly reduced scattering of $s_{\Delta \varphi} = 0.22^{\circ}$. Regarding specimen sets for one layup made from one material scattering of $s_{\Delta \varphi} < 0.10^{\circ}$ is rather realistic.

Based on the cognition that spring-in is dominated by the strains in trough-thickness direction, the so called 'Extended Radford Approach' is developed which measured the through-thickness strain during the complete curing process. Measurement using this technique show that significant scattering from specimen to specimen is observable which is in accordance with experimental findings of other researchers. However, the comparison of the measured strains show almost identical characteristics when they are zeroed at a defined point. This verifies a high reproducibility of the occurring through-thickness strains after the resin passed the gel-point. Consequently, this measurement technique is able to serve as a potential parameter source for the spring-in prediction. Although results are promising, the experimental technique should be extended in order to enable compaction forces.

Analyses on curved L profile specimens show that the spring-in angle obtained for regular L-profiles can be directly transferred to curved profiles.

Within an experimental study, the thermal $\Delta \varphi_{Th}$ and chemical $\Delta \varphi_{Ch}$ fraction of the spring-in angle of different L-profiles are quantified. Experiments show a layup-specific thermal spring-in fraction of 33 % for a quasi orthotropic layup and up to 64 % for a unidirectional layup which is an important information for tool and part designers.

5 Superposition of Distortion Mechanisms

This chapter is dedicated to structures which are affected by spring-in, warpage as well as forced-interaction effects which are a consequence of the part's shape and the used manufacturing process. Within this section manufacturing distortions of an integral prepreg box structure is experimentally evaluated by means of geometrical measurements using the high-resolution measurement system introduced above. Contributions of each mechanism are characterized and their interaction is verified by selected experimental means. Moreover, measurements evaluated here are used for validation of the semi-numerical prediction methodology that is presented in Chapter 6

The manufacturing of more integrated composite structures has been a challenge for years and it is still now. However, highly-integrated composite structures promise a maximum weight-reduction potential due to avoidance of rivets and structural connections. Nowadays, the degree of integration is limited as the process-induced geometrical distortions are not fully understood. Thus, elementary airframe parts such as spars are manufactured with a differential-design. In this section, process distortions of a composite box-structure are experimentally investigated. This box structure represents a cut-out of a highly-integrated wing cover, wherein ribs, stringers and the skin are cured simultaneously within one shot. The integral wing cover and structural cut-out are shown in Figure 5.1 schematically. The tooling concept for this structure contains a slightly curved base tool which forms the outer skin surface and multiple tool cores which form stringers and rips during processing.

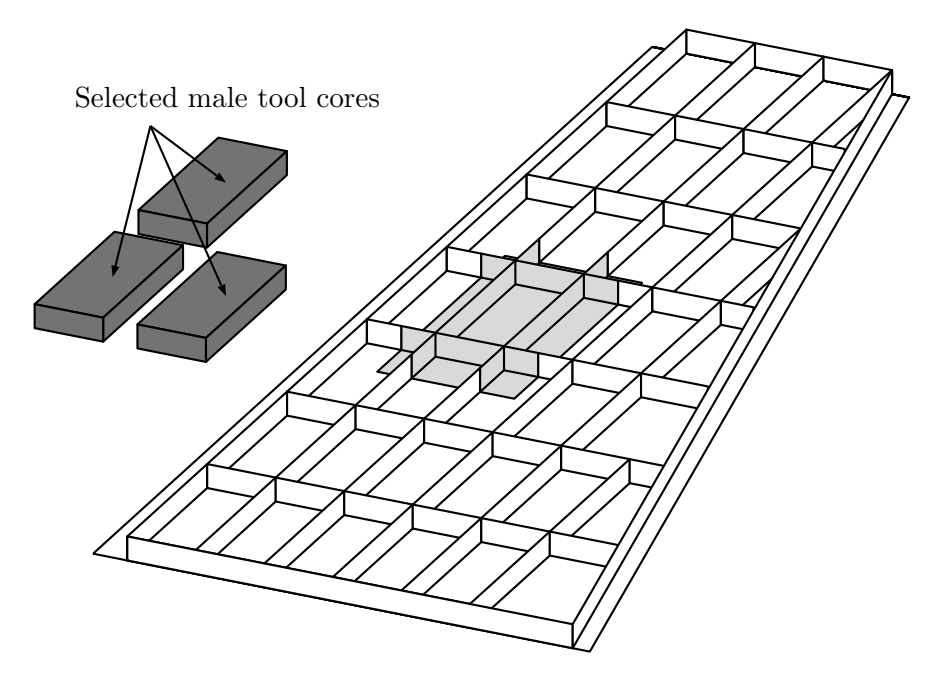


Fig. 5.1: Conceptional wing cover with integrated stringers and rips. Gray section represents the regarded structure cut-out. Selected inner male tool cores are depicted in dark gray

The manufacturing strategy for the highly-integral panel is subject of ongoing research projects

which focus on maximum automation and new filler concepts. Therefore, it deviates massively from state of the art manufacturing processes used in the industry. Consequently, an experimental evaluation of the process distortions of the cut-out is not meaningful, as it might be affected by accompanying effects due to the new tooling concept or other not entirely understood phenomena. However, multiple manufacturing trials of the cut-out structure reveal conspicuous reproducible process distortions which can not entirely explained with spring-in or warpage. This suggests that the structure is likely affected by the forced-interaction effect.

Within this section the inner integral box structure of the cut-out is used for experimental validation as it is believed to dominate the structural behavior of the cut-out structure due to its closed and therefore stiff structural shape. Figure 5.2 shows the cut-out structure and its integral constituents. Considering the whole wing-cover shown in Figure 5.1, it is obvious that only the center box is representative for the entire wing-cover. Thus, the box-structure is used for the evaluation and characterization of occurring process distortions.

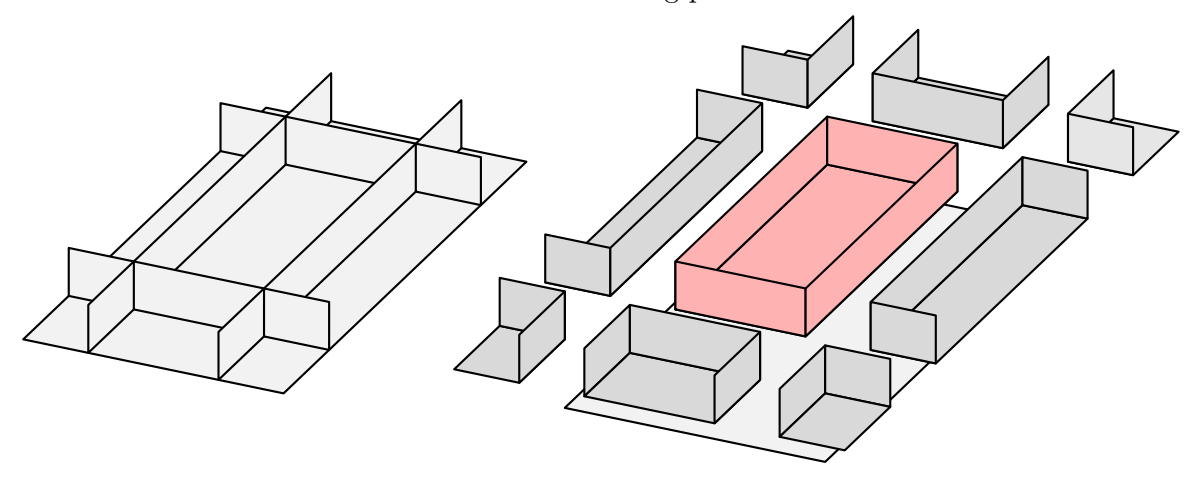


Fig. 5.2: Structural cut out (left) and integral constituents of the cut-out (right). Red box represents the representative box structure

A set of two box specimens is manufactured from M21/T800 prepreg material with a $[0,90]_{3s}$ layup. The nominal ply thickness of the UD prepreg material is 0.25 mm which results in a laminate thickness of t=3 mm. The box's inner nominal length l, width w and height h are 798 mm, 206 mm and 55 mm, respectively. Within the nominal design all angles between ribs, stringers and web measure 90° as shown in Figure 5.3.

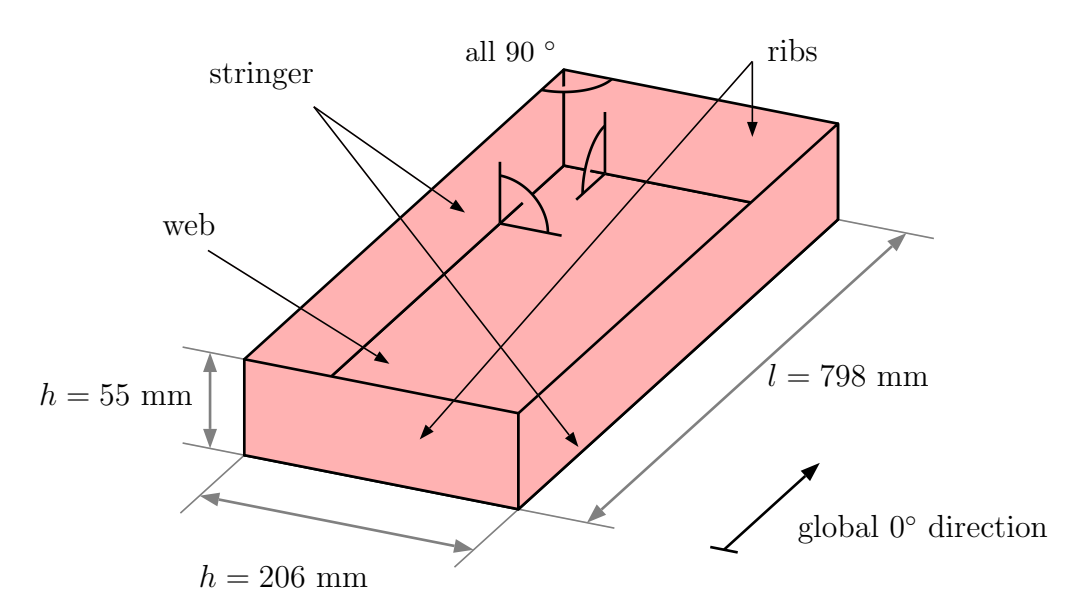


Fig. 5.3: Dimensions of the composite box structure and denotations

A modified MRCC is used, where the first dwell stage lasts three hours at 150 °C while the second dwell stage lasts four hours at 180 °C. Heating and cooling rates are set to ± 1 °C per minute. Within the first manufacturing run, a set of four L-profile test specimens is fabricated under identical boundary conditions and with identical layup. Thus, the characteristic springin behavior of the configuration (material, layup, process, tool) is obtained. Both aluminum tools are hollow, while the material thickness is approximately 10 mm which assures comparable thermal conductivity and heat capacity. Tool-surface roughness is of identical magnitude in the range of $R_a = 1.6 \ \mu m$. Bagging arrangement, vacuum conditions as well as the used releaseagent are identical for both tools. Figure 5.4 shows the prepared manufacturing setup inside the autoclave while Figure 4.13 shows the used bagging arrangement.

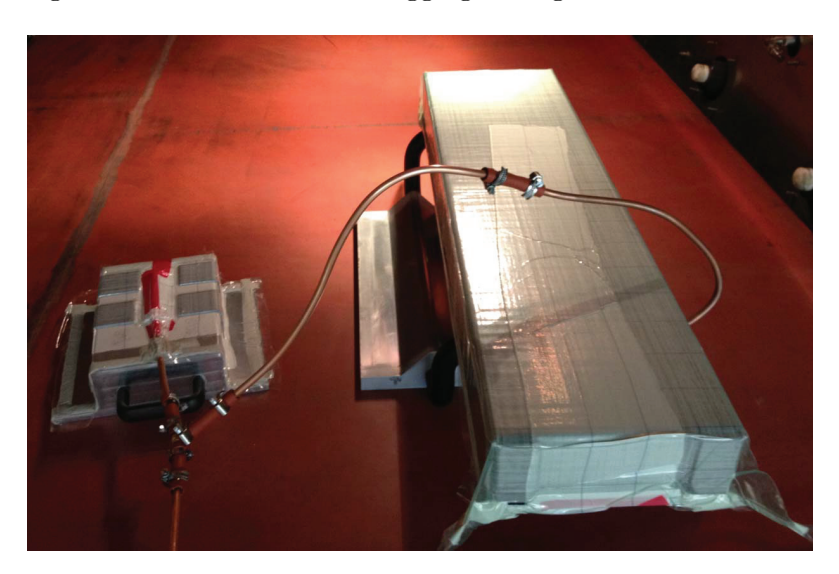


Fig. 5.4: Manufacturing setup for the box structure and one set of representative L-profiles

5.1 Process Distortions of an Integral Composite Box Structure

Two manufactured box specimens are measured using a full-field 3D GOM ATOS measurement system. The obtained point-clouds consist of approximately 1.3 million points which corresponds to a point-density of approximately 4.7 points/mm². A triangulated mesh is derived based on the point cloud. The distortion evaluation is conducted using GOM Inspect software while the tool-sided inner surface of the boxes are inspected. A representative point-cloud and selected cross-section cuts are shown in Figure 5.5 (right). Note that this evaluation focuses mainly on process distortions along the box's length direction for sake of clarity.

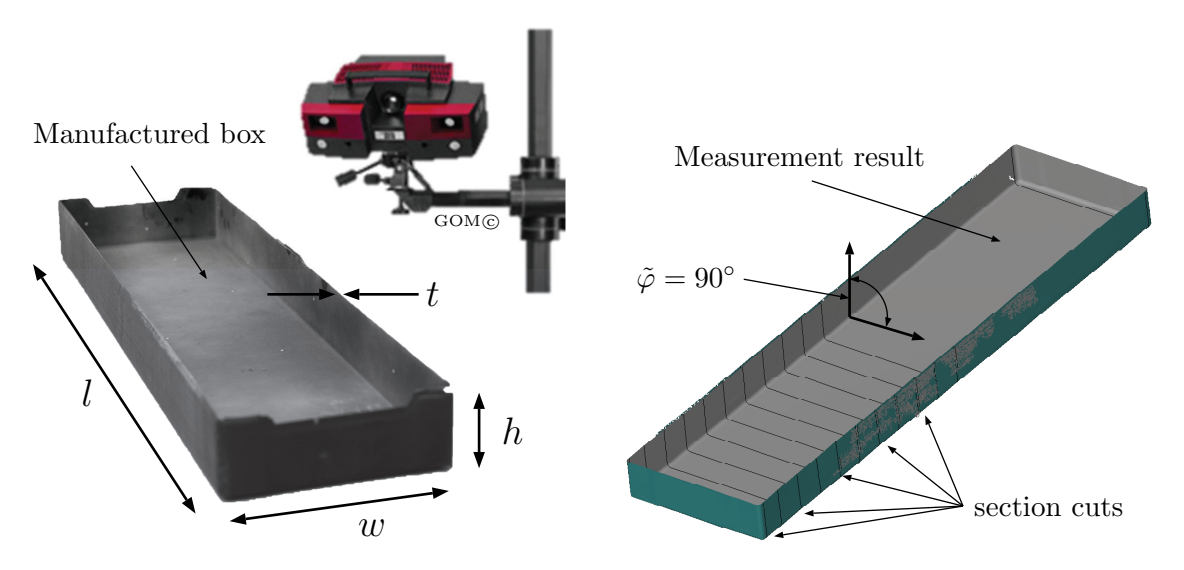


Fig. 5.5: Manufactured box structure and the full-field 3D measurement system (left); Obtained measurement point cloud and selected inspection-sections with a distance of 40 mm (right)

A schematic of the obtained distortions is shown in Figure 5.6. Therein, flange spring-in in length direction is the main type of deformation which is expected according to the investigations conducted by Fernlund et al. [10].

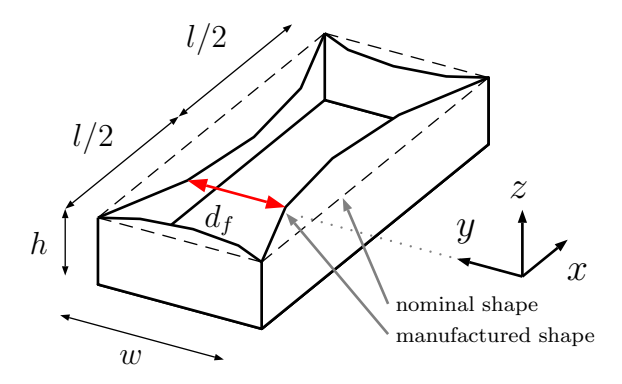
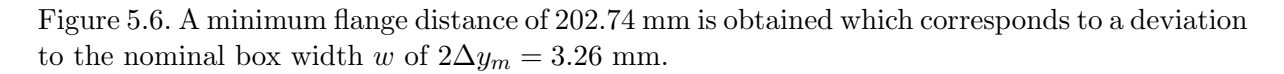


Fig. 5.6: Schematic of the nominal and manufactured (magnified) shape of the CFRP box. Measurand d_f denotes the flange-to-flange distance

As a first step, the flange distance d_f is measured every 40 mm based on inspection cuts which are assigned to the point cloud to characterize the deformation state along the part's length direction. Figure 5.7 shows the part shape with respect to the coordinate system depicted in



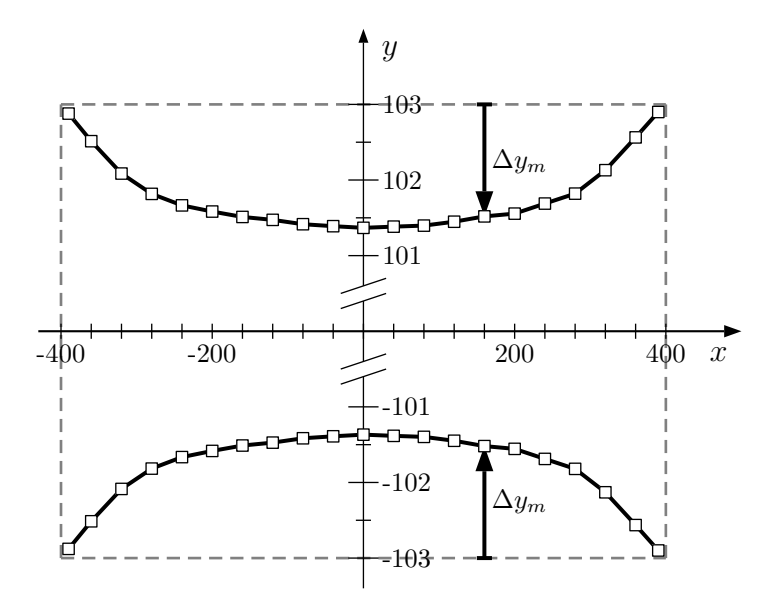


Fig. 5.7: Measured flange shape deviation Δy_m of the box-structure along the part's length direction. Note different axes scales

A direct calculation of the flange spring-in angle based on the measured flange distance d_f , according to Equation 5.1, reveals a maximum spring-in angle of $\Delta \varphi_{max}=1.70^{\circ}$. This equation is used by [10].

$$\Delta \varphi_{max} = \arcsin\left(\frac{w - d_{f,min}}{2h}\right) \tag{5.1}$$

This direct calculation implies no curvature of the web area between the flanges. As inspections of the cross-section cuts reveal a curvature of the base surface area throughout the entire part length, which is likely introduced due to forced tool-part interaction, this direct analytical relation turns out to be slightly inaccurate for the box specimens of this study. Therefore, Equation 5.1 can only give an estimation of the local flange spring-in angle as an over-prediction is to be suspected.

To clearly distinguish between base-surface warpage and local spring-in, two different measurement steps are conducted. The first one evaluates cross-section cuts locally around the corner areas as schematically shown in Figure 5.8. Therein, two local flange spring-in angles $\Delta \varphi_1$ and $\Delta \varphi_2$ are evaluated for each specimen. Obtained flange spring-in angles as well as the maximum spring-in angle $\Delta \varphi_{max}$, derived according to Equation 5.1, are plotted in Figure 5.8 as a function of the part's length coordinate x. As expected, measurement results show a widely symmetric shape. The spring-in angle progressively develops, starting from the ends of the box where it is geometrically constrained by the cross ribs. At a certain distance from the end the spring-in angle is widely constant up to the part's symmetry plane. Interestingly, this distance is approximately twice of the part height h which corresponds to the length coordinates $x = \pm 289$ mm. Note that the standard deviation of the angle calculation is estimated to $s=\pm 0.05^{\circ}$, as it is based on a manual selection of cross-section areas and based on a triangulated mesh within the Inspect software. Deviations between the single spring-in angle measurements are likely related to the manual layup procedure and the aforementioned uncertainty within the evaluation process. A universal statement about fade-away length of the corner effect is not possible as far as there is only one configuration fabricated and the effects are likely to depend on material and geometrical part properties.

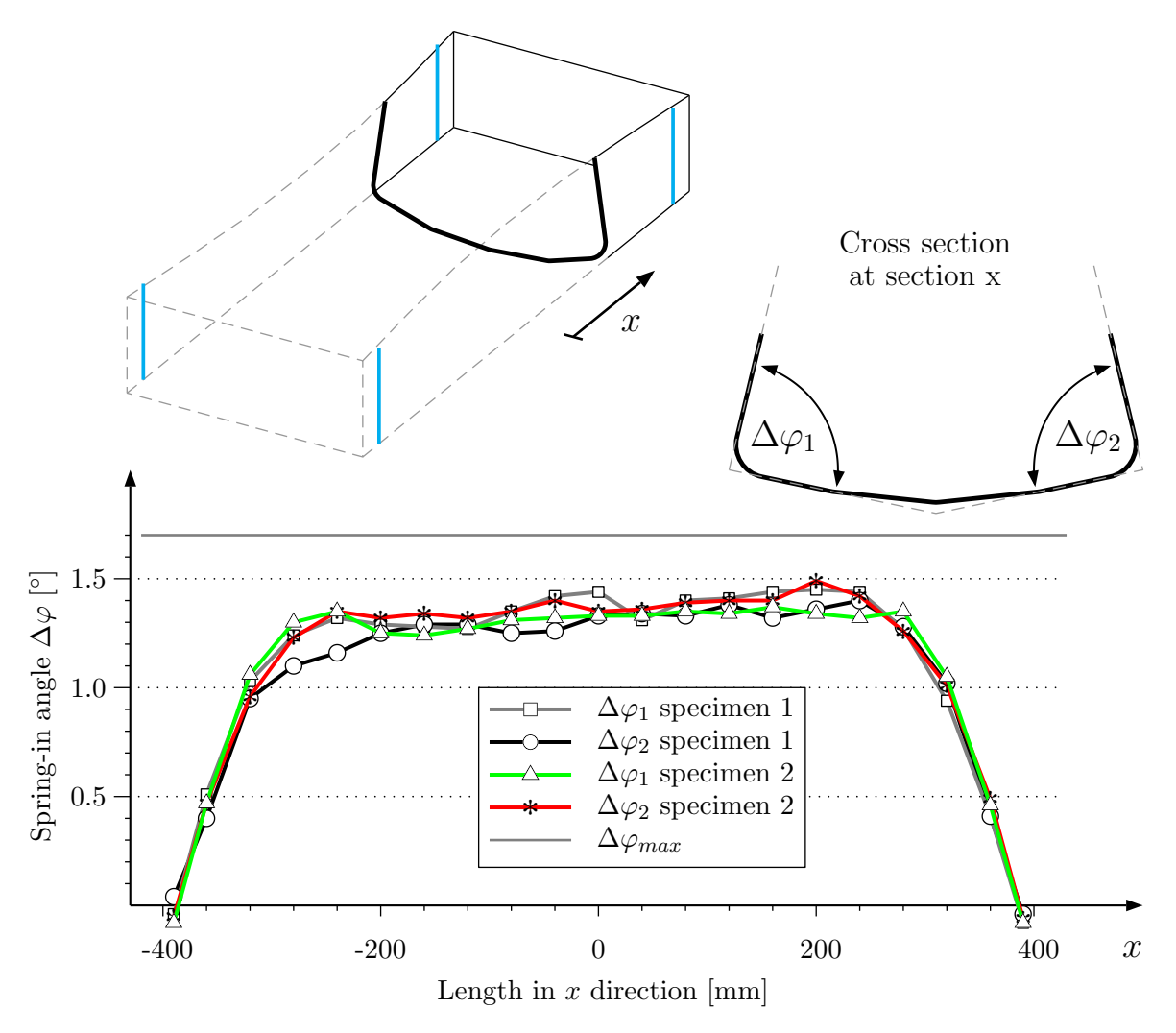


Fig. 5.8: Measured spring-in angles of the box specimen and the maximum derived spring-in using Equation 5.1

Comparing the graphs of the measured flange shape in Figure 5.6 and the measured local flange spring-in angle, qualitatively different characteristics are obtained as the flange shape shows no area where it is widely constant. This indicates that the warpage of the base-surface area interacts with or superposes the local spring-in deformations on the macro-level.

In order to evaluate this interaction, a second measurement step is conducted to examine the base-surface warpage of the box. Therefore, a tangential plane is constructed at the center point of the box's web area based on the measured point cloud. Deviations of the base-surface area are measured in the tangential-plane's normal direction as illustrated in Figure 5.9. Thus, a positive deviation corresponds to a warp away of the box in the tangential plane's normal direction.

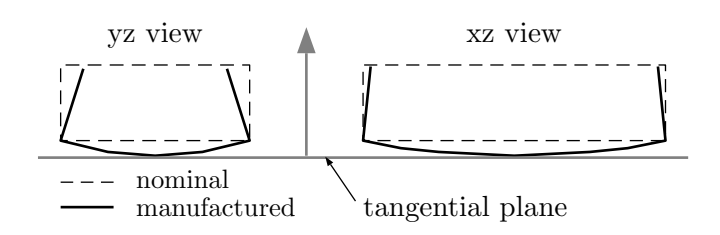


Fig. 5.9: Deviation measurement in tangential plane's normal direction

Up to this point measurement results are directly taken from the manufactured box specimens. Within the following, this configuration is denoted with 'un-modified'. As distortions of both boxes show comparable deviations, only one box is used for detailed examinations. As a first modification step the flanges of one box specimen are cut in order to assess the amount of manufacturing induced stresses. Thus, the constraining effect of the cross ribs is characterized. This experimental step is similar to experiments conducted by Fernlund [10] who obtained an almost constant spring-in angle for a similar rib structure after sectioning the flange areas. Figure 5.8 shows the applied cuts as blue lines which are approximately 20 mm away from the part ends. This modified specimen is referred to as 'modified' in the following.

Figure 5.10 shows the geometrical measurement of the modified and the unmodified box specimens. The evaluation of the un-modified specimen clearly shows as disturbed warped shape. The obtained field of normal deflections substantiate the constraining effect of the corner areas.

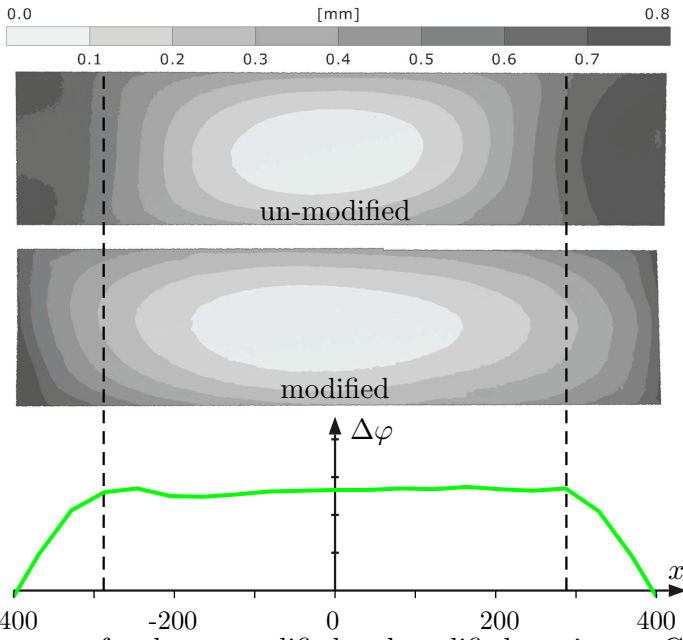


Fig. 5.10: Web-area warpage for the un-modified and modified specimens. Graph of the spring-in angle shows the effect of the geometrical constraints of the cross ribs.

The measurement of the modified specimen shows an undisturbed deflection field for the web area. This verifies that the un-modified structure is within an equilibrium state where process distortions act against the structural stiffness. A comparison of the web-area warpage of the modified and the un-modified configuration with the measured spring-in angle, clearly shows the relation between the spring-in distortion and the disturbed web-area warpage of the un-modified configuration. Therein, the dashed lines represent the length values $x=\pm 289$ mm as outlined in the preceding. As magnitudes of the web-warpage are identical for both configurations these findings substantiate that the base-area warpage has residual character induced by the manufacturing process.

Consequently, it is assumed that overall process-induced distortions D are composed of a spring-in fraction $D_{\Delta\varphi}$ and a fraction due to warpage and in particular forced-interaction effects D_{warp} .

$$D = D_{\Delta\varphi} + D_{warp} \tag{5.2}$$

The magnitude of the web-area warpage induced distortions can be analytically derived supported by Figure 5.11, which represents a constitutive sketch of the box cross section.

Assuming a circular shape of the web area, the radius R is derived based on the parameters

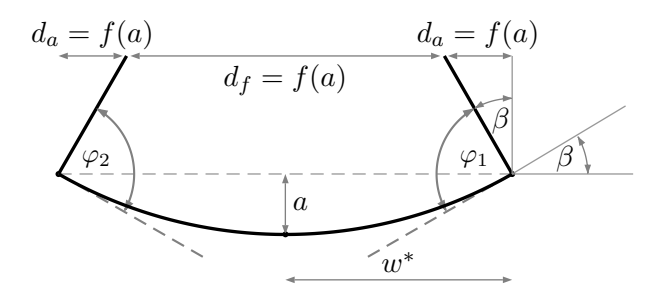


Fig. 5.11: Effect of the global part curvature on the measurands flange distance d_f and manufactured angles $\varphi_i = \tilde{\varphi}_i - \Delta \varphi_i$

 w^* and a according to Equation 5.3.

$$R = \frac{w^{*2} + a^2}{2a} \tag{5.3}$$

With respect to Figure 5.11 the web-area-warpage induced distortion d_a is derived according to Equation 5.4.

$$\sin \beta = \frac{w^*}{R} \quad \wedge \quad \sin \beta = \frac{d_a}{h} \quad \to \quad d_a = \frac{w^*}{R} \cdot h = \frac{w^* 2ah}{w^{*2} + a^2}$$
 (5.4)

Considering warpage of the un-modified configuration shown in Figure 5.10 at the centerline (x=0), the parameter a, depicted in Figure 5.11, is obtained to 0.30 mm. Thus, application of Equation 5.4 gives an additional decrease of the flange distance d_a on both box sides as shown in Figure 5.11, whereas $w^* \approx w/2 = 103$ mm and h = 55 mm.

$$d_a = \frac{w^*}{R} \cdot h = 0.32 \ mm \tag{5.5}$$

This suggests that the measured shape deviations Δy_m shown in Figure 5.7 contain a maximum of 0.32 mm induced by the web-area warpage. This represents an important cognition, as will be seen in Section 7.7, as this needs to be considered when comparing measurements and simulation results.

5.2 Evaluation of the Forced-interaction Effect

However, up to now, the origin of the undesired warpage of the web area remains unclear. According to Fernlund [10] the tool with its high thermal expansion can lead to residual stress gradients inside the laminate at the end of the curing process. Figure 5.12 shows a schematic which is directly applicable for the box structure fabricated here.

To characterize and assess the amount of residual stresses inside the box structure the modified specimen is further separated. Thereby, flanges and ribs are cut off using a conventional diamond saw. Figure 5.13 shows the box after sectioning.

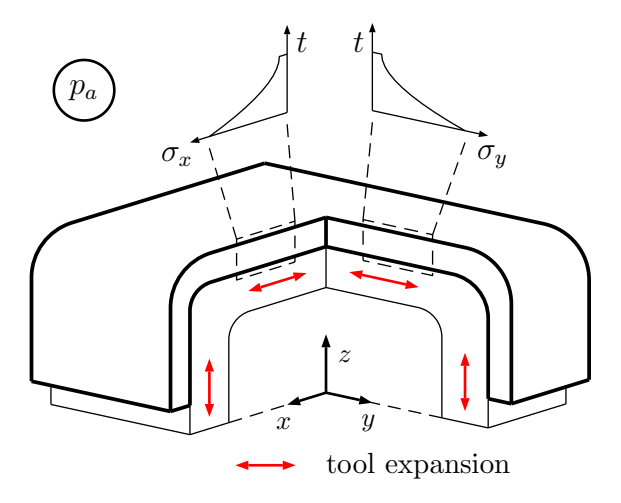


Fig. 5.12: Trough-thickness stress gradients induced by forced tool-part interaction.



Fig. 5.13: Box specimen after separating with a diamond saw

Subsequently, the resulting curvature of the web area is measured using the technique described above. Figure 5.14 shows the obtained result. A widely symmetric warpage distribution is observed with a magnitude of up to 2.80 mm which is approximately 3.5 times the magnitude of the modified configuration with its distortions of up to 0.80 mm. Note that the slight asymmetry of the warpage distribution is likely due to a minimum of misalignment of the single plies as a consequence of the manual layup process or a slight misalignment of the initial reference plane. At the bottom of Figure 5.14 a threshold of 0.30 mm is used to asses warpage in transverse direction by a comparison with the warpage of the modified configuration shown in Figure 5.10. This comparison reveals that the warpage magnitude in transverse direction remains almost constant in the range of 0.30 mm. The increasing warpage along the length direction can be explained with the removal of the stringers, as their moment of inertia does not counteract the residual stresses of the web area any more.

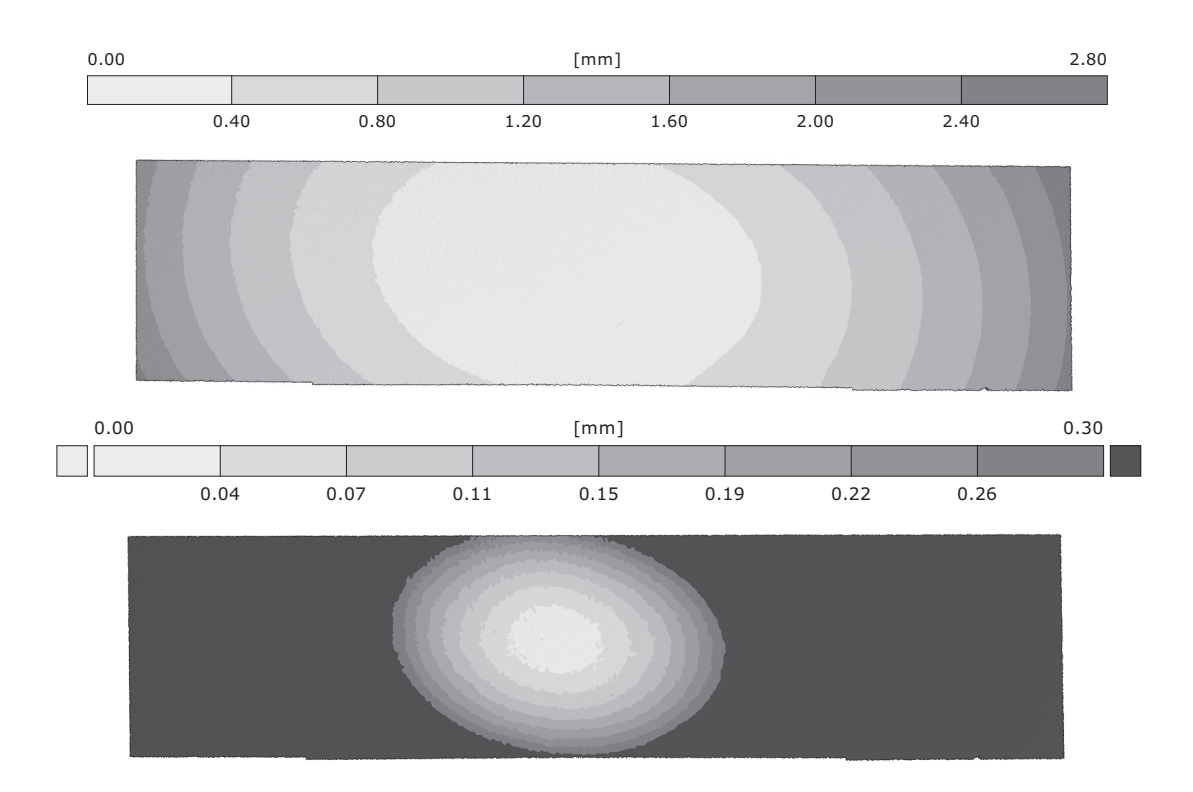


Fig. 5.14: Global web-area warpage (top) and area with a distortion under a threshold of 0.3mm (bottom)

Similar to the web-area, the flanges are inspected for warpage distortions as well. Therefore, both stringers are fixed together while tool-sided surfaces show towards each other. Figure 5.15 shows the simple measurement setup. The maximum distance between both stringer is obtained to 4.77 mm which is measured using a hand caliper. Thereby, the stringer length is 754 mm which is approximately 44 mm less than the initial box length induced by the trimming.



Fig. 5.15: Flange warpage of the separated flanges is obtained to 2.385 mm. Flange centers warp away from the tool

Considering the findings of the warpage investigations described in Chapter 3, the magnitude of the web-area warpage as well as the stringer warpage are of unexpected magnitude, as results presented there suggest that warpage will diminish for structures thicker than 1.5 mm, in particular for non-UD layups. The findings for the box structure clearly substantiate that conventional warpage described in Chapter 3 is not the exclusive source for the distortions obtained here. Therefore, it is assumed that the forced-interaction effects impedes the structural shape to a non-negligible amount. To validate this presumption a set containing three specimens is fabricated while two specimens have a C-shape and one is flat, similar to the warpage specimens shown in the preceding. Figure 5.16 shows the specimen shapes schematically. Experiments are solely done for specimens aligned in part-length direction as measurable distortions are expected to be larger and consequently more accurate to measure.

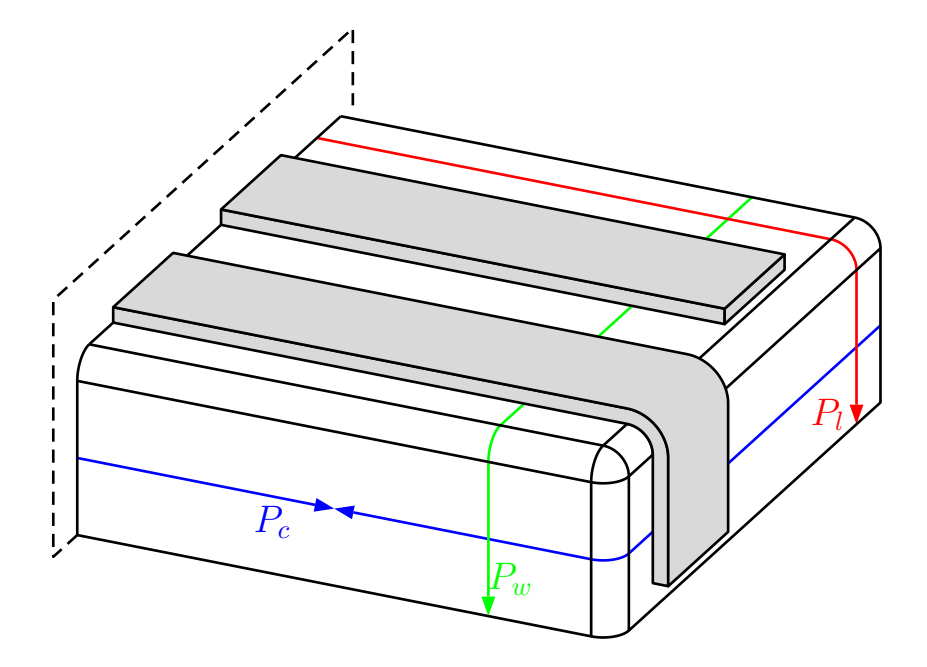


Fig. 5.16: Schematic of the tool geometry with applied flat and angled specimens. Blue, green and red measurands correspond to circumferential, longitudinal and transverse paths on the tool, respectively.

Specimens are fabricated with a UD layup of identical M21/T800 material. The deviation from the box-specimens layup $[0, 90]_{3s}$ is necessary due to material shortage. However, a comparison between the C-shaped parts and the flat specimen allows the quantification of the corner effect and therewith the accompanying geometrical locking. Figure 5.17 shows the fabricated specimens.



Fig. 5.17: Fabricates specimens to characterize the forced-interaction effect. C-shaped and I-shaped parts have a web-length of 798 mm and 754 mm respectively.

The obtained warpage of the stripes is shown in Figure 5.18, while distortions of the C-profiles is obtained twice as high as for the flat specimen.

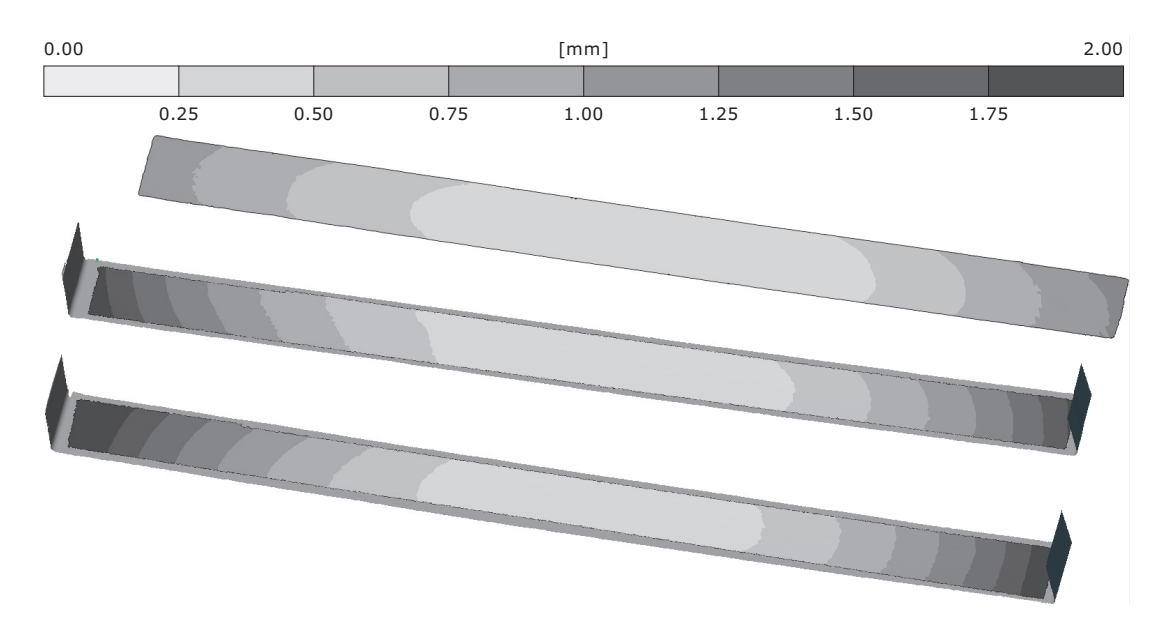


Fig. 5.18: Measurement reveal a warpage increase of 100% comparing C-shape to flat specimen

This clearly underlines the effects that a tool with considerable thermal expansion can lead to significant part distortions when the composite material is cured within a process using high temperature and high pressure. The obtained warpage of the C-shape stripes suggests that the double-curved shape of the entire box could be a result of the type of distortions. However, when considering the geometrical shape of the box this is to be questioned as the warpage of the C-shaped section directly work against the moment of inertia of the stringers which are comparable to I-profiles in the present case. Considering the geometrical properties it is unlikely that comparable small distortions obtained for the C-shape stripes are able to deform the whole structure against its stiffening elements. Inspecting the tool's geometry, depicted in Figure 5.16, three particular paths of the tool surface can be assigned. Thereby, P_l , P_w and P_c denote paths in the tool's length, width and circumferential direction, respectively. With the experiments documented in the preceding it is shown that forced-interaction effects lead to an increased curvature of the box along the C-shaped paths P_l and P_w . However, path P_c is of particular importance, as it has a closed geometry. According to Sun et al. [68] and supported by the experiments described in Section B it is assumed that no ply-to-ply slippage occurs during the process which is due to high resin viscosity and due to the high autoclave pressure. Assuming that the composite material is able to transfer stress shortly after reaching the gel point and that no slippage between the layers occurs, the length of the circumferential path is fixed at a temperature below the final curing temperature which is called T_{fix} in the following. Further temperature increase during the process likely leads to an elastic deformation of the part. As can be seen in Figure 5.16 this effect acts in the ribs and the stringers which are the stiffening, load-carrying elements of the box.

A simple FE model is set up to illustrate this relation. Assuming that ribs and stringers are in a tension stress state at the end of the curing process which is due to the expanding tool, these residual stresses tend to relax when the constraint of the tool diminishes during demolding. Within Figure 5.19 this effect is modeled with a contraction of the lightgray area in circumferential direction. The obtained deformed shape of the box substantiates the assumption that this effect, which acts in circumferential direction, could be responsible for the global box distortions.

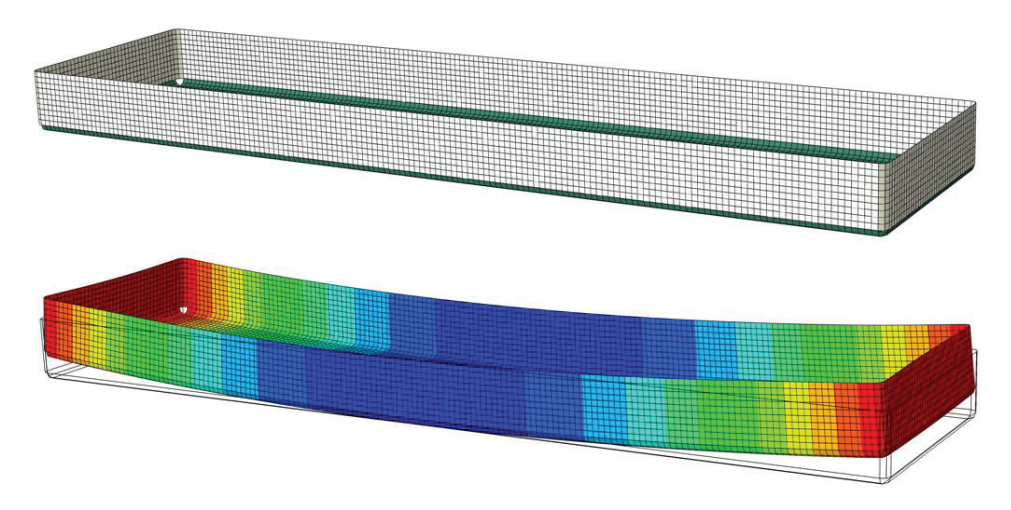


Fig. 5.19: Box FE model. CTE of the lightgray area is manually modified to show effect of residual stresses in circumferential direction. Stresses in circumferential direction induce global warpage of the box

This is supported by the comparison of the obtained web-area warpage of the modified configuration shown in Figure 5.10 with the distortions of the fully separated web-area shown in Figure 5.14. It is obvious that the ribs in the modified configuration enforce higher warpage in transverse direction than in the fully separated configuration. As the CTE of the ribs should be identical to that one of the web area due to the identical layup, this effect can not be explained with differences in thermal contraction. Consequently, it verifies the presumption made before that residual stresses act in the stiffening elements. However, it remains unknown whether the integral design of the ribs and stringers abets or reduces this effect.

As this source is of particular importance for the manufacturing concept of a fully integral stiffened wing cover shown in Figure 5.1 it is experimentally validated with a slightly changed box design. While the overall geometrical dimensions of the box remain identical, a gap between ribs and stringers at the circumferential corners is designed in order to break the circumferential force flux. Figure 5.20 shows a schematic of the modified box geometry as it is manufactured on the identical tool as the previously presented boxes.

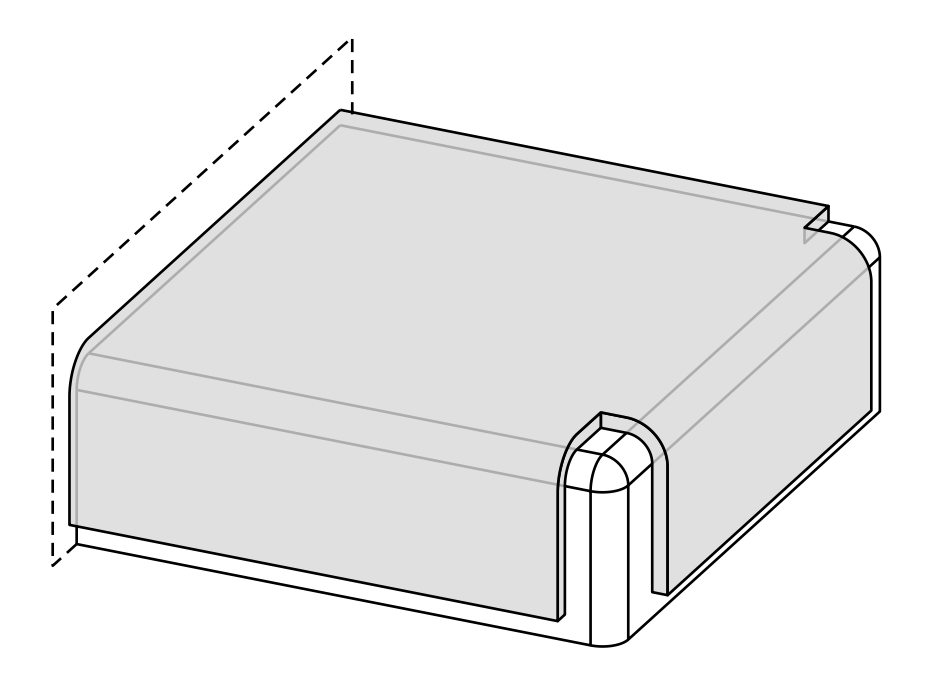


Fig. 5.20: Modified box design with a gap between stringers and ribs to break flux of force in circumferential direction



Fig. 5.21: Modified box structure with broken circumferential force flux

The measured web-area warpage is shown in Figure 5.22. At a first glimpse, the obtained measurement result shows a different character compared to the warpage plots shown above. This is induced by a small twisting of the web-area which is likely induced by misalignment of one ply during the manufacturing process. In addition, the missing connections between the ribs and the stringers lead to a box structure with a decreased torsion stiffness. Thus, misalignment-induced distortions can distort the box more easy compared to the integral box.

However, as shown in the former web-warpage evaluations the maximum warpage is obtained at the box centerline. Thus, the warpage of the box is evaluated based on a section cut at the centerline as shown in Figure 5.22. This is feasible, as this area of the part is unaffected by the twisting.

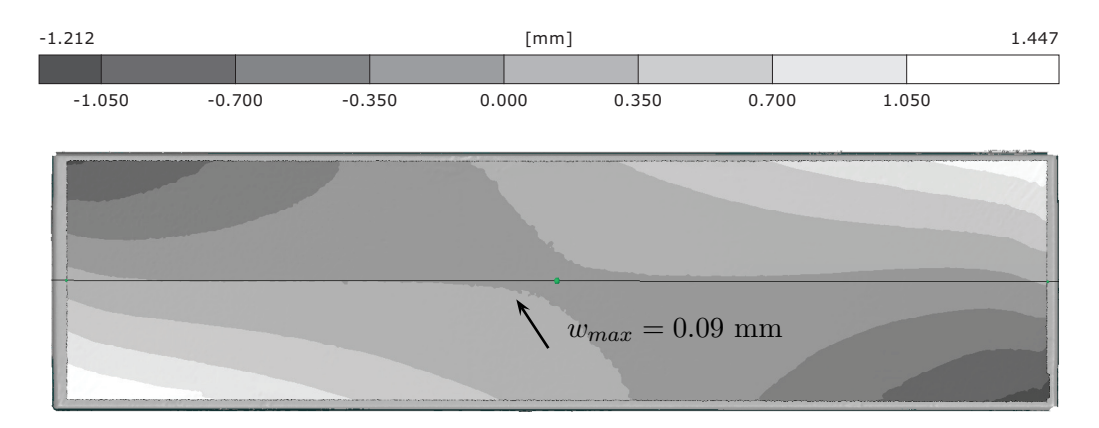


Fig. 5.22: Maximum web-area warpage of the cornerless box is obtained to 0.09 mm. Saddle shape is observed which is likely due to misalignment effects during the manual layup

The measurement procedure utilizes one mid-section point which is generated from two selected point on the part's centerline. This mid-section point is projected to the measured inner-part surface and the distance between both points is derived. It is shown as a big dot in the center of the box depicted in Figure 5.22. The web-area warpage is obtained to w = 0.09 mm which is significantly smaller than that for the fully-separated ($w \approx 2.8$ mm) and the modified ($w \approx 0.8$ mm) configurations.

This result substantiates the assumption that the global warpage obtained for the integral manufactured box is related to the closed force flux acting in circumferential direction along stringers and ribs. Furthermore, it becomes obvious that the warpage distortions along the paths P_l and P_w are not the main drivers of the global warpage, as the structure shows almost no curvature in longitudinal and transversal direction.

Figure 5.23 shows the manufactured box while. For this picture the twist is constrained by double-sided adhesive tape. This allows a better inspection of the shape of the web area. The obtained average deflection of the web area is significantly smaller compared to the box with the closed circumferential path.

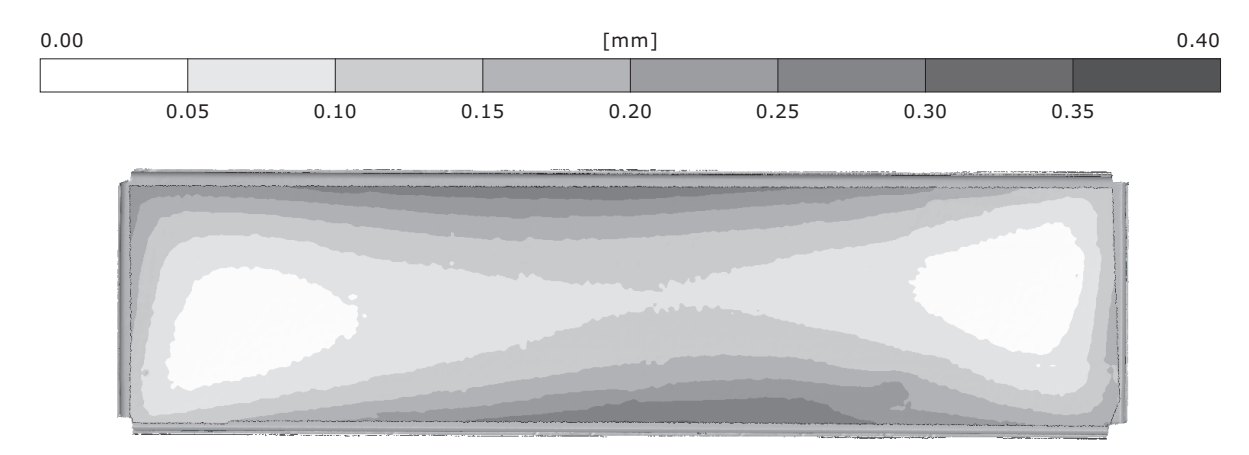


Fig. 5.23: Web-area warpage of the modified box design with interrupted circumferential path

Indicated by the measured flange to web angles shown in Figure 5.8 the structure's behavior is almost undisturbed in the center area. Therefore, it is assumed that the increasing deflection, obtained in the center of the part, next to the stringers, can be traced back to the simple forced interaction effect obtained for the long C-profiles shown in Figure 5.18. However, this is not experimentally verified in this thesis.

5.3 Cognitions from the investigation of the forced-interaction effect

Within the preceding section, manufacturing-induced distortions of an integral box structure are investigated. It is made from UD prepreg material M21/T800 with a $[0, 90]_{3s}$ layup to blank out effects due to layup asymmetry. The box is cured on an aluminum tool and fabricated according to the MRCC ($T_{Cure} = 180^{\circ}C$). After processing, the box shows distortions which cannot be completely explained neither with warpage nor spring-in what is a consequence of the integral design.

Measurements of the flange distance and the spring-in angles along the box's length direction clearly show that spring-in induced distortions are accompanied by a superposing fraction induced by the considerable web-area warpage of the box. By means of selected cuts, the residual stress state of the box is analyzed, while a relation between the box height and the observed deformation state is obtained. Furthermore, it is shown that the forced-interaction effect leads to increased warpage distortions, when comparing C-shaped (geometrically constraint) and flat (no constraint) strips after the manufacturing process. However, the main finding of this experimental investigations is that the global warpage of the box specimen is mainly induced by stresses acting in parts circumferential direction. These, stresses generate during the curing process, while the tool expands and the composite material is in a visco-elastic state. When disconnecting ribs and stringers within a corner-free design the global web area warpage diminishes almost completely.

It should be noted that experimental results presented in this section are strongly focused to answer the question for the main sources of the observed box distortions. Therefore, it is clearly pointed out that further experimental investigations are necessary to achieve a material-unspecific characterization of the forced-interaction effect and to assess corresponding magnitudes of scattering.

5.4 Numerical Analysis of T-Stiffener to Skin Connection

Composite T-joint structures are widely used within composite applications such as airframes for example. In context of this thesis, this kind of connection between stiffening elements and the skin are prone to show manufacturing-induced effects which result in an increase of waviness of the outer skin. For the majority of composite applications this effect can be neglected as no particular requirements are given. However, when thinking of a integrally fabricated wing cover, which should provide natural laminar flow qualified surfaces, this effect must be considered. Figure 5.24 shows a well manufactured micro-section of a T-joint which is extracted from Trask et al. [94].

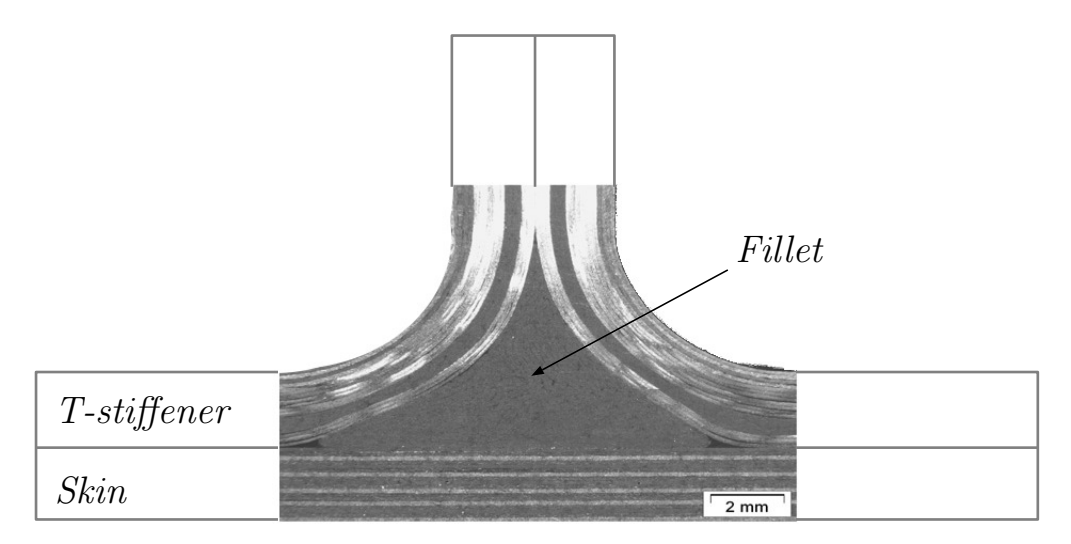


Fig. 5.24: Composite T-section joint with characteristic fillet. Figure extracted from Trask [94] and subsequently graphically modified

A two-dimensional parametric FE model of a T-joint is used to characterize the behavior of this kind of structural connection. The numerical study focuses on the effect of the fillet material, the ratio between the stiffener and the skin bending stiffness which is driven by both, the skin and the laminate layup, the effects of the stiffener foot width and the stiffener radius.

Figure 5.25 illustrates the modeling parameters of the parametric plane-stress FE model. The geometrical parameters A, A_1 , R_i , t, B denote the stiffener height, the half of a complete stiffener foot width, the inner stiffener radius, the nominal ply thickness and the half stringer distance, respectively. The stiffener and the skin laminate can be arbitrarily selected as symmetry is automatically assumed. Symmetry of the layup is presumed as this is a common scenario within current applications. Furthermore, asymmetry effects cannot be regarded with this kind of plane stress model. Indirect asymmetry effects, driven by the stiffener geometry in combination with the applied UD-ply based laminates, remain disregarded here although they can induce a twist of the stiffener.

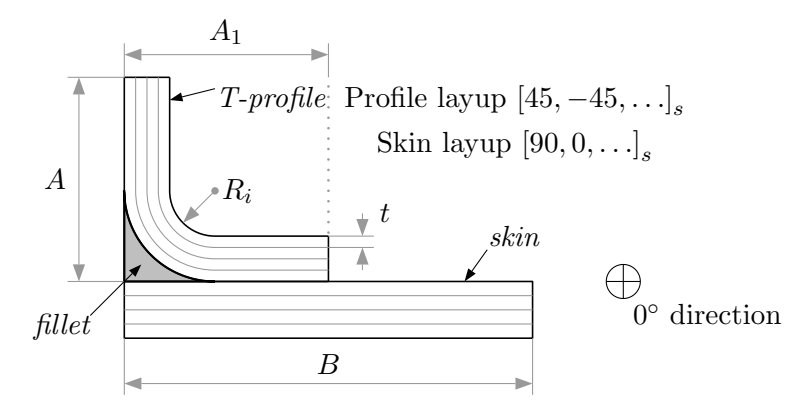


Fig. 5.25: Modeling parameters of the T-joint.

Figure 5.26 shows the assigned boundary conditions within the simulation and the local tangential and radial directions. Within the model the radial direction corresponds to the ply thickness direction while the properties in the models tangential direction are a function of the ply angle and its nominal properties in the ply coordinate system. The global 0° direction of the whole model is perpendicular to the investigated cross section. For sake of clarity, the 0°

direction is illustrated in Figure 5.25. The light gray illustrated configuration represents the case where half of the stringer distance is equal to the stringer foot width $A_1 = B$. In this case, the symmetry boundary condition of the skin is extended to the stiffener laminate. The fillet material is modeled as a homogeneous in-plane isotropic material which properties will be varied later. This approach is in accordance with the modeling technique used by Hélénon et al. [95].

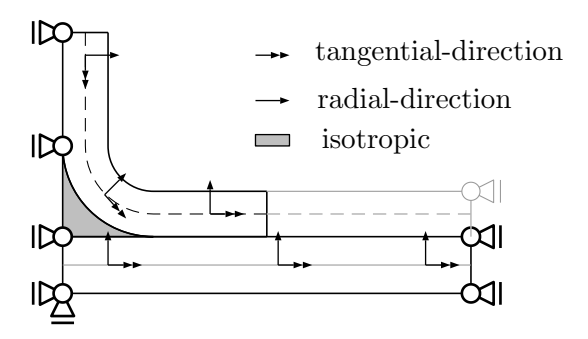


Fig. 5.26: Local material orientations and boundary conditions of the plane-stress model. Light-gray depicted shape represents maximal configuration where stringer foot width A_1 equals the stringer distance B. In this case, symmetric boundary conditions are extended to the stiffener area.

Due to the number of modeling parameters in combination with the design freedom within the laminate stacking the number of different configurations is tremendous. The aim of this study is to gain information about the main drivers and their influence on measurable deflections. Therefore, no optimization tools are used here. Instead, modeling parameters are varied based on engineering judgment. Material properties used within the FE analyses are derived from resin and fiber properties given in Table 4.2, with the exception $\alpha_m = 65 \text{ ppm/K}$. The ply properties of each ply are derived using ESAComp 4.3 while a V_f of 60 % is assumed for the composite plies. The Poisson's ratio and the shear modulus of the UD plies in the transverse plane are derived to $\nu_{23} = 0.45$ and $G_{23} = 3270 \text{ MPa}$. The chemical shrinkage of the resin is assumed to $\Delta V = -5$ %. Corresponding strains in the UD-ply transverse directions are derived using Equation 4.6. Figure 5.27 illustrates the complex stress state schematically.

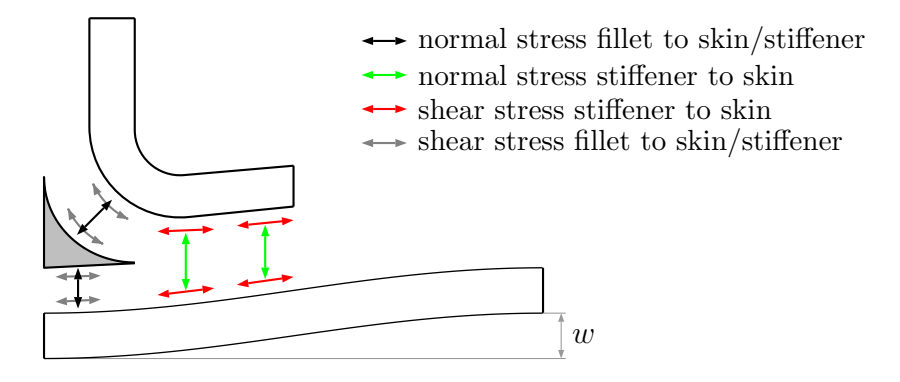


Fig. 5.27: Acting stress state in a T-joint induces global deflection of the skin

The global deflection w along the half of the stringer distance B is evaluated in this study to assess the effect of the varied parameters. It can be assumed that the obtained deflection w is a function of the stiffener and skin layup as well as the fillet properties.

Figure 5.28 shows the FE model for an arbitrarily selected configuration. The geometric parameters are A = 30 mm, $A_1 = 40$ mm, B = 110 mm and $R_i = 4$ mm. The stiffener and the skin layup are $[45, -45, 90, 0, 90, 0]_s$, $[45, -45, 90, 0]_s$, respectively. It should be noted that the mesh density is a parameter within the parametric model as well. However, its value is kept constant for all simulations presented here.

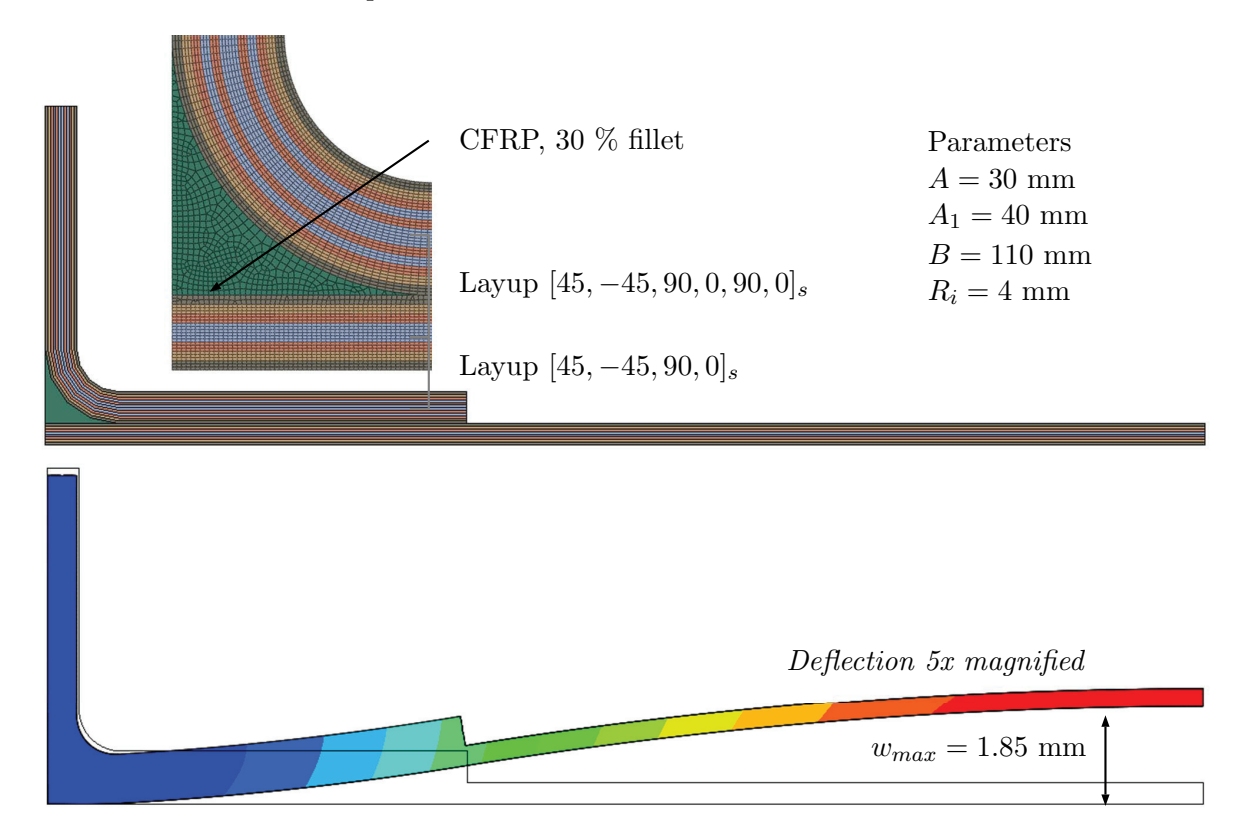


Fig. 5.28: T-joint configuration with 12-ply stiffener and 8-ply skin. Laminate's global 1-direction is perpendicular to the depicted cross section

Effect of the Fillet Properties

Within the first simulations only the fillet properties are modified while the values of the geometrical parameters in the model are kept constant. The initial condition within the thermo-elastic simulation corresponds to the end of the curing process. Starting at a curing temperature of 180°C of the MRCC the thermal contraction is modeled based on conventional CTEs. Effects induced by the chemical shrinkage are considered using equivalent CTE (α_{eq}) which transfers the volumetric shrinkage ΔV of the resin to corresponding strains in the transverse ply directions directions. The same strategy is used for the ply properties, whereat the orientation of the plies are considered in the model.

Eight different fillet material properties are considered which are summarized in Table 5.1. The material properties are calculated with ESAComp whereat the main parameter is the V_f which is the critical parameter of the fillet region. The parameters given in Table 5.1 represent ply properties in the resin dominated transverse direction

Material	E [MPa]	ν [-]	$\alpha [\mathrm{ppm/K}]$	$\alpha_{eq} \; [\mathrm{ppm/K}]$
Neat resin	4670	0.37	65.0	92.6
CFRP, 30%	8117	0.37	47.7	98.1
CFRP, 60%	14950	0.37	30.3	55.8
CFRP, 75 $\%$	21614	0.37	21.65	34.8
E-Glas, $30~\%$	8972	0.37	47.0	98.1
E-Glas, 60%	19489	0.37	29.0	55.8
E-Glas, 75 $\%$	34418	0.37	20.0	34.8
EPDM	1.5	0.48	800.0	0

Tab. 5.1: Mechanical parameters of investigated fillet materials

As can be seen in Table 5.1 an increase of V_f results in an decrease of the CTE as less resin leads to less thermal contraction. A similar effect is observed, whereat an increase of the V_f results in an decrease of the equivalent strains in transverse direction which is analytically describes by Equation 4.6.

The geometrical parameters are set to $A = A_1 = 40$ mm, B = 90 mm, $R_i = 3$ mm and $\Delta T = -160$ °C. To blank out curvature inducing effects due to different laminates of stiffener and skin both layups set to $[45, -45, 90, 0]_s$ which corresponds to a thickness of 2 mm each.

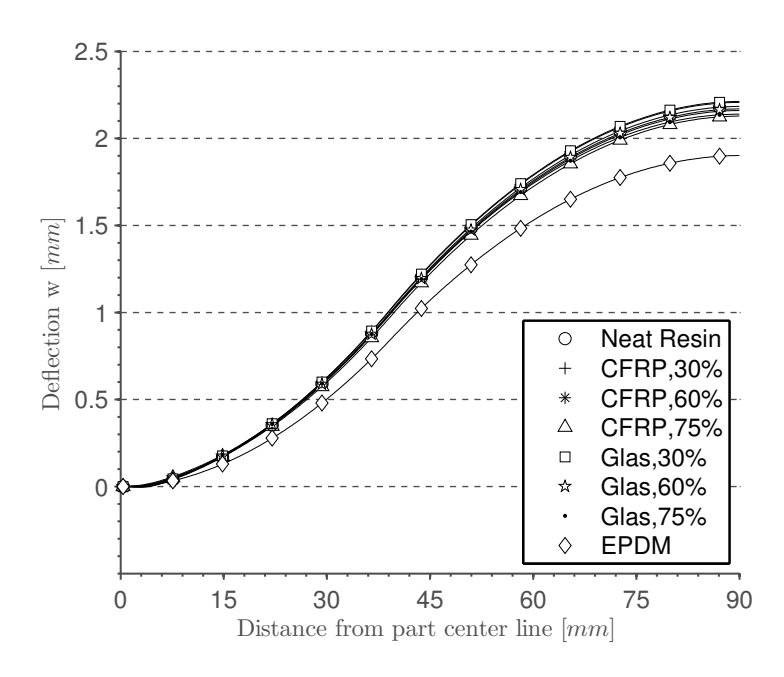


Fig. 5.29: Calculated deflections of the T-joint cut out for varying fillet materials

The derived deflections show a sinusoidal character while the magnitudes are similar for all configurations. Only the EPDM configuration show approximately 15 % less deflection. However, none of the configurations show a local waviness directly under the fillet.

Effect of the Stiffener Foot Width

Within a second step the stiffener foot width is modified within a range of $A_1 = 20 - 60$ mm and to a special configuration where $A_1 = B$. Other geometric properties and both layups remain unchanged (B = 90 mm, A = 40 mm, $R_i = 3$ mm). The fillet material CFRP, 30 % is used for the fillet area.

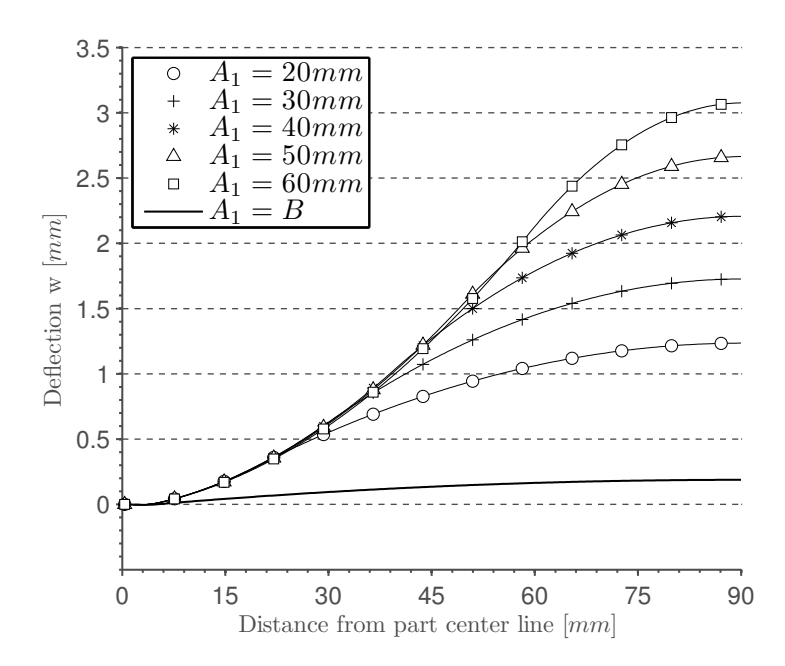


Fig. 5.30: Calculated deflections of the T-joint cut out for varying stiffener foot widths

The obtained deflections illustrated in Figure 5.30 show a similar character which was expected. However, the obtained magnitudes depend strongly on the stringer foot width. From the results it can be concluded that an increasing foot width leads to an increased deflection. However, the extreme configuration where the stiffener foot length is equal to the stringer distance shows only a fractional amount of the total deflection. This is clearly an effect of the doubled laminate thickness which corresponds to an eightfold moment of inertia for the skin. Thus, this stiffener design promises particular benefits when focusing on surface properties with a minimum of waviness as it is required for natural laminar flow for example. Consequently, this design is used for the NLF upper wing cover which is shortly described in Section 7.9. Note that again, no conspicuous local waviness in the fillet area is obtained on the outer skin.

Effect of the stiffener radius width

The stiffener's inner radius is varied within another set of simulations. Thus, the fillet area increases with increasing radius R_i . The geometric properties are set to $A_1 = 40$ mm, B = 90 mm while R_i is varied between 1-12 mm. The fillet material remains CFRP, 30 % Figure 5.31 shows the obtained deflections of the panel for varying radii.

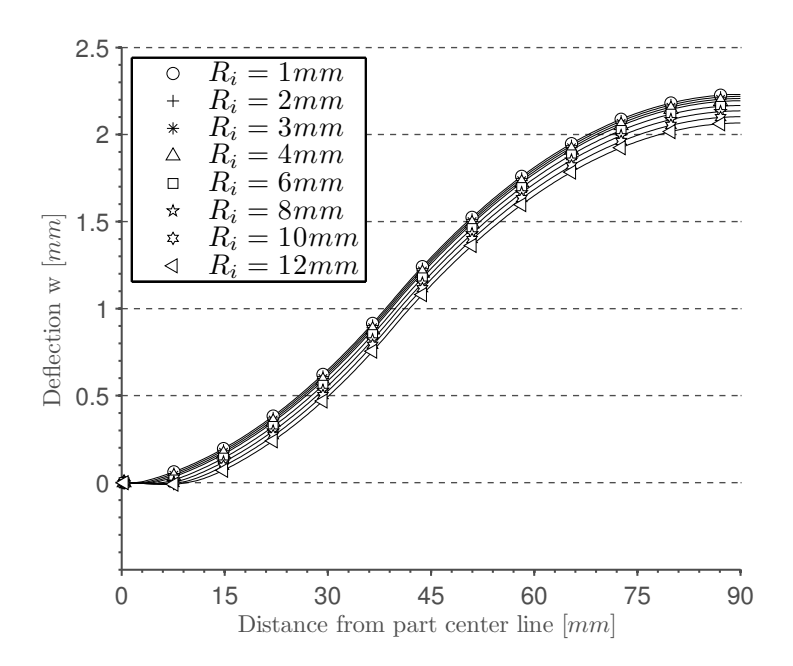


Fig. 5.31: Calculated deflections of the T-joint cut out for varying stiffener inner radius

The obtained characteristics of the deflection curves is identical. However, with increasing radii, the start of the initial curvature is shifted which can be explained with the relation between R_i and A_1 as the first connection between the flange area of the stiffener and the skin is shifted due to the radius increase. Again, the area directly under the fillet shows no waviness.

Effect of the Stiffener to Skin Bending Stiffness Ratio

Up to this point, geometrical and material properties of the T-joint are varied while the layups remain identical for stiffener and skin. The effect of different layups is investigated in this subsection. Therefore, the stiffener layup is varied to find the a relation with the measured deflections w. Different layups affect the coefficients of thermal expansion which leads to increasing or decreasing deflections. On the other hand, is can be assumed that a stringer with a higher stiffness is able to induce larger deflection to a comparable soft skin. For sake of illustration, the deflection w is shown as a function of the ratio of the profile's bending stiffness represented by the parameter $D_{22,profile}$ and the skin's bending stiffness $D_{22,skin}$.

All conceivable multi-angle 8-ply, 12-ply and 16-ply laminates and unidirectional laminates $[0]_i$ and $[90]_i$ with a maximum of 24 plies are considered for the stiffener while the skin layup remains quasi orthotropic $[45, -45, 90 - 0]_s$. The geometrical properties of the T-joint are set to A = 40 mm, B = 90 mm and $R_i = 3$ mm. Furthermore a V_f of 60 % is assumed for the plies and CFRP, 30 % material properties are used for the fillet. Figure 5.32 shows the obtained simulation results. Therein, derived maximum deflections w_{max} are subdivided into groups according to number of plies or their corresponding laminates.

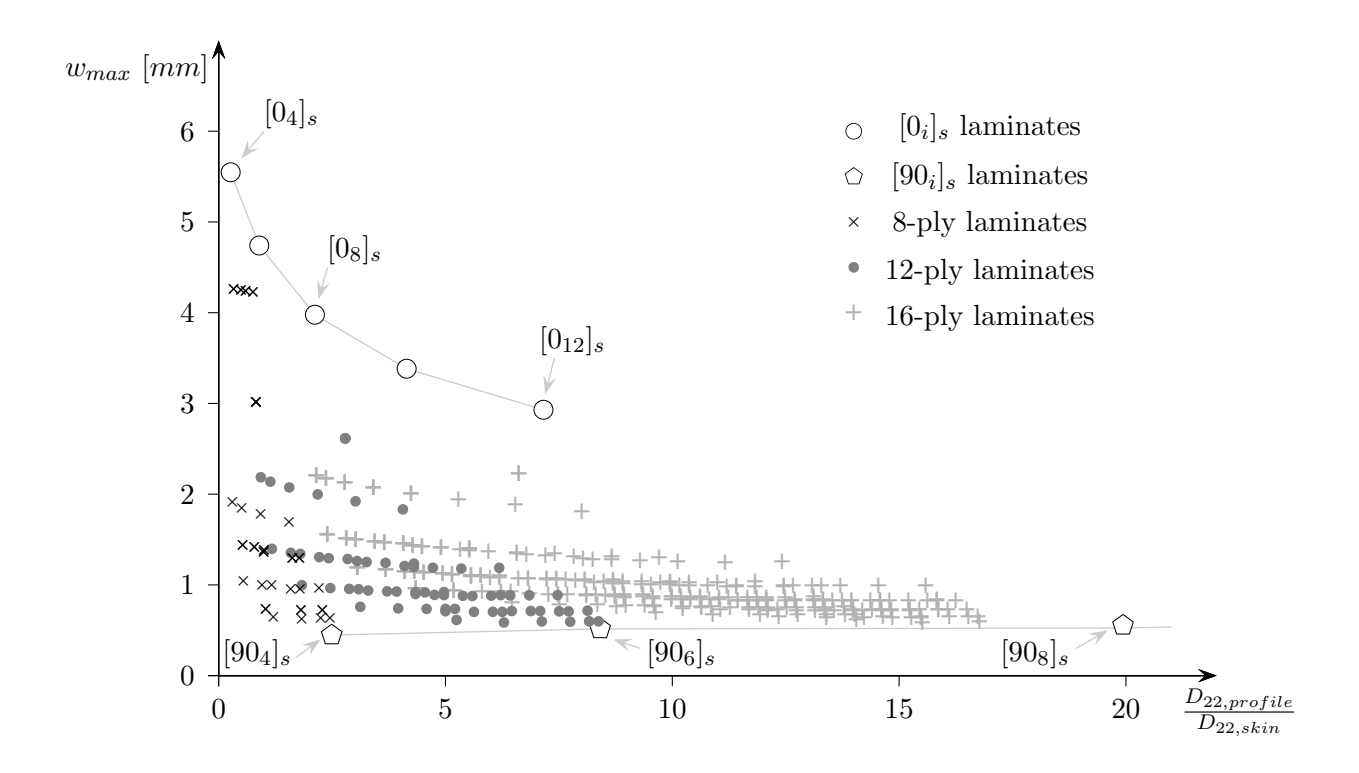


Fig. 5.32: Calculated deflections of the T-joint for varying stiffener layup while skin layup remains $[45, -45, 90, 0]_s$

The results show that for the majority of the cases the maximum deflection is in the range of 0.5 < w < 2 mm. Even for increasing bending stiffness differences this fraction remains constant. However, there are results which are conspicuous as a $[0_4]_s$ layup for example induces the largest global deflections. This effect is driven by the transverse contraction of the plies as no fibers are aligned in the stiffeners circumferential direction. Therefore, the massive curvature is mainly induced by the CTE mismatch between the stiffener and the skin. Furthermore, the simple elastic FE model does not consider strength properties.

Conclusion of the Numerical T-joint Investigation

The preceding numerical study focuses on process-induced distortions which can be induced by conventional T-joint connections between T-shaped stiffeners and the thin flat or slightly curved skin. In contrast to other stiffener geometries such as omega-shaped ones, T-joints show a fillet area which often has deviant material properties. Due to different material parameters in the fillet area and the base laminate due to a lower V_f , the geometry of this area is part of multiple investigations. In the presented numerical study essential geometrical parameters of the T-joint are varied to characterize their relevance in context of process-induced distortions. A parametric FE model is used to investigate the effect of geometrical properties of the T-joint, of different fillet materials and of layup differences between the skin and the stiffener. The obtained results show that the stiffener radius and the fillet material have almost no effect on the maximum deflection w. However, the stringer foot width has significant impact on the measurable deflection, whereat the global deflection increases with decreasing foot-width. Regarding the local waviness induced by the fillet area, none of the conducted simulation reveals a considerable effect. However, the configuration where $B = A_1$ shows very small maximum deflections, which promises that

this design is beneficial for applications where panel waviness is particular importance such as the NLF wing cover shown in Figure 5.1. Within Section 7.6 this tool is applied to a certain configuration while predictions are compared with one fabricated CFRP T-Joint.

6 A Semi-Numerical Prediction Approach

In this chapter the analytical equations are developed which enable a semi-numerical simulation procedure. The fundamental idea is to transfer measured process distortions on specimen level to appropriate simulation parameters which are applicable on part or component level. The model is applicable for warpage as well as spring-in distortions. It is based on the classical laminate theory. The use of shell elements promises almost no model-size limitations which is a drawback of state of the process simulation tools. In the presented form the model focuses mainly on part distortions.

6.1 Intention of the Model and its Area of Application

Composite specific manufacturing deformations are mainly caused by the significantly different material properties between the lamina-plane- and the through-thickness-direction. Accounting for that, existing micro level simulations use fine solid element meshes, whereas single plies are modeled with up to five layers of solid finite elements. In context of an early stage within the process development chain, this kind of modeling is disproportional as part geometry and layup is often not finally defined. Where part deformations are of predominant interest, the main drawbacks of those approaches are the disproportional amount of simulation parameters and high computational efforts due to transient modeling. For thin-walled structures, as they are in the focus of this thesis, transverse stress components σ_{13} , σ_{23} and σ_{33} are assumed to be small in comparison to the in-plane components σ_{11}, σ_{22} and σ_{12} . From a computational perspective, classical laminate theory is suitable for the modeling of the investigated slender structures of this thesis. Both, spring-in and warpage deformations manifest themselves in a curvature-change of a certain reference configuration. Warpage deformations are induced by interactions between tool and part at the interface. Those interactions are certainly distributed across the interface surface. Therefore shell-based modeling is suitable, as only lamina-plane parameters are affected. The main challenge for a shell-based approach is to model the spring-in phenomenon, which is mainly induced by through-thickness strains. As the 'thickness-direction' stress and strain components are excluded within the shell element formulation, this is a challenge. To overcome that barrier, the idea is to derive equivalent in-plane parameters which induce a curvature in the shell. This idea is similar to the well known bi-metal effect. The magnitude of the bending moment is dependent from geometrical measurements on test specimen level as well as the aspired modeling with the FEA, as will be outlined afterwards.

6.2 Model Derivation for Warpage of Flat Laminates

The starting point of the model derivation is the constitutive equation of a laminate in matrix form given in Equation 6.1. This and all other fundamental CLT basics used here are taken from Nettles [96]. In Equation 6.1 the matrices $\underline{\underline{A}}$, $\underline{\underline{B}}$ and $\underline{\underline{D}}$ represent the extensional stiffness matrix, the coupling stiffness matrix and the bending stiffness matrix, respectively.

$$\left\{ \underline{\underline{\varepsilon}}^{0} \right\} = \left\{ \underline{\underline{\underline{A}}} \quad \underline{\underline{\underline{B}}} \right\}^{-1} \cdot \left\{ \underline{\underline{N}} \right\}
 \tag{6.1}$$

Coefficients of those matrices can be written as:

$$(A_{ij}, B_{ij}, D_{ij}) = \sum_{k=1}^{N} \int_{h_{k-1}}^{h_k} \bar{Q}_{ij}^{(k)} (1, z, z^2) dz$$
(6.2)

Therein, \bar{Q}_{ij} , z, k and N are the coefficients of the laminate stiffness matrix $\underline{\bar{Q}}$ in the global laminate coordinate system, the coordinate in thickness direction, the ply identifier and the overall number of plies, respectively. Commonly, different types of loads are considered within the CLT. Within Equation 6.3 the superscripts 'm', 't', 'h' denote 'mechanical', 'thermal' and 'humidity', respectively.

$$\left\{\frac{\underline{N}}{\underline{M}}\right\} = \left\{\frac{\underline{N}^m + \underline{N}^t + \underline{N}^h}{\underline{M}^m + \underline{M}^t + \underline{M}^h}\right\}$$
(6.3)

Regarding a flat laminate composed of n plies as schematically sketched in Figure 6.1,

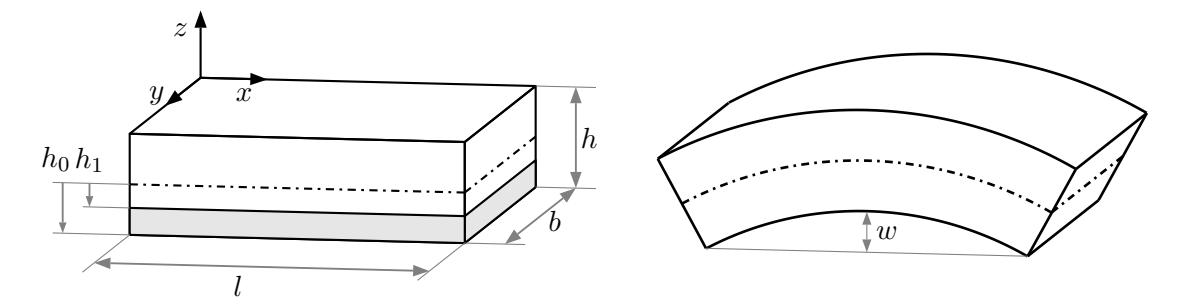


Fig. 6.1: Model parameters and warpage deflection w

a bending moment of the different sources \underline{M}^i can be written as:

$$\underline{M}^{i} = \sum_{k=1}^{n} \left\{ \underline{\underline{Q}}_{k} \cdot \underline{\varepsilon}^{0,i} \int_{h_{k-1}}^{h_{k}} z dz + \underline{\underline{Q}}_{k} \cdot \underline{\varkappa}^{i} \int_{h_{k-1}}^{h_{k}} z^{2} dz \right\}.$$
 (6.4)

From Equation 6.4, it can be seen that moments \underline{M}^i are plywise composed of one fraction induced by midplane strains $\underline{\varepsilon}^0$ and one fraction related to the change of plate curvatures $\underline{\varkappa}$.

For the sake of clarity, the methodology is derived analogously to common thermal loads. The advantage and the convenience of that will be outlined in the following. Assuming thermal strain of a ply to be unequal to zero $\underline{\varepsilon}^{0,t} \neq 0$ and curvature changes equal to zero $\underline{\varkappa}^t = 0$, the thermal bending moments are derived to:

$$\underline{\underline{M}}^{t} = \sum_{k=1}^{n} \underline{\underline{Q}}_{k} \cdot \begin{Bmatrix} \varepsilon_{x} \\ \varepsilon_{y} \\ \varepsilon_{xy} \end{Bmatrix}_{k}^{t} \cdot \frac{1}{2} \left(h_{k}^{2} - h_{k-1}^{2} \right)$$

$$(6.5)$$

It should be noted that the variables h_k and h_{k-1} represent the z-coordinate of the top-surface and the bottom surface of the k-th ply. That is depicted on the left hand side of Figure 6.1. Assuming an arbitrary layup without symmetry, each ply can contract or expand differently in different directions. That results in a thermal moment which leads to warpage (bending) of an originally flat part. That mechanism equals that one of well-known bi-metal principle. Regarding a symmetric (even and odd) single-material-laminate ($\underline{\underline{Q}}_k = \underline{\underline{Q}}_k$, $\forall k$) Equation 6.5 equals zero.

However, due to its characteristics, Equation 6.5 is suitable for the integration of a modification term. Thus, the introduction of a certain asymmetry due to modified expansion properties allows

a target oriented affectation. Note that only a single-sided modification leads to a resulting bending moment, as outlined above. Equation 6.6 gives the bending moments \underline{M}^* for an modified bottom ply k=1. This area is depicted light gray in Figure 6.1.

$$\underline{\underline{M}}^* = \begin{Bmatrix} M_x^* \\ M_y^* \\ M_{xy}^* \end{Bmatrix} = \underline{\underline{\underline{Q}}}_1 \cdot \begin{Bmatrix} \varepsilon_x \\ \varepsilon_y \\ \varepsilon_{xy} \end{Bmatrix}_1^* \cdot \frac{1}{2} \left(h_1^2 - h_0^2 \right) \quad \text{with} \quad \begin{Bmatrix} \varepsilon_x \\ \varepsilon_y \\ \varepsilon_{xy} \end{Bmatrix}_1^* = \Delta T \cdot \begin{Bmatrix} \alpha_x^* \\ \alpha_y^* \\ \alpha_{xy}^* \end{Bmatrix}_1$$
(6.6)

Nevertheless, that area of the manipulation is arbitrary. Regarding monolithic composite structures, the reference to the ply level is obvious as the lamina are the constituents of the laminate. That requirement loses its significance for UD laminates, for homogeneous orthotropic and for isotropic laminates. For remembrance, the aim of this approach is to transfer geometrical measurement on test specimen level to corresponding FEA parameters which induce the measured distortions in the numerical model. That transfer is directly dependent on the underlying properties of the analytical model. In other words, magnitude of the calculated equivalent parameters, can be different with respect to the chosen area of modification. Nevertheless, those different parameters lead to the same deformation within the FE simulation if the model is set up correctly. That means, the dimensions of the modified area within the FE model must be identical to the ones used in the analytical parameter calculation. Note that the area corresponding to $h_1 - h_0$ must not be defined with ply borders when UD or homogenized laminates are considered. Therefore, parameters h_1 and h_0 should be considered as coordinates in through-thickness direction.

Applying the moment vector \underline{M}^* as shown in Equation 6.1 a corresponding vector of curvatures is derived which is shown by Equation 6.7.

$$\underline{\varkappa} = \begin{Bmatrix} \varkappa_{xx} \\ \varkappa_{yy} \\ \varkappa_{xy} \end{Bmatrix} = \underline{\underline{D}}^{-1} \underline{M}^* \tag{6.7}$$

Therein a symmetric laminate is assumed, since the bending moment due to layup asymmetry $\underline{\underline{M}}^t$ equals zero. Moreover, symmetric laminates are commonly used in industry as they do not result in a coupled bending extension behavior. Insertion of 6.6 gives Equation 6.8:

$$\underline{\varkappa} = \underline{\underline{D}}^{-1} \underline{\underline{Q}}_{1} \Delta T \cdot \begin{Bmatrix} \alpha_{x}^{*} \\ \alpha_{y}^{*} \\ \alpha_{xy}^{*} \end{Bmatrix} \cdot \frac{1}{2} \left(h_{1}^{2} - h_{0}^{2} \right). \tag{6.8}$$

Therein the vector of curvature $\underline{\varkappa}$ is calculated with respect to an arbitrary layup, which is symbolized by the bending stiffness matrix $\underline{\underline{D}}$ and the modified bending moments applied to the bottom surface exemplary. Double integration of the components of the vector of curvatures $\underline{\varkappa}$ gives the deflection components w_x , w_y and w_{xy} with respect to the global coordinates x and y. The total deflection of the originally flat part is a superposition of the single fractions of the doubly integrated components of the vector of curvatures $\underline{\varkappa}$. Thus the total deflection is given by:

$$w(x,y) = w_{xx} + w_{yy} + w_{xy}$$
 with $w_{ij} = \int_0^i \int_0^j (-\varkappa_{ij} \ d\xi) \ d\xi.$ (6.9)

Disregarding the contribution of the term w_{xy} , Figure 6.2 shows the corresponding deflections for two conceivable curvatures \varkappa_{xx} and \varkappa_{yy} .

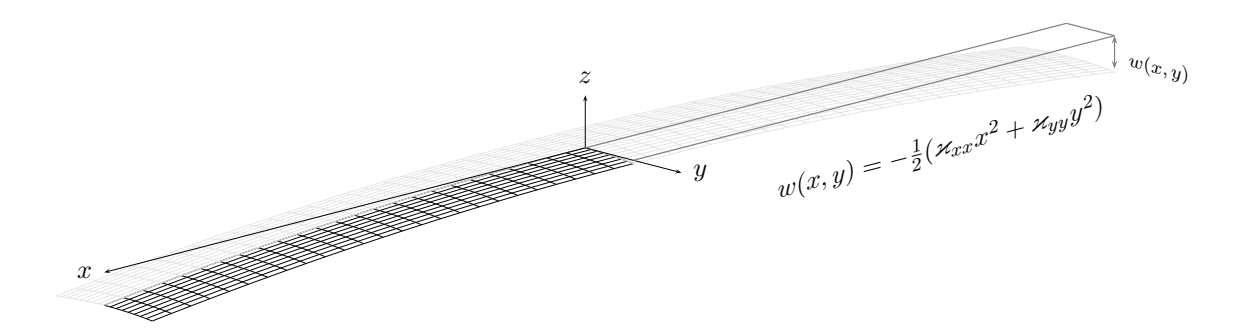


Fig. 6.2: Exemplary warpage deflection when warpage occurs in longitudinal and transversal direction

As the aforementioned equations are suitable for arbitrary layups the underlying relations can be significantly simplified for unidirectional laminates or when smeared material properties are used. Regarding the population of the matrices of Equation 6.8 with respect to that limitation, it is obvious that the system of equations can be reduced, whereat the first and the second line of the system remain. Dots represent non-zero terms of the corresponding matrices or vectors. Parameter Ξ is constant.

$$\underline{\underline{Q}} = \underline{\underline{D}}^{-1} = \left\{ \begin{array}{ccc} \bullet & \bullet & 0 \\ \bullet & \bullet & 0 \\ 0 & 0 & \bullet \end{array} \right\}, \ \underline{\alpha}^* = \left\{ \begin{array}{ccc} \bullet \\ \bullet \\ 0 \end{array} \right\} \qquad \Rightarrow \qquad \underline{\varkappa} = \Xi \cdot \left\{ \begin{array}{ccc} \bullet \\ \bullet \\ 0 \end{array} \right\}$$
 (6.10)

Applying Equation 6.6, the moment components M_x^* and M_y^* are given by equations 6.11 and 6.12.

$$M_x^* = \Delta T \left[\bar{Q}_{11} \alpha_x^* + \bar{Q}_{12} \alpha_y^* \right] \frac{1}{2} \left(h_1^2 - h_0^2 \right)$$
 (6.11)

$$M_y^* = \Delta T \left[\bar{Q}_{12} \alpha_x^* + \bar{Q}_{22} \alpha_y^* \right] \frac{1}{2} \left(h_1^2 - h_0^2 \right)$$
 (6.12)

Inserting those components into Equation 6.7, the components of the curvature vector are given by

$$\varkappa_{xx} = \frac{1}{\det(\underline{\underline{D}})} \cdot \left(D_{22}M_x^* - D_{12}M_y^*\right) \quad \text{and} \quad \varkappa_{yy} = \frac{1}{\det(\underline{\underline{D}})} \cdot \left(-D_{12}M_x^* + D_{11}M_y^*\right). \tag{6.13}$$

$$D_{ij} = \bar{Q}_{ij} \frac{h^3}{12}$$
 and $\det\left(\underline{\underline{D}}\right) = \left(\bar{Q}_{11}\bar{Q}_{22} - \bar{Q}_{12}^2\right) \cdot \left(\frac{h^3}{12}\right)^2$

Insertion and subsequent rearranging gives the curvature component \varkappa_{xx} and \varkappa_{yy} .

$$\varkappa_{xx} = \frac{\bar{Q}_{22} \frac{h^3}{12} \cdot \Delta T \left[\bar{Q}_{11} \alpha_x^* + \bar{Q}_{12} \alpha_y^* \right] \frac{1}{2} \left(h_1^2 - h_0^2 \right)}{\left(\bar{Q}_{11} \bar{Q}_{22} - \bar{Q}_{12}^2 \right) \cdot \left(\frac{h^3}{12} \right)^2} + \frac{\bar{Q}_{12} \frac{h^3}{12} \cdot \Delta T \left[\bar{Q}_{12} \alpha_x^* + \bar{Q}_{22} \alpha_y^* \right] \frac{1}{2} \left(h_1^2 - h_0^2 \right)}{\left(\bar{Q}_{11} \bar{Q}_{22} - \bar{Q}_{12}^2 \right) \cdot \left(\frac{h^3}{12} \right)^2}$$

$$\varkappa_{xx} = \frac{6\Delta T \alpha_x^* \left(h_1^2 - h_0^2 \right)}{h^3} \tag{6.14}$$

$$\varkappa_{yy} = \frac{-\bar{Q}_{12} \frac{h^3}{12} \cdot \Delta T \left[\bar{Q}_{11} \alpha_x^* + \bar{Q}_{12} \alpha_y^* \right] \frac{1}{2} \left(h_1^2 - h_0^2 \right)}{\left(\bar{Q}_{11} \bar{Q}_{22} - \bar{Q}_{12}^2 \right) \cdot \left(\frac{h^3}{12} \right)^2} + \frac{\bar{Q}_{11} \frac{h^3}{12} \cdot \Delta T \left[\bar{Q}_{12} \alpha_x^* + \bar{Q}_{22} \alpha_y^* \right] \frac{1}{2} \left(h_1^2 - h_0^2 \right)}{\left(\bar{Q}_{11} \bar{Q}_{22} - \bar{Q}_{12}^2 \right) \cdot \left(\frac{h^3}{12} \right)^2}$$

$$\varkappa_{yy} = \frac{6\Delta T \alpha_y^* \left(h_1^2 - h_0^2 \right)}{h^3} \tag{6.15}$$

Derived curvatures turned out to be independent from material properties, whereat the area of affectation, represented by the term $(h_1^2 - h_0^2)$, has a direct impact. Double integration of the curvatures with respect to the corresponding coordinate reveals the deflections.

$$w_{xx} = \frac{6\Delta T \alpha_x^* \left(h_1^2 - h_0^2\right)}{h^3} \cdot \frac{x^2}{2} \quad \text{and} \quad w_{yy} = \frac{6\Delta T \alpha_y^* \left(h_1^2 - h_0^2\right)}{h^3} \cdot \frac{y^2}{2} \quad . \tag{6.16}$$

Within Equation 6.16 the parameter w_{xx} and w_{yy} represent measurements of fabricated test specimens. Combining w(x) and w(y) to w(x,y) = w(x) + w(y)

$$w(x,y) = -\frac{1}{2} \left(\varkappa_{xx} x^2 + \varkappa_{yy} y^2 \right)$$
 (6.17)

Thus the transfer between measured deformations to corresponding expansion properties can be calculated with respect to the dimensions of the affected area. The application of that equations is discussed in detail within Section 7.1.

Rearranging Equation 6.16 and solving for α gives:

$$\alpha_x^* = \frac{h^3}{3\Delta T \left(h_1^2 - h_0^2\right)} \cdot \frac{w(x)}{x^2} \quad \text{with} \quad x_{max} = l/2$$
 (6.18)

$$\alpha_y^* = \frac{h^3}{3\Delta T \left(h_1^2 - h_0^2\right)} \cdot \frac{w(y)}{y^2} \quad \text{with} \quad y_{max} = b/2$$
 (6.19)

The preceding equations represent the connection between the measured warpage deflection and the corresponding simulation parameter $\alpha_x^* = f(w(x))$ and $\alpha_y^* = f(w(y))$

6.3 Model Derivation for Spring-In of Single- and Double-Curved Sections

Composite structures can have arbitrary shapes. As shown in the preceding section the proposed simulation strategy transfers a measured specimen deflection into an equivalent simulation parameter. This strategy should be used for the simulation of spring-in deflections as well in order to maintain simplicity of the used models. Therefore, a measured angle change $\Delta \varphi$, obtained from an L-profile specimen, should be transferred to an equivalent simulation parameter α^* what is shown in Table 6.1.

	Warpage	Spring-in
Relation	$w \to \alpha^*$	$\Delta \varphi \to \alpha^*$

Tab. 6.1: Relation between measurement and equivalent simulation parameter

The model approach presented within the preceding section is based on the considerations of a bi-metal. Consequently, a curvature \varkappa is derived which corresponds to a certain combination of two materials with different Young's moduli and different CTEs. Therefore, the derived curvature \varkappa_{xx} , in x-direction for example, is a linear function of the equivalent simulation parameter α_x^* as shown by the following equation which is simplified based on Equation 6.14.

$$\varkappa_{xx} = f_{lin} \left(\alpha_x^* \right)$$

Regarding arbitrary part shapes this linear transfer is not feasible for all shapes what is demonstrated by the following picture. For sake of clarity, cross sections for three different part shapes are illustrated in Figure 6.3. Therein, the curves $y_{arbit}(x)$, $y_{elli}(x)$ and $y_{circ}(x)$ represent an arbitrarily, an elliptically and a circularly curved shape, respectively. As can be seen clearly, only the circular arc has a constant curvature.

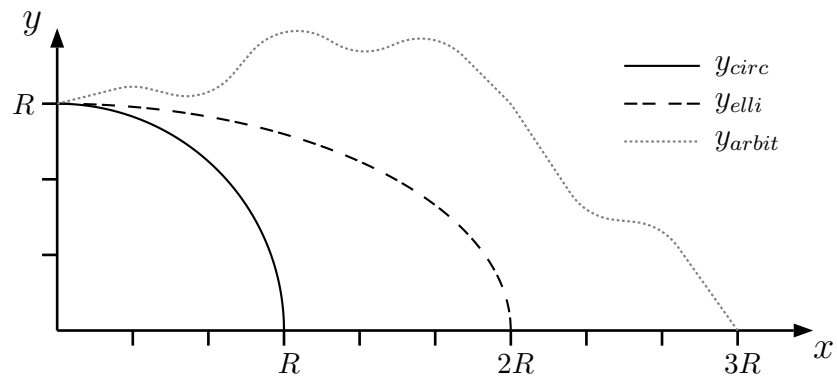


Fig. 6.3: Three different conceivable cross-section shapes

According to Merziger and Wirth [97], the curvature \varkappa of a function y=f(x) is derived according to Equation 6.20 where $y^{'}=dy/dx$ and $y^{''}=d^2y/dx^2$.

$$\varkappa(x) = \frac{y''}{\left(1 + (y')^2\right)^{3/2}} \tag{6.20}$$

Table 6.2 shows that only the circular arc has a constant curvature $\varkappa = 1/R$. Thus, the derived corresponding parameter is independent from the x-coordinate. With other word, a single parameter α^* can be used for a complete circularly-curved section.

	Arbitrarily curved	Elliptically curved	Circularly curved
Function	y = f(x)	$y = b \cdot \sqrt{1 - \left(\frac{x}{a}\right)^2}$	$y = R \cdot \sqrt{1 - \left(\frac{x}{R}\right)^2}$
Curvature	$ \varkappa(x) = \frac{y''}{\left(1 + (y')^2\right)^{3/2}} $	$\varkappa(x) = rac{a \cdot b}{\left(a^2 + x^2 \cdot \left(rac{b^2}{a^2} - 1 ight) ight)^{3/2}}$	$\varkappa = \frac{1}{R}$

Tab. 6.2: Three different part shapes and corresponding curvatures

Therefrom, it is concluded that the proposes strategy must be analytically based on circular curvatures. This is due to the shape of the used L-profile specimens as well as these provide information for a circularly curved part area only. Thus, the measured angle change $\Delta \varphi$ is a function of the arc length s which is the product of the initial angle $\tilde{\varphi}$ and the radius R.

At a first glimpse this is a limitation of the approach. However, when inspecting typical composite frame components circularly curved areas are standard. Therefore, it is not a significant limitation. In addition, curvature changing shapes, such as the elliptic one, shown in Figure 6.4

can be locally approximated by circular curves which allows the application of the approach. For sake of demonstration, this procedure is shown Section 7.5.

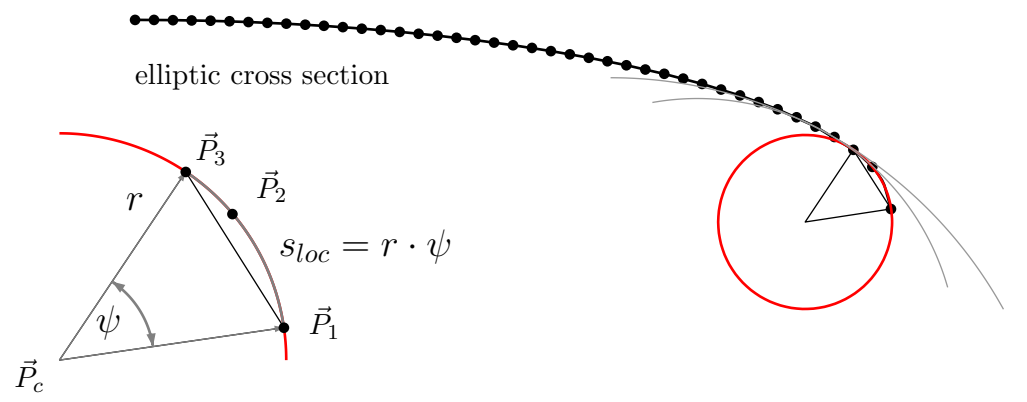


Fig. 6.4: Local circles are used to interpolate curvature-changing shapes

Based on the considerations given above the fundamental analytical equations are derived for circularly curved arcs in the following section. Equation 6.21 shows the benefit of the limitation to curvature-constant shapes. As $\varkappa \neq f(s)$ it acts as a constant during the integration which allows the aspired direct transfer $\Delta \varphi \to \alpha^*$.

$$\varkappa = \frac{d\varphi}{ds} \quad \to \quad \varphi = \int_0^{s_0} \varkappa ds \quad \to \quad \varphi = \varkappa \int_0^{s_0} ds \quad \text{as} \quad \varkappa \neq f(s)$$
 (6.21)

In order to cover shapes with varying curvatures by a corresponding parameter function a more complex, non-circular curved specimen would be necessary and the analytical equations given above must be updated. However, this approach remain unconsidered in this thesis.

Circularly Curved Sections

As warpage mainly affects flat structures mainly, spring-in is omnipresent for curved structures. In general, doubly curved geometries with different radii are conceivable as depicted Figure 6.5. Spring-in and warpage deformations represent a change of an initial curvature.

Thus, the fundamental model assumptions outlined in Section 6.2 are suitable for both phenomena. Slight changes which account for the curvature of the structure need to be introduced.

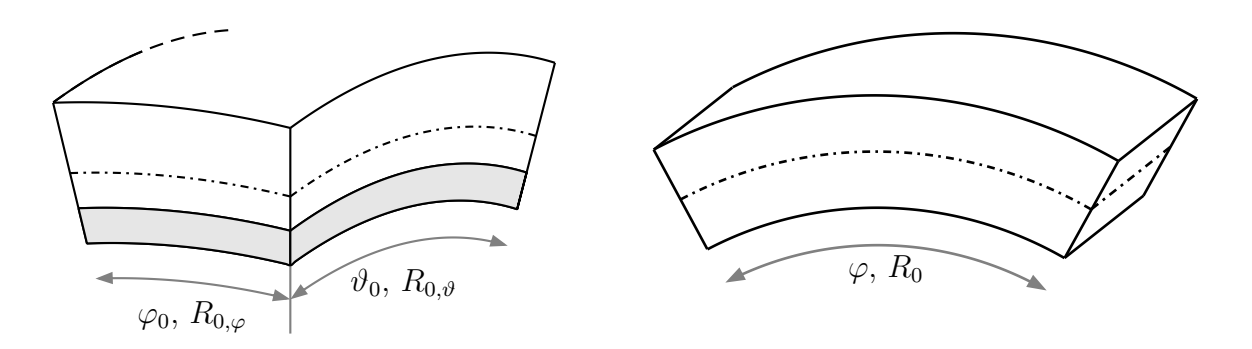


Fig. 6.5: Geometries of a doubly curved structure (left) and a simple-curved structure (right)

Equation 6.22 is equal to Equation 6.7. Therein, φ and ϑ represent the change in curvature with respect to the corresponding arc length s_{φ} or s_{ϑ} , respectively. Within this derivation constant

radii are assumed as those are commonly applied. Nevertheless, the derivation for non-constant radii is possible.

In contrast to the warpage deflection, spring-in deformations are characterized by the deviation of the nominal and the fabricated angle. Consequently, the change in curvature needs to be integrated once only as this is described by the first derivative of the displacement. The integration $\partial \varphi/\partial s_{\varphi}$ along the arc length s_0 gives the corresponding angle change φ , whereas the initial arc length s_0 is the product of the radius $R_{0,\varphi}$ and the section angle φ_0 as shown in Equation 6.23.

$$\varphi = \frac{\partial \varphi}{\partial s_{\varphi}} \int_{-s_0}^{s_0} ds \quad \text{with} \quad s_0 = R_{0,\varphi} \cdot \varphi_0$$
 (6.23)

In order to transfer a measured spring-in angle to a corresponding expansion parameter of the affected area, Equations 6.23 and 6.22 are combined. In order to underline the characteristic as an measured parameter φ_{mes} is introduced wheres $\varphi_{mes} = \varphi$.

$$\varphi_{mes} = \varphi_0 \cdot R_{0,\varphi} \cdot \frac{6\Delta T \alpha_{\varphi}^* \left(h_1^2 - h_0^2\right)}{h^3} = s_0 \cdot \varkappa_{xx}$$

$$(6.24)$$

Inspection of Equation 6.24 reveals that angle change φ_{mes} is given by the product of the initial arc length s_0 and the corresponding change in curvature \varkappa_{xx} which has been introduced in the preceding section. Rearranging Equation 6.24 gives the corresponding equivalent thermal expansion parameters for both directions of curvatures α_x^* and α_y^* .

$$\alpha_{\varphi}^* = \frac{\varphi_{mes}}{\varphi_0} \cdot \frac{1}{R_{0,\varphi}\Delta T} \cdot \frac{h^3}{6(h_1^2 - h_0^2)} \tag{6.25}$$

$$\alpha_{\vartheta}^* = \frac{\vartheta_{mes}}{\vartheta_0} \cdot \frac{1}{R_{0,\vartheta} \Delta T} \cdot \frac{h^3}{6(h_1^2 - h_0^2)}$$

$$(6.26)$$

Equation 6.27 represents the analytical link between the experimental and the numerical part of the proposed semi-numerical simulation approach. Equation 6.27 contains four factors where, factor i is constant, factor ii is the measured spring-in angle of one fabricated specimen or an average obtained from multiple specimens, factor ii is related to the part geometry as it contains part-thickness h and the nominal arc-length of the curved sections s_0 and factor iv, which is a modeling parameter that contains the chosen temperature change and the modified laminate area in thickness direction.

$$\alpha_{\varphi}^{*} = \underbrace{\frac{1}{6}}_{i} \cdot \underbrace{\varphi_{mes}}_{ii} \cdot \underbrace{\frac{h^{3}}{\varphi_{0}\tilde{R}_{0,\varphi}}}_{iii} \cdot \underbrace{\frac{1}{\Delta T \left(h_{1}^{2} - h_{0}^{2}\right)}}_{iv}$$
(6.27)

Therein, the parameter ΔT can be arbitrarily selected. It comes from the transfer of a strain into a quasi-thermal strain composed of a temperature change and corresponding expansion parameters introduced in Equation 6.6. A meaningful selecting for ΔT is the step from the curing temperature to room temperature of for example -160 K. This allows a direct comparison to strains due to the thermal contracting during cool down.

6.4 Advanced Model Formulation

In the preceding model derivation homogeneous orthotropic material properties are assumed which is suitable for UD laminates or when homogenized laminate properties are used. The

main advantage of this simplified formulation is the easy parameter calculation which becomes more complicated when the laminate stacking is considered. It is demonstrated here that this simplification is not a necessary one. Therefore, an analytical relation is derived which assumes that only the tool-sided ply's expansion properties are modified. Origin of the model derivation is again the following Equation.

Therein $\underline{\underline{D}}^{-1}$ denotes the inverse of the laminates bending-stiffness matrix which is derived as follows.

$$\underline{\underline{D}}^{-1} = \frac{1}{\det\left(\underline{\underline{D}}\right)} \cdot adj \ \underline{\underline{D}} \quad \text{with} \quad \det\left(\underline{\underline{D}}\right) = D_{11} \cdot D_{22} - D_{12}^2 \tag{6.29}$$

It should be noted that symmetric laminate properties are presumed. This is due to the fact that asymmetric laminates inherently induce process distortions due to inhomogeneous distributed in-plane stresses. As those deformations are not directly related to the manufacturing process they remain disregarded here. Combining Equations 6.28, 6.29 and 6.6 yields:

Equation 6.30 represents the final expression for the parameter transfer which cannot be further simplified without informations of the laminate layup and the ply thickness. However, it is possible to conduct the following exchange where $h_0 = -\frac{h}{2}$.

$$(h_1^2 - h_0^2) = (h_1 - h_0) \cdot (h_1 + h_0) = t_{ply} \cdot (h_0 + t_{ply} + h_0) = t_{ply} \cdot (t_{ply} - h)$$

$$(6.31)$$

For sake of clarity Equation 6.30 is applied to a simple example. Considering a $[0, 90]_s$ laminate with a ply thickness $t_{ply} = 0.25$ mm the modified expansion parameter is derived according to Equation 6.32

$$\alpha_{\varphi} = \frac{\mathbf{C} \cdot \varphi_{mes}}{-9 \cdot \varphi_{0} \cdot R_{0,\varphi} \cdot \Delta T \cdot (\mathbf{A} + \mathbf{B} \cdot \mathbf{B} \mathbf{1})}$$
with
$$\begin{cases}
\mathbf{A} = 2\bar{Q}_{11}^{2} + 14\bar{Q}_{11}\bar{Q}_{22} - 16\bar{Q}_{12}^{2} \\
\mathbf{B} = 2\bar{Q}_{11}\bar{Q}_{12} - 2\bar{Q}_{22}\bar{Q}_{12} \\
\mathbf{B} \mathbf{1} = \frac{D_{11}\bar{Q}_{12} - D_{12}\bar{Q}_{11}}{D_{12}\bar{Q}_{12} - D_{11}\bar{Q}_{22}} \\
\mathbf{C} = 14\bar{Q}_{11}^{2} + 100\bar{Q}_{11}\bar{Q}_{22} + 14\bar{Q}_{22}^{2} - 8\bar{Q}_{12}^{2}
\end{cases}$$
(6.32)

A more detailed derivation of Equation 6.32 is given in Section A of the Appendix. There, Equation 6.32 is applied for 8552/AS4 prepreg configuration which results in a derived modified expansion parameter of the tool-sided ply of $\alpha_{\varphi}=26.110$ ppm/K which has verified with a FE model of an L-profile. However, the preceding lines show clearly the increasing analytical efforts for the parameter calculation.

6.5 Limitation and Transferability

The preceding model derivation purses the aim to transfer measured process distortions on specimen level to corresponding scale independent simulation parameters analytically. The simulation

approach focuses mainly on the prediction of expectable distortions. Due to the modification of expansion properties in the curved areas obtained stress values are physically not meaningful for this areas. However, stresses in the flat laminate areas are reliable as regular material properties are assigned. To by-bass this, a two-step simulation procedure is possible wherein th first step derived expectable process distortions. The second step re-deforms the structure to the nominal shape while regular material properties are used. As this procedure presumes elasticity it is able to derived in-plane stress components even in the curved laminate areas similar to the numerical study shown in Section 1.4.

Due to shell element based procedure shell-specific limitation are valid for the approach as well. Thus, the approach is not able to account for stress components acting in thickness direction. As usual within shell elements models, local edge effects cannot be analyzed with this kind of elements. Overall part dimensions must be significantly larger that part thickness. As briefly discussed in this section the model assumed constant radius in the curved laminate areas. Thus, curvature changing parts must be simulated using the technique described in Section 7.5.

7 Verification by Means of Numerical and Experimental Studies

This chapter is dedicated to the application and validation of the developed seminumerical prediction approach. The developed procedure is applied to a set of test cases. Among other studies, the approach is applied to a C-profile structure with the aim to derive a compensated tooling geometry. Results are experimentally validated as one nominal tool and one compensated tool is fabricated. Moreover, the process distortion of the CFRP box structure is predicted and compared to the measurements shown in Chapter 5. L-profile shape scattering is transferred to the box scale and the relevance of both effects is discussed. Finally, the approach is applied to a highly integral CFRP upper wing cover and results are compared to three fabricated specimens.

7.1 Application and Extension of the Warpage Prediction Approach

The experimental investigation on the warpage effect shows clearly that the effect depends on the laminate thickness and the specimen length. The developed simulation approach documented in Section 6.2 transfers measured warpage deflections w analytically into an equivalent simulation parameter α_x^* . Equation 6.18, rewritten in the following, describes that analytically.

$$\alpha_x^* = \frac{h^3}{3\Delta T \left(h_1^2 - h_0^2\right)} \cdot \frac{w(x)}{x^2} \quad \text{with} \quad x_{max} = L/2$$
 (7.1)

The use of this simulation procedure is briefly shown in the following. As an example configuration, a 1200 mm long and 0.5 mm thick warpage specimen is considered. Specimens are made from M21E/IMA prepreg material. They show an average warpage deflection of 75.9 mm. As specimens are fabricated with a 180°C process cycle, ΔT to room temperature is -160 K. According to the preceding Equation α_x^* is obtained to 0.87847 ppm/K when assuming that half of the laminate is modified.

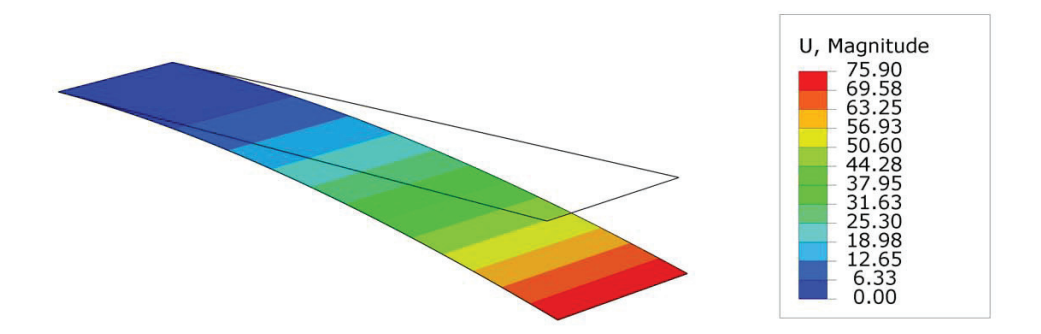


Fig. 7.1: Warpage simulation with the derived parameter

As shown in Figure 7.1, the parameter transfer from measurement data to the simulation parameter works. However, when considering the major findings of the experimental warpage investigation, which showed a direct dependency of the obtained warpage distortions from the

specimen length, the specimen thickness and the CFRP material, the simulation procedure is not very effective as at least one specimen of a certain configuration must be fabricated to derive the equivalent simulation parameter based on the obtained warpage deflection. Due to this high sensitivity of the effect it will not be possible to derive a single analytical relation valid for all specimen configurations. Nevertheless, it is possible to interpolate between the material-specific specimen configurations. Thus, it becomes possible to predict process-induced warpage distortion for configurations which are in between the data points.

Within the experimental warpage studies of Chapter 3, nine configurations with specimen thicknesses of 0.5, 1.0 and 1.5 mm and specimen lengths of 600, 900 and 1200 mm are fabricated. This is done for three different prepreg materials. The idea is to interpolate between these nine configurations in order to achieve a closed 'parameter surface'. Thus, expectable warpage distortions can be reliably estimated for configurations which are not equal to the fabricated ones. Of course this procedure is not limited to 3D parameter surfaces. It can be applied to parameter curves as well. Due to the characteristics obtained in the experimental part, a C^1 steady surface with a simple analytical equation does not seem suitable for the measurement results. Therefore, a C^0 steady bilinear interpolation is done as described by Salomon et al. [98]. Each sub surface is uniquely defined by its four corner points and is valid for a certain length and thickness area. Using this technique, Equation 7.1 can be transferred to a more applicable form given by Equation 7.2.

$$\Delta \alpha_i = \frac{16}{3\Delta T} \frac{t}{L^2} \cdot \underline{p}_i \cdot [u_i, w_i, u_i \cdot w_i, 1]^T$$
(7.2)

Therein t and L describe the specimen thickness and length while $[u_i, w_i, u_i \cdot w_i, 1]$ is the vector of normalized length and thickness coordinates. The parameter vector \underline{p}_i is the basis of the bilinear surface interpolation. It is derived based on the four sub-surface corner nodes specific for each material. Tables 7.1, 7.2 and 7.3 give the corresponding parameters for the investigated prepreg materials M21E/IMA, M21/T700 and 8552/AS4, respectively.

$Area_i$	length-range [mm]	thickrange [mm]	norm. thickness	norm. length	\underline{p}_i [mm]
$area_1$	$600 \le L \le 900$	$1.0 \le t \le 1.5$	$u_1 = \frac{1.5 - t}{0.5}$	$w_1 = \frac{L - 600}{300}$	$[3.433, 2.817, 4.800, 2.517]^T$
$area_2$	$600 \le L \le 900$	$0.5 \le t \le 1.0$	$u_2 = \frac{1.0 - t}{0.5}$	$w_2 = \frac{L - 600}{300}$	$[16.050, 7.617, 29.767, 5.950]^T$
$area_3$	$900 \le L \le 1200$	$1.0 \le t \le 1.5$	$u_3 = \frac{1.5 - t}{0.5}$		$[8.233, 5.233, 7.900, 5.333]^T$
$area_4$	$900 \le L \le 1200$	$0.5 \le t \le 1.0$	$u_4 = \frac{1.0 - t}{0.5}$	$w_4 = \frac{100}{100}$	$[45.817, 13.133, 3.367, 13.567]^T$

Tab. 7.1: Parameter for bilinear parameter-surface interpolation for M21E/IMA corresponding to equation 7.2

$Area_i$	length-range [mm]	thickrange [mm]	norm. thickness	norm. length	$\underline{p}_i \; [\mathrm{mm}]$
$area_1$	$600 \le L \le 900$	$1.0 \le t \le 1.5$	$u_1 = \frac{1.5 - t}{0.5}$	$w_1 = \frac{L-600}{300}$	$[1.667, 1.200, 2.550, 1.1833]^T$
$area_2$	$600 \le L \le 900$	$0.5 \le t \le 1.0$	$u_2 = \frac{0.5}{0.5}$	$w_1 = \frac{2000}{300}$ $w_2 = \frac{L - 600}{300}$ $w_3 = \frac{L - 900}{100}$	$[7.933, 3.750, 18.783, 2.856]^T$
$area_3$	$900 \le L \le 1200$	$1.0 \le t \le 1.5$	$u_3 = \frac{1.5 - t}{0.5}$	$w_3 = \frac{L-900}{300}$	$[4.217, 3.90, -0.0167, 2.383]^T$
$area_4$	$900 \le L \le 1200$	$0.5 \le t \le 1.0$	$u_4 = \frac{1.0 - t}{0.5}$	$w_3 = \frac{1}{300}$ $w_4 = \frac{L - 900}{300}$	$[26.717, 3.883, 5.133, 6.600]^T$

Tab. 7.2: Parameter for bilinear parameter-surface interpolation for M21/T700 corresponding to equation 7.2

$Area_i$	length-range [mm]	thickrange [mm]	norm. thickness	norm. length	\underline{p}_i [mm]
$area_1$	$600 \le L \le 900$	$1.110 \le t \le 1.665$	$u_1 = \frac{1.665 - t}{0.445}$	$w_1 = \frac{L - 600}{300}$	$[2.425, 2.350, 5.250, 0.950]^T$
$area_2$	$600 \le L \le 900$	$0.555 \le t \le 1.110$	$u_1 = \frac{0.445}{0.445}$ $u_2 = \frac{1.110 - t}{0.445}$ $1.665 - t$	$w_1 = \frac{2}{300}$ $w_2 = \frac{L - 600}{300}$ $w_3 = \frac{L - 900}{300}$ $w_4 = \frac{L - 900}{200}$	$[5.250, 7.60, -4.275, 3.375]^T$
$area_3$	$900 \le L \le 1200$	$1.110 \le t \le 1.665$	$u_3 - {0.445}$	$w_3 = \frac{L - 900}{300}$	$[7.675, 4.025, -2.550, 3.300]^T$
$area_4$	$900 \le L \le 1200$	$0.555 \le t \le 1.110$	$u_4 = \frac{1.110-t}{0.445}$	$w_4 = \frac{L - 900}{300}$	$[0.975, 1.475, 3.800, 10.975]^T$

Tab. 7.3: Parameter for bilinear parameter-surface interpolation for 8552/AS4 specimens corresponding to equation 7.2

For sake of clarity, the application of these parameter surfaces, it is exemplary applied for the M21E/IMA configuration. The parameters of the configuration are summarized in Table 7.4. Note that the specimen thickness and the specimen length differ from the ones of the fabricated specimens.

Parameter	value
$\phantom{aaaaaaaaaaaaaaaaaaaaaaaaaaaaaaaaaaa$	1050 mm
thickness t	0.75 mm
ΔT	$-160~\mathrm{K}$

Tab. 7.4: Test case properties

Due to the given length and thickness of the specimens, the suitable parameter \underline{p}_i of $area_4$ listed in Table 7.1. The expected deflection w(t, L) for the given parameters is derived to

$$w(L,t) = \begin{pmatrix} 45.817 \\ 13.133 \\ 3.367 \\ 13.567 \end{pmatrix} \cdot mm \cdot \begin{pmatrix} 0.5 \\ 0.5 \\ 0.25 \\ 1 \end{pmatrix} = 43.884 \ mm. \tag{7.3}$$

Calculation of the equivalent parameter of thermal expansion for the tool-sided laminate area results to:

$$\alpha_{x,II} = -\frac{16t}{3\Delta T L^2} \cdot 43.884 \ mm = 0.9951 \ ppm/K$$
 (7.4)

The simulation results for the new 'in between' configuration are shown in Figure 7.2

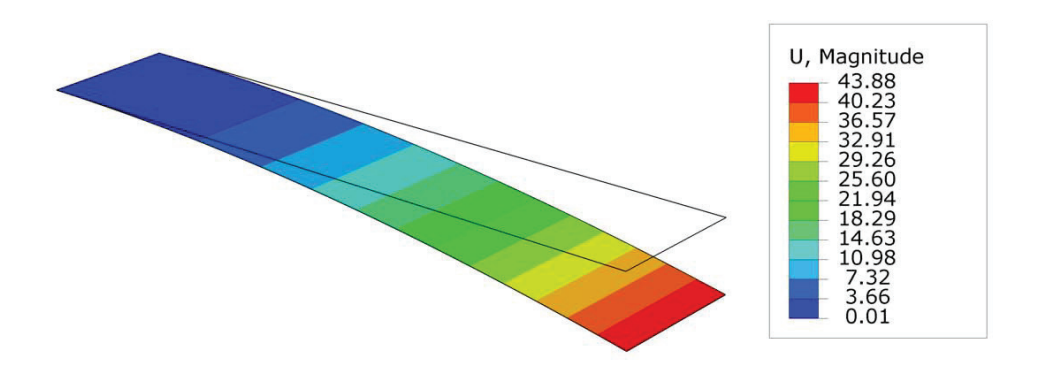


Fig. 7.2: Warpage simulation for the 'in between' configuration

Summarized, it is concluded that the warpage phenomenon cannot be described by one material-independent analytical equation as dependencies from geometry parameters and from the used prepreg materials are large. However, the presented technique, described in the preceding, interpolates between the obtained experimental results to realize a prediction capability based on the conducted experiments. Using this interpolation approach, warpage of 'in between' configurations can be estimated and corresponding equivalent simulation parameters can be derived.

7.2 Numerical Verification for Warpage of Curved Specimens

Within Section 3.6 it is investigated whether the warpage effect is relevant for thin specimens with a considerable curvature. The investigated radius is 350 mm in order to assure comparability

between the flat and the curved specimens while layup and the specimen length values are kept constant. Due to the specimen's shape and due to the manufacturing process it is potentially affected by warpage as well as spring-in what is outlined in Section 3.6. Thus, it is possible to simulate this kind of structure with corresponding parameters obtained from warpage specimens of from spring-in specimens. The experimental findings show that the observed deflection is spring-in dominated as, after manufacturing, the specimen radius is smaller than the tool radius. A dominating warpage effect would have led to an increased specimen radius.

Within this small study it should be investigated whether this finding can be numerically verified. The obtained average measurement results are shown in Figure 3.20.

First, the equivalent simulation parameter is derived with the warpage model. The comparison between the flat and the curved specimen is done for a four-ply configuration. The regarded specimens have a length of 900 mm and a thickness of 0.5 mm. Three flat and three circular specimens are fabricated from 8552/IM7 material. A detailed documentation of this experimental work is given in Prussak [99]. The average warpage deflection \overline{w} of the flat specimens is obtained to 33.3 mm. The equivalent warpage parameter α_{warp} is derived according Equation 7.5.

$$\alpha_{warp} = \frac{-16h}{3\Delta T} \cdot \frac{w}{L^2} = \frac{-16 \cdot 0.5 \ mm \cdot 33.3 \ mm}{3(-160)K \cdot 900^2 \ mm^2} = 0.6852 \ ppm/K \tag{7.5}$$

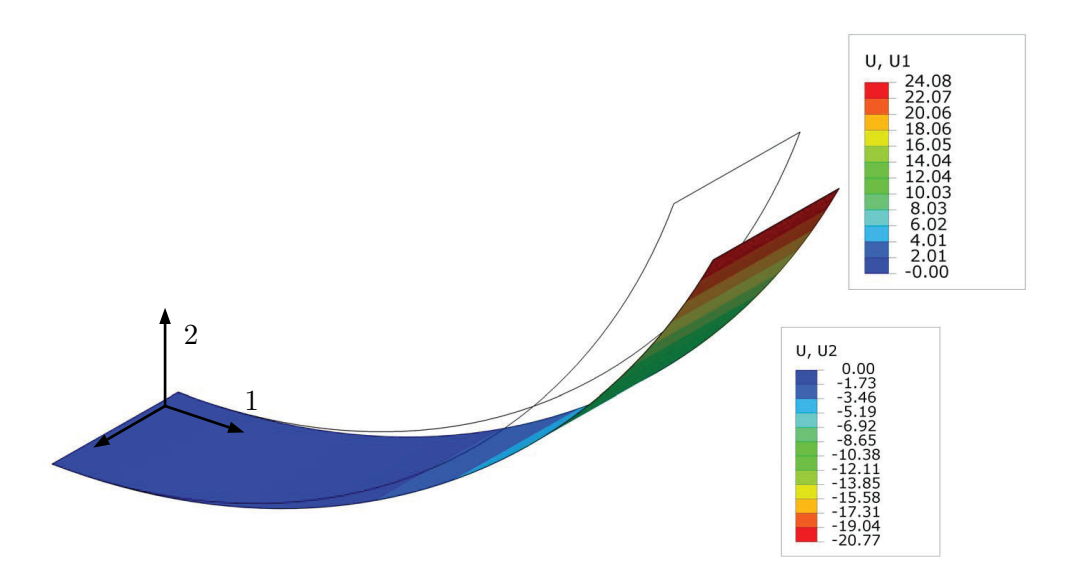


Fig. 7.3: Process distortions predicted with warpage parameters

Simulation results based on this parameter are contrary to the experimental findings. Obtained deflections in x direction (U1) and in y direction (U2) are one magnitude larger than the measured ones and they are oriented in the opposite directions. Parameters demanded for the spring-in based simulation are derived from one representative set of L-profile specimens with a unidirectional four-ply layup. These specimens produced a spring-in of 1.52°. The nominal L-profile radius is 4 mm and the laminate thickness is 0.75 mm due to the use of mid-grade prepreg with a nominal ply thickness of approximately 0.188 mm. According to Equation 6.25 the corresponding parameter for this L-profile is derived to 13.1940 ppm/K as shown in Equation 7.6.

$$\alpha_{L-prof}^* = \frac{-2h}{3\Delta T} \frac{\Delta \varphi}{\varphi_0 R_i} = 13.1940 \ ppm/K \tag{7.6}$$

Equation 7.12 is used to transfer the obtained spring-in results of the L-profiles to the regarded use case. Important parameters are the part radius $R^I = 350$ mm its thickness $h^I = 0.5$

mm. Consequently, the transferred parameter is derived to $\alpha_{trans} = 0.10053$ ppm/K. Predicted distortions derived with this parameter are shown in Figure 7.4.

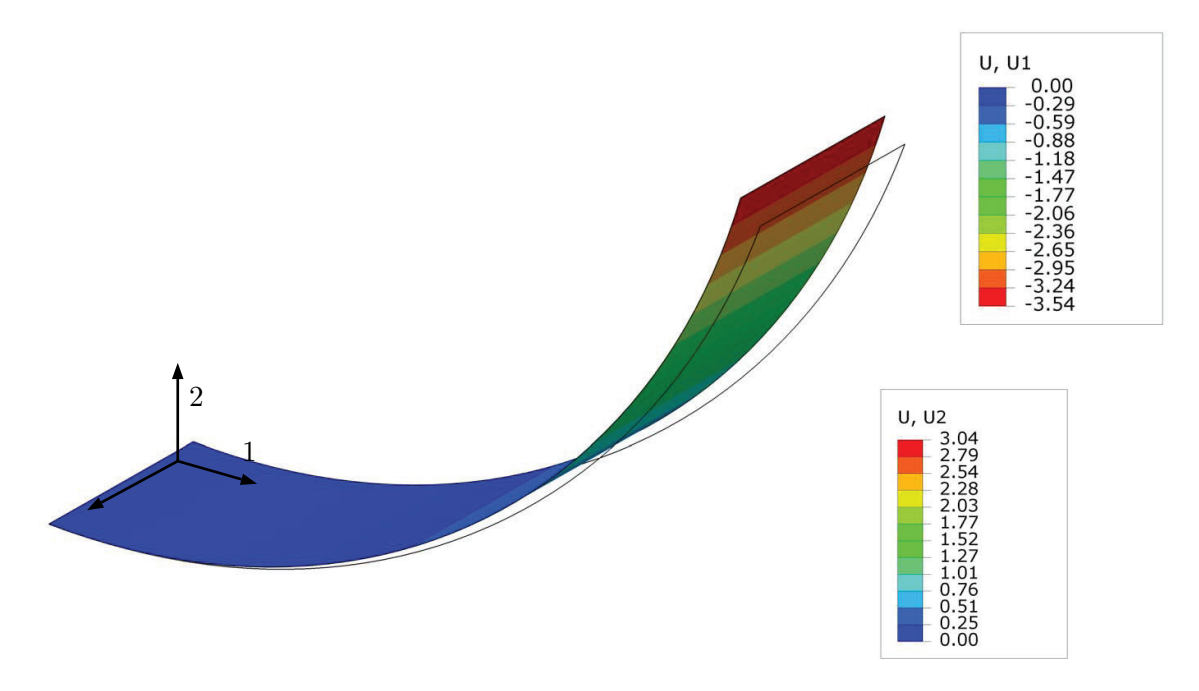


Fig. 7.4: Process distortions predicted with spring-in parameters. Deflections are threefold magnified

Note that deflections are threefold magnified. The predicted distortions are of the same order of magnitude and the direction corresponds to that one of the fabricated specimens. A minor overprediction is observed which was to be expected as interaction between the tool and the part remains disregarded within the spring-in simulation. Nevertheless, this model gives a rather good approximation of the expectable process-induced distortions. Moreover, this study substantiates that the warpage model is valid only for flat geometries and that the spring-in effect is of particular relevance for curved flat laminates.

7.3 Compensation of C-profile Process Distortions

Within this study the general idea of a spring-in compensation due to appropriate tool shape modification is experimentally validated. This is done for prepreg made C-profile specimens. The main aim of this study is to verify whether a 'linear' compensation of a tool is sufficient or if nonlinear effects have to be considered. Moreover, another aim is to exemplary proceed the proposed sophisticated design process shown in Figure 1.19.

The Radford relation given in Equation 7.7 describes the angle change $\Delta \varphi$ of a circular laminate with the section angle φ based on strains in tangential ε_T and radial ε_R direction. The corresponding percentage change is constant as shown in Equation 7.7.

$$\Delta \varphi = \frac{\varepsilon_T - \varepsilon_R}{1 + \varepsilon_R} \cdot \varphi \quad \to \quad \frac{\Delta \varphi}{\varphi} = const. \tag{7.7}$$

For sake of demonstration, an arbitrary L-profile specimen is regarded which shows a presumed spring-in angle of $\Delta \varphi_{spec} = 1.50^{\circ}$ and a nominal angle of $\varphi_{spec} = 90^{\circ}$. This represents a flange to flange angle of 88.50°.

In order to compensate this distortion, the first idea is to add the obtained spring-in angle $\Delta\varphi_{spec}$ to the nominal tool angle. Thus, the angle between the tool's flange surfaces is 91.50°.

This is the most straightforward way of compensation. Therefore, it is used for the fabrication of compensated C-profiles here.

However, when looking at the shape of the composite part, which is fabricated on the modified tooling in detail, the section angle of the profile and the tool decreases due to this geometry modification. According to Equation 7.7 this decrease results in a reduced expectable spring-in angle for the modified configuration. Equation 7.8 shows this. For sake of clarity, please refer to the definition of the spring-in angle and the differentiation between the enclosed and the section angle given in Figure 1.6.

$$\frac{\Delta \varphi_{spec}}{\varphi_{spec}} = \frac{\Delta \varphi_{comp}}{\varphi_{tool}} \quad \text{with} \quad \varphi_{tool} = \varphi_{spec} - \Delta \varphi_{spec}$$
 (7.8)

Consideration of the reduced section angle of the part results in a reduction of the compensation angle $\Delta\varphi_{comp}$ what is given by Equation 7.9.

$$\Delta \varphi_{comp} = \Delta \varphi_{spec} - \frac{\Delta \varphi_{spec}^2}{\varphi_{spec}}$$
 (7.9)

Therein, the angle $\Delta \varphi_{comp}$ represents the increase of the flange to flange angle of the tool. For the regarded L-profile $\Delta \varphi_{comp}$ is derived to 1.475°. Considering the obtained standard deviations of the fabricated L-profile specimens given in Section 4.4, it is obvious that those are one order of magnitude above the derived deviations here. Consequently, the following study pursues the linear compensation strategy presented above in order to compensate process-induced distortions of prepreg C-profiles.

As a kind of worst-case scenario, a layup with a comparatively large spring-in is used for the demonstration of the compensation idea. Thus, four L-profile specimens with a $[45, -45]_s$ layup and a radius of 6 mm are the reference which show an average spring-in angle $\overline{\Delta\varphi}$ of 2.22° and a standard deviation of $s_{\Delta\varphi}=\pm0.11^{\circ}$. This parameter set is taken to verify that a tool compensation is possible even for spring-in angles over two degrees. C-profile specimens are fabricated with a $[45, -45]_{4s}$ layup what results in laminate thickness of approximately 2.1 mm. According to the spring-in investigation, this modification is expected to have no influence on the occurring spring-in angles.

Two aluminum tools are fabricated where one has 90° angles between the web and the flanges and the other has 92.22° angles. Figure 7.5 shows the measured tool surfaces within the GOM Inspect software. Manufactured tool accuracy is verified using the full-field measurement system described before. As shown in Figure 7.5 the deviation from the nominal angles is -0.03° for the nominal tool and $+0.01^{\circ}$ for the compensated tool, which is satisfying.

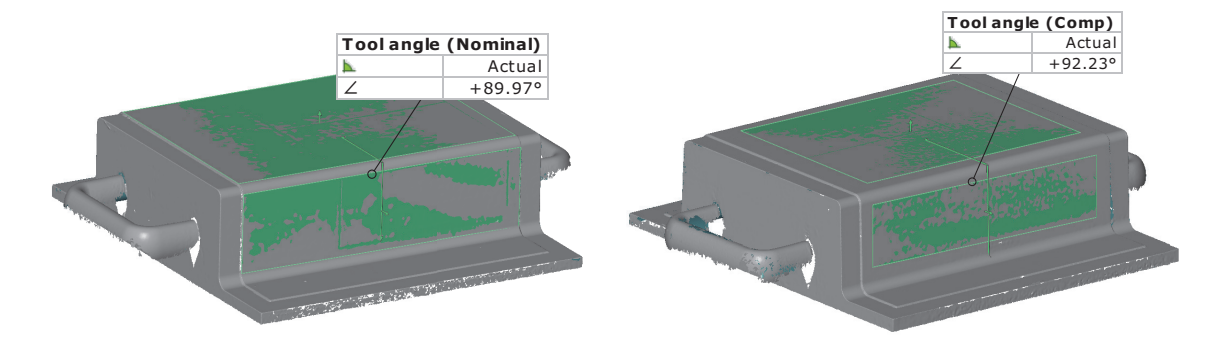


Fig. 7.5: Measured tool angles of the nominal and the compensated tool

To compare the tool shape with that one of the manufactured parts and especially the flange to flange distance, two measurands d_{-10} and d_{-50} are defined according to Figure 7.6.

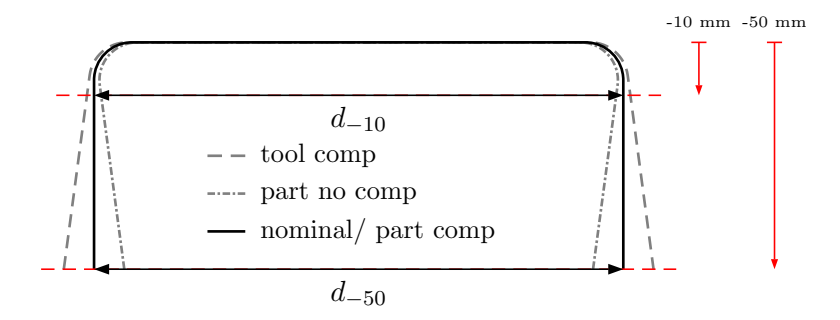


Fig. 7.6: Definition of the two measurands d_{-10} and d_{-50} used for the comparison of tool shapes and manufactured specimens

The distances d_{-10} and d_{-50} are measured for both tools at room-temperature conditions based on the obtained point clouds and with a hand caliper for the fabricated C-profile specimens. Note that d_{-50} corresponds to the flange-tip distance as illustrated in the preceding figure. In this case study one specimen of each tool is manufactured whereat both tools and both specimens are shown in Figure 7.7.



Fig. 7.7: Nominal and compensated tool and both fabricated specimens

Table 7.5 lists the conducted measurements and the nominal design data from the CAD model. Therein the angle θ is derived according to the following Equation.

$$\theta = \arctan \frac{d_{-50} - d_{-10}}{2 \cdot 40 \ mm} \tag{7.10}$$

It describes the deviation to the nominal design for each configuration. A positive θ indicates that the flanges of the regarded configuration are outside the nominal shape as shown by the 'tool comp' configuration shown in Figure 7.6 for example. An evaluation of the measured distances and in particular the comparison of the 'Tool compensated' and the 'CAD comp nominal' configuration reveals a slight offset of approximately 0.44 mm between both measurements, which is likely a result of the milling process. However, as the obtained flange angle is correct, this has no impact on the expectable spring-in distortions.

Configuration	$d_{-10} \; [{\rm mm}]$	$d_{-50} [{\rm mm}]$	θ [°]
CAD nominal	150.00	150.00	0
CAD comp nominal	150.32	153.42	2.22
Tool nominal	150.04	150.05	0.01
Tool compensated	150.76	153.83	2.22
Part nominal	149.97	147.20	-1.98
Part compensated	150.84	151.09	0.18

Tab. 7.5: Measured dimensions d_{-10} and d_{-50}

The evaluation of the 'Part nominal' configuration shows that the specimen fabricated on the nominal tool reveals a θ of -1.98° which is 0.24° less than the obtained L-profile-based average used for the compensation. The evaluation of the 'Part compensated' configuration reveals a θ of 0.18° which represents a slight overcompensation. However, when comparing this result to the 'Part nominal', the deviation is almost as large as the aforementioned difference between the measured C-profile spring-in and the L-profile-bases average of 2.22° used for the compensation. An application of the 'nonlinear' compensation described in Equation 7.9 derives $\Delta\varphi_{comp}$ to 2.17° . Thus, a consideration of the nonlinearity within the tool design would lead to a reduction of θ to 0.13° .

The origin of the obtained deviations between the L-profile spring-in magnitudes and that one of the C-profiles is not further investigated in this case study. Nevertheless, it is recommend to fabricate more specimens in order to achieve a statistical verification. Figure 7.8 visualizes the effect of the tool compensation strikingly.



Fig. 7.8: Effect of the tool compensation. Distance between red lines is approximately 2 mm

Summing up, the fabrication of this kind of C-profiles without a spring-in compensation leads to a flange to web angle deviation from the nominal (90°) of approximately 2° which is accompanied by a decrease of the flange to flange distance of approximately 4 mm. Using the 'linear' compensation approach shown here, a reduction about 93.75 % to 0.25 mm is achieved which represents a significant improvement. Using the 'nonlinear' compensation, this value can be further reduced to $2 \cdot \sin(0.13^{\circ}) \cdot 40 \text{ mm} = 0.18 \text{ mm}$. The gained improvement within the assembly

process is schematically illustrated in Figure 7.9. Assuming a structural bonding process, desired adhesive layer thicknesses t_{bond} are roughly in the range of 0.3 mm to 0.7 mm. The thickness variation of this bond layer, as a consequence of process-induced distortion, is denoted with $t_{bond,vari}$ in Figure 7.9.

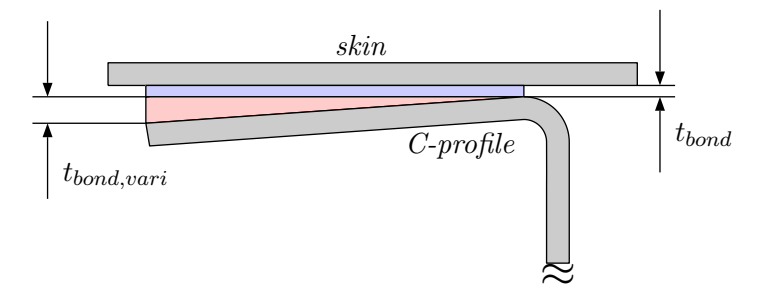


Fig. 7.9: Illustration of the variation of the adhesive layer thickness due to process-induced distortions

Regarding the C-profile fabricated on the uncompensated tool, $t_{bond,vari}$ is obtained to 1.98 mm which is approximately three up to seven times a realistic adhesive layer thickness t_{bond} . Regarding the specimen fabricated on the compensated tool, $t_{bond,vari}$ is reduced to 0.09 mm which is significantly smaller than t_{bond} . Within a riveted assembly the advantages shown for the bonded joint are transferable and will lead to a massive reduction of cost intensive hard and soft shim use and to a reduction of assembly-induced stresses due decreasing part deformation during assembly which are detrimental to the part's performance.

7.4 Spring-in Simulation for a Curved L-profile

In Section 4.7 curved L-profiles are experimentally analyzed. Cross section analysis of the fabricated curved specimens reveals identical spring-in angles as obtained for the regular L-profiles. This suggests that the whole profile is dominated by the spring-in effect although affectations by the curved flanges are conceivable as well. A shell-element model of the curved profile is set up in order to apply the developed simulation process. For sake of convenience, the laminate is modeled utilizing homogenized material properties. These parameters are derived with ESAComp to $E_I = 47760$ MPa, $E_{II} = 23590$ MPa, $G_{12} = 29130$ MPa and $\nu_{12} = 0.792$. The corresponding part coordinate system is depicted in Figure 7.10.

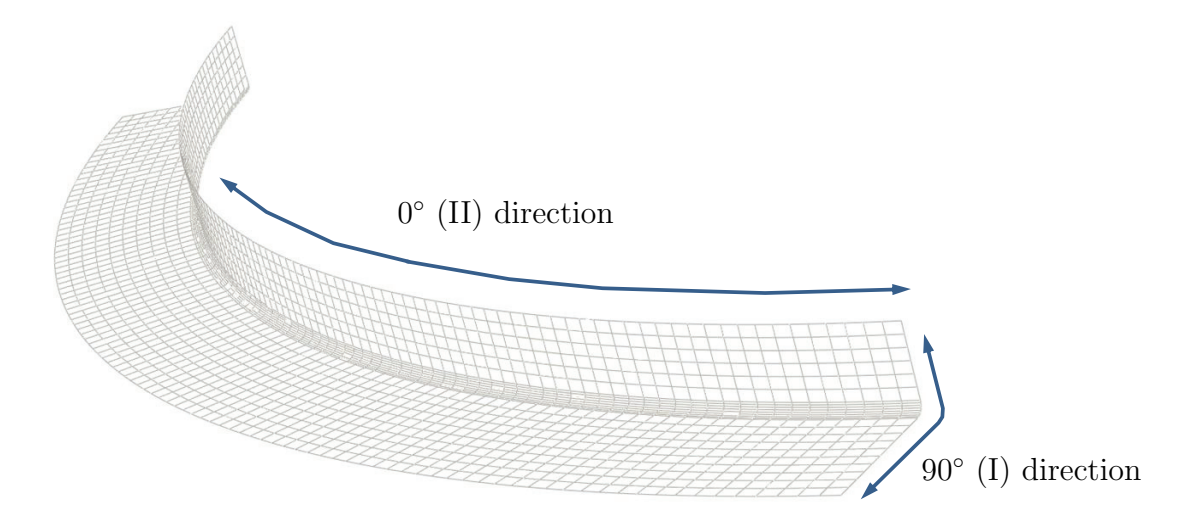


Fig. 7.10: Material orientation within the shell model

The modified laminate parameters are derived based on Equation 6.27. Regular L-profiles with a similar layup show an average spring-in angle of 1.43°. The local radius of the part is 4 mm while is has a constant laminate thickness of 2 mm. The local section angle of the regular L-profiles is 90°. Therefrom, the equivalent expansion parameter is derived to 33.1713 ppm/K. The application of the model to the curved flange demands the transfer of the derived simulation parameter to this new geometry. Therefore Equation 7.12 is applied while the nominal parameters of the curved profile are inserted.

$$\frac{\alpha^I \cdot R^I}{h^I} = \frac{\alpha^{II} \cdot R^{II}}{h^{II}} \quad \to \quad \alpha^{II} = 0.2696 \ ppm/K \tag{7.11}$$

The resulting parameter for the curved flange is calculated to 0.2696 ppm/K. These parameters are applied to the corresponding curved areas while elastic properties are equally set for all areas. Figure 7.11 shows the derived distortions of the curved profile. The applied boundary conditions are depicted on the left of Figure 7.14, whereat the black illustrated edge of the model. There, all translations and rotations are constraint.

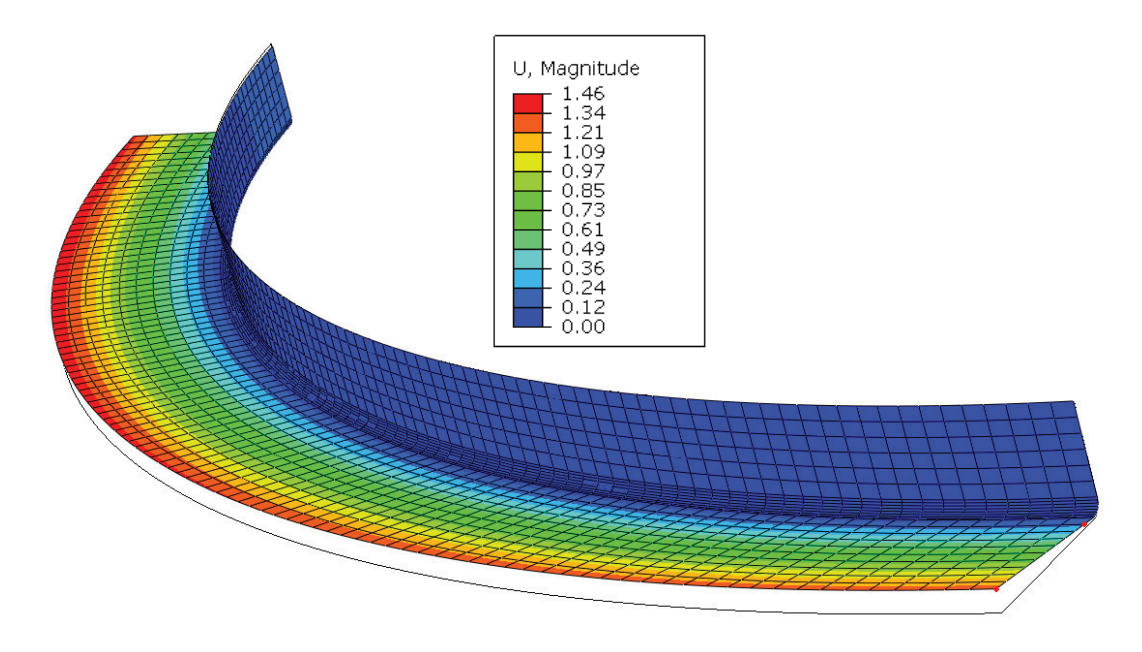


Fig. 7.11: Simulation result for representative boundary conditions

A simple measurement setup is used to verify the accuracy of the simulation. A schematic of the utilized measurement setup is given in Figure 7.12. Therein, two steel squares are clamped together while the part is clamped against one square. A simple steel rule is used to measure the gap between the steel square and the part.

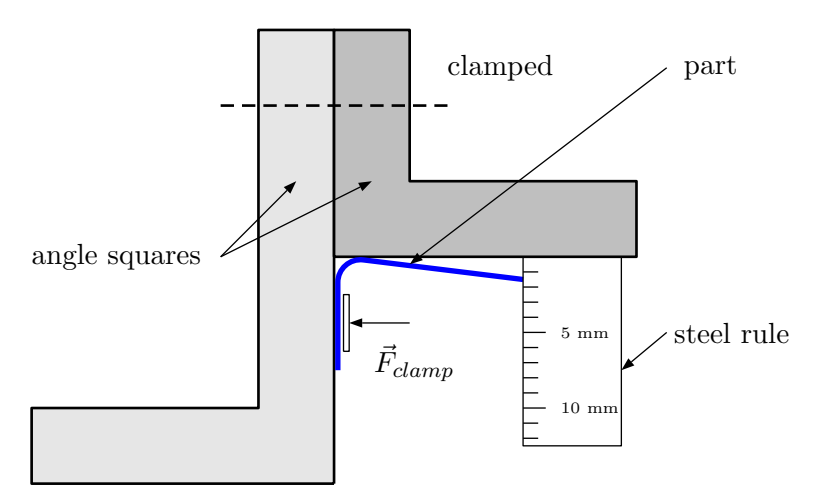


Fig. 7.12: Schematic of the used measurement setup



Fig. 7.13: Measurement using setup of Figure 7.12

Figure 7.13 shows the obtained gap which is slightly below 1.5 mm which matches excellently to the conducted simulation shown in Figure 7.11. Nevertheless, the conducted simulation is used to exemplary illustrate how different boundary conditions can induce massive misinter-pretations of occurring distortions. Figure 7.14 shows the results of three simulation runs. The underlying material properties are kept constant while only boundary conditions are varied. The derived distortions of the structure are identical for all three configurations. Nevertheless, the different results suggest completely different cognitions. This must be kept in mind when evaluating process-distortions of composite structures as badly chosen boundary conditions within the simulation can lead to massive misinterpretations. In Figure 7.14 boundary conditions are illustrated by a black rectangular. At these selected nodes all translational and rotational DoFs

are constraint. The boundaries are assigned to three different regions: the flange centerline, the flange end and the web end.

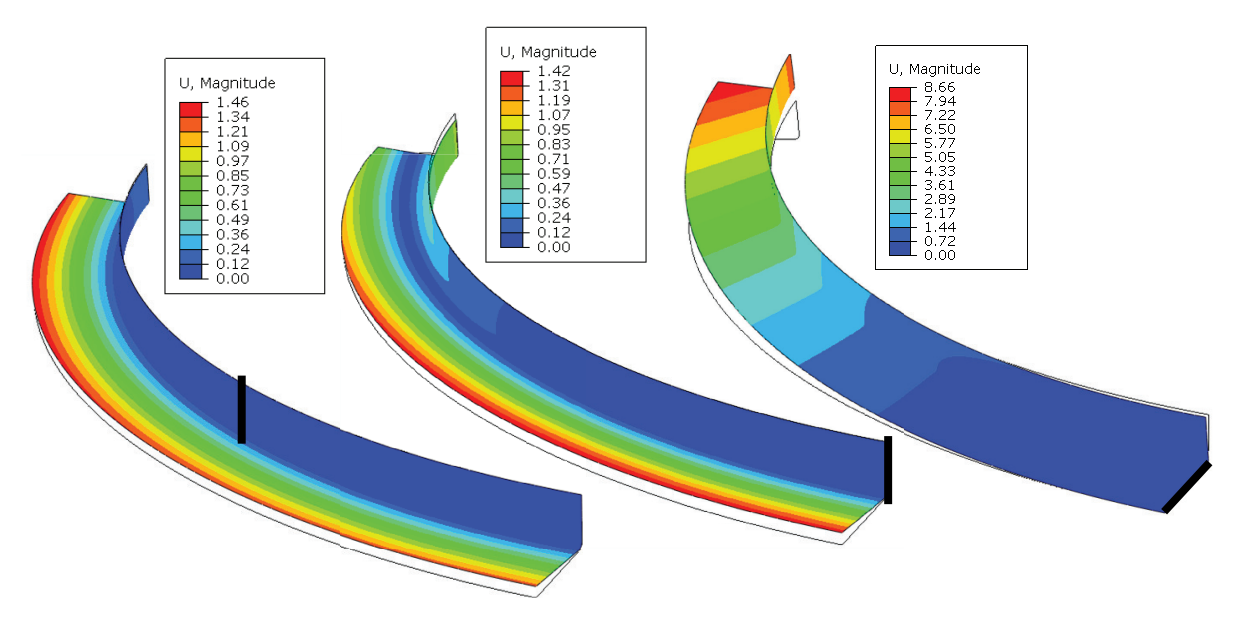


Fig. 7.14: Deceiving simulation results. Boundary conditions apparently affect part distortions. 'Encastre' properties ($U_i = UR_i = 0$ for i = 1, 3) are assigned to the black marked areas while other model parameters remain constant

While the first boundary condition (left) allows a direct comparison to the measurements shown in Figure 7.13 both others are widely inadequate. To prevent this kind of error-proneness a local shape evaluation based on node to node measurements should be conducted, as it is independent from the coordinate system of the simulational model.

7.5 Spring-in of Curvature-Changing Structures

The majority of structural components used in aerospace is composed of flat, simple- and double-curved areas as illustrated in Figure 7.15. In addition, it is common that curved areas have a constant radius. However, there are applications with more complex curvatures or a varying curvature along the part length. These components are in the focus of this section.

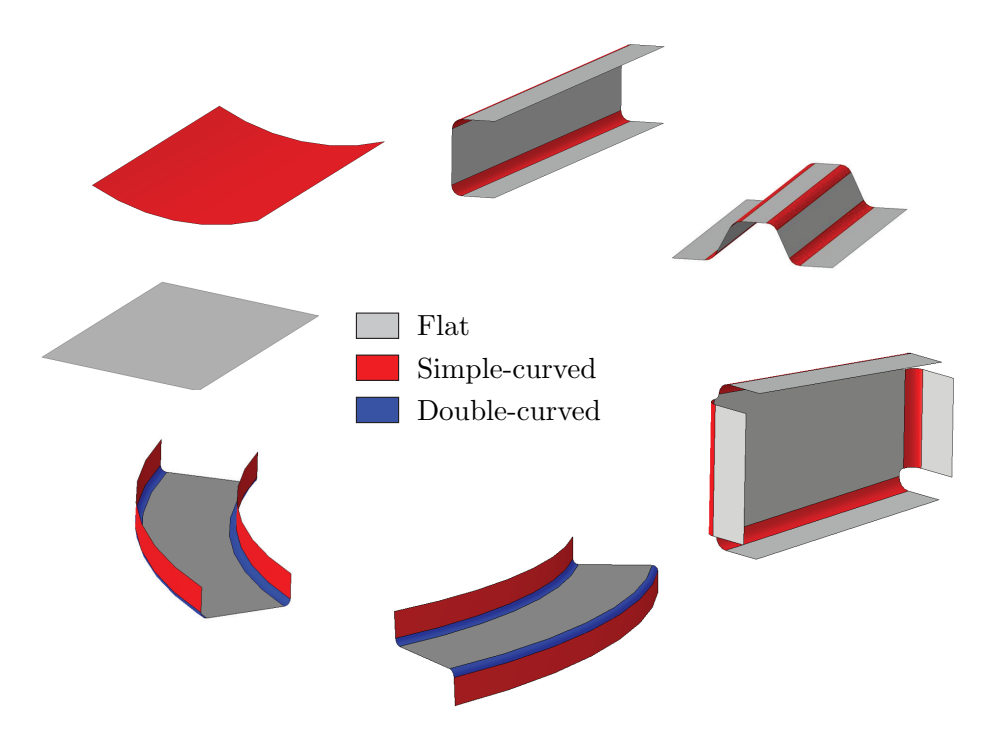


Fig. 7.15: Structural components in aerospace applications are commonly composed of flat, simple-curved and double-curved sections

Figure 7.16 shows a CFRP leading edge which has a varying curvature along its cross section.



Fig. 7.16: Small demonstrator of a CFRP leading edge as an example of a curvature changing structure. Picture taken from [100]

Regarding Equation 6.21, the angle change φ is derived from the gradient $\partial \varphi/\partial s_{\varphi}$ integrated along the arc length s_0 . This equation is very simple for constantly curved areas. However, it becomes more complicated for curvature varying surfaces as the arc-length becomes a function of the changing radius $R = f(\varphi)$.

The main problem is the relation between a measured spring-in angle and a corresponding equivalent expansion parameter α^* which is part of Equation 6.23. For constantly curved areas

a constant coefficient of thermal expansion is derived. This is only feasible when assuming that the spring-in effect generates homogeneously along the arc length as no curvature change occurs.

In the following, a simple strategy is proposed to use the measured spring-in angles of L-profile specimens for structures with varying curvature.

There, the equivalent coefficient of thermal expansion α_{φ}^* describes the angle change for a circular section with the section angle φ and the laminate thickness h. Substantiated by the experimental experience, the spring-angle is invariant to the profile's radius but linearly dependent on the section angle φ . Although experiments showed that the spring-in angle is independent from the laminate thickness, the modeling parameter depends on the thickness as this information directly affects the second moment of inertia of the profile. Consequently, the modeling parameter depends on the thickness. Equation 7.12 describes this analytically.

$$\frac{\alpha_{\varphi}^* \cdot R^*}{h^*} = \frac{\alpha_{\varphi}^I \cdot R^I}{h^I} \quad \to \quad \alpha_{\varphi}^I = \frac{\alpha_{\varphi}^* \cdot R^* \cdot h^I}{h^* \cdot R^I} \tag{7.12}$$

For sake of clarity, the use of the parameter transfer is exemplary demonstrated for an arbitrary profile. The initial equivalent parameter α_{φ}^* is calculated from L-profile specimens with a $[0]_4$ with a laminate thickness of 0.75 mm and an average spring-in angle of 1.52°. Therefore, α_{φ}^* is derived to 10.556 ppm/K. Figure 7.17 shows the cross section of the profile. The area with the enclosed section angle of 45° has a laminate thickness of 3 mm for sake of demonstration while the rest of the laminate has a thickness of 0.75 mm. Figure 7.17 shows the cross section of the profile while the render shell thickness option of Abaqus is used to visualize the different shell thicknesses. Nevertheless, the model uses shell element modeling.

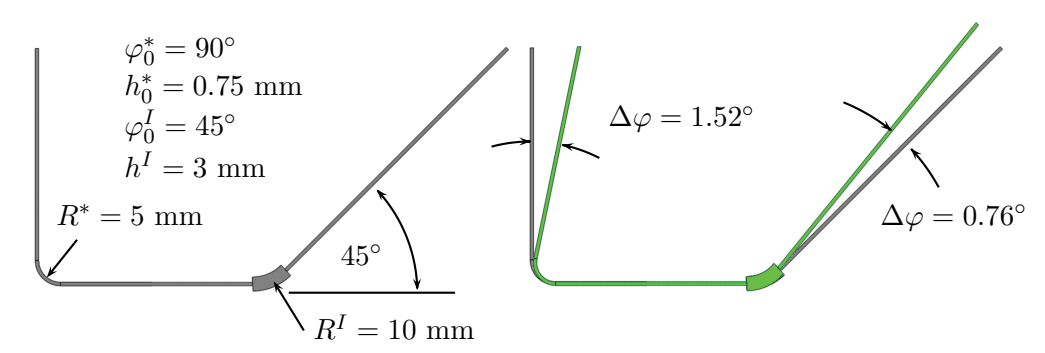


Fig. 7.17: Verification of the parameter transfer approach. Green part represents the derived deformed part geometry

The corresponding parameter for the thicker laminate area is derived according to Equation 7.12. Therefore, α_{φ}^{I} is derived to 21.112 ppm/K. As can be seen in Figure 7.17, the obtained spring-in angles of the profile match the expected behavior as the 45° section produces only half of the spring-in compared to the 90° section.

The use of this simple equation to transfer from one shape to another promises significant cost saving potential as the number of L-profile specimens, which are necessary for the simulation of a more complex part, can be reduced. However, according to Equation 7.12 the model is derived for homogeneously curved shapes. This is contrary to the aim of modeling parts with changing curvature.

Therefore, the idea is to interpolate inhomogeneous simple-curved surfaces locally with circles, which are derived based on the FE nodes. Given that a circle is entirely described by three points, the node coordinates of these points $\vec{P}_1, \vec{P}_2, \vec{P}_3$ are necessary to derive a corresponding circle. This circle is characterized by a certain radius r and its center \vec{P}_c . Of course, this results in a mesh dependency of the predicted results as quality of the circle-based interpolation of an arbitrarily curved surface depends directly on the mesh density. Nevertheless, providing that the mesh

density is sufficient for a reliable interpolation, the approach should give a good estimation of the real distortions. As demonstrated in Figure 7.17, the section angle of the regarded corner is important for the parameter transfer. Equation 7.14 derives the section angle on the interpolation circle based on the points \vec{P}_1 , \vec{P}_3 , and \vec{P}_c . The radius of a circle trough three points is described by Barycentric coordinates. The utilized equations 7.13 are taken from [101].

$$r = \frac{|\vec{P}_1 - \vec{P}_2||\vec{P}_2 - \vec{P}_3||\vec{P}_3 - \vec{P}_1|}{2|(\vec{P}_1 - \vec{P}_2) \times (\vec{P}_2 - \vec{P}_3)|}$$
(7.13)

The local arc length along the interpolation circle is derived according to Equation 7.14.

$$\psi = \arccos \frac{(\vec{P}_1 - \vec{P}_c) \cdot (\vec{P}_3 - \vec{P}_c)}{|\vec{P}_1 - \vec{P}_c| \cdot |\vec{P}_3 - \vec{P}_c|}$$
(7.14)

Therein, it is important that the $|\vec{P}_1 - \vec{P}_3|$ represents the largest distance obtained in the triangle shown in Figure 7.18.

For sake of clarity, the procedure is exemplary illustrated for a surface with an elliptical shape. Figure 7.18 shows the cross section of the part while black dots illustrate nodes of the FE model. The red circle represents the circular interpolation of the first three nodes, whereat the gray lines are fractions of the second and the third interpolation circle.

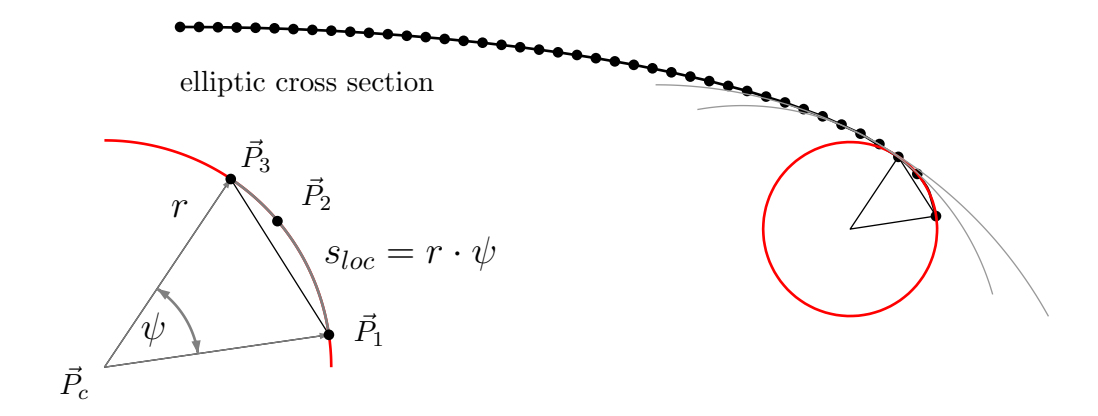


Fig. 7.18: Derivation of the local circles and the corresponding arc length

Moreover, Figure 7.18 shows the section angle ψ which depends on the coordinates of \vec{P}_1, \vec{P}_2 and \vec{P}_3 . Although this approach is applied manually for this test case, it promises automation potential within the FE environment as node coordinated are easy accessible.

The center point \vec{P}_c is of particular importance for this approach. It is derived according to Equation 7.15 based on the node coordinates of \vec{P}_1, \vec{P}_2 , and \vec{P}_3 .

$$\vec{P}_{c} = \alpha \vec{P}_{1} + \beta \vec{P}_{2} + \gamma \vec{P}_{3} \quad \text{with} \quad \begin{cases} \alpha &= \frac{|\vec{P}_{2} - \vec{P}_{3}|^{2} (\vec{P}_{1} - \vec{P}_{2}) (\vec{P}_{1} - \vec{P}_{3})}{2|(\vec{P}_{1} - \vec{P}_{2}) \times (\vec{P}_{2} - \vec{P}_{3})|^{2}} \\ \beta &= \frac{|\vec{P}_{1} - \vec{P}_{3}|^{2} (\vec{P}_{2} - \vec{P}_{1}) (\vec{P}_{2} - \vec{P}_{3})}{2|(\vec{P}_{1} - \vec{P}_{2}) \times (\vec{P}_{2} - \vec{P}_{3})|^{2}} \\ \gamma &= \frac{|\vec{P}_{1} - \vec{P}_{2}|^{2} (\vec{P}_{3} - \vec{P}_{1}) (\vec{P}_{3} - \vec{P}_{2})}{2|(\vec{P}_{1} - \vec{P}_{2}) \times (\vec{P}_{2} - \vec{P}_{3})|^{2}} \\ \vec{P}_{i} &= (x_{i}, y_{i}, z_{i})^{T} \end{cases}$$

$$(7.15)$$

To visualize the application within the FE environment, it is applied to an elliptic surface with the semi axes a = 1000 mm and b = 250 mm. The corresponding analytical Equation is:

$$y = 250 \ mm \cdot \sqrt{1 - (x/1000 \ mm)^2}. \tag{7.16}$$

Figure 7.19 shows the simulation process. For sake of clarity, the surface is subdivided into only twenty distinct areas what can be seen on the gray surface. Local interpolation circles are evaluated and the equivalent parameters are derived according to Equation 7.12. The second figure shows the assigned material properties which vary locally according to the derived local curvature. The third figure shows the FE mesh whereat the fourth Figure shows the calculated deformations for the surface which is approximately 22 mm at the tip. Symmetry boundary conditions are applied to the edge with the coordinates x=0 mm and y=250 mm.

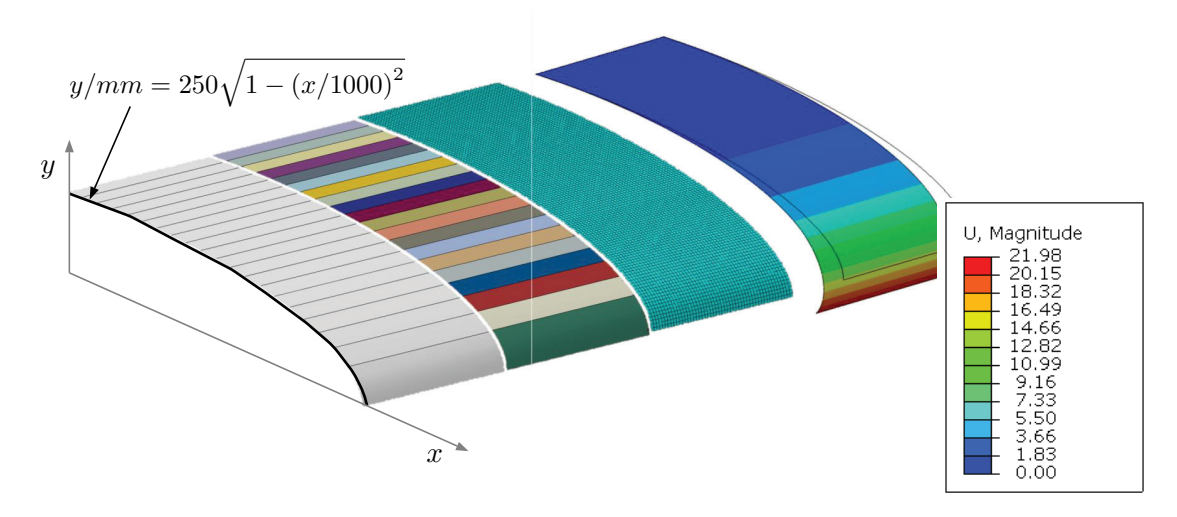


Fig. 7.19: Curvature variable elliptic surface. Partitioned surface, locally varying layups, FE mesh and derived Distortions (f.l.t.r)

The presented approach is not limited to simple-curved surfaces with changing curvature. It can be applied to double-curved surfaces as well. Figure 7.20 shows a partial area of an ellipsoid. It is described by Equation 7.17

$$\frac{x^2}{a^2} + \frac{y^2}{b^2} + \frac{z^2}{c^2} = 1 \quad \text{with} \quad \begin{cases} a = 1000 \text{ mm} \\ b = 250 \text{ mm} \\ c = 450 \text{ mm} \end{cases}$$
 (7.17)

Similar to the procedure in the preceding, local fitting circles are derived based on the node coordinates. This is visualized for a very coarse mesh in Figure 7.20. Therein, the normal vector of the red circle is parallel to the x-axis whereat the normal vector of the blue circle is parallel to the z-axis. However, this concentricity is not necessary. Within the model it should be ensured that circle normal orientations are parallel to the assigned material orientations.

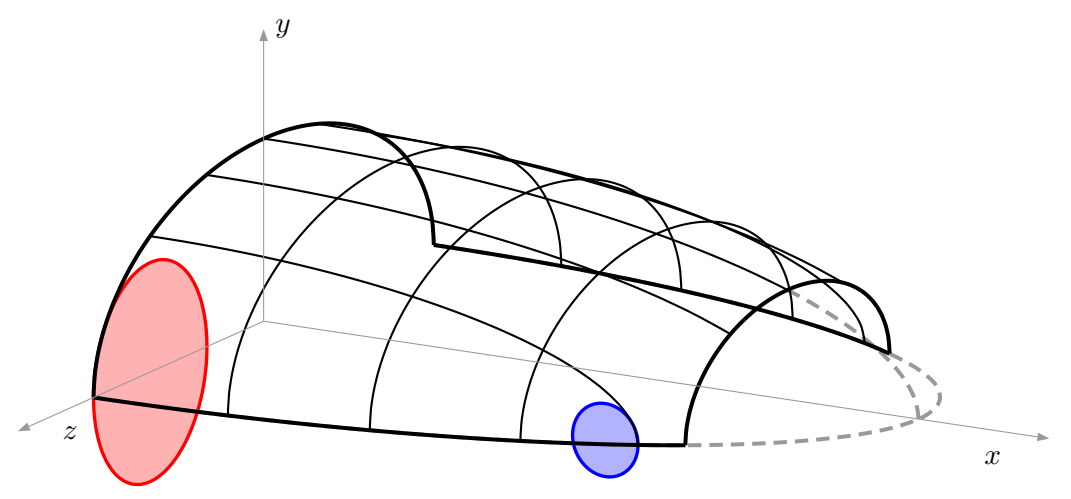


Fig. 7.20: Local interpolation of a double-curved surface with circles

Consequently, each surface area of the double-curved surface demands two equivalent expansion parameters.

The proposed approach implies a direct transferability independent from the part scale. With other words, experimental results obtained on L-profile level can be used for structures with deviating angles and structures of a different scale. While the linearity from the section angle has been experimentally validated by Ding et al. [49] the transferability to completely different structures needs further experimental validation as perhaps other effects as warpage for example can affect the final shape of the part.

7.6 Verification of the T-joint Tool by Experimental Means

For sake of verification, one T-joint configuration is manufactured. Both, skin and stiffener have the same $[0, 90]_{4s}$ layup. The T-joint in manufactured from 8552/AS4 prepreg material. A modified MRCC is used wherein the autoclave pressure is reduced within the first dwell stage. The idea of this simple experiment is to verify whether the tool predicts distortions of reasonable magnitude. Figure 7.21 shows the manufactured specimen during the measurement.

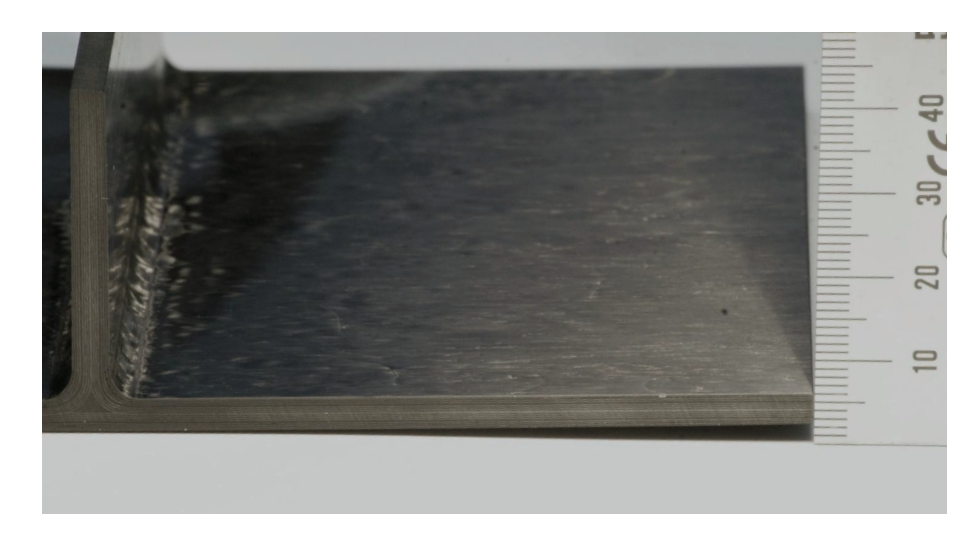


Fig. 7.21: Measured distortion of one exemplary T-joint

Figure 7.22 shows a schematic of the used measurement technique. Therewith, deviation d is obtained to 2.0 mm while the half skin length is 90 mm. Consequently, the obtained spring-in

angles on both sides are obtained to $\gamma = 0.63^{\circ}$. This corresponds to a deviation of 1.0 mm at the skin tip in comparison to the simulated T-joint.

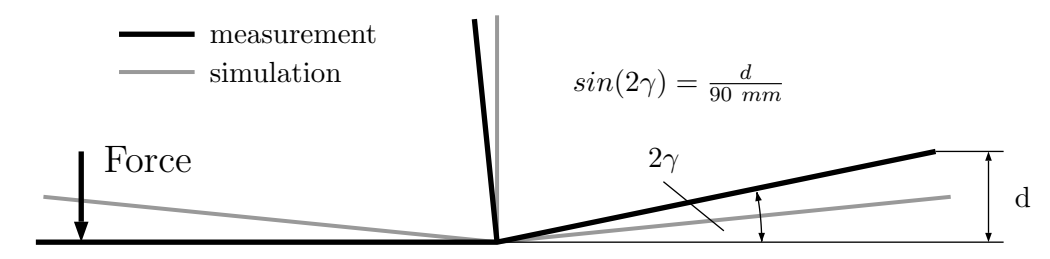


Fig. 7.22: Measurement principle used for the photo

Regarding the simulation results given in Figure 7.23, an underprediction is observed, as only 0.60 mm deflection is derived. Please note the different alignments within the simulation and during the measurement which are illustrated in Figure 7.22. As the simulation does not account for the varied process conditions this could be a possible explanation for this deviations. Furthermore, a parameter adjustment is recommended.

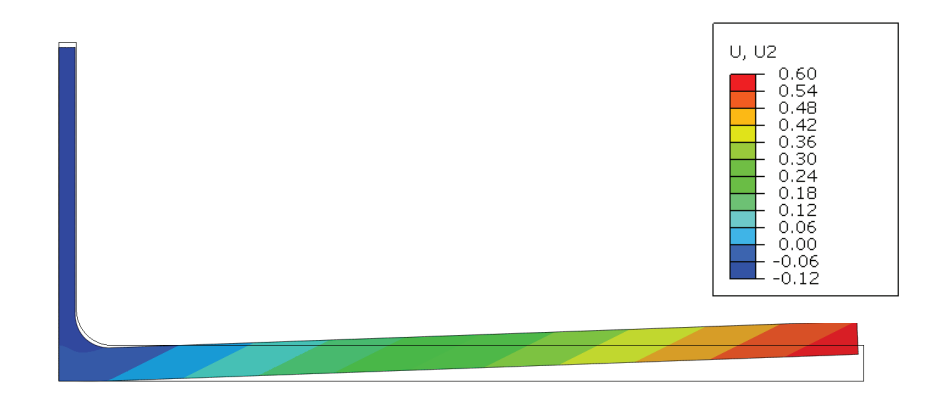


Fig. 7.23: Simulation result for the regarded T-Joint configuration

Additional specimens are necessary to assess that thoroughly. However, the study proves that the T-joint tool predicts deflections of realistic magnitude.

7.7 Prediction of Process Distortions for the Integral CFRP Box Structure

The simulation strategy proposed in Section 6.3 is applied to the box structure which is experimentally investigated in Section 5.1. According to the flow-chart of the simulation shown in Figure 1.2, one set of L-profile specimens is manufactured using the box's prepreg material M21/T800. Specimens have the same layup as the box $[0, 90]_{3s}$. Both, the box tooling as well as the L-profile tooling are made from the same aluminum and bagging conditions including release agent application is identical. Fabricated specimens have a flange length of 50 mm and a width of 40 mm.



Fig. 7.24: L-profile specimens and the fabricated box

The fabricated specimens are measured using the full-field measurement system described above. The average spring-in angle is obtained to $\overline{\Delta\varphi}=1.38^{\circ}$ while the standard deviation is obtained to $s_{\Delta\varphi}=\pm0.03^{\circ}$ which substantiates the good reproducibility of the spring-in angle for multi-angle laminates as shown in Section 4.4. The tool-sided surface of the box is used for the FE model. Note that the outer as well as the mid-plane surface would lead to identical results. In Figure 7.25 arrows point at the areas which are modified according to the model definition.

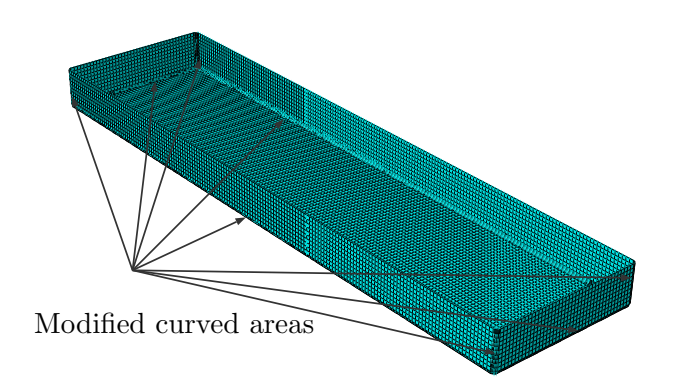


Fig. 7.25: Shell-element model of the box structure

To capture the structural behavior of the layup UD material properties of one unidirectional ply are used. Table 7.6 contains the used data of the single ply and the homogenized data of the $[0,90]_{3s}$ derived with ESAComp. Within the simulation composite shell elements are used which considers the laminate stacking appropriately in order to capture the bending stiffness correctly. However, within the curved areas homogenized parameters are used as this leads to a comparable simple modeling as shortly described in Section 6.3.

Material	E_1 [GPa]	E_2 [GPa]	$\nu_{12} \ [-]$	G_{12} [GPa]	$\alpha_1 [\mathrm{ppm/k}]$	$\alpha_2 [ppm/k]$
M21/T800 UD	177.00	7.86	0.284	3.18	0	25.00
M21/T800 homog.	92.71	92.71	0.0242	3.18	1.33	1.33
$[0, 90]_{3s}$						

Tab. 7.6: M21/T800 material parameters for UD-ply and homogenized parameters $[0, 90]_{3s}$ layup derived with ESAComp Software

According to Equation 6.25 the equivalent expansion parameter is derived to 38.33 ppm/K. The modeling parameter of Equation 6.27 is derived to $1/360 \ Kmm^2$. In order to focus entirely on process-induced distortions and to distinguish them from the homogeneous distortions due to the quasi-isotropic expansion of the layup, the laminate CTEs are zeroed in the model. Thus, distortions are directly related to the spring-in and not superposed by other effects.

Similar to the experimental procedure, the flange distance is evaluated within the FE model. Subsequently, spring-in angles are evaluated using similar techniques as in the evaluation of the measured point cloud. To realize this, multiple node sets are defined in the FE model, whereat node translations of set ae are used for the angle evaluation and set d_f is used for the flange distance evaluation. Figure 7.26 depicts the evaluation node-sets and the derived vectors \vec{a} and \vec{b} for the spring-in angle $\angle(\vec{a}, \vec{b})$ evaluation.

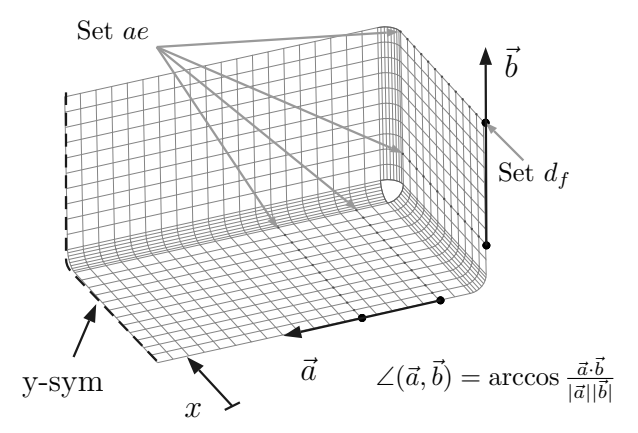


Fig. 7.26: Spring-in angle and flange-distance evaluation in the FE shell-model

Within the first step the simulation focuses on spring-in distortions only. Result related to this simulation are denoted with I in the following.

The second configuration accounts for the forced-interaction effect, whereas parameter modification is done based on engineering judgment and supported by former warpage investigations documented in [9, 102].

Figure 7.27 illustrates the predicted flange shape changes $\Delta y_{s,1}$ in length direction and the corresponding deviation from the measurement Δy_m as red lines. As simulation results are symmetrical, only one half of the results are depicted in Figure 7.27.

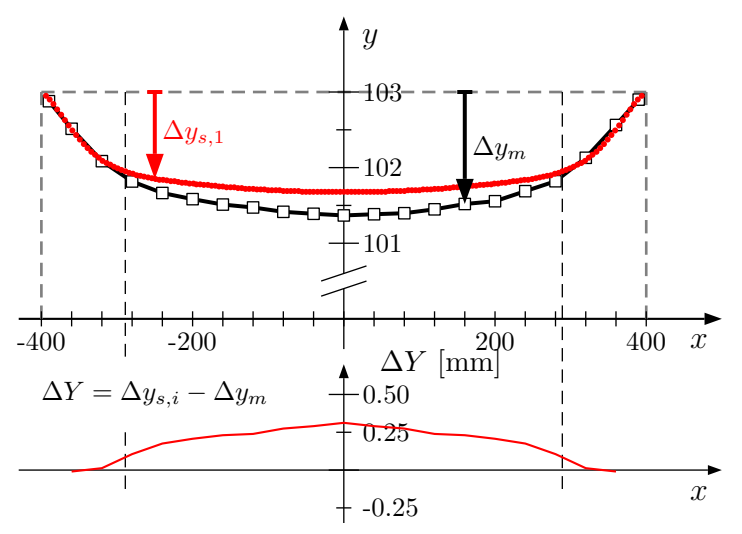


Fig. 7.27: Predicted flange deformations for spring-in-only simulation. ΔY denotes the difference between predicted and measured flange deformation

The match of the obtained results is good for the areas where $|x| \geq 289$ mm. Characteristics of the predicted and measured flange shape are very similar. However, deviations up to 16 % are obtained for the center area of the box ($|x| \leq 289$ mm) which corresponds to a difference between measured and predicted $\Delta Y = \Delta y_{s,1} - \Delta y_m$ of 0.31 mm. However, the evaluation of the spring-in angle along the box length reveals excellent match between the experimentally measured results and the predicted ones as shown in Figure 7.28. Therein, the dashed lines represent the average spring-in angle obtained from the L-profile specimens. At a first glimpse the results presented

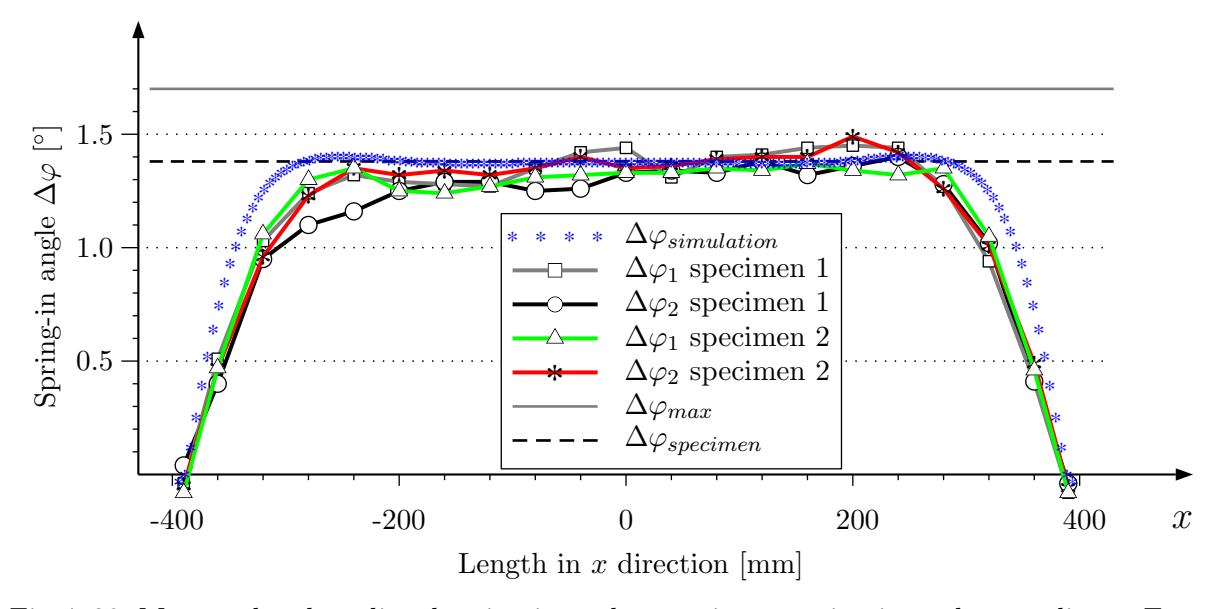


Fig. 7.28: Measured and predicted spring-in angles, maximum spring-in angle according to Equation 5.1 and the average spring-in angle obtained for the manufactured L-profile specimens

here are somehow conspicuous as spring-in angles match the measurements good while the flange distance still show deviations. As indicated within Section 5.1 the explanation for this behavior is comparably simple as the spring-in distortions are superposed by distortions induced due to forced-interaction which induces a considerable curvature of the box's web area. The following figure shows this schematically again.

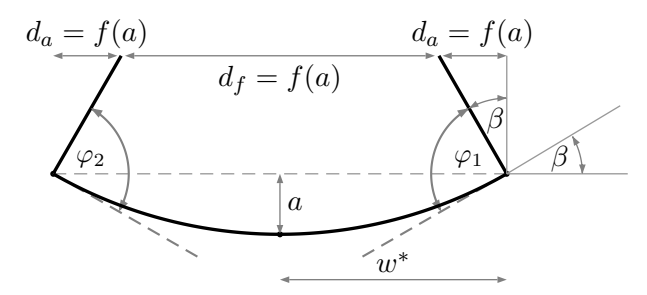


Fig. 7.29: Effect of the global part curvature on the measurands flange distance d_f and manufactured angles $\varphi_i = \tilde{\varphi}_i - \Delta \varphi_i$

As shown in the preceding the predicted flange distance deviates about 0.30 mm (half global deviation) from the measured one. According to Equation 5.5, which is given here again, the effect of the web-area warpage is derived to 0.32 mm which matches almost exactly the difference between simulation an measurement.

$$d_a = \frac{w^* \cdot 2ah}{w^{*2} + a^2} = \frac{(103 \cdot 2 \cdot 0.3 \cdot 55)mm^3}{(103^2 + 0.3^2)mm^2} = 0.32mm$$
 (7.18)

Thus, it is concluded that the semi numerical simulation approach is able to predict the spring-in distortion of the box structure convincingly. As expected, deviations between the prediction and the measurement occur which can be clearly related to other distortion-inducing effects such as forced interaction. Nevertheless, the prediction of the manufactured parts is very good, as the obtained deviations at the flanges are only 0.30 mm to the nominal. Assuming realistic tolerance requirements, typically used in the industry is $\pm 0.5^{\circ}$, would result in a tolerable deviation of ± 0.48 mm when considering a flange height of 55 mm.

Nevertheless, a set of simulations is conducted in order to assess the magnitude of the acting effect qualitatively. Based on the cut box, shown in Figure 7.30, the single areas are inspected. According to Figure 5.14 the cut web area shows considerable warpage of up to 3 mm. This is induced and enforced by forced-interaction effects as demonstrated in Section 5.2. Inspired by the warpage investigations and the developed warpage simulation strategy this approach is used to account for the forced-interaction effects within the simulation.



Fig. 7.30: Box structure after sectioning

According to the experimental findings presented in section 5.2 and shown in Figure 5.14 the expansion parameters of this area are modified based on engineering judgment. The aim of this approach is not to find the physical reason for the global box curvature. Moreover, the aim is to qualitatively explain the acting direction of the induced stresses. Therefore, two additional simulation runs are conducted wherein the thermal expansion parameters of the tool-sided ply are modified. Table 7.7 shows which direction of the thermal expansion properties is modified in each run.

Simulation run	Bottom-ply CTE modified in:				
	x-direction	y-direction			
I	х	X			
II	-	X			

Tab. 7.7: Parameters of the modified simulation runs

The modification of the expansion parameters is done with a constant value of 10 ppm/K. In run I the x- and the y- direction are modified whereat in run II only the y-direction is modified. As this modification does not affect the spring-in behavior of the box, only the web area is evaluated. Figure 7.31 shows the comparison between the measured distortions of the box, the spring-in only simulation and the two modified simulation runs.

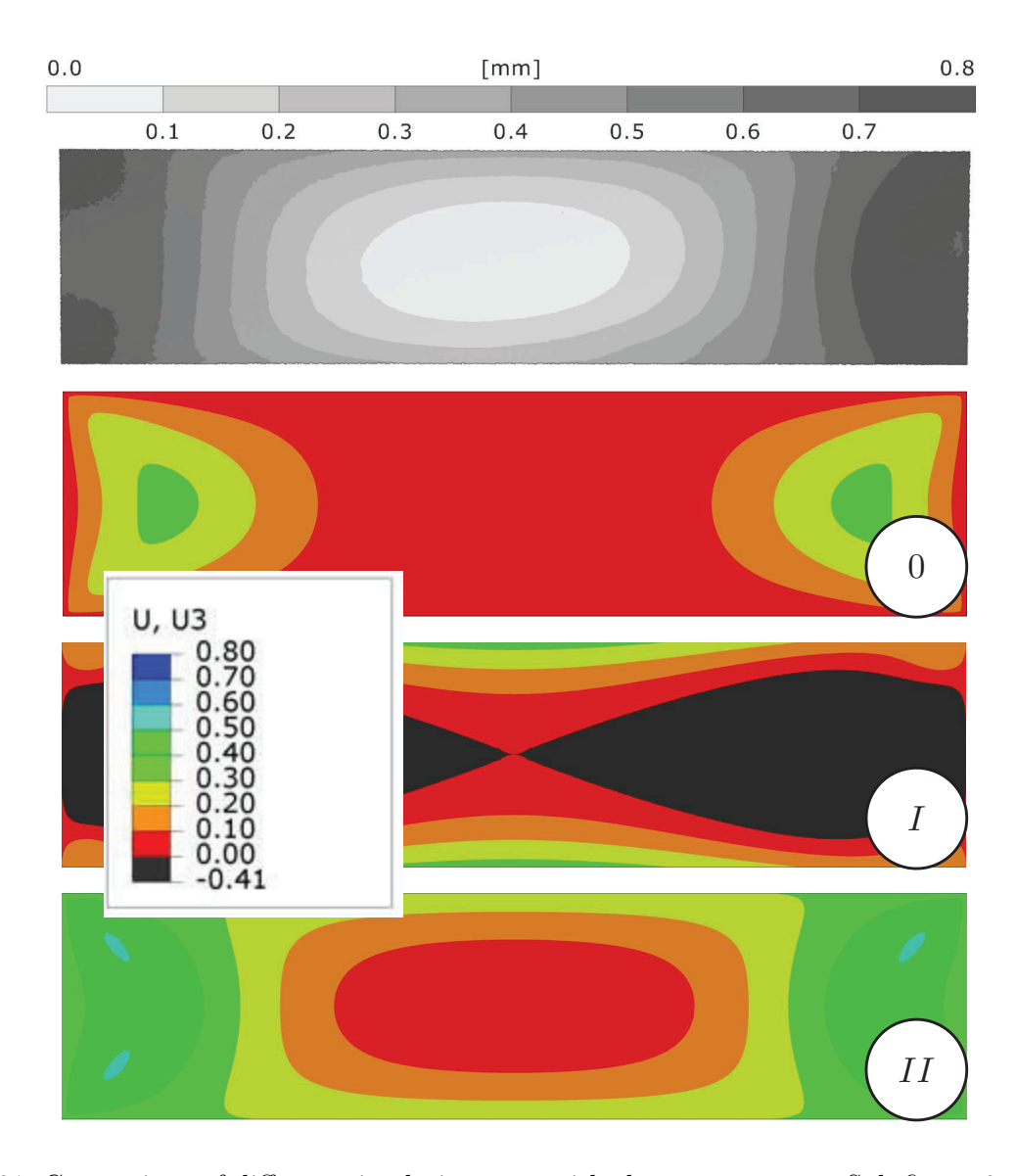


Fig. 7.31: Comparison of different simulation runs with the measurement. Sub-figure 0 denotes the spring-in only simulation

The results clearly show that the a homogeneous in-plane thermal expansion cannot explain the obtained global box curvature. However, simulation run II substantiates that the relevant acting direction is the y-direction. Evaluating the flange distance, as conducted for the spring-in only simulation what is done in Figure 7.32, shows that the predicted flange distance is almost equal to the measured one. Therein, $\Delta y_{s,2}$ denotes the results of the simulation run II.

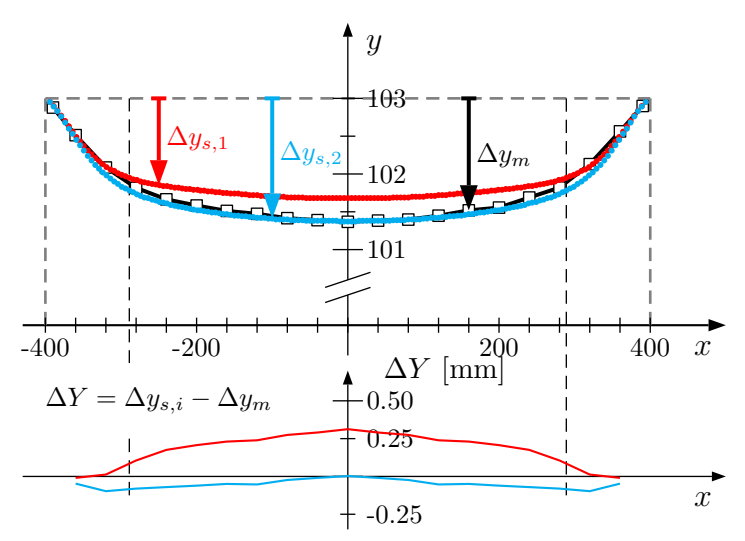


Fig. 7.32: Predicted flange deformations for spring-in-only simulation. ΔY denotes the difference between predicted and measured flange deformation

In summary, based on the modified simulations it is demonstrated that a superposing effect is acting which leads to a global curvature of the box. Based on the modified simulation runs it is shown that the acting direction of this effect is most likely in y-direction. However, the simulation is not able to show whether the web-area is the driving force of this distortions or if residual stresses in the stringers and the ribs lead to the obtained distortion. Experimental findings obtained from a slightly modified box design convincingly showed that the web-area warpage almost disappears when the circumferential path (2 stringer + 2 ribs) is sectioned. Figure 7.33 shows the initial and the modified box design.



Fig. 7.33: Original (left) and modified (right) box design used for the investigation of the forced-interaction effect

As a conclusion of the conducted case study it can be summarized that the simulation approach is able to predict manufacturing-induced distortions of an integrally fabricated composite box with good quality. However, the evaluation of a spring-in only simulation substantiates the experimental findings of Section 5.2. Figure 7.34 shows the simulation result of the simulation run II while deviations from the nominal shape are illustrated.

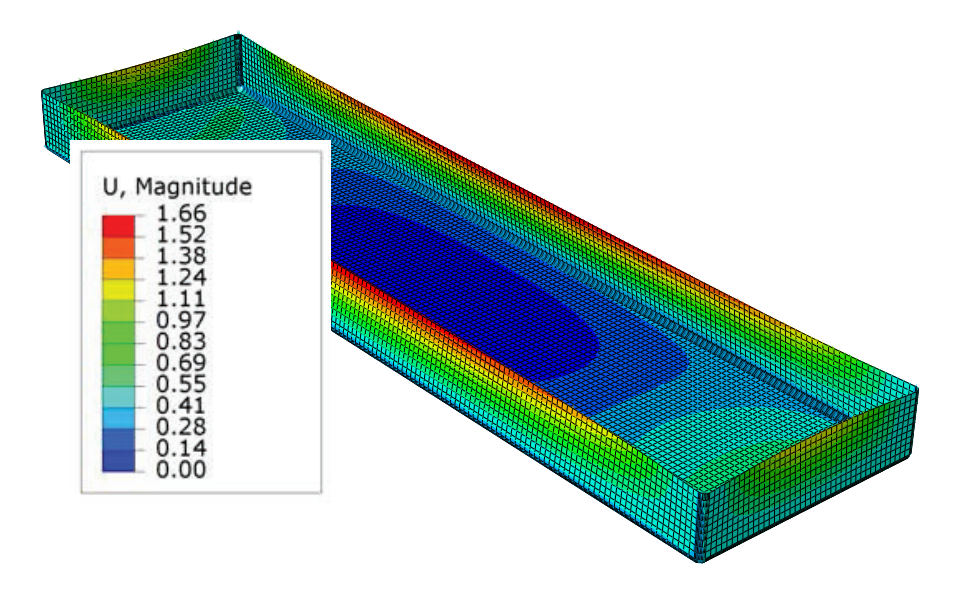


Fig. 7.34: Predicted manufacturing deformations of the box structure. Magnitude of node-translations [mm] is depicted, which correspond to the deviation of the manufactured shape from the nominal shape

It was demonstrated that forced-interaction effects induce global curvature of the part. This is verified experimentally in Section 5.2 as a modified design of the box showed only a small fraction of the web-area warpage compared to the initial design. Of course this design change affects the structural behavior of the box massively which must be considered in the structural sizing. Nevertheless, when focusing on highly integrated design for example, this kind of design modification can be a promising solution in order to reduce undesired process distortions. From an experimental point of view the forced interaction effect needs more detailed investigations in order to identify and quantify the essential drivers.

7.8 Consequences of Process Scattering on Box Distortions

The prediction of expectable process-induced distortions of the CFRP box structure shown in the preceding section uses the average spring-in angle obtained from four nominal identical L-profile specimens. However, as shown in Section 4.4 composite parts commonly show a certain amount of scattering. For a designer it is important to know whether a fabricated structure fulfills or violates tolerance requirements. Furthermore the magnitude of expectable scattering is of particular importance. As long as scattering is observed on L-profile level it is most likely present on the more complex part level.

In this study the effect of scattering is quantified for the CFRP box structure investigated before. Therein, three levels are observed where the first one represents excellent manufacturing conditions with a standard deviation of the expectable spring-in angle of $s_{\Delta\varphi,I}$ is $\pm 0.03^{\circ}$. The second level considers a standard deviation of $s_{\Delta\varphi,II} = \pm 0.10^{\circ}$ which is a rather realistic value as shown in Section 4.4. The third level assumes a standard deviation of $s_{\Delta\varphi,III} = \pm 0.15^{\circ}$ which is considered as the worst cast. Nevertheless, there are selected layups where scattering can exceed these values. However, layups which are used in industry applications are well circumscribed with the chosen scattering intervals.

Figure 7.35 illustrates the different scattering intervals while the blue line corresponds to the predicted spring-in angle along the box's length. Therein, the gray-scaled area represents the expectable range of spring-in based on the scattering levels for an uncompensated manufacturing. Note that level one cannot be differentiated from the blue line as the area is too small.

The green areas represent the expectable scattering for manufacturing on a compensated tool. It is obvious that a tool compensation leads to a significant improvement although the scattering is still present.

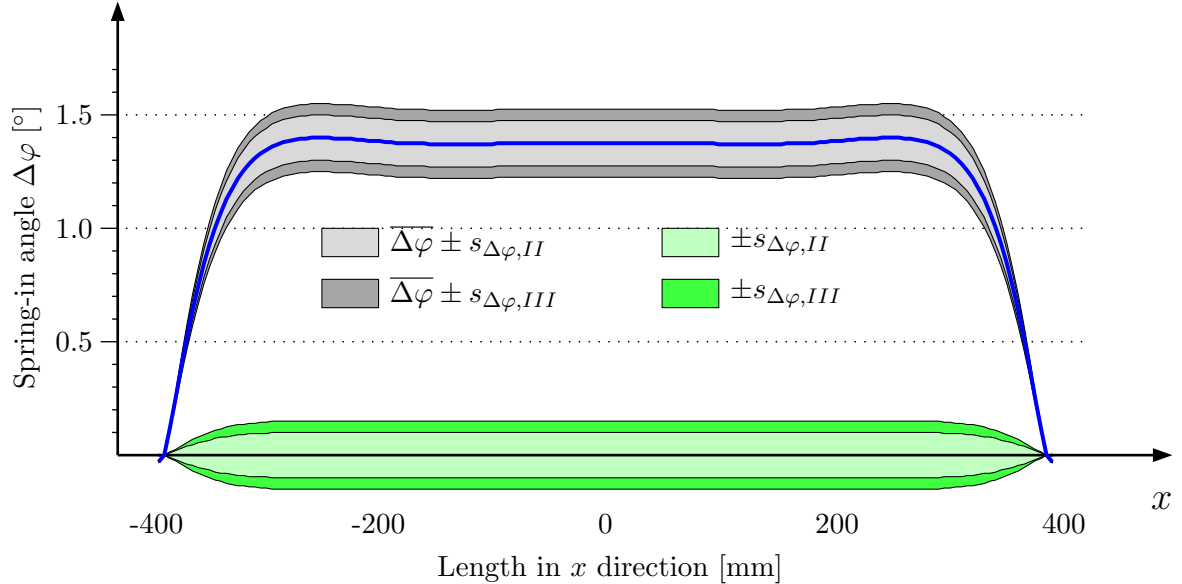


Fig. 7.35: Range of expectable spring-in angles without compensation (gray scale) and with compensation (green scale)

As outlined before the connecting dimensions are of particular importance within the assembly. Based on the assumption that the average spring-in angle can be compensated due to appropriate tool modifications there is still some scattering. Figure 7.36 illustrates the expectable scattering after the average spring-in angle is compensated within the tool. The red line represents the simulation result whereat the black line is the measurement.

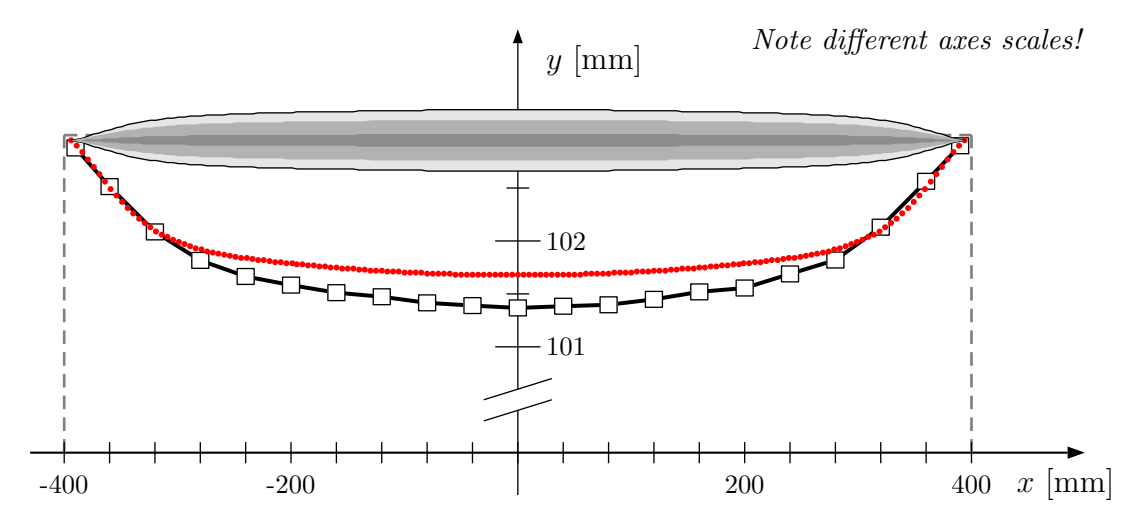


Fig. 7.36: Expectable variation of connecting dimensions due to angle spring-in scattering. Note the different axes scales

The maximum deviation from the nominal shape at the section x=0 mm is 0.29 mm which is a rather good result. Although compensation by tool modification is a promising strategy for the CFRP box regarded here, this approach is not feasible for all applications. Section 7.10 outlines suitable and less suitable geometries.

7.9 Process Distortions of a Highly Integrated CFRP Upper-Wing Cover

Originally the aim was to develop a straightforward strategy for the prediction of process-induced distortions of profile-like structures as stringers and spars. As shown in the preceding section the developed approach is able to predict process distortion for integral structures as well. Therefore, as a next step, it is applied to an integrally fabricated panel what is content of this section. This panel represents a cut out of an integrally fabricated wing skin which is schematically shown in Figure 5.1. The main aims of the wing study are the establishment of a highly automatable and therefore cheap manufacturing process and the realization of a high precision part providing shape tolerances suitable to achieve more natural laminar flow. The integral design concept is a consequence of the NLF requirements as neither steps and gaps are allowed nor a rivet-based assembly is feasible.

Within this study the developed approach is used for the prediction of process distortions. Predicted distortions are compared to measured ones whereat three panels are the experimental basis within this study. As the manufacturing strategy for this panel is still in stage of development, each panel is manufactured with slight differences. As an example, the filler materials are varied from one to another item. Furthermore, the layup is modified as $+45^{\circ}$ and -45° UD plies are substituted by $\pm45^{\circ}$ fabric prepreg. Consequently, geometrical variations from panel-to-panel are observed which are not a consequence of the scattering observed on L-profile level. These deviations are a result of the aforementioned process modifications. Figure 7.37 shows the CAD model of the panel and selected dimensions.

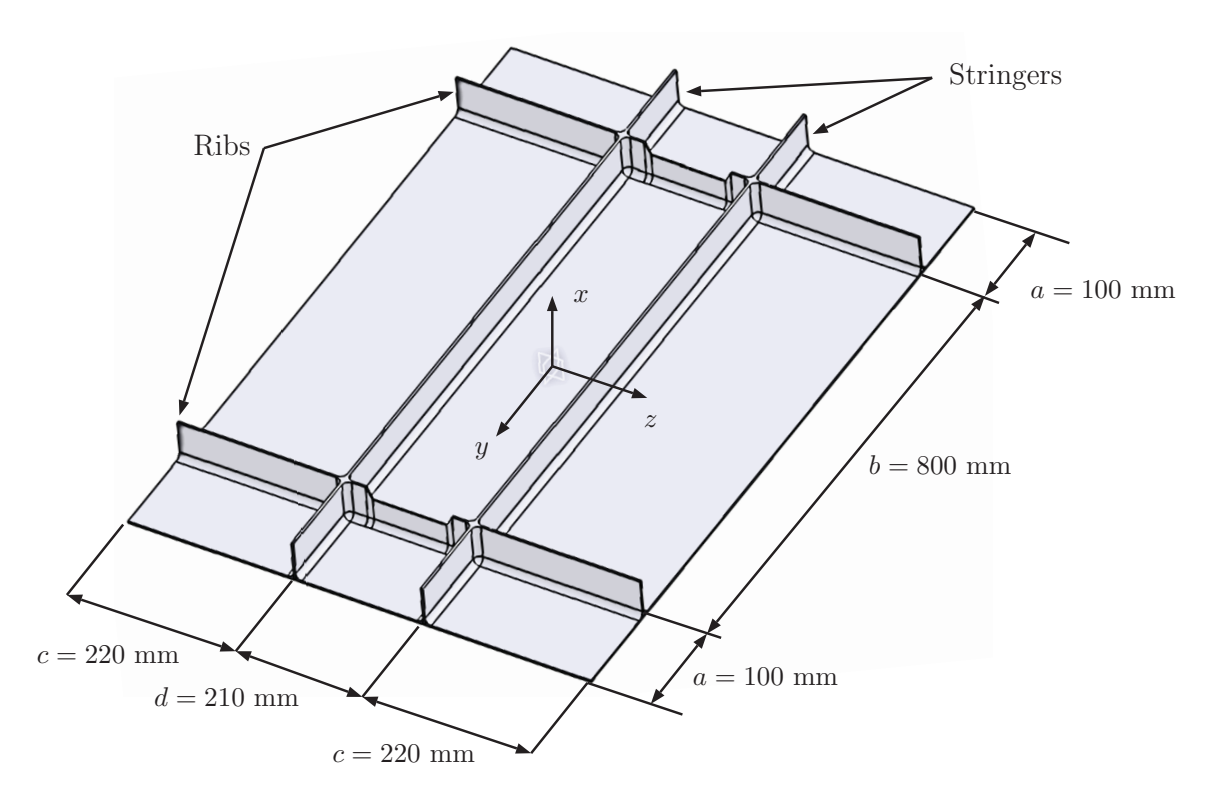


Fig. 7.37: CAD model with selected dimension. Rib and stringer height between 50 mm and 65 mm

Nevertheless, all three panels show comparable characteristic distortions. Obtained magnitudes vary slightly between the three panels. The aim of this study is to verify whether the prediction approach is able to reliably predict the characteristics of the obtained deformations

and a realistic magnitude. The boxes are made from M21/T800 prepreg material with a nominal ply thickness of 0.25 mm. The panels are cured with a double-sided aluminum mold concept. An autoclave curing process with two dwell stages is used which is very similar to the prepreg's MRCC. Figure 5.2 shows the constituents of the integral panel in terms of sub laminates. The inner box structure is equal to that one investigated in detail in Section 5.1. A detailed description of the manufacturing process and the developed tool concept is skipped here as this is neither a part of this thesis nor is it necessary to evaluate the process-induced distortions.

After manufacturing the geometry of all three panels is measured using the full-field measurement system. The obtained high-density point clouds are the basis for the detail measurement presented in the following. Figure 7.38 shows the obtained shape ob the first fabricated panel.

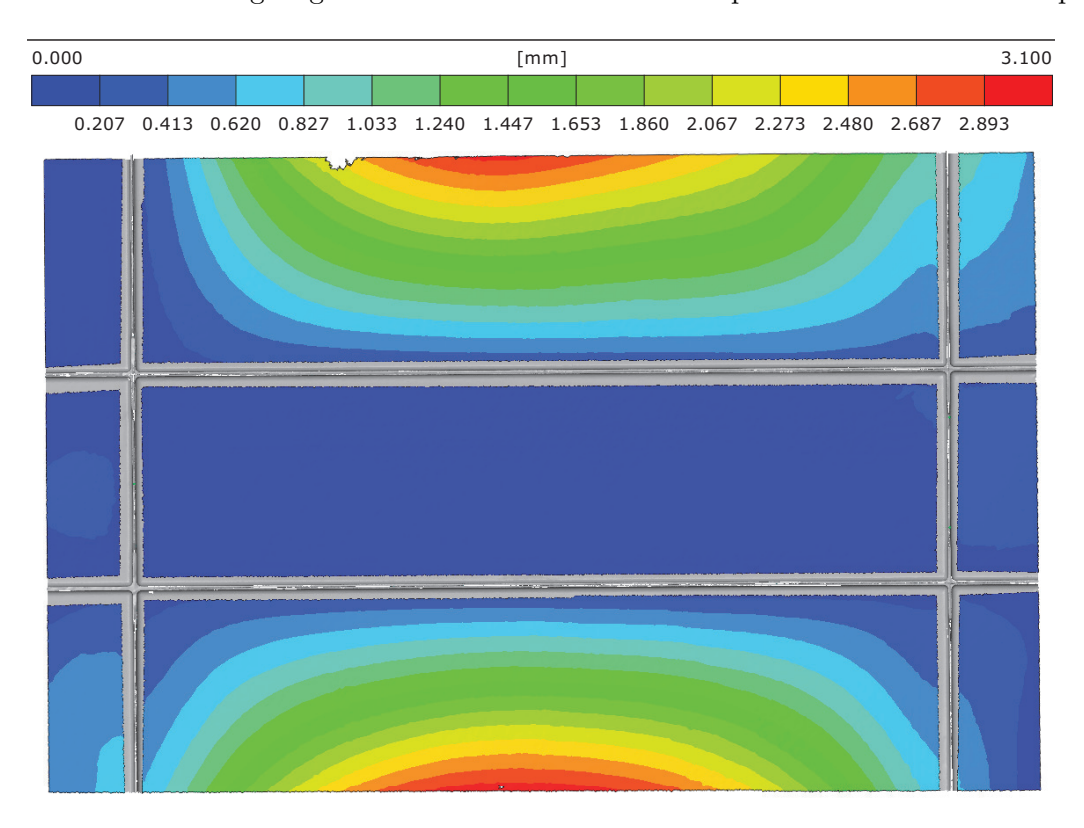


Fig. 7.38: Deviations from the nominal shape of manufactured panel #2

As expected the panel structure shows undesired process-induced distortions. Within the center area, circumscribed by the inner closed box, out-of-plane distortions are below 0.21 mm, while the distortions increase up to three millimeters at both open surface areas. As will be seen in the following, this effect is not critical for the wing concept. Nevertheless, it represents the manufactured shape of the structure which should be predicted by the approach. The model is set up based on the inner surfaces of the boxes and the outer surface of the skin as schematically depicted in Figure 5.2. These surfaces have been extracted from a volume model within the CAD system and than transferred to the FE tool. Single surfaces are kinematically connected within the FE model. The layup of the panel is symmetrical. Consequently it is divided into two unsymmetric layups which are assigned to adjacent shell areas. The global layup symmetry is assured due to the coupling. Similar to the CFRP box model, the flat areas are modeled using the composite module in Abaqus. In flat areas the layup is considered within the simulation while in the curved laminated areas homogenized material parameters are used. One set of L-profile specimens is used for the parameter calculation. The L-profiles showed an average spring-in angle of 1.40°. The simulation results are shown on Figure 7.39.

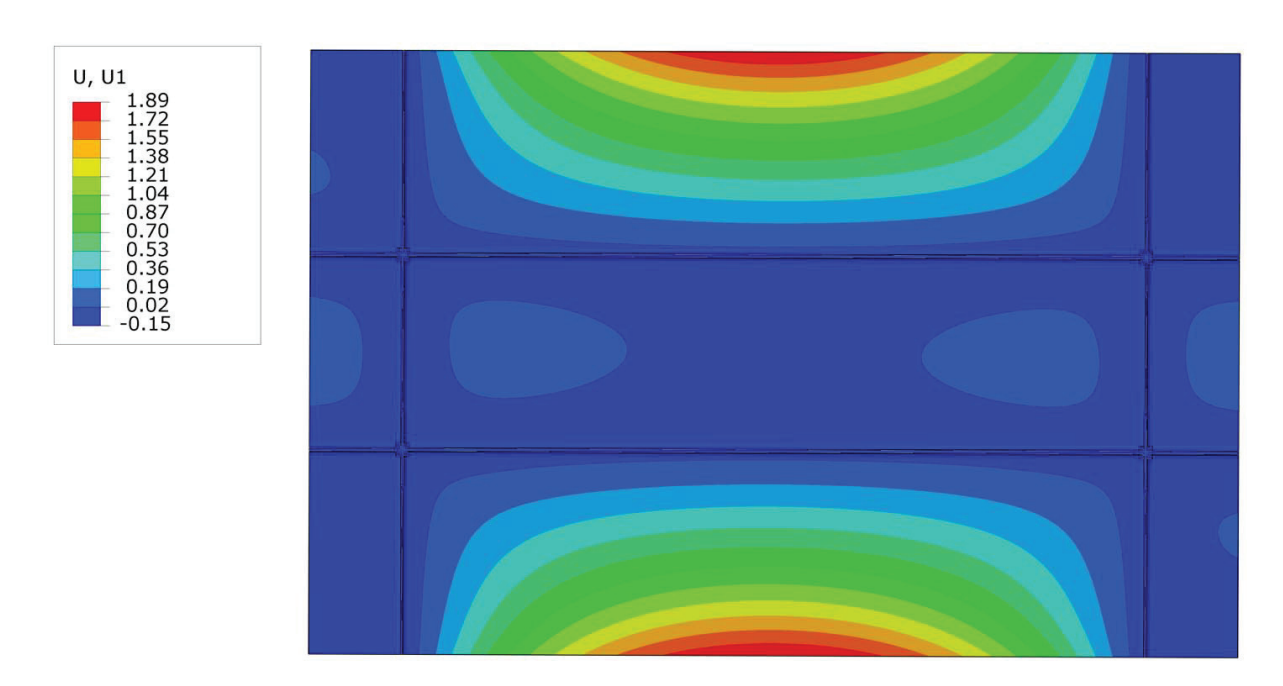


Fig. 7.39: Predicted process distortions of the panel structure

The characteristics of the distortion mode match excellently between simulation and measurement. However, the magnitude of the derived distortions is almost identical as the measurement reveals a maximum deflection of 3.10 mm the simulation predicted 1.89 mm.

The three manufactured panels show variations. Therefore, the simulation result is compared to the deflections of the measurements. This is done by two representative cuts. The first cut is described by the xz-plane as the second one is described by xy-plane. Figure 7.40 shows the obtained results for the xz-plane cuts. Only the first millimeters of the stringers are illustrated for sake of clarity.

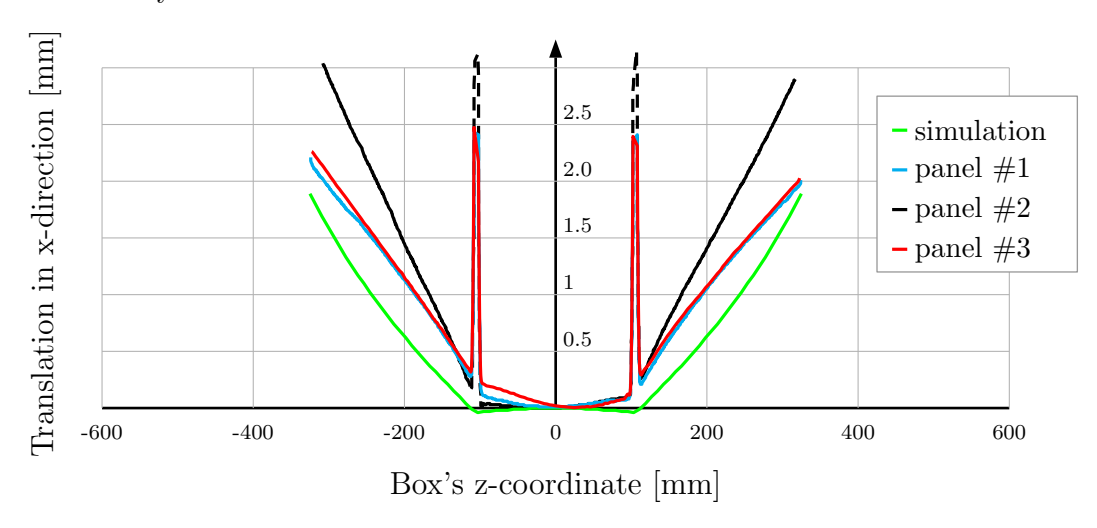


Fig. 7.40: Simulation result vs. measurements of the three panels. Axis scale differs for sake of illustration

As indicated before the panel configurations show differences what is substantiated by the section cuts shown in Figure 7.40. However, panel #1 and panel #3 show almost identical deflections in this cut while panel #2 shows an increased deflection. The characteristics of the simulation result is quiet similar on a global level.

These findings relativize the deviations between simulation and the measurement of panel #2 as this panel shows extraordinary high deflections.

Figure 7.41 shows the section cuts along the xy-plane. Used scales are identical to Figure 7.40. Obtained deflections are one order of magnitude below that one obtained in the perpendicular direction.

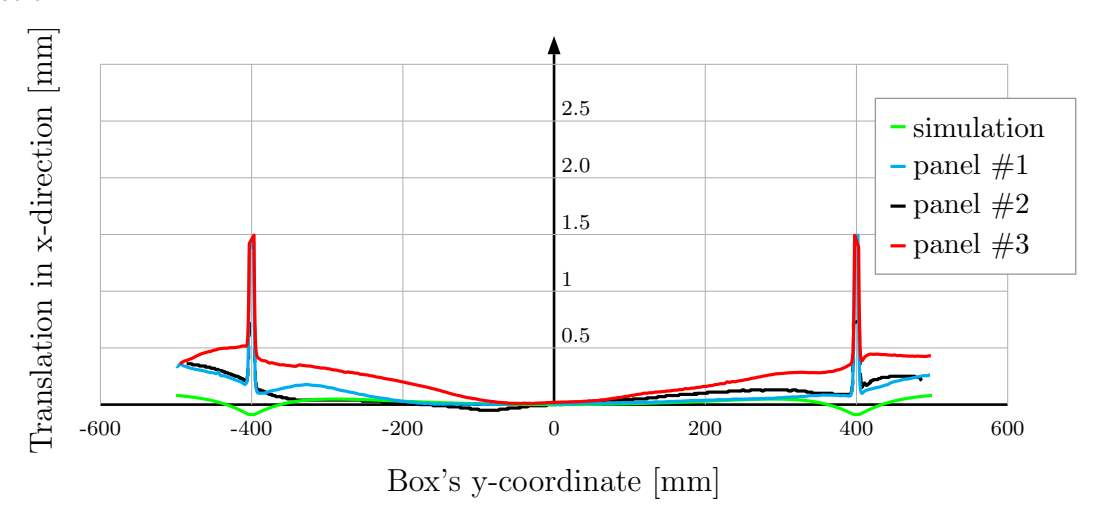
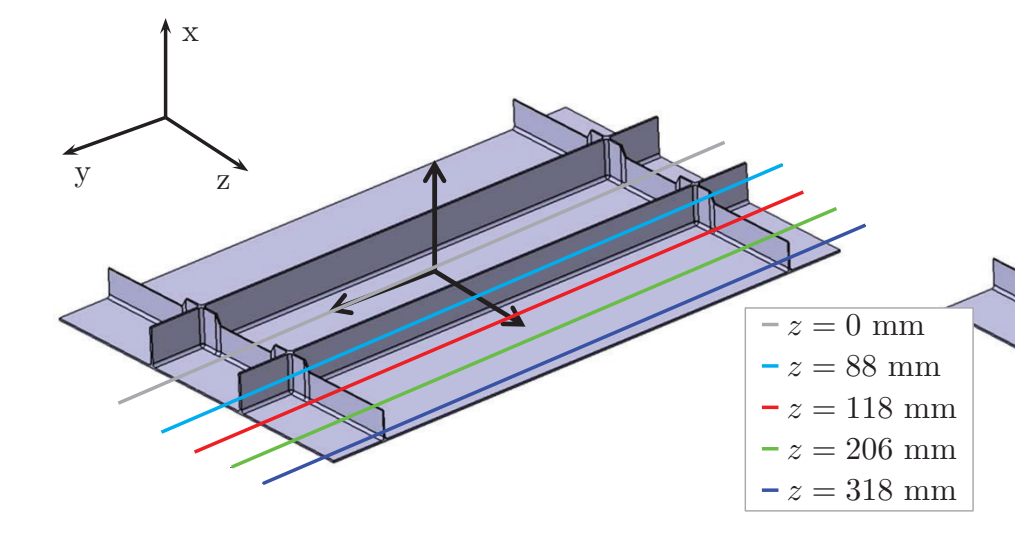


Fig. 7.41: Simulation result vs. measurements of the three panels. Axis scale differs for sake of illustration

Again the simulation underpredicts the measured deflection. As a parallel to the CFRP box investigations the panel measurements show a slight curvature of the center area between both ribs.

As discussed in Section 5.1 the box is affected by forced-interaction effects. Therefore, it is assumed that the panel structure is affected as well. This is substantiated by the obtained double-curvature of the center area between the ribs and the stringers. The simulation run shown here does not account for the forced-interaction effect. Consequently, the obtained deviation is not surprising.

Nevertheless, the simulation result is used to characterize the shape of the manufactured panels in detail. Figure 7.42 shows five sections with different offsets in z-direction.



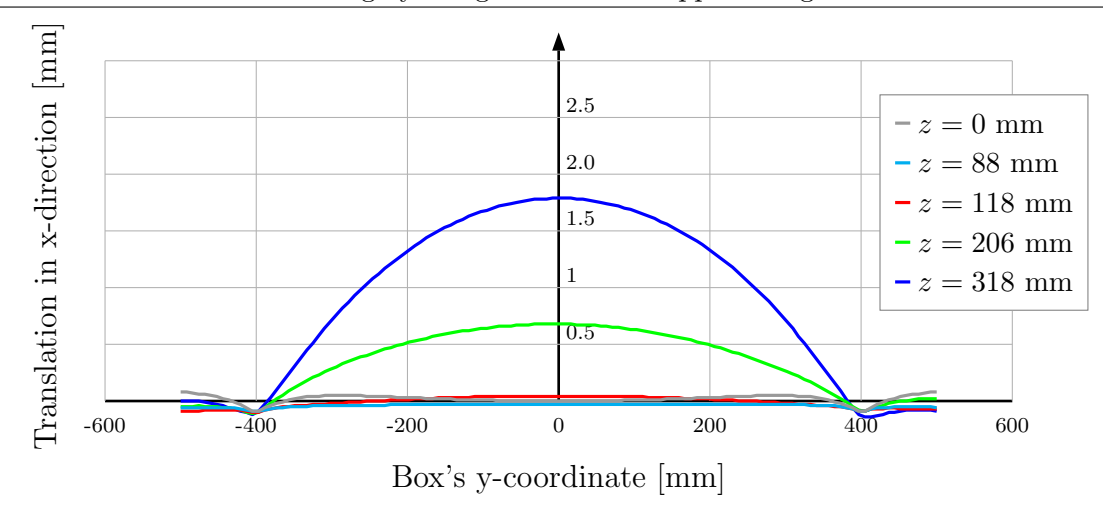


Fig. 7.42: Multiple offset sections to the xy-plane

It becomes obvious that for z>120 deflection increases massively which is a result of the missing adjacent stringer. Within the area enclosed by ribs and stringers the deflection is in the range of ± 0.1 mm.

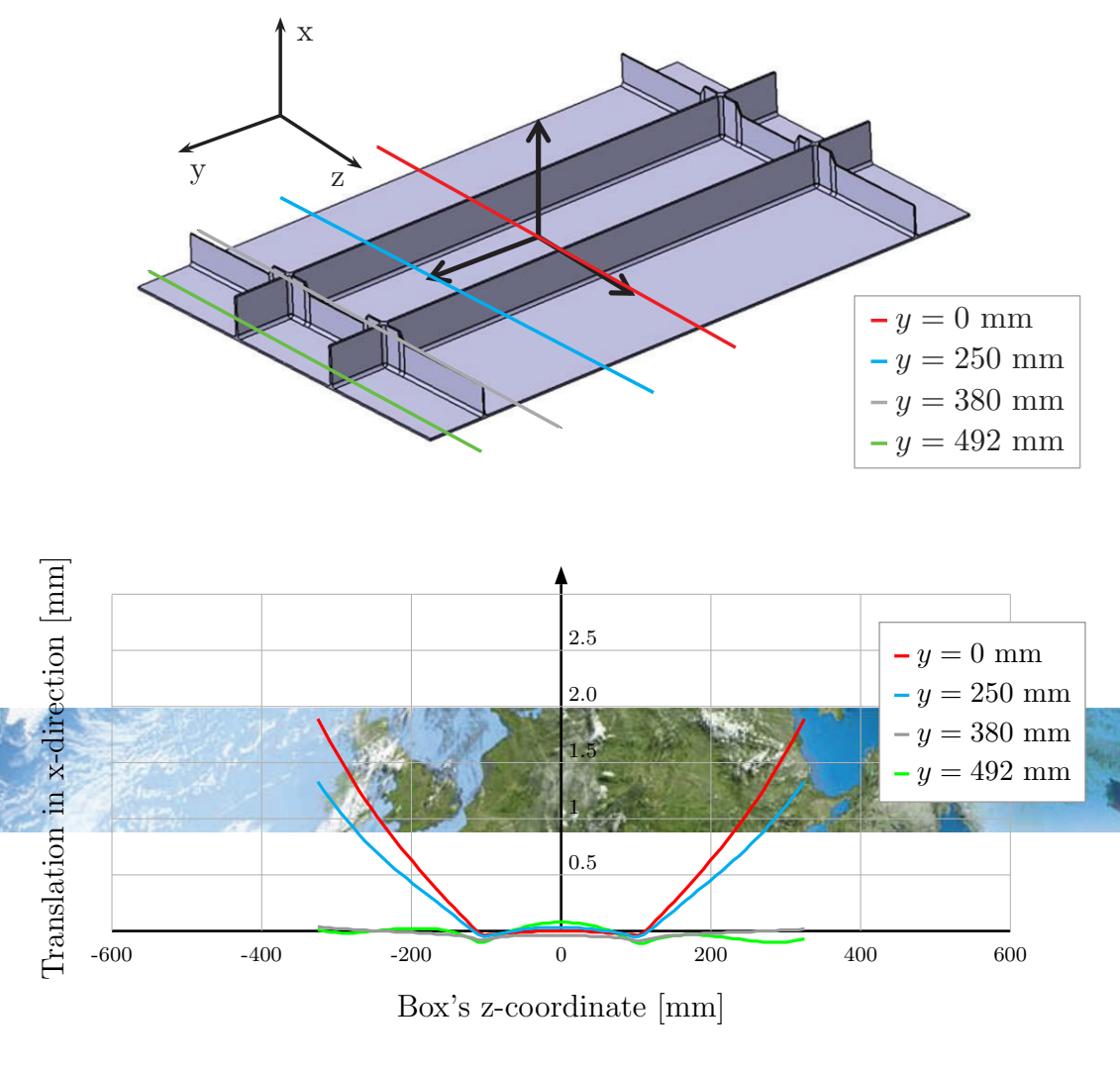


Fig. 7.43: Multiple offset sections to the xz-plane

This is verified by four offset section cuts in y- direction shown in Figure 7.43. The preceding results lead to two main cognitions. First, the panel structure is suitable for the validation of the manufacturing process. Due to its design it is well suited for the investigation of process-induced distortions as they are not constrained. However, the panel design makes it impossible to assess the suitability for NLF as it is not representative for the in-service situation. Figure 7.44 illustrates that schematically. Obtained deflections of the panels are far away from NLF waviness requirements what is an effect of the missing stingers for |z| = 325mm

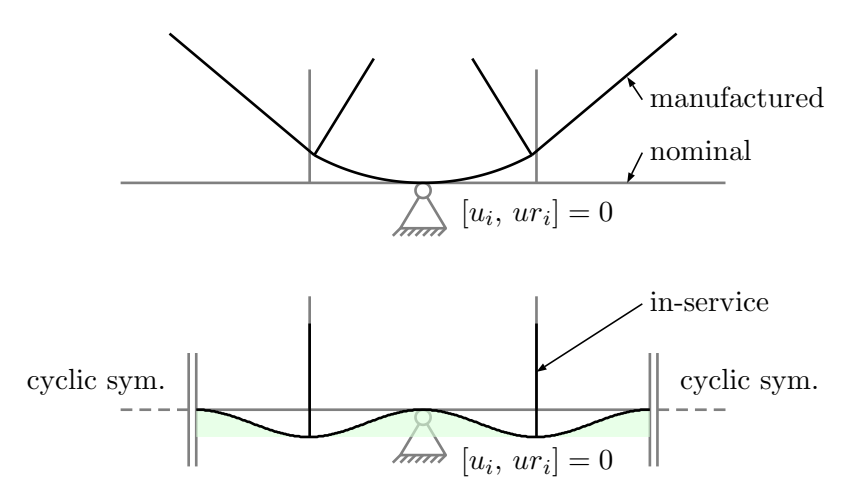


Fig. 7.44: After-manufacturing boundary condition (top) differs from in-service condition (bottom) for the stiffened panel

Consequently, the areas where |z| > 200 mm can freely deform which results in that large distortions. Based on the cognition that the simulation is able to predict the process-induced distortions with good accuracy it is used to derive the expectable structural shape for in-service conditions illustrated by the Figure 7.44 (bottom). Therefore, the geometry of the FE model is modified in order to apply symmetry boundary conditions to the structure. Therefore, dimensions are modified to $a \to a^* = 400$ mm and $c \to c^* = 105$ mm. Figure 7.45 shows the set up simulation model and the derived deflections for applied symmetry conditions.

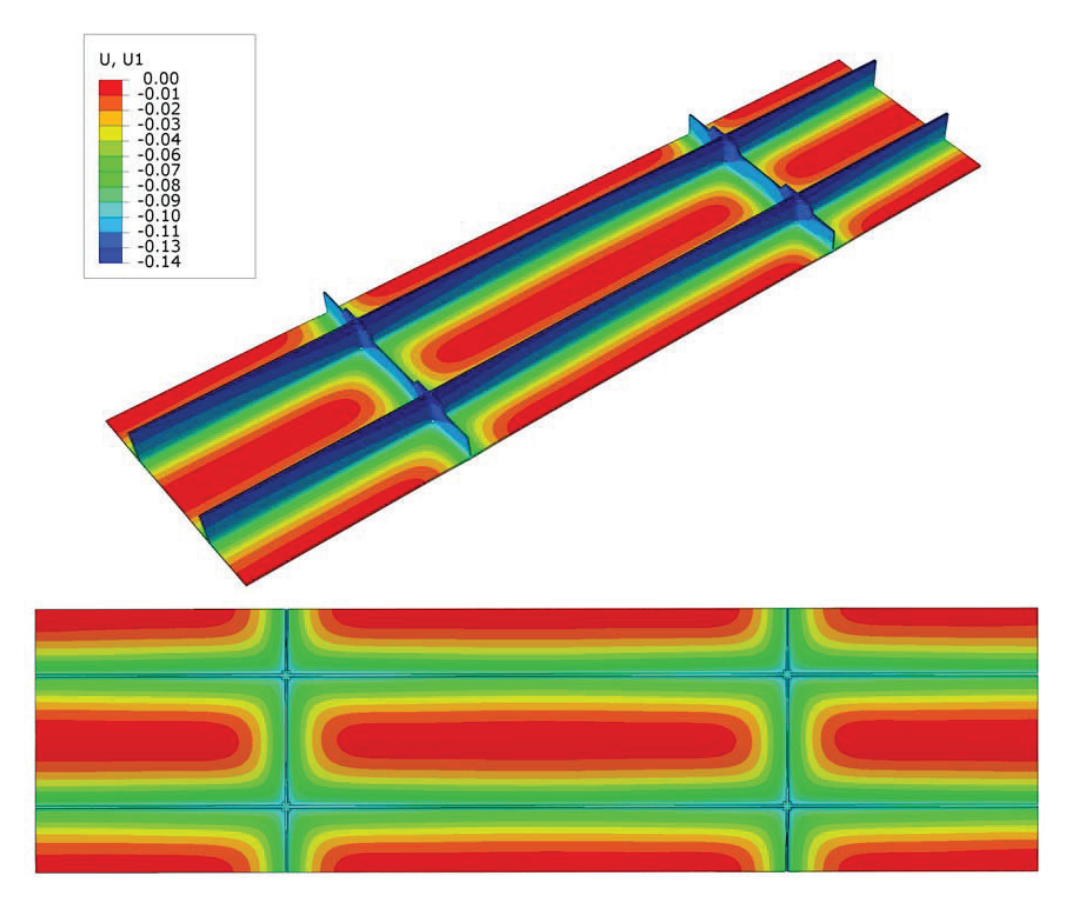


Fig. 7.45: Simulation of a representative panel in for-in-service conditions using symmetry conditions

This Figure shows that the idea to balance process-induced distortions with in-service distortions due to aerodynamic loads is a promising approach as the manufacturing distortions lead to a warp-in behavior of the areas between the stringers and the ribs. These warp-in will be counteracted by a warp-out effect induced due to the aerodynamic suction acting on the outer wing skin during flight. Nevertheless, forced-interaction effects are still an issue which must be considered in order to reach this challenging goal.

7.10 Feasibility of the Tool-Compensation Approach

A reliable prediction of process-induced distortions is one essential step towards a sophisticated design process. One major part of this approach is the derivation of appropriate measures to counteract process-induced distortions by tool-compensation. On the one hand, the prediction of expectable deformations and the derivation of corresponding tool modifications reduce costs. Multiple cost-intensive tool-rework loops can be avoided as the tool geometry is virtually modified prior to the part's first fabrication. On the other hand, a reliable prediction can help to substitute invar tools by less expensive aluminum tools. This is desirable, as raw aluminum is significantly cheaper, milling speeds are higher and the thermal conductivity is one order of magnitude higher than the one of steel. This promises faster and therefore more efficient processing. However, as aluminum tools are prone to induce higher process distortions due to warpage or forced-interaction, the prediction approach must account for these effects thoroughly. Common aerospace structural components are illustrated in Figure 7.46.

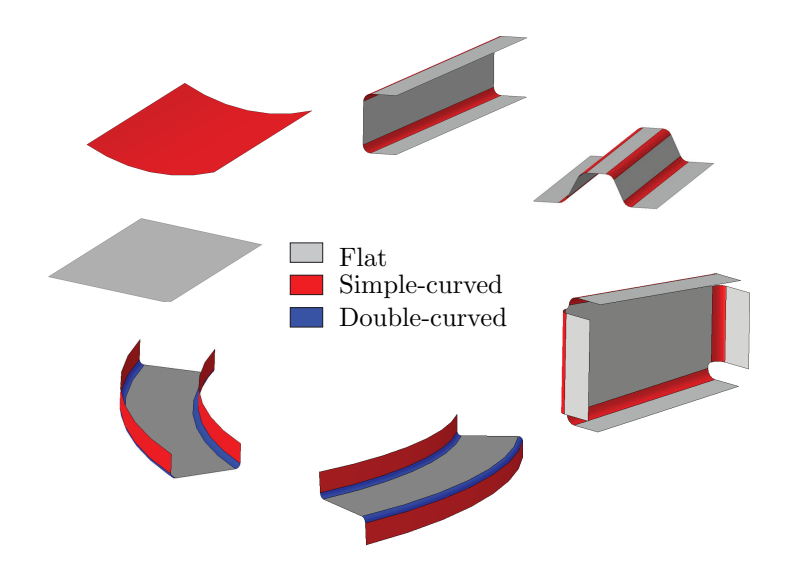


Fig. 7.46: Common structural components in aerospace industry

Most of these structures are suitable for the tool-compensation approach independent of the tool material. However, tool compensation can become impossible, or at least complex, when multiple tools interact within one large tool assembly. Figure 7.47 illustrates that for a cross-section of an integrally stiffened panel, which is similar to the one investigated in Section 7.9.

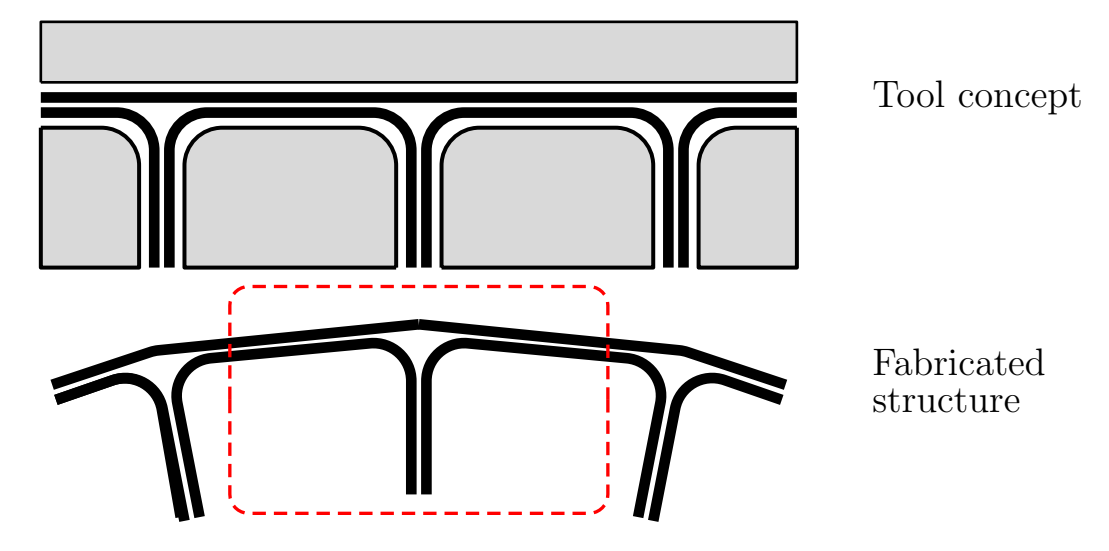


Fig. 7.47: Schematic of a tool concept for integrally fabricated stiffened panel

Fabricating this kind of structure with a nominal tool, while process distortions remain disregarded, results in measurable part deviations. This is supported by the results obtained from the manufactured T-joint which is investigated in Section 7.6.

Results from the C-profile compensation, reported in Section 7.3, show that tool-compensation can lead to parts with almost no deviation from the nominal design, what is schematically illustrated in Figure 7.48.



Fig. 7.48: Feasible compensation concept verified in Section 7.3

However, a simple transfer of this approach to the tooling concept of the whole panel is not possible what is shown in Figure 7.49.

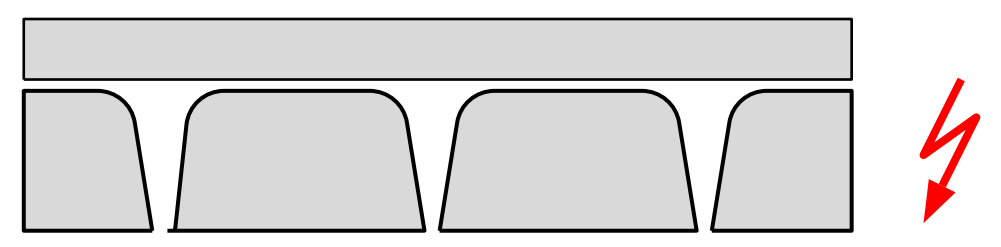


Fig. 7.49: Unfeasible manufacturing

This kind of tooling concept will not be able to assure homogeneous compaction of the stiffening elements. Thus, it is not suitable.

Consequently, stronger tool modifications are necessary to achieve an improved part. This is schematically illustrated in Figure 7.50.

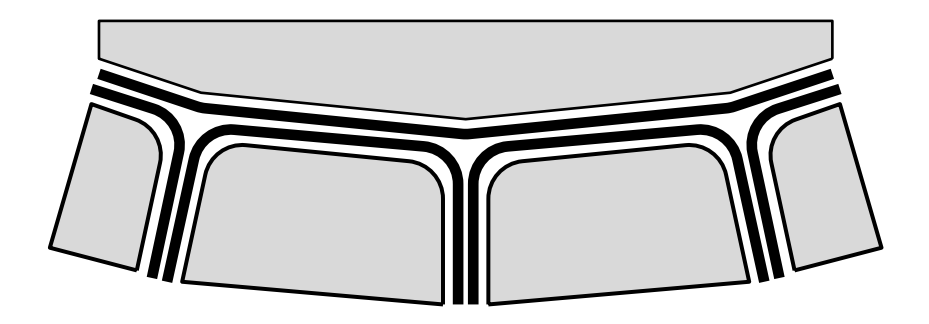


Fig. 7.50: Improved tool concept for integrally fabricated stiffened panel

This kind of tool might be a solution for linearly extruded parts. However, regarding a complete wing skin with integrated ribs and stringers for example, the complexity of the tool concept will increase disproportionally. For this kind of structures, a process-based compensation seems to be a promising approach. Nevertheless, modified processes with modified dwell stages or temperature ramps demand cost intensive material characterizations in order to enable certification. To summarize: tool compensation is a promising solution for the majority of structural components. However, as the complexity of compensated tools commonly increases, it is the designers task to find a best balance between compensation and part design modifications.

8 Conclusions and Outlook

This thesis investigates phenomena that cause process-induced distortions within composite manufacturing. In accordance with the definition of Albert and Fernlund [8] it is distinguished between the three major effects: warpage, spring-in (-back) and forced-interaction.

The superior goal of this thesis is to provide an efficient methodology for the prediction of occurring process distortions. The main aim is to overcome drawbacks of existing numerical-based process simulations which demand extensive material characterizations, complex solid-element modeling and transient calculations. To characterize the acting effects thoroughly, extensive experimental and numerical investigations are conducted to work out the particular main drivers. Within this thesis it is focused on state of the art prepreg materials. Nevertheless, the developed simulation strategy as well as essential findings are similar for RTI and RTM manufacturing technologies. The investigation of the warpage effect reveals a strong dependency from the toolsurface properties as a rougher surface leads to increased warpage. Measured deflections show a strong nonlinear dependency from the specimen length and the specimen thickness. In general, the qualitative behavior is similar for different materials. However, the obtained magnitudes are material dependent as specimens from materials with discrete interleaf layers produce more warpage than specimens without interleaf layers. Although deflections can reach considerable magnitudes for very thin specimens, the relevance for the majority of structural components is limited as warpage is only relevant for flat structures of thicknesses below 1.5 mm. Moreover, warpage is driven by single-sided tool concepts using tool material with considerable thermal expansion such as aluminum or steel. Experiments with a double-sided tool concept reveal no measurable warpage. The spring-in effect turns out to be relevant for all composite structures that contain curved laminate areas. Analytical investigations verify that spring-in is mainly induced by the resin's chemical shrinkage and the thermal contraction. The effect depends linearly on VF for technically relevant VF of 40 up to 70 percent. A comprehensive test program on L-profile level reveals that neither the part thickness, the profile's section radius, the tool material nor the tool surface roughness have an impact on the obtained spring-in distortions. Even different state of the art prepreg materials results in almost identical distortions what is proved for a single UD layup. Statistical analysis based on the whole experimental test program confirms the findings of Jain et al. [19], Nelson and Cairns [20] and Radford [5] as the obtained spring-in angles can be limited to a range of 1.09° to 2.23° for technical relevant layups made from the used carbon epoxy prepreg materials. These layups produce a representative average spring-in angle of 1.57 °. However, even on L-profile level, a representative scattering of up to 10 % is observed for a set of four nominal identical specimens fabricated within one autoclave run. However, specimen sets with only 2 % scattering are fabricated as well. The sources of this scattering are not investigated in detail in this thesis. Scattering of the supplied prepreg material as well as slight misalignment during the hand-layup process are conceivable reasons for this scattering. Moreover, varying consolidation effects during processing can result in distortion scattering, what is indicated by experimental tests measuring the through-thickness strains, during processing. This technique is used based on the idea of the developed 'Extended Radford approach'. As spring-in is almost completely driven by the resin dominated through-thickness strains this approach measures these strains throughout the entire curing process. This is done for circular specimens with dimensions of a few millimeters. Measured process strains for different layup reveal considerable scattering even for one nominal identical configuration. According to Garstka et al. [14], this is related to consolidation processes which vary slightly from specimen

to specimen. However, analysis of the obtained strain graphs shows that a certain point can be derived which can be found in every strain graph. Zeroing different strain graphs of one configuration at this point reveals that almost identical strain is observed after passing this point. The position of this point is related to the gelation of the resin during the process. As a first step this characteristic point is used for the spring-in prediction. However this turns out not to be the correct choice. Indicated by a reverse analysis, the inflection point is more suitable for the spring-in prediction. Apart from that, the developed experimental technique is able to derive the thermal fraction of the spring-in effects and the laminate's CTE in thickness direction. The thermal fraction of the spring-in angle is experimentally obtained to a fraction of 36 % up to 67 % for different laminates. That correlates with findings of Nelson and Cairns [20]. Experiments on circular extruded L-profile specimens show that the spring-in angle obtained from regular L-profiles is equal to that one obtained in the cross section of the curved profiles. One essential finding of the experimental spring-in investigations is that L-profile specimens are excellently suited to characterize the dependencies of the spring-in effect. Therefore, the distortions of these specimens are used as the input parameter for the proposed simulation strategy.

The forced-interaction effect is exemplary analyzed for one integrally fabricated CFRP box structure. Full-field measurements of the structure reveal that spring-in distortions dominate the box shape after manufacturing. However, spring-in is superposed by additional distortions induced due to forced-interaction. By experimental means it is verified that the obtained global curvature of the box is induced by residual stresses acting in the stiffening elements of the structure. Within a modified box design this closed force path is cut what result in almost no residual double-curvature of the box. The developed simulation methodology uses conventional shell elements. This reduces modeling and computational efforts massively, while almost no model-size limitations remain. The approach is based on the classical laminate theory. Measured deflection on specimen level is transferred to a corresponding simulation parameter. This is done analytically based on the derived Equations. Within the model, this parameter is assigned to the curved laminate areas while flat part areas are modeled with conventional material properties. Simulations are linear elastic while conventional shell elements are used.

The application of the methodology to various use cases verifies the suitability of the approach. Good agreement is achieved when comparing predicted with measured process distortions of the CFRP box structure. Deviation obtained for a spring-in only simulation can be clearly related to the forced-interaction effect. Even for a highly integrated upper wing cover predicted distortions are in good agreement. However, this comparison is superposed by process modifications of the cover's manufacturing process which remain disregarded. The proposed sophisticated design process, which considers manufacturing-induced distortion within the tool design, is applied to a C-profile structure. A modified tool geometry is derived based on the predicted process distortions. The part fabricated on this tool shows almost no deviation from the desired nominal shape. This verifies the general idea of 'tool compensation' as it leads to significantly reduced shape deviations of the fabricated parts.

Outlook

This thesis contains a variety of experiments. Some of these experiments are conducted only once in order to answer a single specific question. Consequently, the evidence from a statistical point of view is rather limited for these experiments. Therefore, it is necessary to repeat some experiments conducted in this thesis to statistically verify the results. In particular, the investigations of the forced-interaction effect should be extended in order to substantiate and broaden findings of this thesis. Therefore, the presented box structure should be fabricated on an invar tool in order to experimentally verify the effect of the significant smaller tool CTE. Moreover essential part parameters such as layup and thickness should be varied. This is essential in order to predict

distortions due to forced-interaction reliably. Especially for highly integral structures, which often demand complex tooling concepts, the forced-interaction can be a show-stopper.

The idea of the 'Extended Radford Approach' is based on the cognition that spring-in is driven almost exclusively by the resin dominated through-thickness strains. The experimental technique yields very interesting results as strain is measured with extraordinary high reproducibility. This suggests the developed technique as a suitable alternative for the determination of simulation parameters applicable with the developed approach. Due to specimen dimensions of a few millimeters, this technique promises additional cost saving potential compared to the L-profile manufacturing process. However, the experimental setup should be upgraded in order to achieve realistic process conditions in terms of pressure. Currently, it cannot be concluded whether this affects the obtained results significantly. As consolidation pressure is supposed to affect only the pre-gelation phase of the curing process it is not unlikely that the simple technique used in this thesis is suitable.

Within this thesis prepreg manufacturing is considered. The cognitions of this thesis should be extended to infusion technologies such as RTI and RTM. Out of Autoclave manufacturing should be investigated as well as it promises reduced process distortions due to curing at room temperature. Based on the findings of this thesis a significant spring-in reduction of more than 50~% is expected. As the developed prediction methodology is material independent, it should be used for other material systems as well.

Considering sandwich applications, the model should be extended as shear deformations of the core are not realistically captured by the current model which is based on CLT.

The idea to modify the tool geometry to counteract process distortions should be experimentally verified to more complex structures. As outline in Section 7.10 and experimentally verified for a C-profile in Section 7.3, this approach is suitable for the majority of structural components such as stringers or spars. However, it must be verified for integral structures such as the regarded box structure. The aim must be to establish aluminum as the standard tool material as this promises significantly reduced costs compared to invar tools, as the raw material is comparably cheap and faster machining is possible. Therefore, further experiences must be generated using the developed tool compensation process. Considering highly integral parts such as a stiffened panel or even the integrally fabricated upper wing cover, simple tool compensation is not possible as this would lead to conical shapes of the male cores. This will hinder the alignment of the cores within the complete tool assembly. Therefore, process-based compensation must be considered as an alternative solution. Beside the experimental verification, the approach should be applied to large structures. Tools should be compensated using the approach and finally fabricated parts should be compared to full field measurements to verify the accuracy of the prediction. Obtained accuracy for the structures is convincing, in particular when considering the simple and fast simulation procedure.

A Verification of the Advanced Model Formulation

In this section the advanced model formulation is exemplary applied to one L-profile specimen. The essential equations of Section 6.4 are listed in the following.

$$\left\{ \begin{array}{l}
 \partial \varphi / \partial s_{\varphi} \\
 \partial \vartheta / \partial s_{\theta} \\
 0
 \end{array} \right\} = \underline{\underline{D}}^{-1} \cdot \underline{M}^{*}
 \tag{A.1}$$

$$\underline{\underline{D}}^{-1} = \frac{1}{\det\left(\underline{\underline{D}}\right)} \cdot adj \ \underline{\underline{D}} \quad \text{with} \quad \det\left(\underline{\underline{D}}\right) = D_{11} \cdot D_{22} - D_{12}^2 \tag{A.2}$$

$$\begin{cases}
\frac{\partial \varphi/\partial s_{\varphi}}{\partial \vartheta/\partial s_{\vartheta}} \\
0
\end{cases} = \Delta T \cdot \frac{1}{2} \cdot \frac{h_{k}^{2} - h_{k-1}^{2}}{\det(\underline{\underline{D}})} \begin{bmatrix}
D_{22} & -D_{12} & 0 \\
-D_{12} & D_{11} & 0 \\
0 & 0 & \frac{1}{D_{66}}
\end{bmatrix} \cdot \begin{bmatrix}
\bar{Q}_{11} & \bar{Q}_{12} & 0 \\
\bar{Q}_{12} & \bar{Q}_{22} & 0 \\
0 & 0 & \bar{Q}_{66}
\end{bmatrix}_{1} \cdot \begin{Bmatrix} \alpha_{\varphi} \\ \alpha_{\vartheta} \\ 0
\end{cases} (A.3)$$

$$\partial \varphi / \partial s_{\varphi} = \Delta T \cdot \frac{1}{2} \cdot \left(h_{k}^{2} - h_{k-1}^{2} \right) \cdot \frac{1}{\det(\underline{\underline{D}})} \cdot \left(D_{22} \left(\bar{Q}_{11} \cdot \alpha_{\varphi} + \bar{Q}_{12} \cdot \alpha_{\vartheta} \right) - D_{12} \left(\bar{Q}_{12} \cdot \alpha_{\varphi} + \bar{Q}_{22} \cdot \alpha_{\vartheta} \right) \right)$$
(A.4)

Application to an L-profile structure

An L-profile with a $[0, 90]_s$ laminate is regarded. The nominal ply thickness is $t_{ply} = 0.25$ mm while the initial section angle is 90° . Equation A.5 gives the ply stiffness matrices for the 0° and the 90° with respect to the global coordinate system.

$$\begin{bmatrix} \underline{\bar{Q}}_{0} \\ \bar{Q}_{12} & \bar{Q}_{22} & 0 \\ 0 & 0 & \bar{Q}_{66} \end{bmatrix} \quad \text{and} \quad \underline{\underline{\bar{Q}}}_{90^{\circ}} \begin{bmatrix} \bar{Q}_{22} & \bar{Q}_{12} & 0 \\ \bar{Q}_{12} & \bar{Q}_{11} & 0 \\ 0 & 0 & \bar{Q}_{66} \end{bmatrix}
 \tag{A.5}$$

Equations A.6 gives the coefficients of the bending stiffness matrix \underline{D} and its determinant.

$$D_{11} = \frac{1}{192} \left(14 \cdot \bar{Q}_{11} + 2 \cdot \bar{Q}_{22} \right) \tag{A.6}$$

$$D_{22} = \frac{1}{192} \left(2 \cdot \bar{Q}_{11} + 14 \cdot \bar{Q}_{22} \right) \tag{A.7}$$

$$D_{12} = \frac{1}{192} \cdot 16 \cdot \bar{Q}_{12} \tag{A.8}$$

$$\rightarrow det\left(\underline{\underline{D}}\right) = \frac{1}{192^2} \cdot 2 \cdot \left(14\bar{Q}_{11}^2 + 100\bar{Q}_{11}\bar{Q}_{22} + 14\bar{Q}_{22}^2 - 8\bar{Q}_{12}^2\right) \tag{A.9}$$

Inserting the preceding equations in Equation A.4 gives:

$$\partial \varphi / \partial s_{\varphi} = \Delta T \cdot \frac{-18}{192^{2} \cdot \det\left(\underline{\underline{D}}\right)} \cdot \left(\left(2\bar{Q}_{11} + 14\bar{Q}_{22}\right) \cdot \left(\bar{Q}_{11} \cdot \alpha_{\varphi} + \bar{Q}_{12} \cdot \alpha_{\vartheta}\right) - 16\bar{Q}_{12} \cdot \left(\bar{Q}_{12} \cdot \alpha_{\varphi} + \bar{Q}_{22} \cdot \alpha_{\vartheta}\right)\right). \tag{A.10}$$

Rearranging and introduction of $det(\underline{\underline{D}})$ gives:

$$\partial \varphi / \partial s_{\varphi} = \Delta T \cdot \frac{-18}{192^{2}} \cdot \frac{192^{2}}{2 \cdot \left(14\bar{Q}_{11}^{2} + 100\bar{Q}_{11}\bar{Q}_{22} + 14\bar{Q}_{22}^{2} - 8\bar{Q}_{12}^{2}\right)} \cdot \left(\left(2\bar{Q}_{11}^{2} + 14\bar{Q}_{11}\bar{Q}_{22} - 16\bar{Q}_{12}^{2}\right) \cdot \alpha_{\varphi} + \left(2\bar{Q}_{11}\bar{Q}_{12} - 2\bar{Q}_{22}\bar{Q}_{12}\right) \cdot \alpha_{\vartheta}\right). \quad (A.11)$$

Integration of the terms A, B and C yields:

$$\partial \varphi / \partial s_{\varphi} = \Delta T \cdot (-9) \cdot \frac{(\mathbf{A} \cdot \alpha_{\varphi} + \mathbf{B} \cdot \alpha_{\vartheta})}{\mathbf{C}}$$
(A.12)

Equation A.12 shows that the curvature change in φ -direction depends on the expansion parameter in φ and in ϑ direction which is due to the consideration of lateral contraction. An analogous relation can be find for the ϑ - direction Enforcing zero curvature in direction of $\partial\vartheta/\partial s_{\vartheta}$, as is the fact for an L-profile, allows the combination of both relations what is given in Equation A.13. Therein, **B1** represents the interaction coefficient.

$$\partial \vartheta / \partial s_{\vartheta} \stackrel{!}{=} 0 \quad \rightarrow \quad \alpha_{\vartheta} = \frac{D_{11}\bar{Q}_{12} - D_{12}\bar{Q}_{11}}{D_{12}\bar{Q}_{12} - D_{11}\bar{Q}_{22}} \cdot \alpha_{\varphi} = \mathbf{B1} \cdot \alpha_{\varphi}$$
 (A.13)

$$\partial \varphi / \partial s_{\varphi} = \Delta T \cdot (-9) \cdot \frac{(\mathbf{A} + \mathbf{B} \cdot \mathbf{B1}) \cdot \alpha_{\varphi}}{\mathbf{C}}$$
 (A.14)

Integrating along the arc length and solving for α_{φ} gives:

$$\alpha_{\varphi} = \frac{\mathbf{C} \cdot \varphi_{mes}}{-9 \cdot \varphi_{0} \cdot R_{0,\varphi} \cdot \Delta T \cdot (\mathbf{A} + \mathbf{B} \cdot \mathbf{B} \mathbf{1})}$$
with
$$\begin{cases}
\mathbf{A} = 2\bar{Q}_{11}^{2} + 14\bar{Q}_{11}\bar{Q}_{22} - 16\bar{Q}_{12}^{2} \\
\mathbf{B} = 2\bar{Q}_{11}\bar{Q}_{12} - 2\bar{Q}_{22}\bar{Q}_{12} \\
\mathbf{B} \mathbf{1} = \frac{D_{11}\bar{Q}_{12} - D_{12}\bar{Q}_{11}}{D_{12}\bar{Q}_{12} - D_{11}\bar{Q}_{22}} \\
\mathbf{C} = 14\bar{Q}_{11}^{2} + 100\bar{Q}_{11}\bar{Q}_{22} + 14\bar{Q}_{22}^{2} - 8\bar{Q}_{12}^{2}
\end{cases}$$
(A.15)

This Equation can approximated by Equation A.16 as will be demonstrated in the following.

$$\alpha_{\varphi,approx} = \frac{\mathbf{C} \cdot \varphi_{mes}}{-9 \cdot \varphi_0 \cdot R_{0,\varphi} \cdot \Delta T \cdot (\mathbf{A})}$$
(A.16)

Application

The model parameters are:

$$\varphi_0 = 90^{\circ}$$

$$\varphi_{mes} = 1.5^{\circ}$$

$$\Delta T = -100^{\circ} \mathrm{C}$$

 $E_1 = 149460 \text{ MPa}, E_2 = 6870 \text{ MPa}, G_{12} = 3900 \text{ MPa}, \nu_{12} = 0.268.$

The corresponding lamina stiffness matrix is given by:

$$\underline{\underline{Q}} = \begin{bmatrix} 149955.00 & 1847.26 & 0\\ 1847.26 & 6892.76 & 0\\ 0 & 0 & 3900 \end{bmatrix}. \tag{A.17}$$

The term A, B, B1 and C are derived to:

$$\mathbf{A} = 0.59390959069 \cdot E11 \tag{A.18}$$

$$\mathbf{B} = 0.00528542612.4 \cdot E11 \tag{A.19}$$

$$\mathbf{B1} = 0.036418556 \tag{A.20}$$

$$(\mathbf{BB1} = 0.00001924875 \cdot E11) \tag{A.21}$$

$$\mathbf{C} = 4.11824 \cdot E11 \tag{A.22}$$

The derived equivalent parameter and the approximated parameter is derived to:

$$\alpha_{\varphi} = 26.11002 \ ppm/K \rightarrow \Delta \varphi_{mes,FEM} = 1.498^{\circ}$$
 (A.23)

$$\alpha_{\varphi} = 26.11002 \ ppm/K \rightarrow \Delta \varphi_{mes,FEM} = 1.498^{\circ}$$

$$\alpha_{\varphi,approx} = 26.1185 \ ppm/K \rightarrow \Delta \varphi_{mes,FEM} = 1.498^{\circ}.$$
(A.23)

The comparison of both parameters clearly shows that the approximated solution is suitable as both results are identical for up to the third decimal place.

Experimental Study on Interply Slippage

By means of a single experiment it is investigated whether interply slippage occurs during processing. Therefore, three C-profile strips are fabricated on an aluminum tool in one autoclave run. As demonstrated for the CFRP box forced-interaction affects this kind of structure. A [0]₈ layup is used for all specimens. For the modified configuration I the tool sided ply is cut at the symmetry line of the C-profile. In configuration II the tool sided ply is cut twice at both ends of the web area. Both modified configurations and the experimental setup are schematically depicted in Figure B1.

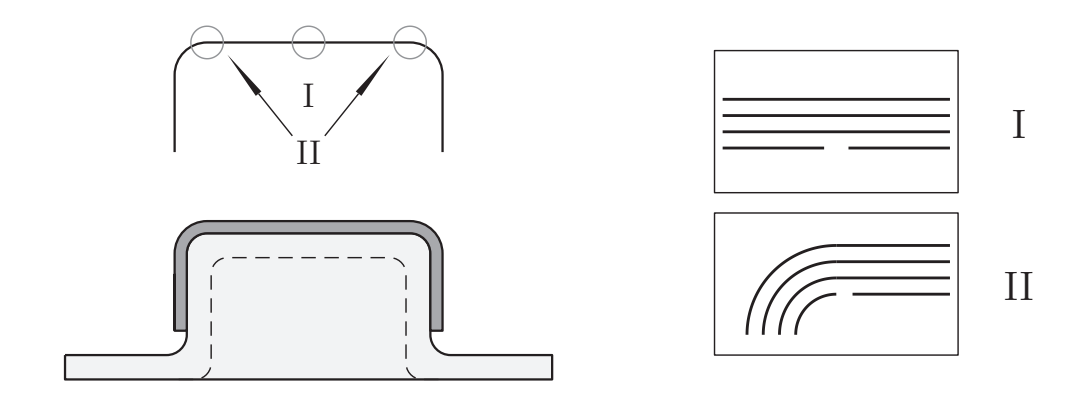


Fig. B1: Experimental setup for the interply-slippage investigation

This simple experiment allows the evaluation whether any slippage between the tool-sided ply and the rest of the laminate occurs during processing. This is an important information in context of a process-based spring-in compensation. When slippage occurs, this might be used to counteract spring-in by modified process cycles. However, in this small study it is investigated whether slippage occurs during a conventional MRCC.

As discussed in Section 5 high process temperature leads to considerable tool expansion of the tool during processing. As forced-interaction enforces the specimen curvature, as experimentally verified in Section 5, an additional stress gradient must act inside the part, as a homogeneous tension would not lead to an additional curvature. Similar to the warpage investigation, the gradient can be driven by the tool-sided ply or the entire laminate.

Specimens are fabricated with a 180°C process cycle with an absolute pressure of $0.7~N/mm^2$. After manufacturing, the specimen I and the regular specimen are cut and micro section analyses are performed. Due to the thermal mismatch between the aluminum tool CTE $\approx 24~\rm ppm/K$ and the CFRP CTE of ≈ 0 -1 ppm/K frictional forces are expected during processing as the laminate is forced to stay in contact with the expanding tool what is induced due to the autoclave pressure. When ply-to-ply interaction is stronger than ply-to-tool interaction no gaps will be observed areas adjacent to the cut. When ply-to-tool interaction increases ply-to-ply interaction, a gap will be observed in the micro section analysis of the cut configuration I. Figure B2 shows two micrographs of configuration I (top) and the regular configuration (bottom).

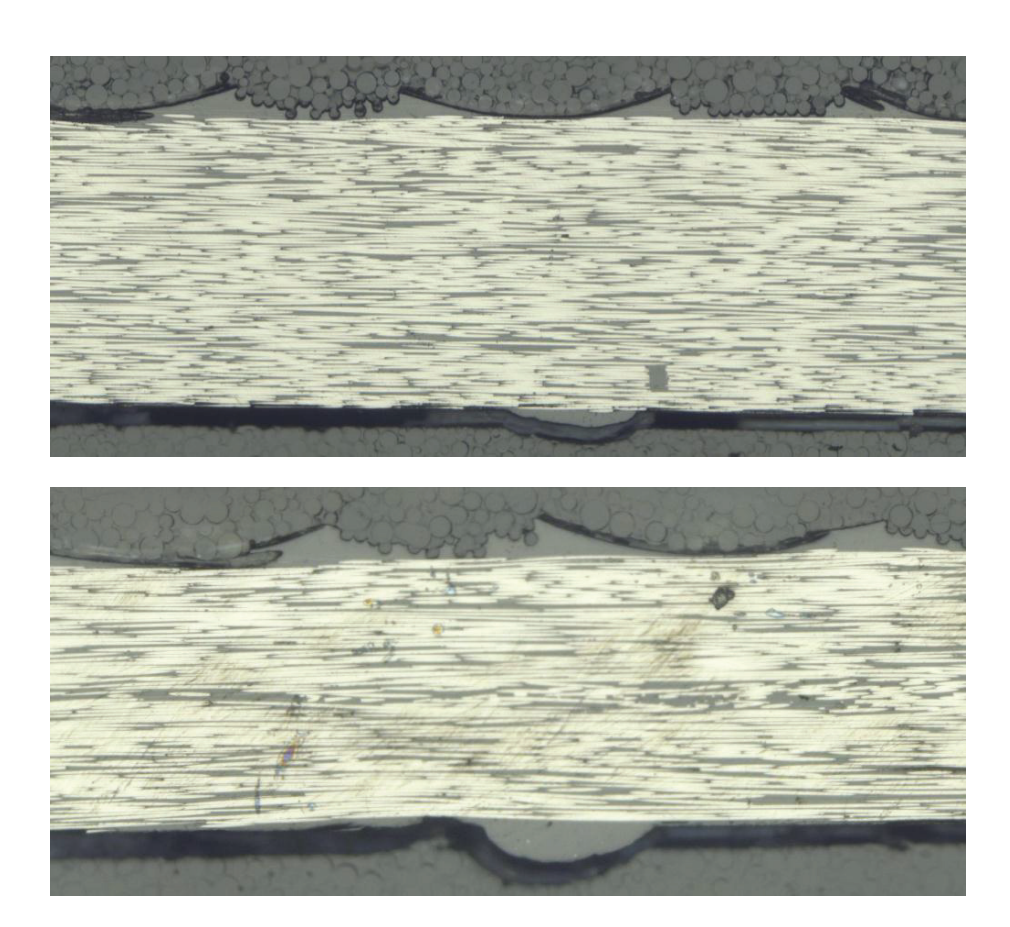


Fig. B2: Microscopic analysis for the configuration I (top) and the regular configuration (bottom)

The bottom side of each figure represents the tool-sided surface. The bump, located approximately in the center of both figures, represents one chamfer on the tool surface. A comparison between both figures shows that no interply slippage occurs as no residual gap is observed after manufacturing. This is in accordance with Ersoy et al. [63] who measured higher ply-to-ply friction properties compared to ply-to-tool interfaces. Nevertheless, this experiment needs to be conducted a number of times in order to gain statistical evidence. Moreover, this setup should be used for process-cycles variations.

C Spring-in Prediction Tool in MATLAB

The GUI of the developed Matlab-based spring-in prediction tool is given in Figure C3.

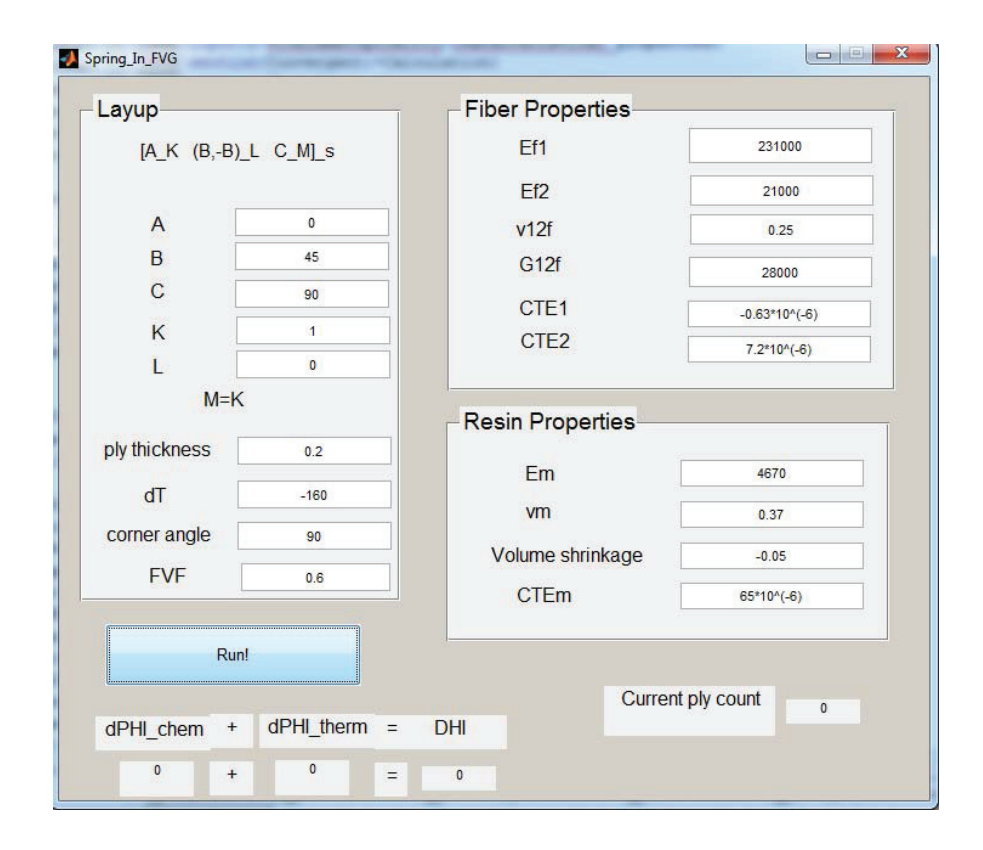


Fig. C3: Spring-in prediction tool GUI

The underlying CLT based code is summarized in the following Figure.

Matlab Code

Input

Arbitrary layup $[45, -45, ..., ...]_s$ Ply thickness t_k Resin shrinkage Section angle φ Cool-down temperature ΔT

Mechanical

$$E_{1} = E_{f1} \cdot FVF + E_{m} (1 - FVF)$$

$$E_{2} = \frac{E_{m}}{1 - \nu_{m}^{2}} \cdot \frac{1 + 0.85FVG^{2}}{(1 - FVG)^{1.25} + \frac{E_{m} \cdot FVF}{(1 - \nu_{m}^{2})E_{f2}}}$$

$$\nu_{12} = \nu_{f12} \cdot FVF + \nu_{m} (1 - FVF)$$

$$\nu_{21} = \nu_{12} \frac{E_{2}}{E_{1}}$$

$$G_{12} = G_{m} \cdot \frac{G_{f12} + G_{m} + FVF(G_{f12} - G_{m})}{G_{f12} + G_{m} - FVF(G_{f12} - G_{m})}$$

Extensional Stiffness Matrix

$$Q_{ij} \to \bar{Q}_{ij} \to \underline{\underline{A}} = \sum_{k=1}^{N} \underline{\underline{Q}}_{k} \cdot t_{k}$$

Thermal (Laminate)

$$\begin{split} & \underline{Asum}_{FVF} = \sum_{k=1}^{N} \underline{\underline{Q}}_{k} \underline{\alpha}_{global_{k}} \cdot t_{k} \\ & \underline{\alpha}_{global,lam} = \underline{\underline{A}}^{-1} \cdot \underline{Asum}_{FVF} \\ & \underline{Chemical} \ (Laminate) \\ & \underline{Bsum}_{FVF} = \sum_{k=1}^{N} \underline{\underline{Q}}_{k} \underline{shrink}_{global_{k}} \cdot t_{k} \end{split}$$

$$\underbrace{\frac{1}{k-1}}_{k} = \underbrace{\underline{A}}^{-1} \cdot \underline{Bsum}_{FVF}$$

Mechanical Properties

$$E_{f1}, E_{f2}, \nu_{f12}, G_{f12}, \alpha_{f1}, \alpha_{f2}$$

Matrix
 E_m, ν_m, α_m

Thermat (1 ty)
$$\alpha_{1,FVF} = \frac{FVF \cdot E_{f1}\alpha_{f1} + (1 - FVF)E_{m}\alpha_{m}}{FVF \cdot E_{f1} + (1 - FVF)E_{m}}$$

$$\alpha_{2,FVF} = FVF \cdot \alpha_{f2} + (1 - FVF)\alpha_{m}$$

$$\underline{\alpha}_{local} = \{\alpha_{1,FVF}, \alpha_{2,FVF}, 0\}^{T}$$

$$\underline{\alpha}_{global} = \underline{T}^{-1}\underline{\alpha}_{local}$$

Chemical (Ply)

$$shrink_{eff} = (1 - FVF) shrinkage$$

$$shrink_{vec} = -1 + \sqrt{1 - shrink_{eff}}$$

$$\underline{shrink_{local}} = \{0, shrink_{vec}, 0\}^T$$

$$\underline{shrink_{global}} = \underline{\underline{T}}^{-1} \underline{shrink_{local}}$$

$$m{Spring-In\ fractions}
ightarrow f\left(FVF
ight)$$

$$\Delta \varphi = \varphi \left\{ \frac{(\alpha_T - \alpha_R)\Delta T}{1 + \alpha_R \Delta T} + \frac{\xi_T - \xi_R}{1 + \xi_R} \right\}$$

$$\Delta \varphi = \Delta \varphi_{thermal} + \Delta \varphi_{chemical}$$

$$\begin{split} & \textit{Spring-In fractions} \rightarrow f\left(FVF\right) \\ & \Delta \varphi = \varphi \left\{ \frac{(\alpha_T - \alpha_R)\Delta T}{1 + \alpha_R \Delta T} + \frac{\xi_T - \xi_R}{1 + \xi_R} \right\} \\ & \Delta \varphi = \Delta \varphi_{thermal} + \Delta \varphi_{chemical} \\ & \Delta \varphi = \varphi \left\{ \frac{\alpha_T \Delta T}{1 + \alpha_R \Delta T} + \frac{-\alpha_R \Delta T}{1 + \xi_R} + \frac{-\xi_R}{1 + \xi_R} \right\} \\ & \Delta \varphi = \Delta \varphi_{T,R} + \Delta \varphi_{T,T} + \Delta \varphi_{R,R} + \Delta \varphi_{R,T} \end{split}$$

Shrinkage - isotropic, anisotropic

Chemical shrinkage is one major contributor to spring-in distortions. Due to the massive anisotropy of current ply-based composites with their resin dominated properties in thickness direction, this effect needs to be considered as outlined in the preceding. Within Section 4.1 the volumetric shrinkage of the resin is transferred to equivalent shrinkage in the ply's transversal direction.

This is based on the assumption that a unidirectional ply does not shrink in fiber direction as the fiber stiffness is significantly larger than the resin stiffness. Thus, it is physically reasonable that shrinkage occurs almost completely in the un-constrained transverse direction. However, when using the CLT, homogenized ply parameters are necessary which are derived from the fiber and the resin properties.

As only the resin shrinks during processing, this must be transferred to an equivalent shrinkage of the homogenized ply. To account for shrinkage effects within the CLT the resin shrinkage ΔV

is transferred to equivalent strains in transverse direction. Figure D4 shows a homogeneous continuum in the initial \tilde{K} and the actual configuration.

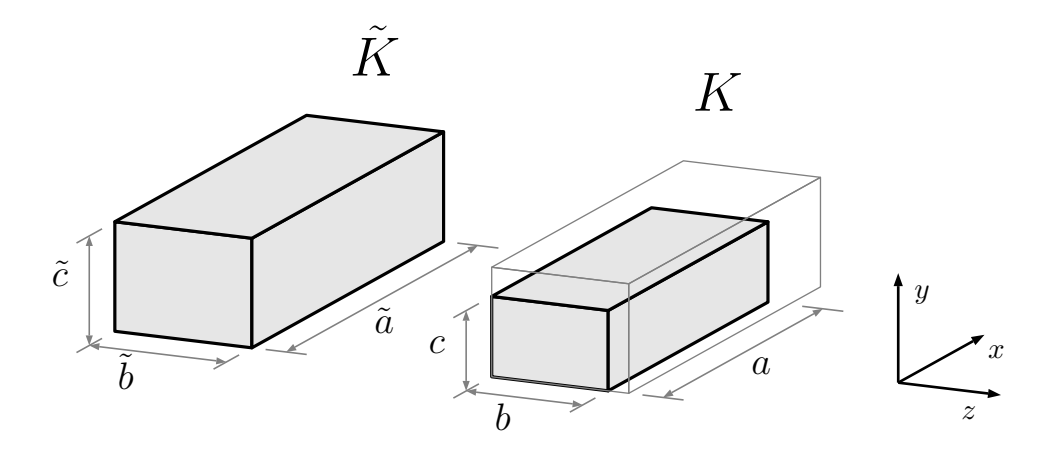


Fig. D4: A homogeneous continuum in reference configuration \tilde{K} and as-built configuration K. Volume change due to cure shrinkage

Corresponding parameters are summarized in Table 8.1

 $\begin{array}{lll} V & \text{actual-volume } [m^3] \\ \tilde{V} & \text{reference-volume } [m^3] \\ \tilde{a}, \tilde{b}, \tilde{c} & \text{reference-lengths } [m] \\ a, b, c & \text{actual-lengths } [m] \\ \epsilon_i & \text{strain in i-direction } [\%] \\ \lambda_i & \text{elongation in i-direction } [\%] \\ \Delta V & \text{volume-shrinkage } [\%] \end{array}$

Tab. 8.1: Parameters for the derivation of orthotropic shrinkage

The volume of the reference \tilde{V} and the actual configuration V are given by:

$$\tilde{V} = \tilde{a} \cdot \tilde{b} \cdot \tilde{c}$$
 and $V = a \cdot b \cdot c$ (D.25)

Therein, the actual length \tilde{a} is derived based on the reference length a multiplied with the elongation λ_a .

$$a = \lambda_a \cdot \tilde{a} \quad \text{with} \quad \lambda_i = \varepsilon_i + 1$$
 (D.26)

The volume change of the continuum is described by:

$$\Delta V = \frac{V - \tilde{V}}{\tilde{V}} = \frac{V}{\tilde{V}} - 1 \quad . \tag{D.27}$$

Using this equation and introducing Equation D.26 for each dimension yields:

$$\Delta V = \frac{abc}{\tilde{a}\tilde{b}\tilde{c}} - 1 = \frac{\lambda_a \lambda_b \lambda_c \tilde{a}\tilde{b}\tilde{c} - \tilde{a}\tilde{b}\tilde{c}}{\tilde{a}\tilde{b}\tilde{c}} = \lambda_a \lambda_b \lambda_c - 1 \tag{D.28}$$

This represents the volume change ΔV as a function of the elongation in each x,y and z direction. Replacing elongation terms with strain terms gives:

$$\Delta V = (\varepsilon_a + 1)(\varepsilon_b + 1)(\varepsilon_c + 1) - 1 \tag{D.29}$$

Expanding of Equation D.29 gives ΔV as a function of the strains which is, of course, independent from the volume.

$$\Delta V = \varepsilon_a \varepsilon_b \varepsilon_c + \varepsilon_a \varepsilon_b + \varepsilon_a \varepsilon_c + \varepsilon_b \varepsilon_c + \varepsilon_a + \varepsilon_b + \varepsilon_c \tag{D.30}$$

Regarding an isotropic material which is described by $\varepsilon_a = \varepsilon_b = \varepsilon_c = \varepsilon$ Equation D.31 simplifies to:

$$\Delta V = \varepsilon^3 + 3\varepsilon^2 + 3\varepsilon = 3\varepsilon \cdot (1 + \varepsilon + \frac{1}{3}\varepsilon^2). \tag{D.31}$$

Rearranging and the neglect of higher order terms allows gives the often cited Equation $\varepsilon \approx \frac{\Delta V}{3}$. For sake of comparison to thermal strains this this can be related to a arbitrary temperature change For regarding chemical shrinkage as a function of temperature the following transformation is necessary.

$$\varepsilon = \frac{\Delta V}{3} \rightarrow \alpha_{therm,equi} = \frac{\Delta V}{3\Delta T} \text{ with } \varepsilon = \alpha_{therm,equi} \cdot \Delta T$$
 (D.32)

Transversal Expansion only

Regarding an orthotropic material such as an homogenized prepreg ply for example, Equation D.30 must be used. No strains in fiber direction (parallel to x) and homogeneous strains in the transverse plane are described by:

$$\varepsilon_a = 0$$
 and $\varepsilon_b = \varepsilon_c = \varepsilon^*$. (D.33)

Introducing these terms to Equation D.30 gives:

$$\varepsilon^{*2} + 2\varepsilon^* = \Delta V \tag{D.34}$$

Solving for ε^* yields:

$$\varepsilon^* = -1 + \sqrt{1 + \Delta V} \tag{D.35}$$

Assuming that the orthotropic continuum shrinks 3% during processing this is equivalent to $\Delta V = -3\%$. The corresponding strain in transverse direction is:

$$\varepsilon^* = -1 + \sqrt{0.97} \to -0.0151 \to -1.51\%$$
 (D.36)

Transferring this to a quasi-thermal strain in order to compare thermal contraction with strains due to chemical shrinkage Equation D.36 is divided by the acting ΔT . Assuming a cool down from curing temperature to room temperature of -160 K, $\alpha_{therm,equi}$ is derived to 94.375 ppm/K.

Note that Equation D.35 is derived for homogeneous orthotropic material. Regarding a common composite this must be adapted as only the resin shrinks. Therefore, the effective volume change is a function of the fiber volume fraction as $V_{resin} = V \cdot (1 - V_f)$. Consequently, Equation D.35 is extended by this factor.

$$\varepsilon^* = -1 + \sqrt{1 + (1 - V_f) \cdot \Delta V} \tag{D.37}$$

- [1] AIRBUS. Growth and replacement needs for more eco-efficient aircraft. Press Release, November 22th 2011. (Cited on page 1).
- [2] Composites World. Audi, Voith create partnership for composites development. Article, February 28th 2011. (Cited on page 1).
- [3] Composites World. BMW rolls out prototypes of composites-intensive I3, I8. Article, August 8th 2011. (Cited on page 1).
- [4] D.Person. EADS CEO: Airbus production ramp-up depends on supply chain. Dow Jones Newswires, July, 29th 2011. (Cited on page 1).
- [5] D.W.Radford. Shape Stability in Composites. PhD thesis, Rensselaer Polytechnic Institute, Troy, New York, 1987. (Cited on pages 2, 3, 5, 6, 8, 10, 17, 18, 20, 21, 22, 22, 24, 24, 37, 55, 64, 80, 169).
- [6] A.A.Johnston. An Integrated Model of the Development of Process-Induced Deformation in Autoclave Processing of Composite Structures. PhD thesis, The University of New Brunswick, 1992. (Cited on pages 2, 27).
- [7] F.C.Campbell. Manufacturing Technology for Aerospace Structural Materials. Elsevier, 2006. (Cited on page 3).
- [8] C.Albert and G.Fernlund. Spring-in and warpage of angled composite laminates. *Composite Science and Technology*, 62:1895–1912, 2002. (Cited on pages 3, 7, 7, 11, 11, 12, 21, 22, 169).
- [9] D.Stefaniak, E.Kappel, T.Spröwitz, and C.Hühne. Experimental identification of parameters inducing warpage of autoclave-processed CFRP parts. *Composites: Part A*, 43:1081–1091, 2012. (Cited on pages 3, 4, 10, 37, 41, 47, 152).
- [10] G.Fernlund, A.Osooly, and A.Poursatip. Finite element based prediction of process-induced deformation of autoclaved composite structures using 2d process analysis and 3d structual analysis. *Composite Structures*, 62:223–234, 2003. (Cited on pages 3, 11, 13, 16, 23, 102, 103, 105, 106).
- [11] G.Twigg, A.Poursartip, and G.Fernlund. An experimental method for quantifying tool-part shear interaction during composites processing. *Composite Science and Technology*, 63:1985, 2003. (Cited on pages 3, 4, 5, 22, 23, 90).
- [12] T.Wille, S.Freund, and R.Hein. Comparison of methods to predict process induced residual stresses and distortions of CFRP components. In *NAFEMS Seminar: Progress in Simulating Composites*, 2011. (Cited on pages 4, 27).
- [13] M.Kleineberg. *Präzisionsfertigung komplexer CFK-Profile am Beispiel Rumpfspant*. PhD thesis, Carolo Wilhelmina University Braunschweig, Braunschweig, 2008. (Cited on pages 5, 31, 65, 97).

[14] T.Garstka, N.Ersoy, K.D.Potter, and M.R.Wisnom. In situ measurements of through-the-thickness strains during processing of AS4/8552 composite. *Composites: Part A*, 38:2517–2526, 2007. (Cited on pages 5, 19, 48, 82, 84, 84, 85, 169).

- [15] H.W.Wiersma, L.J.B.Peters, and R.Akkerman. Prediction of springforward in continuous-fibre/polymer l-shaped parts. *Composites Part A*, 29:1333–1342, 1998. (Cited on page 7).
- [16] H.Sarrazin, B.Kim, S.-H.Ahn, and G.S.Springer. Effects of processing temperature and layup on springback. *Journal of Composite Materials*, 29:1278, 1995. (Cited on pages 7, 18).
- [17] G.Fernlund, A.Floyd, and S.McKay. Process analysis and tool compensation for curved composite l-angles. *The Sixth Canadian-International Composites Conference, Winnipeg, Canada*, 2007. (Cited on page 7).
- [18] D.A.Darrow and L.V.Smith. Isolating components of processing induced warpage in laminated composites. *Journal of Composite Materials*, 36:2407–2418, 2002. (Cited on pages 7, 19).
- [19] L.K.Jain, B.G.Lutton, Y.-W.Mai, and R.Paton. Stresses and deformations induced during manufacturing. part ii: A study of the spring-in phenomenon. *Journal of Composite Materials*, 31 No.7:696–719, 1997. (Cited on pages 7, 18, 19, 21, 169).
- [20] R.H.Nelson and D.C.Cairns. Prediction of dimensional changes in composite laminates during cure. 34th international SAMPE Symposium, 34:2397–2410, 1989. (Cited on pages 8, 19, 19, 20, 24, 24, 24, 24, 89, 93, 169, 170).
- [21] G.Fernlund, N.Rahman, R.Courdji, M.Bresslauer, A.Poursartip, K.Willden, and K.Nelson. Experimental and numerical study of the effect of cure cycle, tool surface, geometry and lay-up on the dimensional fidelity of autoclave-processed composite parts. *Composites Part A*, 33:341–351, 2002. (Cited on pages 10, 22, 70).
- [22] D.Stefaniak. Experimentelle Untersuchung der Warpage Verformung ebener, warmgehärteter CFK-Prepreg-Laminated in Abhängigkeit schichtweise variierender Lagenorientierungen. Insitute of Composite Struttures and Adaptive Systems, Diploma Thesis,
 German Aerospace Center (DLR), 2010. (Cited on page 10).
- [23] N.Ersoy, K.Potter, M.R.Wisnom, and M.J.Clegg. Development of spring-in angle during cure of thermosetting composite. *Composites: Part A*, 36:1700–1706, 2005. (Cited on pages 10, 20, 48).
- [24] M.R.Wisnom, M.Gigliotti, N.Ersoy, M.Campbell, and K.D.Potter. Mechanisms generating residual stresses and distortion during manufacture of polymer-matrix composite structures. *Composites: Part A*, 37:522–529, 2006. (Cited on pages 11, 20, 24).
- [25] K.D.Potter, M.Campbell, C.Langer, and M.R.Wisnom. The generation of geometrical deformations due to tool/part interaction in the manufacture om composite components. *Composites Part A*, 36:301, 2005. (Cited on page 11).
- [26] J.M.Svanberg. Predictions of Manufacturing Induced Shape Distortions high performance thermoset composites. PhD thesis, Lulea University of Thechnology, 2002. (Cited on pages 14, 27, 29).
- [27] T.Nguyen. Effect of curvature on the stresses of curved laminated beams subjected to bending. PhD thesis, The University of Texas at Arlington, 2010. (Cited on page 15).

[28] A.Jumahat, C.Soutis, F.R.Jones, and A.Hodzic. Fracture mechanisms and failure analysis of carbon fibre/toughened epoxy composites subjected to compressive loading. *Composite Structures*, 92(2):295–305, 2009. (Cited on page 15).

- [29] Torayca. T300 Technical Data Sheet, 2012. (Cited on page 15).
- [30] C.K.Huang and S.Y.Yang. Warping in advanced composite tools with varying angles and radii. *Composites: Part A*, 28A:891–893, 1997. (Cited on page 16).
- [31] C.K.Huang and S.Y.Yang. Study on accuracy of angled advanced composite tools. *Materials and Manufacturing Processes*, 12:3:473–486, 1997. (Cited on page 16).
- [32] T.Spröwitz, J.Tessmer, and T.Wille. Thermal aspects for composite structures from manufacturing to in-service predictions. *26th International Congress of the aeronautical sciences*, 1:1–10, 2008. (Cited on pages 17, 20, 25).
- [33] L.K.Jain, M.Hou, L.Ye, and Y.-W.Mai. Spring-in study of the aileron rib manufactures from advanced thermoplastic composite. *Composites Part A*, 29A:973–979, 1998. (Cited on pages 18, 19, 19, 24, 24, 24, 24).
- [34] A.Beukers P.P.Parlevliet, H.E.N.Bersee. Residual stresses in thermoplastic composites a study of the literature part i: Formation of residual stresses. *Composites: Part A*, 37:1847–1857, 2006. (Cited on page 18).
- [35] A.Beukers P.P.Parlevliet, H.E.N.Bersee. Residual stresses in thermoplastic composites a study of the literature partii: Experimental techniqes. *Composites: Part A*, 38:651–655, 2007. (Cited on page 18).
- [36] A.Beukers P.P.Parlevliet, H.E.N.Bersee. Residual stresses in thermoplastic composites a study of the literature parr iii: Effects of thermal residual stresses. *Composites: Part A*, 38:1581–1596, 2007. (Cited on page 18).
- [37] L.P.Kollar. Approximate analysis of the temperature induced stresses and deformations of composite shells. *Journal of Composite Materials*, 28:392, 1994. (Cited on pages 18, 24).
- [38] C.K.Huang and S.Y.Yang. Warping in advanced composites tools with varying angles and radii. *Composites Part A*, 28A:891–893, 1997. (Cited on pages 18, 24).
- [39] K.J.Yoon and J.-S.Kim. Effect of thermal deformation and chemical shrinkage on the process induced distortion of carbon/epoxy curved laminates. *Journal of Composite Materials*, 35:253–263, 2001. (Cited on pages 19, 20, 21, 24, 89, 93).
- [40] D.A.Darrow and L.V.Smith. Evaluation the spring-in phenomenon of polymer matrix composites. *J33rd International SAMPE Technical Conference*, 2001. (Cited on page 19).
- [41] D.W.Radford. Volume fraction gradient induced warpage in curved composite laminates. *Composite Engineering*, 5:923, 1995. (Cited on pages 19, 24, 66).
- [42] D.W.Radford and R.J.Diefendorf. Shape instabilities in composite resulting from laminate anisotropy. *Journal of Reinforced Plastics an Composites*, 12:58, 1993. (Cited on pages 19, 21).
- [43] J.M.Svanberg and J.A.Holmberg. An experimental investigation on mechanisms for manufacturing induced shape distortions in homogeneous and balanced laminates. *Composites Part A*, 32:821–838, 2001. (Cited on pages 20, 25, 30).

[44] J.M.Svanberg and J.A.Holmberg. Prediction of shape distortions part i. fe-implementation of a path dependent constitutive model. *Composites Part A*, 35:711–721, 2004. (Cited on page 20).

- [45] J.M.Svanberg and J.A.Holmberg. Prediction of shape distortions part ii: experimental validation and analysis of boundary conditions. *Composites Part A*, 35:723–734, 2004. (Cited on pages 20, 24).
- [46] S.T.Bapanapalli and L.V.Smith. A linear finite element model to predict processing-induced distortion in frp laminates. *Composites Part A*, 36:1666–1674, 2005. (Cited on pages 20, 21, 50).
- [47] A.Salomi, T.Garstka, K.Potter, A.Greco, and A.Maffezzoli. Spring-in angle as molding distortion for thermoplastic matrix composite. Composite Science and Technology, 68:3047–3054, 2008. (Cited on page 20).
- [48] T.Spröwitz, J.Tessmer, and T.Wille. Process simulation in fiber composite manufacturing spring-in. *Nafems Seminar: Simulating Composite Materials and Structures*, pages 1–10, 2007. (Cited on pages 20, 25, 31).
- [49] Y.Ding, W.K.Chiu, and X.L.Liu. Anisotropy related spring-in of angled composite shells. *Polymers & Polymer Composites*, 6:393–401, 2001. (Cited on pages 21, 149).
- [50] D.W.Radford and T.S.Rennick. Separating sources of manufacturing distortion in laminated composites. *Journal of Reinforced Plastics and Composites*, 19:621–641, 2000. (Cited on pages 21, 24).
- [51] T.Nyman, M.Svanberg, and E.Hörberg. A simplified method for predictions of shape distortions. Technical report, Saab Aerostructures, Linöping Sweden, 2008. (Cited on page 21).
- [52] N.Ersoy M.R.Wisnom, K.D.Potter. Shear-lag analysis of the effect of thickness on springin of curved composites. *Journal of Composite Materials*, 41:1311, 2007. (Cited on page 22).
- [53] G.Fernlund. Spring-in of angled sandwich panels. Composite Science and Technology, 65:317–323, 2005. (Cited on page 22).
- [54] X.Zeng and J.Raghavan. Role of tool-part interaction in process-induced warpage of autoclave-manufactured composite structures. *Composites: Part A*, 41:1174–1183, 2010. (Cited on page 22).
- [55] G.Fernlund. Risk reduction in composites processing using prototype data, process simulation, and bayesian statistics. *Composites: Part A*, 41:295–303, 2010. (Cited on pages 22, 24).
- [56] G.Twigg, A.Poursatip, and G.Fernlund. Tool-part interaction in composites processing. part i experimental investigation and analytical model. *Composites*, Part A 35:121–133, 2004. (Cited on pages 22, 22, 23, 37, 39, 43).
- [57] G.Twigg, A.Poursatip, and G.Fernlund. Tool-part interaction in composites processing. part ii- numerical modelling. *Composites Part A*, 35:135–141, 2004. (Cited on pages 22, 23, 23).

[58] J.D.D.Melo and D.W.Radford. Modeling manufacturing distortions in flat symmetric, composite laminates. *International SAMPE Technical Conference*, 31:592–603, 1999. (Cited on pages 23, 47).

- [59] Y.Zhang, Q.Ren, and Y.-P.Zhao. Modeling analysis of surface stress on a rectangular cantilever beam. *Journal of Physics D: Applied Physics*, 37:2140, 2004. (Cited on page 23).
- [60] O.Kopmaz and Ö.Gündogdu. On the curvature of an euler-bernoulli beam. *International Journal of Mechanical Engineering Education*, 31:132–142, 2003. (Cited on page 23).
- [61] K.D.Potter, M.A.Campbell, and M.R.Wisnom. Investigation of tool/part interaction effects in the manufacture of composite components. *Proceedings ICCM 14, San Diego*, 2003. (Cited on page 23).
- [62] W.-K.Jung, W.-S.Chu, S.-H.Ahn, and M.-S.Won. Measurement and compensation of spring-back of a hybrid composite beam. *Journal of Composite Materials*, 41:851, 2007. (Cited on pages 23, 24).
- [63] N.Ersoy, K.Potter, M.R.Wisnom, and M.J.Clegg. An experimental method to study the frictional processes during composites manufacturing. *Composites: Part A*, 36:1536–1544, 2005. (Cited on pages 23, 47, 47, 176).
- [64] A.R.A.Arafath, R.Vaziri, and A.Poursatip. Closed-form solution for process induced stresses and deformation of a composite part cured on a solid tool: Part i flat geometries. Composites: Part A, 39:1106–1117, 2008. (Cited on pages 23, 51).
- [65] A.R.A.Arafath, R.Vaziri, and A.Poursatip. Closed-form solution for process induced stresses and deformation of a composite part cured on a solid tool: Part ii curved geometries. *Composites: Part A*, 40:1545–1557, 2009. (Cited on page 23).
- [66] S.Wijskamp. Shape Distortions in Composites Forming. PhD thesis, University of Twente, 2005. (Cited on page 27).
- [67] P.Hubert. Aspects of Flow and Compaction of Laminated Composite Shapes During Cure. PhD thesis, The University of British Columbia, 1996. (Cited on page 27).
- [68] J.S.Sun, Y.Gu, M.L.Xianxing Ma, and Z.Zhang. Effect of forming temperature on the quality of hot diaphragm formed c-shaped thermosetting composite laminates. *Journal of Reinforced Plastics and Composites*, 31:1074, 2012. (Cited on pages 29, 47, 47, 110).
- [69] R.Hill. Theroy of meachanical properties of fibre-strengthened materials. *Journal of Applied Mechanics*, 31:223–232, 1962. (Cited on page 29).
- [70] S.W.Tsai and H.T.Hahn. Introduction to Composite Materials. *Technomic Publishing Company*, 1980. (Cited on page 29).
- [71] Z.Hashin. Analysis of composite materials A survey. *Journal of Applied Mechanics*, 50:481–505, 1983. (Cited on page 29).
- [72] C.C.Chamis. Simplified composite micromechanics equations for hygral, thermal, and mechanical properties. *SAMPE*, 15:14–23, 1984. (Cited on page 29).
- [73] B.Gorenc, R.Tinyou, and A.Syam. *Steel Designer's Handbook (6th Edition)*. University of New South Wales Press, 2004. (Cited on page 38).

- [74] H.Hoischen. Technisches Zeichnen. Cornelsen Girardet, 2003. (Cited on page 38).
- [75] HexCel-Composites. *HexTow AS4 Product Data*, 2009. (Cited on pages 40, 40, 60, 60, 60, 60, 66, 81).
- [76] HexCel-Composites. HexPly M21- Product Data, Dec. 2010. (Cited on pages 40, 71).
- [77] X.Zhang, M.Boscolo, Figueroa-Gordon, G.Allegri, and P.E.Irving. Fail-safe design of integral metallic aircraft structures reinforced by bonded crack retarders. *Engineering Fracture Mechanics*, 78:114–133, 2009. (Cited on page 40).
- [78] K.Rohwer, E.Kappel, D.Stefaniak, and T.Wille. Spring-in and warpage progress in simulating manufacturing aspects. MCM 2012, -:-, 2012. (Cited on page 41).
- [79] F.Gao, G.Jiao, Z.Lu, and R.Ning. Mode ii delamination and damage resistance of carbon/epoxy composite laminates interleaved with thermoplastic particles. *Journal of Composite Materials*, 41:111, 2007. (Cited on page 42).
- [80] G.Marsh. Wing worker for the world. *Reinforced Plastics*, page 25, 2010. (Cited on page 46).
- [81] M.Gigliotti, M.R.Wisnom, and K.D.Potter. Development of curvature during the cure of as4/8552 [0/90] unsymmetric composite plates. *Composites Science and Technology*, 63:187–197, 2003. (Cited on page 48).
- [82] N.Ersoy, T.Garstka, K.Potter, M.R.Wisnom, D.Porter, and G.Stringer. Modelling of the spring-in phenomenon in curved parts made of a thermosetting composite. *Composites:* Part A, 41:410–418, 2010. (Cited on page 48).
- [83] H.Schürmann. Konstruieren mit Faser-Kunststoff-Verbunden. Springer, 2007. (Cited on pages 59, 81).
- [84] M.S.Anghelescu and M.K Alam. Carbon foam tooling for aerospace composites. *SAMPE*, *Journal*, 44:6–13, 2008. (Cited on page 60).
- [85] HexCel-Composites. HexPly 8552 Product Data, 2008. (Cited on page 60).
- [86] Sergio Pellegrino. Ultra-thin carbon fiber composites:constitutive modeling and applications to deployable structures. California Institute of Technology. (Cited on page 60, 60, 60).
- [87] B.P.Row. *Probability and Statistics in Experimental Physics*. Springer, Berlin, 1992. (Cited on page 68).
- [88] A.Hamamoto. Curing of l-shaped composite parts. *Proceedings of International Symposium on Composite Materials and Structures*, pages 1092–1097, 1986. (Cited on page 69).
- [89] R.Flanagan. The Dimensional Stability of Composite Laminates and Structures. PhD thesis, Queen's University of Belfast, 1997. (Cited on page 70).
- [90] T.Blochowicz and F.Laeri. Einführung in die Messdatenanalyse für das Physikalische Grundpraktikum. TU Darmstadt, Darmstadt, 2011. (Cited on page 78).
- [91] S.A.Mihnea and K.M.Alam. Carbon foam tooling for aerospace composites. Department of Mechanical Engineering, Ohio University, Athens, OH 45701. (Cited on page 81, 81, 81).

[92] GOM Gesellschaft für optische Messtechnik. GOM Inspect V7-SR2 Direkthilfe, 2011. (Cited on page 90).

- [93] P.Hubert and A.Poursatip. Aspects of the compaction of composite angle laminates: An experimental investigation. *Journal of Composite Materials*, 35:1, 2001. (Cited on page 92, 92).
- [94] R.S.Trask, S.R.Hallett, F.M.M.Helenon, and M.R.Wisnom. Influence of process induced defects on the failure of composite t-joint specimens. *Composites Part A: Applied Science and Manufacturing*, 43:748–757, 2012. (Cited on pages 114, 115).
- [95] F.Hélénon, M.R.Wisnom, S.R.Hallett, and R.S.Trask. Numerical investigation into failure of laminated composite t-piece specimens under tensile loading. *Composites Part A: Applied Science and Manufacturing*, 43:1017–1027, 2012. (Cited on page 116).
- [96] A.T.Nettles. Basic mechanics of laminated composite plates nasa reference publication 1351. Technical report, NASA, 1994. (Cited on page 123).
- [97] G.Merziger and T.Wirth. Repetitorium der höheren Mathematik. Binomi, März 2006. (Cited on page 128).
- [98] David Salomon. Curves and Surfaces for Computer Graphics. Department of Computer Science, 2006. (Cited on page 134).
- [99] R.Prussak. Experimentelle validierung des bestehenden warpage konzepts und erweiterung auf einfach gekrümmte, flächige und dünnwandige strukturen. *Technische Universität Dresden*, 2012. (Cited on page 136).
- [100] J.Schmidt. Konzeptentwicklung zur Fertigung einer laminaren Flügelvorderkante. *DLR IB 131-2011/01*, 2010. (Cited on page 145).
- [101] Wikipedia. Barycentric coordinates as a function of the side lengths, December 2012. (Cited on page 147).
- [102] E.Kappel, D.Stefaniak, T.Spröwitz, and C.Hühne. A semi-analytical simulation strategy and its application to warpage of autoclave-processed CFRP parts. *Composites: Part A*, 42:1985–1994, 2011. (Cited on page 152).

Own Publications

Journal Papers

- **E.Kappel, D.Stefaniak, T.Spröwitz, C.Hühne** A semi-analytical simulation strategy and its application to warpage of autoclave-processed CFRP parts, Composites: Part A, 42:1985–1994, 2011.
- **E.Kappel, D.Stefaniak, C.Hühne** Manufacturing distortions of a CFRP box-structure A semi-numerical prediction approach, Composites: Part A, Submitted for publication
- K.Rohwer, E.Kappel, D.Stefaniak, T.Wille-Spring-in and Warpage Progress in Simulating Manufacturing aspects, Mechanics of Composite Materials, Publication in progress
- **D.Stefaniak**, **E.Kappel**, **T.Spröwitz**, **C.Hühne** Experimental identification of parameters inducing warpage of autoclave-processed CFRP parts, Composites: Part A, 43:1081–1091, 2012.
- **E.Kappel, D.Stefaniak, C.Hühne** A semi-analytical Simulation strategy and its application accounting for manufacturing induced deformations of autoclave-processed CFRP parts, Nafems Proceedings: Progress in Simulating Composites

Conference Papers

- E.Kappel, D.Stefaniak, C.Hühne- Semi-analytical Spring-in Analysis to Counteract CFRP Manufacturing Distortions by Tool Compensation, ICAS Conference 2012, Brisbane
- **D.Stefaniak, B.Kolesnikov, E.Kappel, C.Hühne** Improving Impact Endangered CFRP Structures by Metal-Hybridisation, ESA Estec Conference 2012
- **D.Stefaniak, B.Kolesnikov, E.Kappel, C.Hühne** Improving Impact Endangered CFRP Structures by Metal-Hybridisation, Venedig 2012
- K.Rohwer, E.Kappel, D.Stefaniak and T.Wille Spring-in and Warpage Progress in Simulating Manufacturing aspects, MCM 2012 Riga
- **T.Spröwitz, C.Hühne, E.Kappel** Thermal Aspects for Composite Structures From Manufacturing to In-Service Predictions, CEAS Conference 2009

Other Publications

E.Kappel, D.Stefaniak, C.Hühne. About the Spring-In Phenomenon: Quantifying the Effects of Thermal Expansion and Chemical Shrinkage. Adaptive, Tolerant and Efficient Composite Structures - Research Topics in Aerospace. Springer Berlin Heidelberg 2012. Seiten 275-283.

190 Own Publications

ISBN 978-3642291890

C.Hühne, E.Kappel, D.Stefaniak. Compliant Aggregation of Functionalities Adaptive, Tolerant and Efficient Composite Structures Research Topics in Aerospace. Springer Berlin Heidelberg 2012. Seiten 225-235. ISBN 978-3642291890

Patents and Patent applications

- $\bf E.Kappel$ Verformungsanalyse Verfahren zur Bestimmung der zu erwartenden, fertigungsinduzierten Deformation von Verbundstrukturen aus vorimprägnierten Halbzeugen (Prepreg) , 2012062813462400 DE
- **E.Kappel** Modellieren der Raumform eines einen Schichtaufbau aufweisenden Faserverbundbauteils nach dessen Aushärtung auf einem Formwerkzeug DE 10 2010 030 448.4-16
- **H.Köke, A.Stahl, E.Kappel**, Prüfverfahren Verfahren zum Bestimmen einer Verschereigenschaft eines aus Fasern gebildeten Faserhalbzeuges
- D.Stefaniak, B.Kolesnikov, J.Wolff, A.Fink, A.Hindersmann, E.Kappel Verfahren zur Herstellung von Hybridbauteilen aus faserverstärktem Kunststoff mit integriertem metallischem Formwerkzeug DE 102011050304

Curriculum Vitae

Name: Erik Kappel
Date of Birth: April 2, 1983
Nationality: German
Address: Weidegrund 1

30900 Wedemark

Education

1989-2002 Primary school, secondary school and gymnasium 2002-2003 Military service 2003-2009 Mechanical engineering at Leibniz University Hannover Subjects: Mechanics & Design

. Mechanics & Design

Robotics

Diploma Thesis: Generalization of one-dimensional material models

with the concept of representative directions

Career

2008	Student assistant - Mechanics Institute - Leibniz University of Hannover
2008	Internship - Continental CONTITECH, Hannover
2008-2009	Diplomate - Deutsches Institut für Kautschuktechnologie e.V. (DIK)
since 2009	German Aerospace Center (DLR), Braunschweig